AD-A198 685 PROCEEDINGS OF WORKSHOP 15 OF THE COSPAR MEETINGS HELD IN TOULOUSE FRANCE (U) AIR FORCE GEOPHYSICS LAB HANSCOM AFB MA K S CHAMPION 21 JAN 88 AFGL-TR-88-0016 1/2

UNCLASSIFIED F/G 4/1 NL

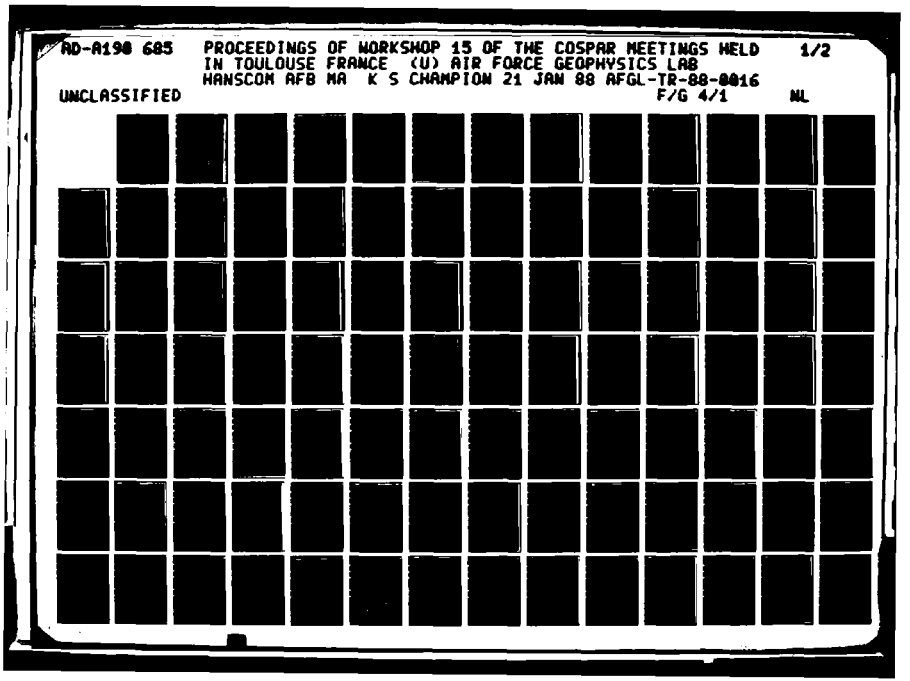

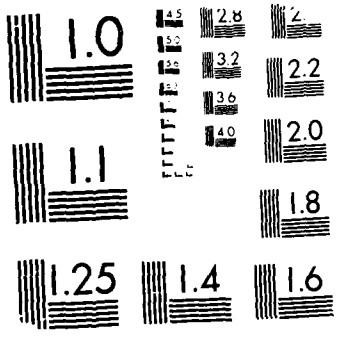

MICROCOPY RESOLUTION TEST CHART
NATIONAL BUREAU OF STANDARDS 1963-A

AFGL-TR-88-0016

DTIC FILE COPY

AD-A190 685

Chapter 2

Reference Atmospheres and Thermospheric Mapping (Workshop XV)

DTIC
ELECTE
FEB 05 1988
S D
H

DISTRIBUTION STATEMENT A
Approved for public release;

88 2 2 096

Unclassified

SECURITY CLASSIFICATION OF THIS PAGE

REPORT DOCUMENTATION PAGE

1a. REPORT SECURITY CLASSIFICATION Unclassified	1b. RESTRICTIVE MARKINGS
2a. SECURITY CLASSIFICATION AUTHORITY	3. DISTRIBUTION / AVAILABILITY OF REPORT Approved for public release; Distribution unlimited
2b. DECLASSIFICATION / DOWNGRADING SCHEDULE	
4. PERFORMING ORGANIZATION REPORT NUMBER(S) AFGL-TR-88-0016	5. MONITORING ORGANIZATION REPORT NUMBER(S)
6a. NAME OF PERFORMING ORGANIZATION Air Force Geophysics Laboratory 6b. OFFICE SYMBOL (If applicable)	7a. NAME OF MONITORING ORGANIZATION
6c. ADDRESS (City, State, and ZIP Code) Hanscom AFB Massachusetts 01731	7b. ADDRESS (City, State, and ZIP Code)
8a. NAME OF FUNDING / SPONSORING ORGANIZATION 8b. OFFICE SYMBOL (If applicable)	9. PROCUREMENT INSTRUMENT IDENTIFICATION NUMBER
8c. ADDRESS (City, State, and ZIP Code)	10. SOURCE OF FUNDING NUMBERS PROGRAM ELEMENT NO. 62101F; PROJECT NO 6670; TASK NO 18; WORK UNIT ACCESSION NO 04

11. TITLE (Include Security Classification)
Chapter 2 - Reference Atmospheres and Thermospheric Mapping (Workshop XV)

12. PERSONAL AUTHOR(S)
K.S.W. Champion (Editor)

13a. TYPE OF REPORT	13b. TIME COVERED	14. DATE OF REPORT (Year, Month, Day)	15. PAGE COUNT
REPRINT	FROM _____ TO _____	1988 January 21	

16. SUPPLEMENTARY NOTATION
Reprinted from Advances in Space Research "The Earth's Middle and Upper Atmosphere"
Vol 7, #10, pp 51-254, 1987

17 COSATI CODES		
FIELD	GROUP	SUB-GROUP

18. SUBJECT TERMS (Continue on reverse if necessary and identify by block number)
Atmospheric structure
Rocketsonde data
Global radar network
Mass spectrometer
Icoherent scatter

19. ABSTRACT (Continue on reverse if necessary and identify by block number)

This Chapter contains the Proceedings of Workshop XV of the COSPAR meetings held at Toulouse, France during 30 June-12 July 1986.

The first session was primarily concerned with middle atmosphere models and data.

The second session was concerned with properties of the upper middle atmosphere, and the third session covered thermospheric models and data.

20. DISTRIBUTION / AVAILABILITY OF ABSTRACT ☐ UNCLASSIFIED/UNLIMITED ☐ SAME AS RPT ☐ DTIC USERS	21. ABSTRACT SECURITY CLASSIFICATION Unclassified
22a. NAME OF RESPONSIBLE INDIVIDUAL K.S.W. Champion	22b. TELEPHONE (Include Area Code) (617) 377-3033 22c. OFFICE SYMBOL AFGL/LY

DD FORM 1473, 84 MAR 83 APR edition may be used until exhausted. All other editions are obsolete.

SECURITY CLASSIFICATION OF THIS PAGE
Unclassified

PREFACE

This Chapter contains the Proceedings of Workshop XV of the COSPAR meetings held at Toulouse, France during 30 June - 12 July 1986. The Workshop title was Presentation of CIRA* 1986 and Comparisons with Other Models, Data and Theories. The Workshop was divided into three sessions. The first session was primarily concerned with middle atmosphere models and data. There were introductory papers on atmospheric structure and its variations in the middle atmosphere. Presentations during this session included a discussion of the contribution of satellite temperature data to the development of middle atmosphere models and a determination of the variability of atmospheric properties obtained from analysis of rocketsonde data. Analysis of Meteorological Rocket Network temperature and wind data yielded the amplitudes and phases of their annual and semiannual variations. Another paper showed a 6K temperature increase at the 30 mb level (about 24 km altitude) as a result of increased heating due to dust injected into the atmosphere by the El Chicon volcanic eruption. Monthly mean temperature profiles for high latitude winter were compared with the corresponding profiles from the preliminary CIRA. A new set of ozone reference models was presented and also a proposed international reference tropical atmosphere.

The second session of the Workshop was concerned with properties of the upper middle atmosphere. The first paper contained preliminary structure models for the 80 to 120 km altitude range. They linked to lower altitude models but not to any thermospheric models. A unique set of data obtained from instruments on-board shuttle during reentry was presented. In a number of flights large density changes and fluctuations were observed above 70 km altitude. A major analysis of wind data from the Global Radar Network yielded mean zonal and meridional winds for altitudes from 75 to 110 km. Important differences were found when these winds were compared with geostrophic winds derived from rocket and satellite data. Possible explanations were presented. In another study, winds at these altitudes were analyzed for long period oscillations, with

*COSPAR International Reference Atmospheres

QUALITY INSPECTED 2

A-1

periods ranging from two to twenty days. Planetary and gravity waves contribute to the variability of middle atmosphere properties. This was demonstrated by the improved understanding of the spatial and temporal variability of wave fields that has resulted from recent radar and satellite studies. A review was presented on the present state of knowledge of turbulence in the upper middle atmosphere. An empirical global zonal mean wind and temperature model was developed from meteor radar and partial reflection drift data for the 70-110 km altitude region.

The third session covered thermospheric models and data. The session started with a paper on a theoretical general circulation thermospheric model for CIRA. This was followed by a presentation of an empirical model, MSIS 86 (Mass Spectrometer and Incoherent Scatter). A detailed analysis of high latitude rocket mass spectrometer data showed areas of agreement and of differences with existing thermospheric models. A number of papers presented results of measurements of thermospheric temperatures and winds using different techniques. These techniques included satellite in situ measurements, satellite optical remote sensing, and ground-based incoherent scatter and optical measurements. Other topics covered in the session included semi-annual density variations, changes in thermospheric density caused by turbopause height variations, effects of thermospheric storms, and the investigation of solar extreme ultraviolet, calcium plage and infrared emission as possible alternatives to the 10.7 cm flux as the primary index of solar activity.

K. S. W. CHAMPION
AFGL/LY
HANSCOM AFB, MA
U.S.A.

Adv. Space Res. Vol. 7, No. 10, pp. (10)57–(10)62, 1987
Printed in Great Britain. All rights reserved.

0273-1177/87 $0.00 + .50
Copyright © 1987 COSPAR

STANDARD DEVIATIONS OF METEOROLOGICAL PARAMETERS IN THE MIDDLE ATMOSPHERE, AS REVEALED BY ROCKETSONDE DATA

S. S. Gaigerov, Yu. P. Koshelkov, D. A. Tarasenko, V. V. Fedorov and E. N. Kovshova

Central Aerological Observatory of the State Committee of the U.S.S.R. for Hydrometeorology and Control of Natural Environment, 123376 Moscow, U.S.S.R.

Standard deviation (σ) is a parameter commonly used to characterize atmospheric variability within a month. Some results on temperature (σ_T) and zonal wind (σ_u) variability were obtained by Barnett (1974),Hirota et al (1983),Hopkings (1975),Khanevskaya (1968),Knittel (1976), Koshelkov (1980, 1983,1984),Voskresensky and Sveshnikov (1980), etc. Typical values of standard deviations based on rocketsonde information are presented in tables 1–4 for some stations. It should be noted that contributions of observational errors into the total variance have not been considered,hence the values of the standard deviations in tables 1–4 should be greater than real atmospheric values of the deviations.

General increase of with height is observed which is in accordance with the analysis of aerological data for the polar stratosphere (Khanevskaya, 1968; Voskresensky and Sveshnikov,1980). It should be stressed, however, that the magnitude of errors of rocketsonde observations generally also tends to increase with height (Lysenko et al, 1982; Schmidlin et al, 1980), and sometimes reveals a maximum near the 50 km - height as is the case for the Soviet chute wind measurements.Besides this, observational techniques may change above 60 km. So the vertical distribution of requires further investigation.

That a rapid growth of variability from summer to winter occurs,is confirmed. It should be remembered that the relative contribution of errors of observations into the total variance is greater in summer than in winter.Values of shown in tables 1 and 2 for the summer-time are close to accuracy astimates of the rocketsonde measurements (particularly for the Soviet sites), i.e. real atmospheric variability in summer is much lower than that shown in the tables, and seasonal changes of real σ are greater than those calculated from the tables.

The seasonal variation in the Antarctic lower and middle stratosphere reveals some specific features, with a maximum of σ falling not in winter (as is usually observed) but in the spring season. Differences in the time

of occurrence of seasonal maximum of σ in the Antarctic and Arctic are undoubtedly related to the nature and occurence of stratospheric warmings in these regions.

Hemispheric asymmetries are revealed in the variability of meteorological parameters in winter when it is greater in the stratosphere of the northern hemisphere than in the southern hemisphere. So, in winter, differences in σ_p between Volgograd and Kerguelen $\mathcal{I}_s$ (or between Heiss Is. and Molodezhnaya) in the 30 to 50 km layer are significant at the 0,05-0,01 levels according to the F -test (Panofsky and Brier, 1972). Similar significance of the hemispheric asymmetry in variance is observed in winter in the case of zonal wind, with greater values of σ in the southern than in the northern hemisphere up to the 60 km level (hemispheric differences could not be analysed above that level). In spring, however, σ_p and σ_u are greater at Molodezhnaya than at high northern latitudes; a similar hemispheric effect has been found by Hirota et al (1983) from satellite radiance data. In summer and autumn, differences between the hemispheres are smaller.

Values of σ at the tropical sites are comparable to those obtained during summer in higher latitudes and are much lower than the latter during winter and spring. Seasonal variations of σ in the tropics are less pronounced than those outside the tropical zone. For σ_u, maxima in the upper stratosphere usually coincide with periods of easterlies (in the beginning and the middle of the year (Hopkings, 1975; Koshelkov, 1983), while seasonal trends of σ_p need to be further examined.

REFERENCES:

1. Barnett J.J. Quart.J.Roy.Meteor.Soc., 100, 505,(1974).
2. Hirota I., T.Hirooka and M. Shiotani, Quart.J.Roy.Met.Soc.,109,443, (1983).
3. Hopkins R.H. J.Atmos.Sci.,32,712, (1975).
4. Khanevskaya I.V. Temperature Regime of the Free Atmosphere. Gidrometeoizdat, Leningrad, 1968.
5. Knittel J. Meteor. Abh.Inst.Met.Inst.Geophys.Wiss., A 2,1, (1976).
6. Koshelkov Yu.P. Circulation and Structure of the Stratosphere and Mesosphere of the Southern Hemisphere. Leningrad,Gidrometeoizdat, 1980.
7. Koshelkov Yu.P.,A.I. Boutko, A.N.Kovshova. Proc. Indo-Soviet Symposium on Space Research, Feb.21-25,1983, Bangalore,India, 1983.
8. Koshelkov Yu.P. J.Atmos.Terr.Phys., 46, 781, (1984).
9. Voskresensky A.I. and A.M.Sveshnikov. In: Investigations of Climate of Antarctica. Leningrad, Gidrometeoizdat, 1980.
10. Lysenko E.V.,S.Kh. Rosenfeld and K.A.Speransky, Meteorologia i Gidrologia, 10,46, (1982).
11. Schmidlin F.J. and J.R.Duke, A.I.Ivanovsky, Y.M.Chernyshenko. NASA Ref. Publ.,1053,(1980).
12. Panofsky A.H.,and G.W.Brier. Some Applications of Statistics to Meteorology, Pennsylvania, 1958.

TABLE 1 Standard Deviations of Temperature (K) (The Number of Temperature Measurements is Shown for Level 50 km in Brackets)

Hight(km)	Heiss Is.				Volgograd			
	I	IУ	УП	X	I	IУ	УП	X
80	20.5	II.0	I0.0	I4.8	I4.4	I3.2	I0.7	I0.7
70	2I,0	I0.7	8.0	I2,7	I2,8	7.6	I0.0	9.2
60	I7.9	I0.0	5.5	II.2	I0.7	7.I	6.8	8.9
50	I5.9	9.2	3.9	9.5	9.2	5.2	3.6	6.5
40	I6.7	7.2	3.8	5.2	I3.6	5.8	3.0	4.7
30	I0.5	7.0	2.6	5.6	II.4	4.5	2.8	4.5
	(324)	(3I0)	(284)	(298)	(3I8)	(305)	(279)	(293)
	Molodezhnaya				Thumba			
80	9.8	9.0	I3.5	7.6	II.9	II.I	7.7	7.2
70	8.7	II.7	I9.9	9.3	I0.6	6.9	I0.3	6.8
60	7.4	I2.7	I6.2	8.0	7.2	6.I	7.9	7.3
50	4.2	8.I	II.3	8.8	5.3	3.3	4.7	3.7
40	3.4	7.9	I0.3	II.0	5.2	4.4	6.0	4.I
30	3.0	6.0	8.4	8.4	4.0	3.4	3.4	3.4
	(249)	(236)	(2I0)	(224)	(20I)	(I87)	(I6I)	(I75)
	Thule				Primrose Lake			
60	9.0	4.2	3.6	5.8	7.6	5.5	3.2	5.2
50	8.7	3.6	2.8	II.8	II.7	3.5	2.0	6.5
40	I2.6	3.6	3.5	8.6	6.0	5.I	I.0	7.I
30	6.0	2.2	2.0	4.0	4.7	3.0	I.4	4.8
	(243)	(229)	(203)	(2I7)	(223)	(209)	(I84)	(I97)
	Wallops Is.				Ascension Is.			
80	I6.0	I6.0	27.0	8.0	6.I	8.I	I0.8	8.I
70	9.3	9.8	II.8	8.4	4.8	7.3	6.3	7.3
60	7.7	5.0	6.2	6.5	4.2	4.0	5.0	4.8
50	6.7	3.7	3.9	4.0	5.0	3.3	3.7	3.2
40	7.6	3.7	3.5	6.3	5.2	4.0	5.6	4.4
30	6.2	3.5	I.7	2.8	2.2	2.2	4.2	4.0
	(667)	(654)	(628)	(642)	(507)	(492)	(467)	(480)

TABLE 2 Standard Deviations of Zonal Wind (Numerator) and Meridional Wind (Denominator) (m/s)

Height (km)	Heiss Is.				Volgograd			
	I	IУ	УП	X	I	IУ	УП	X
80	I3.0	I7.7	4.6	I7.2	I6.6	I7.5	5.3	2.6
	I9.8	I9.9	4.0	I7.2	28.0	I9.6	I4.6	24.4
70	I9.8	7.9	7.8	I0.2	I6.7	I4.3	I4.7	9.2
	24.8	I4.6	4.9	I6.8	I8.0	9.2	3.5	6.0

TABLE 2 Continuation

Height (km)	Heiss Is. I	IУ	УП	X	Volgograd I	IУ	УП	X
60	36.3	I5.4	8.5	22.7	35.I	II.4	8.0	I8.3
	37.0	I8.5	I5.2	23.9	26.7	I4.2	8.6	I4.6
50	4I.7	I9.7	I7.3	I5.6	44.4	I7.4	I4.5	20.6
	40.6	I9.3	I5.0	23.5	28.3	I6.4	I5.2	I7.I
40	34.9	9.I	4.5	9.7	33.5	I2.2	I4.8	I8.I
	39.7	I2.7	6.3	I5.7	23.8	7.9	4.2	I0.9
30	23.2	6.9	3.3	6.8	2I.I	I5.3	3.4	9.6
	I6.0	8.6	3.6	7.9	I6.I	7.5	2.9	6.8
	Molodezhnaya				Thumba			
	I	IУ	УП	X	I	IУ	УП	X
80	I7.7	29.2	25.8	I0.5	I8.0	II.2	I3.I	20.9
	I0.8	I9.5	I7.7	II.4	I0..	4.7	8.4	2.6
70	8.4	I6.0	28.6	I6.9	24.8	I2.I	I7.3	20.6
	7.5	I8.0	I5.8	I4.I	8.8	I3.I	I0.I	9.3
60	I3.0	I8.I	24.6	2I.7	2I.0	II.7	I7.I	I4.5
	5.4	I6.8	23.5	II.0	I3.0	I0.2	8.2	9.9
50	I6.8	I6.7	20.I	26.7	23.3	I9.8	2I.0	I8.0
	5.7	2I.8	I6.9	23.4	2I.9	I4.8	I3.6	I4.2
40	5.8	I4.2	2I.3	22.2	I5.9	I4.3	I5.4	II.I
	5.5	I3.5	I5.3	I9.8	7.3	4.5	5.9	6.9
30	4.7	I0.6	I4.0	22.2	I8.5	I6.I	I4.2	I3.0
	3.8	7.6	I0.2	25.4	5.9	4.2	4.5	2.4
	Thule				Primrose Lake			
60	32.4	I3.7	6.3	I7.9	3I.I	20.3	I0.4	I9.9
	34.I	8.2	5.6	23.9	I7.0	II.5	I2.4	19.3
50	39.9	I2.6	4.7	I5.5	42.3	I6.4	I4.0	I4.2
	42.3	7.6	3.2	22.4	28.9	6.5	6.0	II.0
40	28.7	8.5	4.8	9.4	29.3	I3.2	7.3	II.I
	37.7	8.7	2.6	23.9	27.3	6.0	3.2	I0.8
30	25.8	7.I	2.6	7.5	26.8	9.0	3.6	7.3
	23.7	8.I	2.2	22.2	2I.2	5.6	I.7	8.I

TABLE 2 Continuation

Height(km)	Wallops Is.				Ascension Is.			
	I	IУ	УП	X	I	IУ	УП	X
80	29.0	I8.2	I8.5	30.0	20.0	35.0	I2.0	35.0
	27.0	3I.6	9.0	20.2	7.5	I6.0	2I.0	6.0
70	30.4	I6.I	I4.4	24.6	20.0	I5.0	II.0	23.0
	I8.2	9.2	3.5	6.0	7.5	I8.0	I5.8	I4.I
60	28.7	I9.2	I5.3	24.2	I7.2	I3.5	I6.9	I0.5
	I6.2	I0.I	II.7	I0.6	I6.3	I0.0	II.2	9.4
50	32.8	I6.6	I0.6	23.7	27.4	9.4	I6.7	I0.6
	I9.5	6.6	6.5	8.9	9.6	7.I	7.I	7.3
40	29.7	I4.8	6.6	I7.4	I0.6	I6.3	I4.4	I3.5
	I6.0	6.8	3.7	8.4	7.2	5.5	5.2	5.3
30	I8.4	9.4	3.7	I0.5	I4.6	I7.3	I4.5	I4.9
	II.I	4.5	2.0	6.6	4.I	3.6	3.3	3.9

TABLE 3 Standard Deviations of Pressure ($\frac{\delta p}{p} \cdot 100$)
(p - Mean Pressure in Present Month)

Height (km)	Heiss Is.				Volgograd				Molodezhnaya				Thumba			
	I	IУ	УП	X	I	IУ	УП	X	I	IУ	УП	X	I	IУ	УП	X
80	32	20	22	I7	I9	I4	I3	24	I4	25	24	I8	I7	8	II	I7
70	20	I8	I0	I3	I6	I5	I0	I7	I3	23	I7	I8	II	I5	I7	9
60	I8	I6	8	II	I5	I0	5	I3	7	I6	I4	I3	7	5	6	5
50	I8	I2	6	II	I5	7	4	9	5	I3	I3	9	4	3	7	6
40	I8	9	4	9	II	6	3	8	3	I0	II	II	3	3	5	4
30	I3	7	2	5	8	4	2	5	2	7	7	I0	2	2	4	2

	Thule				Primrose Lake				Wallops Is.				Ascension Is.			
80									I0	I0	I0	I0	9	22	22	II
70									9	I2	9	I2	9	8	I4	I0
60	25	II	5	I7	II	6	3	II	7	8	6	I0	5	6	7	5
50	2I	9	5	I2	II	5	3	I0	5	6	I0	7	3	3	5	4
40	20	5	3	7	9	3	2	7	4	5	3	5	2	2	3	3
30	I6	4	I	3	6	2	I	3	3	3	2	3	I	I	I	2

TABLE 4 Standard Deviations of Density ($\frac{\delta\rho}{\rho} \cdot 100$)
(ρ - Mean Density in Present Month)

Height(km)	Heiss Is.				Volgograd				Molodezhnaya				Thumba			
	I	IУ	УП	X	I	IУ	УП	X	I	IУ	УП	X	I	IУ	УП	X
80	28	22	I9	I5	22	I4	I6	2I	9	26	23	27	I7	3	23	30
70	I8	I8	9	I2	I7	I4	6	I5	I0	I9	I6	I6	9	8	I2	7
60	20	I5	8	I3	I7	9	5	II	6	I5	I4	I0	6	5	8	9
50	I9	II	5	II	I4	7	2	9	4	II	I3	II	4	3	7	5
40	I8	9	3	8	I0	5	2	7	3	9	9	I3	3	6	5	4
30	9	6	2	4	7	4	I	4	2	5	6	I0	3	5	3	3

	Thule				Primrose Lake				Wallops Is.				Ascension Is.			
60									I3	II	II	I2	I6	25	I2	I2
70									9	8	8	I0	8	7	I0	9
60	25	I2	4	I4	I2	6	3	I0	6	6	4	7	5	4	5	5
50	2I	8	4	8	II	4	2	8	5	5	3	6	3	3	3	3
40	20	4	2	5	8	3	2	4	5	4	2	4	2	2	2	2
30	I2	3	2	3	5	2	I	2	2	2	I	2	I	2	2	I

Adv. Space Res. Vol. 7, No. 10, pp. (10)63–(10)66, 1987
Printed in Great Britain. All rights reserved.

0273-1177/87 $0.00 + .50
Copyright © 1987 COSPAR

COMPARISON OF MIDDLE ATMOSPHERIC DATA OBTAINED BY CHINESE ROCKETS WITH THE DRAFT OF THE NEW CIRA

H. C. Zhuang, G. Q. Zao, J. H. Tian, R. P. Ma and Y. F. Wu

Institute of Space Physics, Academia Sinica, P.R.C.

Two methods of exploration of the middle atmosphere by meteorolo-gical rockets are used in china: The rocketsonde parachute method for altitudes between 20 and 60 km and the inflatable falling sphere method for 30-80 km. The data from Chinese rocket measurements at two launching sites, Gansu (40°N) and Yunnan (24°N), after 1974 are analysed and compared with the draft of CIRA1986. The data were usually obtained between altitudes of 20 and 60 km. Fig.1 shows the altitude ranges of the measurements in 1979 for examples.

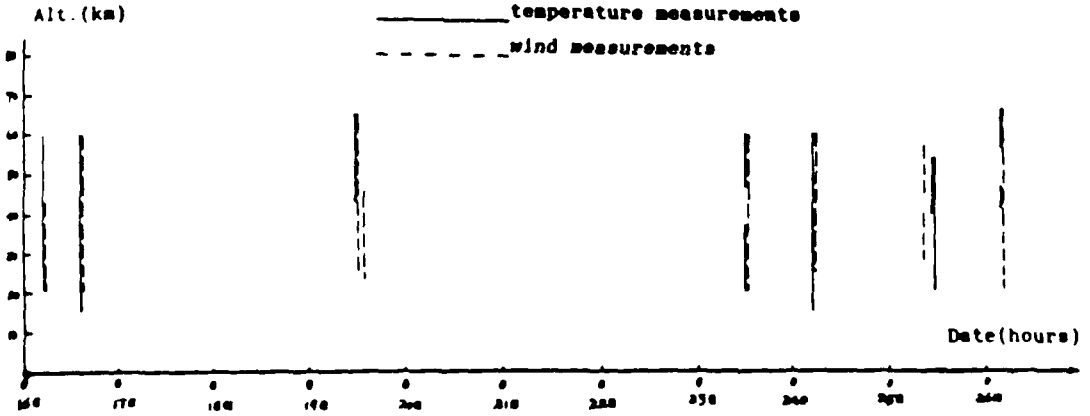

Figure 1. Altitude ranges of the Chinese rocket measurements in December, 1979.

COMPARISON WITH THE DRAFT OF NEW MODEL CIRA1986

Global mean middle atmospheric temperatures given by the draft of CIRA1986 consists of three components : zonal mean To, wave number one and two of planetary waves.

$$T = T_0 + T_1 \cos(\lambda - \Phi_1) + T_2 \cos(2\lambda - \Phi_2)$$

where T_1 and T_2 are wave number one and two amplitudes, Φ_1 and Φ_2 are wave number one and two phases, and λ is longitude (deg. E). We compared the measured temperature profiles obtained by the Chinese rockets with the new model mean temperature calculated by the above equation. The results are shown in Figure 2 for May, June, July and December. The right half of each panel of the figures is the difference between the Chinese rochet data and the draft of CIRA1986. Please notice the difference of the scales of abscissas between the two halves. From the figures we can see that: 1.the data from the Chinese rockets are around the profiles of the new CIRA. It is acceptable to use the new CIRA as the mean middle atmosphere above the rocket sites of China. 2. The differences of Chinese rocket data of temperatures from the new model are mostly within ±5 C,and occasionally over 10 C. 3. The fluctuation deviations are obviously not measurement errors of rockets, but an evidence of the existence of gravity waves of various wavelengths. Because of the international comparison of rocketsondes from different countries being agreed within 5 C, we therefore have the confidence that the accuracy of Chinese rocket measurements is close to the other countries.

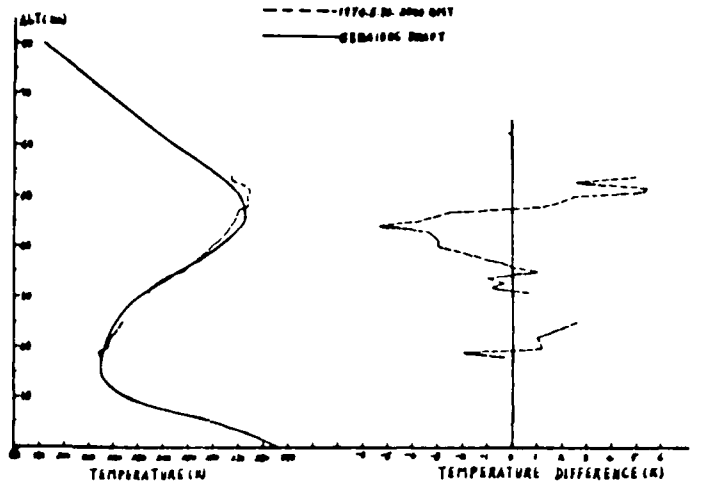

(a) May, 40°N

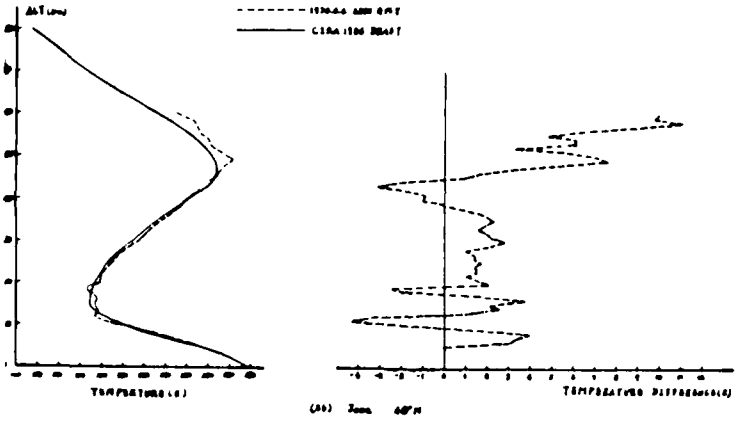

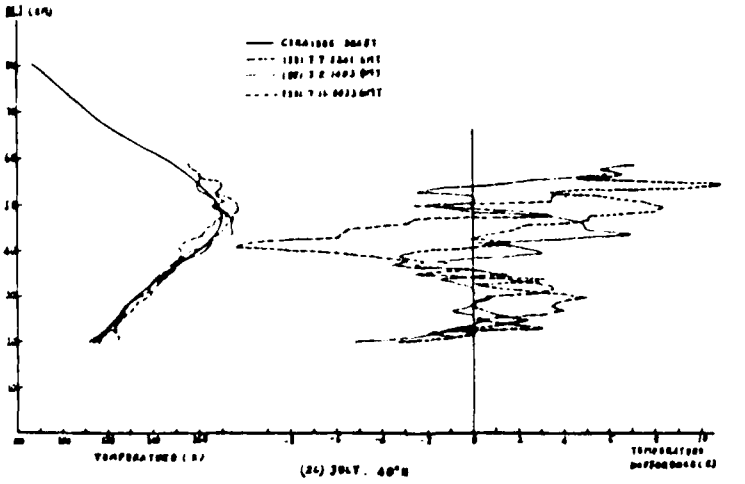

(c) JULY, 40°N

Although the data of Chinese rocket measurements are sparse and not enough to analyse the annual variation of the atmospheric winds, the wind directions measured by the Chinese rockets still show the seasonal characteristics clearly (see Fig. 3): west winds dominate in December; east winds in June and July. For wind directions measured in May at Gansu station, it is east wind on 20th and 30th but still west wind on 13th and below 45 km. Therefore, we can say that the spring reversal of middle atmospheric winds above Gansu station appears in the first half of May. From the Chinese rocket data, we could always see the gravity waves clearly (Figures 2 & 3). According to the definition given by the draft of CIRA1986, mean values of gravity wave intensities from Chinese rocket data averaged for each month and each station are shown in Figure 4 together with the estimate of the standard deviation around the monthly mean (denoted by vertical bars in the figure). In the figure, May, June and July are for the station of 40°N, but December is for the station

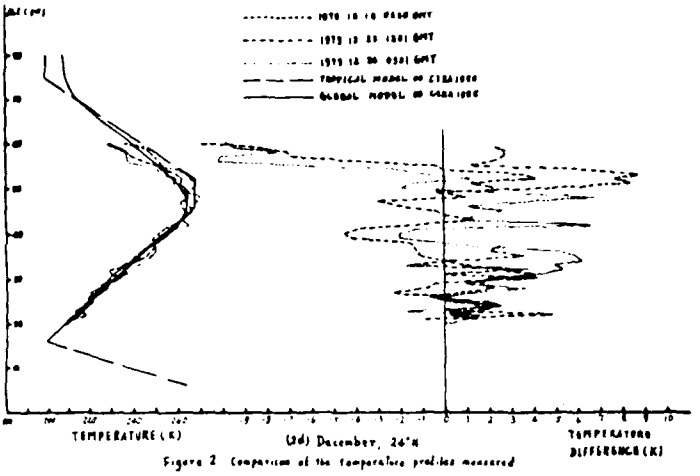

(2d) December, 24°N

Figure 2 Comparison of the temperature profiles measured by the Chinese rockets with global mean middle atmosphere temperature of the draft of CIRA1986

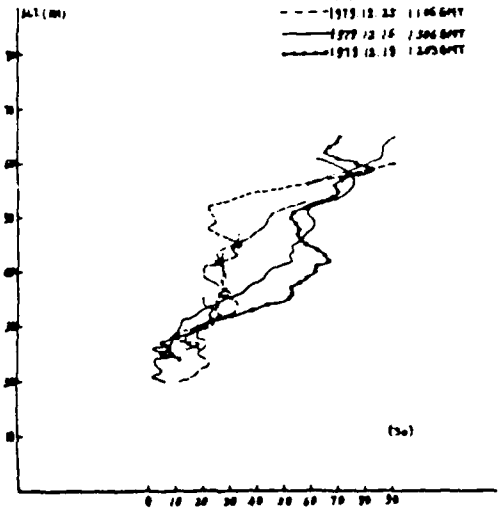

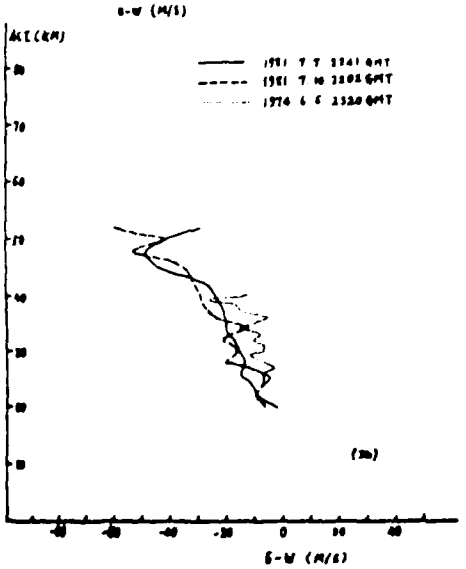

are msec^{-1} km^{-2} for wind and Kkm^{-2} for temperature. Figures above the abscissa are total number of intensities used in these statistics for temperature (above), northsouth wind (middle) and eastwest wind (below). From Fig. 4, the transient variability characteristics of the gravity waves indicated by the draft of new CIRA can be observed.

The rocket launching site of 24°N is located within the region of tropical conditions for the International Tropical Reference Atmosphere proposed by the draft of CIRA1986. We have already shown the ITRA in Figure 2 d), from which we can see that between 20 and 45 km, the tropical model is very close to the global model and also agrees with our rocket data. But for the altitudes between 45 and 60 km, the tropical model is higher than the global one. The largest difference is up to 11 degrees. Our data are lower than the tropical model and more close to the global model.

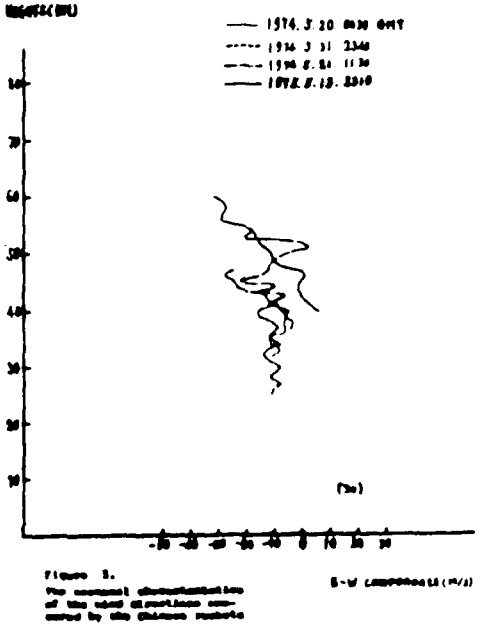

Figure 3.

CONCLUDING REMARKS

From the comparison of the data obtained by the Chinese rocket measurements with the draft of CIAA1986, we will come to some conclusive concepts:

1. The altitude profiles of the middle atmospheric temperature measured by chinese meteorological rockets are fluctuating around the basic global temperature constructions given by the draft of CIRA1986, the agreement is very good. It shows that the CIRA1986 is a suitable representative for the mean situation of the middle atmosphere above our country. In the mean time, it is shown that the accuracy and resolution of Chinese rocket measurements are at the same level as those of other countries.

2. The wind data from Chinese rockets show clearly the seasonal characteristics: the east winds prevail in summer and west winds in winter, the wind reversal in spring above the 40°N station is in the first half of May.

3. The order of magnitudes and the trends of gravity wave intensi-ties are similar with those in the draft of new CIRA.

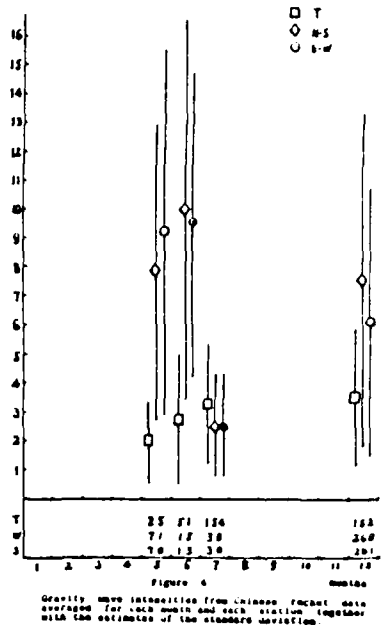

Figure 4. Gravity wave intensities from Chinese rocket data averaged for each month and each station together with the estimates of the standard deviation.

4. The tropical model proposed by the new model is commonly higher than the global model in the altitude region of 45-60 km and also higher than the temperature profiles measured by Chinese rockets at the Yunnan station of 24°N.

ACKNOWLEDGMENTS

The authors are deeply indebted for support to their colleagues who developed the instrumentations of the meteorological rockets and conducted the experiments, especially to Prof. J. W. Yang who was the director of the Rocket Division. The authors would like to thank J. Mu and G. L. Zhang for their crea-tion of the illustrations.

REFERENCES

[1] Institute of Space Physics, Academia Sinica, A review of the instruments on the payload of small meteorological rockets, private letter, May 1985.

[2] J.W. Yang and Y.F. Wu, Measurements of upper atmosphere wind and temperature from meteorological rocket experiments during winter 1979, Adv. Space Res., 2, pp.177-180, (1983).

[3] K. Labitzke, J. J. Barnett and B. Edwards, Handbook for MAP, 16, SCOSTEP Secretariat (1985).

Adv. Space Res. Vol. 7, No. 10, pp. (10)67–(10)76, 1987
Printed in Great Britain. All rights reserved.

0273-1177/87 $0.00 + .50
Copyright © 1987 COSPAR

COMPARISON OF TIME-PERIODIC VARIATIONS IN TEMPERATURE AND WIND FROM METEROLOGICAL ROCKETS AND SATELLITES

A. D. Belmont

Control Data, P.O. Box 1249, Minneapolis, MN 55440, U.S.A.

ABSTRACT

Although the Meteorological Rocket Network operated by or in cooperation with the United States has decreased from fourteen to nine stations since 1979, there have been many observations accumulated in the years since CIRA 1972 was prepared with data up to 1969. The mean, annual and semiannual variations of temperature and wind are presented and compared with the Oxford SCR-PMR five-year data set, the CDC-SCR seven-year data, and CIRA 1972 with respect to both temperature and zonal winds, as far as presently available. The agreement among the data sets is generally very good.

INTRODUCTION

The purpose of this paper is to review the available variability statistics for temperature and wind in the region from 20 to 70 km to help in the selection of the best information available for a revised CIRA. There are many different data sources but they will be limited here to those with at least five years of record. They will be intercompared with respect to their means, and periodic time variations. The satellite data were not operational, real-time data, but were processed years after the observations were made, taking account of all corrections that became known in the interim. These three sets are:

Variables	Source	Abbr.	Instrument & Period of Record
T,H,W,	Oxford	OXF	Two years of SCR (1973-1974) plus three years PMR (1975-1977)
T	CDC	SCR	Seven years of SCR (April 1970-April 1977)
T,W,	WDC-A	MRN	Meteorological rockets (MRN) (1960-1982)

(T = temperature, H = geopotential altitude, W = wind)

An evaluation of the differences of these data sets will be reviewed here.

The atmosphere's variability extends over a wide range of time and space scales including solar cycles, quasi-biennial, interannual, annual, semiannual, and terannual periods and diurnal and semidiurnal tides, and by space scales of planetary waves, gravity waves, and local turbulence. Hence, statistical estimates of these variations will vary with the observational sampling rates in time and space and the total number of observations. This summary will discuss only the means, and annual and semiannual variations.

CIRA 1972 /1/ contained no satellite data for the range 25 to 60 km. Tables and graphs were based entirely on meteorological rocket data. In revising CIRA it was agreed that both satellite and rocket data would be examined and compared before deciding which data or combination of data would suit the purpose most reliably at this time.

Each instrument has its advantages and disadvantages. Satellite data, taken by a single instrument during the life of a given satellite, are consistent with each other and observations are on a global scale. Satellite radiometers, however, generally need to be recalibrated during their lifetimes because of degradation problems. Downward sensing radiometers have relatively coarse vertical resolution of 10-20 km. Scanning radiometers provide excellent horizontal coverage but the SCR and PMR instruments, for which data sets are now available, provided orbital plane data only, consisting of 13 and a fraction orbits a day separated by about 26° of longitude. The orbits shift continually from day to day returning to the same observation orbits at approximately two week intervals. Data for fixed grids can be obtained by interpolation between orbits on a daily basis. It is not possible to obtain tidal variations from a single orbiting satellite.

For climatological purposes, variations are primarily required as a function of altitude, latitude, and time, although longitudinal variations may also be important. Meteorological satellite temperature observations have only been available since about 1970. The reduction of the radiance data to provide temperatures is generally done by one or two methods. The first is the inversion of the Planck radiative equation which requires estimates of the instrument's weighting function for each frequency observed, and a good first guess of the temperature profile in advance. It should be stressed that the inversion technique does not provide a unique solution, and that the first guess strongly influences the final result. First guesses are commonly based on climatology derived from meteorological rocket and radiosonde data. The second technique is a statistical approach which simply regresses observed radiances in several channels against coincidental rocket observations as close as possible in space and time to the radiance observations. These statistics generally produce reasonable results at those locations where there are adequate rocket observations. As will be seen below, this is not always possible. The method, however, is simple and straightforward and involves few assumptions, but depends largely on an adequate sample to provide reliable regression coefficients.

Meteorological rocket data provide direct measurements of temperature and wind as a function of altitude at a given place. Vertical resolution is 1 to 2 Km. The main limitation is the paucity of rocket stations. Unfortunately for scientific users, rocket observation locations have been grouped mainly in the latitude belt from 30° to 40°N. North American rocket observations began about 1960, and the network gradually increased to its maximum density about 1975, and thereafter declined rapidly over North America losing five stations from 1979-82. At present, there are no operational stations in North America north of 55° and only two remain in the Southern Hemisphere, at 8°S and 68°S, although there are Russian rocket-launching ships which are gradually accumulating observations grouped by latitude and month /2/. A table of the available rocket data used in this report is given in Table 1. It will be noticed that most of the Northern Hemisphere stations used here are in North America. Three Russian stations, at 80°N, 48°N, and 68°S, use the M-100 instrument which appears not to be compatible above 50 km with the sensors used in the North American rockets. Continuing efforts at intercalibration have been made, but the necessary corrections to be applied to the past M-100 observations are apparently not available. The correction history changes in time, and it is difficult to learn whether data provided by the World Data Center-A have been corrected and if so, by how much, and whether this correction varied in time. A variety of sensors has also been used in American rockets. A description of rocket errors and intercalibration can be found in /2,3/.

So long as one depends upon satellite data for future requirements, there will be a need for direct rocket measurements at a wide range of latitudes and throughout the year with which to verify and calibrate satellite data.

DATA

OXF

The Oxford satellite temperatures and derived heights and winds were assembled from two years (1973-74) of radiances from the Selective Chopper Radiometer plus three years (1975-77) from the Pressure Modulator Radiometer. A discussion of the data will be given in a following paper of this session /5/. It should be noted, however, that the PMR instrument

retrieves temperatures up to near 85 km, and thus provides information beyond the reach of standard meteorological rockets. This means that only radiative equation inversions can be used to obtain temperatures with PMR.

SCR

The SCR temperature data from CDC for the seven years (1970-1977) were obtained from radiances calibrated by Oxford, or by CDC with Oxford calibration factors, and the use of a multiple non-linear regression against rocket data. The regressions were done by winter and summer seasons with April 1 and October 1 being the dividing dates. To account for possible drifts in the radiances, the regressions were recomputed every six months. The errors of regression were generally 2 to 4C as estimated from five different, random, independent sets of rocket data, each set consisting of 15% of the total data available. As there are so few reliable rocket data in the Southern Hemisphere, the regressions for the Northern Hemisphere were applied to the Southern Hemisphere radiances six months later. This means that for any northern hemisphere winter which experienced large sudden warmings, the regression coefficients may be slightly different from true Southern Hemisphere winter coefficients where warmings are not as frequent or as intense. To extend the cross section downward from 30 to 20 km, north of 20°N, NMC radiosonde data were added to the altitude-latitude sections for the same dates.

MRN

Only meteorological rocket network data as available from World Data Center-A were used here. Unfortunately, despite very long delays in processing rocket data at WDC-A, there is no real quality control of any of the observations. It is assumed that each individual station, or its processing center, carefully does this. Meteorological rocket data received by teletype for operational use frequently contain serious errors and are not recommended for any scientific purpose when there is time to obtain more reliable data. Russian rocket data taken since 1975 are not available from WDC-A, so it is doubly unfortunate that many North American stations at high latitudes have been closed since 1977. This also prevents the future use of rocket data to retrieve satellite temperatures at high latitudes.

With respect to possible solar cycle influences above 50 km, the dates of the establishment and the reduction of the rocket network were not helpful. The major solar maximum of 1959, and the recent one of 1980, both occurred at a time when there were few rocket stations, especially at high latitudes where any solar effect is likely to be strongest.

Only stations with the most observations were used at a given latitude where there were several to choose from (e.g. Thumba was not used). Stations with less than 150 observations were generally not used unless there was no other station near that latitude; also if the distribution of observations was not spread over the year, the station was not used (Can). It is highly recommended that meteorological rocket network stations be distributed more evenly with respect to latitude, including the southern hemisphere.

The influence of standing planetary waves introduces much irregularity when stations from all longitudes are combined onto a single cross section. Elimination of five Pacific region stations (Poker Flat/Ft. Greely, Shemya, Ryori, Barking Sands, Kwajalein), despite the many observations at the latter two stations, would have produced smoother analyses. The five stations were analyzed separately from the continental stations and the altitude-latitude patterns were very similar although absolute values differed due to planetary wave influence as shown in /5/.

A further caveat in the interpretation of all rocket and satellite data is that there are no tidal corrections presently available although the region to which the data apply are known to have large tides. It is possible that tidal estimates will become available in the near future which can be applied to both past and future observations.

TABLE 1 Rocketsonde Stations Used

	Latitude	Longitude	N	Period of Record
Heiss Island	80°37'N	58°03'E	601	1957-75 *
Thule	76°33'N	68°49'W	1199	1965-80
Poker Flat	65°07'N	147°29'W	838	1972-79
Fort Greely	64°00'N	145°44'W	1222	1960-72
Fort Churchill	58°44'N	93°49'W	2005	1960-79
Primrose Lake	54°45'N	110°03'W	1238	1964-82
Shemya	52°43'N	174°06'E	532	1975-82
Volgograd	48°41'N	44°21'E	423	1965-75 *
Kyori	39°02'N	141°50'E	175	1970-72, 79-82
Wallops Island	37°50'N	75°29'W	2890	1960-82
Pt. Mugu	34°07'N	119°07'W	3432	1960-82
White Sands	32°23'N	106°29'W	4698	1959-82
Cape Kennedy	28°27'N	80°32'W	3792	1960-82
Barking Sands	22°02'N	159°47'W	2580	1960-82
Grand Turk Island	21°26'N	71°09'W	223	1963-66
Antigua	17°09'W	61°47'W	1319	1963-82
Fort Sherman	09°20'N	79°59'W	1554	1966-79
Kwajalein	08°44'N	167°44'E	1668	1963-82
Natal	05°55'S	35°10'W	78	1969-76
Ascension Island	07°59'S	14°25'W	2316	1962-82
Woomera	30°56'S	136°31'E	96	1962-72
Mar Chiquita	37°45'S	57°25'W	58	1969-76
Molodezhnaya	67°40'S	45°51'E	253	1969-75 *

* Later data exist but unavailable from WDC-A

ANALYTICAL METHOD

A multiple linear regression is used to determine the amplitudes and phases of the periodic features in the biweekly averages of daily data. Sine and cosine function pairs are used to represent the annual, semiannual, and terannual oscillations; a mean and trend are also determined during the regression. The QBO is represented by two empirically-determined time series of amplitudes derived from tropical data. The method by which these series are generated requires further elaboration.

The QBO is observed to have a continuously variable period and amplitude. For these reasons, the QBO signal in the tropical lower stratosphere was used to define a reference signal with variable period and amplitude from cycle to cycle. This signal was then used in the regression. A second time series of equal variance which was orthogonal to and 90° out-of phase with the original QBO signal was created using a Hilbert transform. This transformed signal was also used in the regression. The original QBO reference signal was obtained from the zonal winds at 30 km altitude from Fort Sherman (9.33°N), Kwajalein (8.73°N), and Ascension (7.98°S). Thirty-day means were obtained from each station, and the mean, trend, annual, semiannual, and terannual signals were removed using the regression technique. The residual means were then averaged over the three stations to provide a continuous QBO record from late 1962 through 1982. The exact values of the series at biweekly intervals are obtained through three-point Lagrangian interpolation.

The errors in fitting periodic functions to the data were used to evaluate the reliability of the data in the contouring of amplitudes and phases. Diagrams of the annual, semiannual, terannual, and QBO were made using only those amplitudes (and corresponding phases) that were equal to or larger than the associated standard deviation. Also, at least 45 bi-weekly periods of data were required. The means for all stations were adjusted to a common reference date (1972) to avoid the effect of long period trends. In Figs. 1-10, tick marks along the upper edge indicate rocket launch sites.

COMPARISON OF VARIATIONS

Figs. 1-13 present the amplitudes of the means, annual, semiannual and quasi-biennial waves. The values in Figs. 1-6 are for the amplitudes of

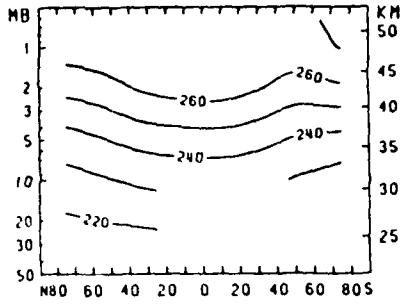

Fig. 1. Mean Temperature, K, 1970-1977, from SCR.

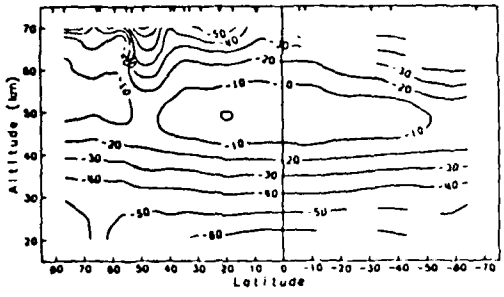

Fig. 2. Mean temperature, C, 1960-1982, from MRN.

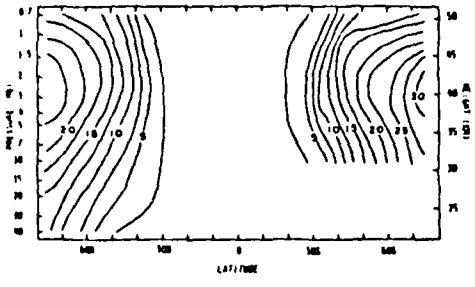

Fig. 3. Amplitude of the annual wave in temperature, K, from SCR, 1970-1977.

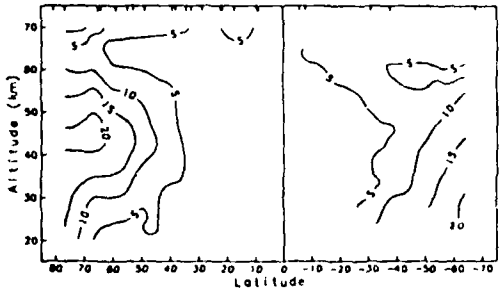

Fig. 4. Amplitude of the annual wave in temperature, K from MRN, 1960-1982.

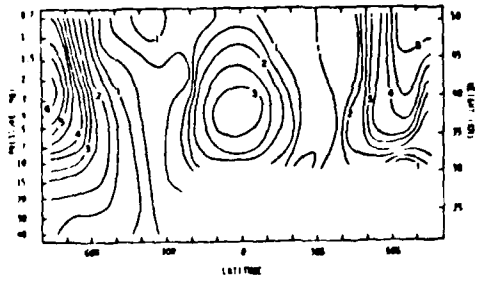

Fig. 5. Amplitude of the semiannual wave in temperature, K from SCR, 1970-1977.

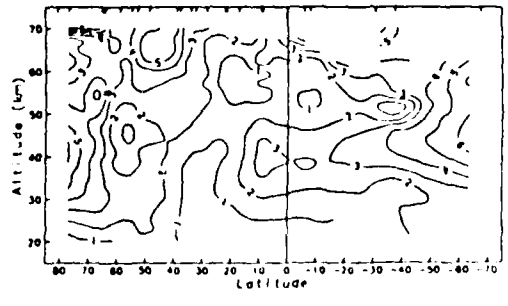

Fig. 6. Amplitude of the semiannual wave in temperature, K from MRN, 1960-1982.

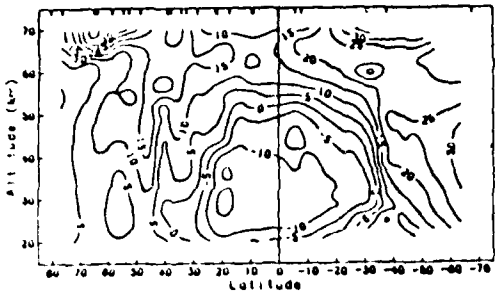

Fig. 7. Amplitude of the mean zonal wind, m/s, from MRN, 1960-1982.

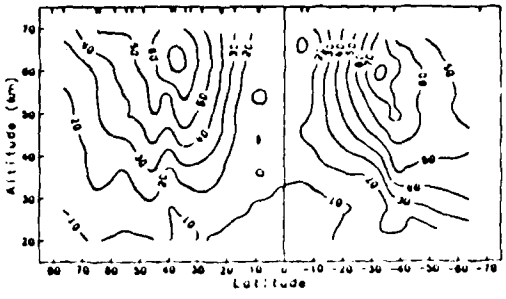

Fig. 8. Amplitude of the annual wave in zonal wind, m/s, from MRN, 1960-1982.

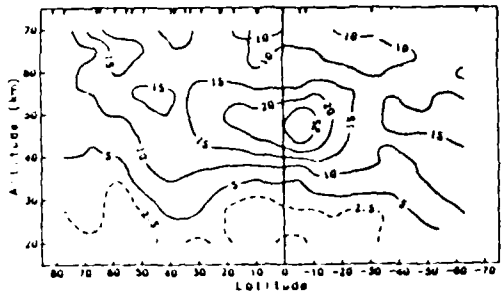

Fig. 9. Amplitude of the semiannual wave in zonal wind, m/s, from MRN, 1960-1982.

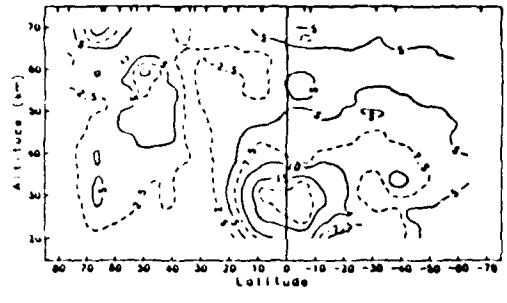

Fig. 10. Amplitude of the quasi-biennial wave in zonal wind, m/s, from MRN, 1960-1982.

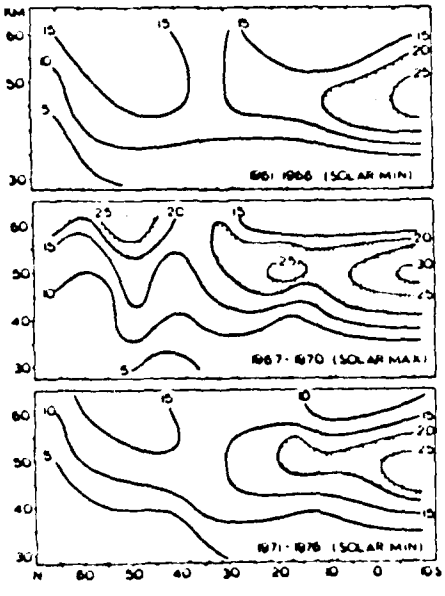

Fig. 11. Semiannual variation in MRN zonal wind for periods of solar activity minimum (1961-66, 1971-76) and maximum (1967-70), (from /9/).

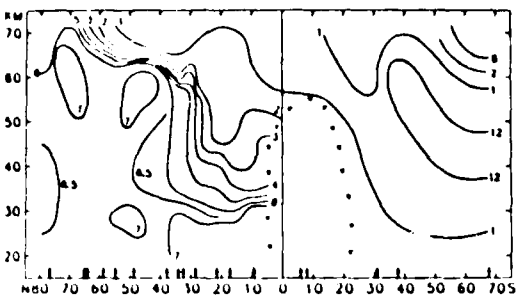

Fig. 12. Phase dates of the annual variation in temperature from MRN. 1 = January first. Triangles indicate a region of 1°K amplitude or less.

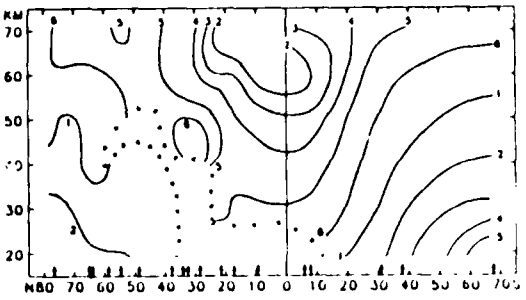

Fig. 13. Phase dates of the semiannual variation in temperature from MRN. 1 = January first. Triangles indicate a region of 1°K amplitude or less.

SCR and MRN temperature, and those in Figs. 7-11 are for MRN wind. Figs. 12 and 13 present the corresponding phases of MRN temperature waves. The values of OXF are discussed in more detail in Section 2.3.5. Periodic variations of the wind are presently available only from MRN. Note that these cross sections are machine contoured and lack smoothness, especially at highest altitudes due to the inhomogeneity of the data. The general patterns of maxima are not affected, however, and the amplitude and phase values discussed below were taken from tabulations rather than the plots, whenever possible.

Sample values at three latitudes are summarized in Table 2. The agreement is far better than expected considering the different sensors, data sources, methods of reduction of the raw data, interpolations to latitude-altitude grids for automated contouring, graphical smoothing techniques, and problems of different longitudes of the stations, periods of record, sample size and uneven distribution of data in space and time. For the annual variation in temperature (Figs. 3,4 and also Fig. 1 in Section 2.3.5; note latitude scales), the most noticeable difference is in the altitudes of the maximum amplitude shown by SCR and OXF. SCR shows a maximum near 3 mb (40 km) at 80°S, while the OXF maximum lies near 11 mb (29 km). OXF is in fair agreement with MRN, where their data overlap. Phase dates are at the solstices (Fig. 11). The corresponding annual amplitude of the wind (Fig. 8) shows large mid-latitude maxima centered near 60 km, in general agreement with Fig. 38 in CIRA 1972.

The semiannual wave in temperature (Figs. 5,6, Table 2; cf. 2.3.5, Figure 1), is of interest because it is as strong or stronger at both polar regions than at the equator. Although the polar waves have generally not been recognized, they are shown in /6, 10/, and they are strongly confirmed by all three present data sources (Table 2). The phase of the maximum amplitude in the equatorial semiannual wave in temperature (Fig. 12) is equinoctial and propagates downward, while those of the polar centers are solstitial. The OXF and MRN data show the semiannual amplitude pattern in temperature at high latitudes as a vertical sequence of cells continuing into the upper mesosphere where the semiannual variation in wind has been reported earlier /7/.

The MRN semiannual wave in the wind (Fig. 9) shows the well-known tropical maximum near 50 km, displaced south of the equator, with bands of maximum extending poleward. The semiannual wind phase dates at these centers of maximum amplitude in both the polar regions and the tropics is equinoctial and agrees in general with /4/. Where the amplitude is weak, below 35 km, the phase may appear occasionally as solstitial. It has been suggested that the amplitude of this wave may be related to the solar cycle, showing higher values during solar maximum /8/. Fig. 11 shows how the amplitude of the semiannual maximum in wind near 50°N apparently changes with solar cycle. It is not yet possible to confirm this solar cycle hypothesis with satellite data because there are only 8 years of SCR data (1970-78), and high latitude MRN data have ended in North America. The recent solar maximum years 1978-82 were examined, but there were only

Shemya and Primrose Lake with any data to 1982 and these stations had too few observations above 50 km to permit any conclusions. Possibly later satellite data for this region will clarify the matter.

The quasi-biennial wave in zonal wind (Fig. 10) from MRN data has no counterpart in the other data sets with which to compare it. The tropical values agree well with those in /4/. The other areas remain uncertain due to lack of adequate data. The QBO temperature field in the tropics agrees with /6/, but its magnitudes elsewhere are unreliable, and are not reproduced here. The terannual waves are also omitted for the same reason and for the growing expectation that this harmonic does not represent a physical phenomenon.

TABLE 2 Comparison of OXF, SCR, MRN, CIRA 1972

	Temperature (K)					Wind (m/s)		
	OXF	SCR	MRN	CIRA		OXF	MRN	CIRA
				Annual Mean (1 MB)				
80°N	263	264	263	(264)	70°N	18	5	(1)
0	268	270	271	(269)	10°N	-	-5	(-13)
80°S	270	271	263	-	70°S	30	30	-
				Annual Mean (10 MB)				
80°N	224	227	224	(223)	70°N	10	5	(17)
0	233	234	232	(231)	10°N	-	-10	(-21)
80°S	222	226	226	-	70°S	35	30	-
				July Mean (1 MB)				
80°N	284	285	-	283				
0	263	268	-	269				
80°S	254	259	-	-				
				December Mean (1 MB)				
80°N	247	250	-	257				
0	265	269	-	271				
80°S	288	291	-	-				

	OXF	SCR	MRN
	Maximum Annual Temperature Amplitude K (at any altitude)		
80°N	42 (.006 mb)	-	-
80°N	26 (2.5 mb)	24 (3 mb)	28 (44 km) (1.3 mb)
0	3 (0.1 mb)	1 (1 mb)	4 (42 km) (2.5 mb)
80°S	41 (.006 mb)	-	-
80°S	-	31 (3 mb)	-
80°S	35 (11 mb)	-	24 (26 km) (25 mb)
	Maximum Semi-Annual Amplitude K (at any altitude)		
80°N	11 (4 mb)	6 (3 mb)	6 (40 km) (3 mb)
0	4 (1.5 mb)	3 (3 mb)	3 (40 km) (3 mb)
80°S	6 (0.3 mb)	-	-
80°S	4 (1.5 mb)	6 (1 mb)	7 (46 km) (1.5 mb)

Notes to Table 2

1. Values are taken from tables, if available, interpolating when necessary. Figures are used if tables not available.

2. Values in parentheses were estimated from mean of January and July values read from tables.

3. No SCR data available below 10 mb south of 20°S.

SUMMARY OF RESULTS

1. The three sets of data agree remarkably well. This may be due in part to ultimate reliance upon a climatology based on meteorological rocket profiles which still serves as the only large body of independent data for the middle atmosphere.

2. Semiannual variations in wind and temperature at high latitudes of both hemispheres are confirmed, but the cause of the semiannual oscillation at high latitudes is still unknown.

3. Possible solar modulation of the semiannual wave during the 1979-81 maximum could not be detected at high latitudes due to reduction in the MRN rocket network.

4. Meaningful comparisons of data require data for the same years and place, not just for equal periods of record.

5. Resultant, observed temperatures or winds are made up of many periodic and quasi-periodic components, possibly including solar effects, that modeling must take into account.

RECOMMENDATIONS

1. Best present estimates of middle atmosphere climate are from satellite global data. A data set consisting of PMR and SAMS to 85 km for 8 years, plus 5 years of SCR, plus continued SSU and similar instruments which sense to 50 km, is now within reach. Resumption of the PMR type measurements is highly recommended.

2. MRN data must be separated by region. Longitudinal variations due to planetary waves may be large. Thus the sparse MRN data are best used for vertical resolution at a given place, and not for representative global coverage.

3. Added MRN stations are needed for satellite temperature retrievals, calibration and verification, especially at high latitudes.

4. MRN data need to be carefully quality controlled.

5. Tidal corrections are needed to adjust single observations per day into more representative values.

ACKNOWLEDGEMENT

Thanks are extended to D.E. Venne and J. Roe for computations and figure preparation.

REFERENCES

1. The Committee for the COSPAR International Reference Atmosphere (CIRA) of COSPAR Working Group 4, CIRA 1972, Akademie-Verlag, Berlin, 1972.

2. Yu. P. Koshelkov, Reference middle atmospheres for the Southern Hemisphere, COSPAR, 25, (1984).

3. F.J. Schmidlin, J.R. Duke, A.I. Ivanovsky, and Y.M. Chernyshenko, Results of the August 1977 Soviet and American Meteorological Rocketsonde Intercomparison Held at Wallops Island, Virginia, NASA Reference Publication 1053, NASA, Washington, D.C., 1980.

4. A.D. Belmont, D.G. Dartt, and G.D. Nastrom, Periodic variations in stratospheric zonal wind from 20 to 65 km, at 80°N to 70°S, Quart. J. of the Royal Meteorological Society 100, #424, 203-211 (1974).

5. J.J. Barnett and M. Corney, A middle atmosphere temperature reference model from satellite measurements, this issue.

6. G.D. Nastrom and A.D. Belmont, Periodic variations in stratospheric-mesospheric temperature from 20-65 km at 80°N to 30°S, J. of Atmos. Sci. 32, #9, 1715-1722 (1975).

7. G.V. Groves, Annual and semiannual zonal wind components and corresponding temperature and density variations, 60-130 km, Planet. Space Sci. 20, 2099-2112 (1972).

8. G.D. Nastrom and A.D. Belmont, Apparent solar cycle influence on long-period oscillations in stratospheric zonal wind speed, Geo. Res. Lett. 7, #6, 457-460 (1980).

9. H.K. van Loon, K. Labitzke, and R.L. Jenne, Half-yearly wave in the stratosphere, J. Geophys. Res., 77, #21, 3846-3855 (1972).

Adv. Space Res. Vol. 7, No. 10, pp. (10)77–(10)82, 1987
Printed in Great Britain. All rights reserved

0273-1177/87 $0.00 + .50
Copyright © 1987 COSPAR

MIDDLE ATMOSPHERE MODELS AND COMPARISON WITH SHUTTLE REENTRY DENSITY DATA

K. S. W. Champion

Air Force Geophysics Laboratory, Hanscom AFB, MA 01731, U.S.A.

ABSTRACT

Several middle atmosphere models will be reviewed, including a new set of models produced by Groves in 1985. The latter models are based on rocket and rawinsonde in situ measurements and satellite remote sounding temperature data. The models are compared with measurements made with instruments on board U. S. Shuttles during their reentry. Very useful atmospheric density data have been obtained in the altitude region from 50 to 80 km. The measurements are unique in that they are made by a vehicle travelling almost horizontally through the atmosphere at a velocity of 6 to 7 km/sec. This results in measurements along a path of approximately 8,000 km in a time interval of about 20 minutes. The results show some unique features.

MIDDLE ATMOSPHERE MODELS

Several middle atmosphere models will be reviewed and compared with data derived from instruments on board reentering U. S. shuttle vehicles. The first set of models is contained in the COSPAR International Reference Atmosphere (CIRA) 1972/1/. The middle atmosphere models were developed by Prof G. V. Groves and extend in altitude from 25 to 110 km (with some values at the higher altitudes uncertain). Monthly models are presented for latitudes at 10 degree intervals from the equator to 70° N. Properties include temperature, density and presssure. In addition, monthly models are given for west-east winds for altitudes from 25 to 130 km and latitudes from 0 to 80°. There are many gaps in the wind tables for regions where data were not available. Separate winter models are presented for North America and Europe/West Asia.

The second set of models is the AF Reference Atmospheres 1978/2/. They extend from the ground to an altitude of 90 km and contain values of temperature, density and pressure. The principal tables contain monthly values for northern latitudes at 15 degree intervals from the equator to the pole. There are also tables for the median high and low percentile values of temperature and density at altitudes to 80 km for January and July for northern latitudes from 30° to 75°.

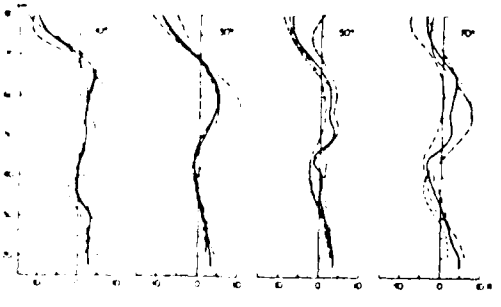

Fig. 1. Average monthly mean rocket models minus satellite temperatures for Koshelkov -.-, AF Reference Atmospheres —, CIRA 1972—... Weighted mean of the rocket models—.

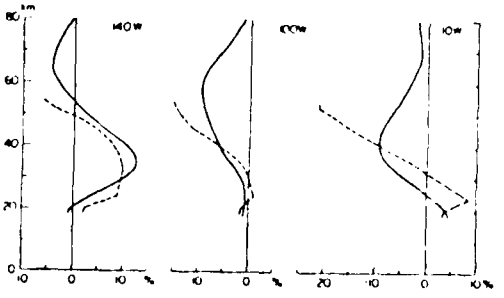

Fig. 2. Comparisons of January mean density deviations from zonal mean values for AF Reference Atmospheres-- and Groves model — for 3 longitudes.

Groves/3/recently completed a new set of models for the 18 to 80 km altitude region. The new models are based on rocket and rawinsonde in situ measurements and the satellite remote sounding temperature models of Barnett and Corney/4/. In addition to northern hemisphere in situ data, results from a large number of Russian southern hemisphere rocket measurements are included/5/. The rocket and remote sounding temperature profiles for comparable conditions are not in complete agreement and so we evaluated the relative errors and empirically determined mean profiles. Thus the new models are based on the integrated evaluation of all available in situ and remote sounding data. The relative temperature profiles are plotted in Figure 1. What are plotted in the figure are the differences between the temperature profiles in three reference atmospheres based on rocket data and the satellite temperature profiles for corresponding conditions. Average monthly mean (excluding winter values) profiles are given for four latitudes for CIRA 1972, AF Reference Atmospheres 1978 and Koshelhov 1983/5/. (Note that northern hemisphere rocket values were compared with northern hemisphere satellite values and correspondingly the southern hemisphere rocket and satellite values were compared.) The solid curves represent the adjustments made to the satellite temperatures based on weighted averaging of the other curves. Table 1 contains a sample page of the zonal mean densities for November from Grove's new models/3/. Longitudinal dependent models were also developed based on the wave 1 and wave 2 models of Barnett and Corney/6/. Figure 2 contains comparisons of density deviations for January from the zonal mean profiles for the new models and the AF Reference Atmospheres 1978 for three longitudes. The agreement is moderately good, but the new models are global, extend to higher altitudes and are probably more accurate due to the inclusion of the satellite remote sounding data. Groves models can be entirely represented by analytical expressions.

The models we have considered so far are mean models. For many applications we need information on short term systematic variations and also on the extent of variability about mean values. One set of systematic variations are those due to tides induced by solar heating. Forbes/1/ has investigated theoretically the diurnal and semidiurnal tides. As might be expected, the largest tidal effects occur at low to middle latitudes. The amplitudes are relatively small in the stratosphere and mesosphere, increasing with altitude until they provide major variations in the lower thermosphere. Some aspects of atmospheric variability will be considered when we analyze data obtained during the reentry of Shuttle vehicles.

SHUTTLE REENTRY DATA

Density data obtained during the reentry of four Shuttle flights, STS-1, STS-2, STS-4, and STS-5 are presented and compared with several models. All these vehicles were launched from the Kennedy Space Center, Florida and landed at Edwards Air Force Base, California. The landing times are given in Table 2. The data were obtained from the drag measured by the Inertial Motion Units (IMUs) which contain accelerometers with sensitivity in the milli-g range.

FLIGHT	LANDING
STS-1	APRIL 14, 1981 1021 PST
STS-2	NOVEMBER 14, 1981 1323 PST
STS-4	JULY 4, 1982 0809 PST
STS-5	NOVEMBER 16, 1982 0633 PST

TABLE 2. Landing dates and times

In Figure 3 is plotted the ratio of the density derived from the drag acceleration on STS-1 during reentry to the density from the U. S. Standard Atmosphere 1976/8/. The meteorological profile provided for the reentry is also given. In addition, the ratios of the densities to the Standard for April from the CIRA 72 and Groves 85 models for 25° N latitude and from the Air Force Reference atmospheres 78 (AFRA 78) for 30° N latitude are plotted. It should be noted that the time during reentry passes from right to left. The meteorological profile based on rocketsonde data agrees better with the models than does the Shuttle data. Note that the Shuttle data exhibits fine scale fluctuations, particularly at the higher altiudes. These fluctuations may be due to turbulence or gravity waves in the atmosphere, but it is impossible to rule out that some part may be due to turbulence induced by the very high speed shuttle flight or due to small changes in the vehicle attitude modifying the drag.

Figures 4 and 6 show data from the STS-2 and STS-5 flights. These flights were both in mid-November, but one year apart. The meteorological profiles for the two

DECEMBER ZONAL MEAN DENSITY (KG/M CU)

HR	LAT →	-80	-70	-60	-50	-40	-30	-20	-10	0	10	20	30	40	50	60	70	80	DEG	
18		1.037	1.082	1.146	1.222	1.296	1.350	1.372	1.369	1.363	1.360	1.343	1.299	1.236	1.181	1.144	1.120	1.102		- 1
19		0.895	0.933	0.986	1.044	1.099	1.137	1.150	1.146	1.141	1.142	1.133	1.102	1.055	1.012	0.983	0.963	0.949		
20		7.687	8.015	8.456	8.920	9.323	9.576	9.640	9.592	9.560	9.576	9.533	9.322	8.986	8.663	8.429	8.263	8.142		- 2
21		6.590	6.872	7.245	7.615	7.908	8.067	8.088	8.040	8.016	8.034	8.015	7.879	7.645	7.403	7.213	7.070	6.969		
22		5.642	5.884	6.200	6.497	6.708	6.802	6.796	6.750	6.731	6.746	6.742	6.659	6.501	6.321	6.163	6.037	5.949		
23		4.828	5.036	5.302	5.541	5.693	5.742	5.720	5.678	5.661	5.673	5.677	5.632	5.529	5.394	5.260	5.146	5.065		
24		4.132	4.309	4.532	4.724	4.832	4.854	4.824	4.786	4.770	4.779	4.788	4.768	4.703	4.601	4.485	4.379	4.303		
25		3.538	3.688	3.874	4.037	4.104	4.109	4.078	4.043	4.028	4.034	4.046	4.042	4.002	3.923	3.821	3.721	3.647		
26		3.033	3.160	3.313	3.432	3.487	3.484	3.454	3.423	3.409	3.412	3.426	3.431	3.406	3.344	3.252	3.157	3.084		
27		2.602	2.709	2.834	2.927	2.965	2.958	2.931	2.905	2.891	2.893	2.907	2.916	2.901	2.848	2.766	2.675	2.602		
28		2.236	2.325	2.426	2.497	2.523	2.516	2.493	2.470	2.457	2.459	2.472	2.482	2.471	2.425	2.350	2.263	2.192		
29		1.924	1.999	2.079	2.132	2.149	2.142	2.124	2.105	2.093	2.094	2.106	2.116	2.105	2.064	1.995	1.913	1.844		
30		1.659	1.720	1.784	1.822	1.833	1.827	1.814	1.797	1.786	1.787	1.798	1.805	1.794	1.757	1.693	1.615	1.549		
31		1.432	1.483	1.532	1.559	1.565	1.561	1.551	1.537	1.528	1.529	1.538	1.542	1.530	1.494	1.435	1.363	1.301		
32		1.239	1.280	1.318	1.336	1.338	1.336	1.329	1.318	1.310	1.311	1.318	1.319	1.305	1.271	1.217	1.150	1.091		
33		1.073	1.107	1.136	1.146	1.146	1.145	1.141	1.132	1.125	1.126	1.131	1.130	1.113	1.081	1.031	0.969	0.915		
34		9.311	9.592	9.801	9.853	9.836	9.830	9.807	9.739	9.683	9.692	9.726	9.683	9.508	9.197	8.739	8.174	7.679		- 3
35		8.094	8.323	8.474	8.486	8.456	8.455	8.447	8.396	8.350	8.359	8.376	8.311	8.126	7.829	7.409	6.896	6.447		
36		7.047	7.234	7.341	7.325	7.285	7.287	7.288	7.251	7.216	7.223	7.226	7.144	6.952	6.669	6.285	5.827	5.418		
37		6.147	6.299	6.372	6.336	6.290	6.293	6.301	6.274	6.248	6.253	6.244	6.148	5.955	5.686	5.336	4.921	4.560		
38		5.370	5.494	5.541	5.493	5.444	5.445	5.457	5.440	5.420	5.423	5.404	5.300	5.108	4.855	4.537	4.165	3.844		
39		4.700	4.801	4.829	4.774	4.722	4.722	4.736	4.725	4.711	4.712	4.685	4.576	4.388	4.151	3.862	3.531	3.247		
40		4.120	4.203	4.217	4.158	4.106	4.105	4.118	4.112	4.102	4.101	4.069	3.958	3.777	3.556	3.294	3.000	2.750		
41		3.617	3.685	3.691	3.631	3.580	3.576	3.588	3.585	3.579	3.577	3.541	3.430	3.257	3.052	2.816	2.554	2.335		
42		3.181	3.237	3.237	3.178	3.128	3.122	3.133	3.132	3.128	3.124	3.086	2.979	2.815	2.625	2.412	2.180	1.988		
43		2.802	2.849	2.844	2.788	2.741	2.733	2.741	2.741	2.738	2.734	2.695	2.592	2.438	2.264	2.071	1.866	1.698		
44		2.472	2.511	2.504	2.452	2.407	2.397	2.404	2.404	2.402	2.397	2.358	2.260	2.117	1.957	1.783	1.602	1.456		
45		2.184	2.217	2.209	2.160	2.118	2.108	2.112	2.112	2.110	2.105	2.067	1.975	1.843	1.696	1.539	1.380	1.252		
46		1.933	1.961	1.952	1.908	1.869	1.857	1.859	1.858	1.857	1.851	1.816	1.730	1.608	1.473	1.333	1.192	1.080		
47		1.713	1.736	1.728	1.687	1.652	1.639	1.639	1.638	1.636	1.630	1.597	1.518	1.406	1.283	1.157	1.033	0.935		
48		1.520	1.540	1.531	1.495	1.462	1.450	1.448	1.446	1.444	1.438	1.407	1.335	1.232	1.120	1.007	0.897	0.812		
49		1.350	1.367	1.359	1.327	1.297	1.284	1.281	1.278	1.276	1.270	1.242	1.176	1.082	0.980	0.879	0.782	0.708		
50		1.201	1.216	1.208	1.179	1.151	1.139	1.135	1.131	1.128	1.123	1.098	1.037	0.952	0.860	0.769	0.684	0.619		
51		1.069	1.082	1.075	1.048	1.023	1.011	1.006	1.002	0.999	0.994	0.971	0.917	0.839	0.755	0.674	0.599	0.543		
52		9.525	9.633	9.566	9.329	9.102	8.987	8.931	8.880	8.851	8.810	8.601	8.106	7.401	6.647	5.921	5.259	4.767		- 4
53		8.493	8.584	8.519	8.306	8.100	7.990	7.929	7.876	7.846	7.810	7.623	7.175	6.536	5.856	5.209	4.627	4.198		
54		7.577	7.652	7.596	7.396	7.210	7.104	7.047	6.987	6.959	6.927	6.759	6.354	5.776	5.183	4.587	4.076	3.703		
55		6.762	6.822	6.762	6.586	6.416	6.316	6.253	6.200	6.173	6.145	5.994	5.628	5.105	4.554	4.043	3.595	3.270		
56		6.035	6.083	6.023	5.863	5.708	5.614	5.552	5.500	5.476	5.451	5.315	4.984	4.511	4.018	3.563	3.173	2.890		
57		5.386	5.422	5.363	5.216	5.075	4.987	4.926	4.877	4.856	4.835	4.712	4.411	3.985	3.543	3.144	2.801	2.556		
58		4.806	4.831	4.772	4.638	4.509	4.426	4.367	4.322	4.304	4.286	4.174	3.901	3.517	3.123	2.771	2.473	2.240		
59		4.286	4.302	4.243	4.119	4.001	3.924	3.869	3.827	3.812	3.797	3.693	3.447	3.101	2.751	2.441	2.182	1.997		
60		3.820	3.827	3.768	3.654	3.547	3.474	3.423	3.385	3.373	3.361	3.267	3.042	2.731	2.420	2.149	1.924	1.764		
61		3.401	3.401	3.343	3.238	3.140	3.072	3.024	2.991	2.982	2.971	2.885	2.680	2.401	2.126	1.890	1.695	1.557		
62		3.025	3.019	2.961	2.865	2.775	2.713	2.669	2.639	2.632	2.623	2.545	2.358	2.108	1.866	1.660	1.491	1.372		
63		2.688	2.676	2.619	2.530	2.449	2.392	2.351	2.325	2.320	2.312	2.240	2.072	1.848	1.634	1.456	1.310	1.207		
64		2.385	2.369	2.313	2.231	2.158	2.106	2.068	2.045	2.041	2.035	1.969	1.817	1.617	1.430	1.275	1.150	1.061		
65		2.112	2.093	2.039	1.964	1.898	1.851	1.817	1.795	1.793	1.787	1.728	1.590	1.413	1.249	1.115	1.007	0.931		
66		1.868	1.847	1.794	1.726	1.667	1.625	1.593	1.573	1.571	1.566	1.513	1.390	1.233	1.089	0.974	0.881	0.815		
67		1.649	1.626	1.576	1.514	1.461	1.424	1.395	1.376	1.374	1.370	1.323	1.213	1.074	0.949	0.850	0.770	0.713		
68		1.453	1.430	1.382	1.325	1.278	1.245	1.219	1.201	1.198	1.195	1.154	1.056	0.934	0.825	0.740	0.677	0.622		
69		1.278	1.254	1.209	1.157	1.116	1.088	1.063	1.046	1.042	1.040	1.004	0.919	0.811	0.717	0.644	0.586	0.542		
70		1.122	1.099	1.056	1.009	0.973	0.948	0.926	0.909	0.904	0.903	0.872	0.798	0.704	0.623	0.560	0.510	0.472		
71		9.853	9.656	9.307	8.778	8.466	8.253	8.048	7.875	7.825	7.816	7.562	6.917	6.102	5.401	4.868	4.434	4.103		- 5
72		8.597	8.382	8.010	7.621	7.349	7.168	6.980	6.808	6.749	6.746	6.539	5.987	5.283	4.680	4.226	3.852	3.562		
73		7.502	7.301	6.957	6.603	6.366	6.212	6.040	5.869	5.803	5.805	5.642	5.174	4.568	4.052	3.666	3.344	3.089		
74		6.532	6.348	6.030	5.708	5.500	5.370	5.212	5.044	4.973	4.979	4.854	4.463	3.945	3.505	3.178	2.900	2.675		
75		5.676	5.509	5.217	4.923	4.740	4.629	4.484	4.321	4.247	4.257	4.165	3.841	3.401	3.028	2.752	2.512	2.314		
76		4.921	4.772	4.505	4.237	4.073	3.976	3.844	3.688	3.614	3.626	3.563	3.298	2.927	2.612	2.379	2.174	1.999		
77		4.256	4.125	3.882	3.637	3.489	3.403	3.287	3.136	3.064	3.078	3.037	2.823	2.513	2.249	2.054	1.877	1.724		
78		3.672	3.558	3.339	3.114	2.978	2.899	2.789	2.655	2.588	2.603	2.579	2.408	2.151	1.932	1.769	1.618	1.484		
79		3.159	3.062	2.866	2.659	2.531	2.457	2.358	2.237	2.176	2.191	2.180	2.045	1.835	1.654	1.518	1.390	1.274		
80		2.710	2.627	2.453	2.264	2.142	2.070	1.980	1.874	1.821	1.836	1.833	1.727	1.557	1.409	1.298	1.190	1.090		

Table 1

flights are very similar. The Shuttle data, on the other hand, are in good agreement up to 70 km, with differences ranging between zero and 5%, but above 70 km the data diverge with differences up to about 15%. The local time of reentry was different by about 7 hours and possible tidal variations were investigated. The amplitude of the semi-diurnal tide in this altitude region is less than 1% and the maximum amplitude of the diurnal tide is 4% at 80 km and rapidly falls with altitude to about 1% at 75 km. Thus the tidal component will constitute a small part of the observed difference. Whether the large differences above 70 km are due to atmospheric variability is discussed in a later section.

The densities plotted in Figures 3 to 6 from Groves 85 models are the zonal mean values. Thus the effects of correcting for the longitudes corresponding to the Shuttle measurements were investigated. These corrections in Figures 4 and 6 (November flights) result in reducing the plotted Groves 85 model values by 2% up to an altitude of 60 km, 1.5% at 65 km, 1% at 70 km and 0.5% at 75 km. These corrections result in small improvements in the agreement between the model values and the data. The corresponding corrections for the STS-1 April flight (Figure 3) are an increase of 1% at all altitudes up to 75 km and 0.5% at 80 km. The effect of these corrections is negligible.

Figure 5 contains data from the STS-4 flight. The reentry took place in July and the appropriate models are plotted for comparison. The models agree well with the meteorological profile, with the Groves 85 model being the closest. The Shuttle data also agree well up to an altitude of nearly 70 km, but again above that altitude there are large excursions of the drag. The corrections to the Groves 85 model values for variations due to longitude amount only to an increase of 1% at all altitudes.

Although changes in density with longitude are small for the four flights considered in this paper, this is not the case for all sets of conditions. The changes with longitude are smallest at low latitudes and increase markedly with increasing latitude up to high latitudes. In addition, the changes are small in the summer and become larger in the winter. The maximum climatological variations are ±15% at 50 km and ±8% at 80 km at high northern latitudes in winter.

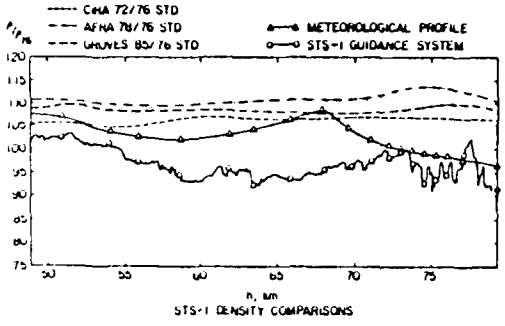

Fig. 3. The ratio to the U. S. Standard 76 of density from drag on STS-1 during reentry, the meteorological profile and the CIRA 72, AF Reference Atmospheres (AFRA) 78 and Groves 85 model values.

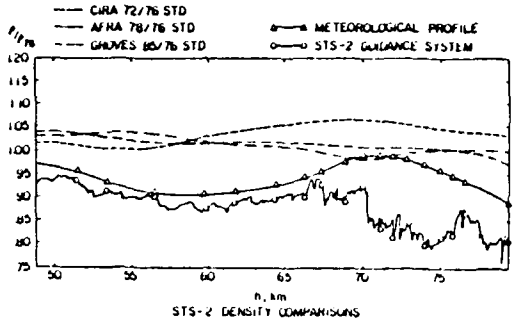

Fig. 4. The ratios of density for the reentry of STS-2.

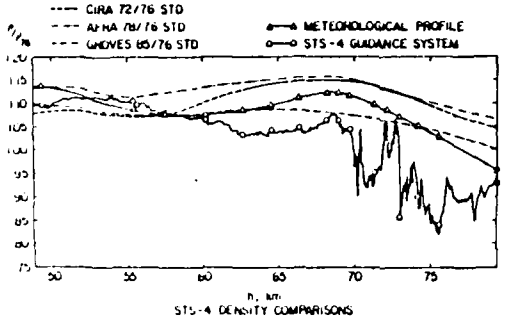

Fig. 5. The ratios of density for the reentry of STS-4.

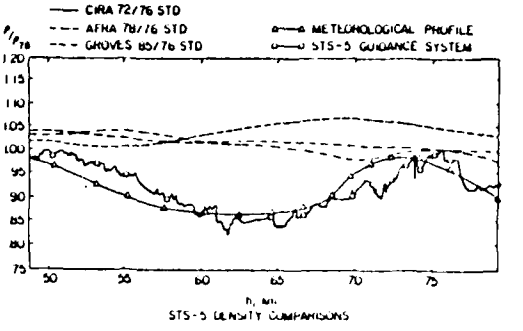

Fig. 6. The ratios of density for the reentry of STS-5.

SHUTTLE DATA AND ATMOSPHERIC VARIABILITY

In this section the same data from the reentry of STS-1, -2, -4 and -5 are compared with models which present known atmospheric variability based on climatological models. The AF Reference Atmospheres 1978 were chosen for this comparison because they include mean values, already used in Figures 3 to 6, median values and low and high values expected 10% and 1% of the time.

Figure 7 includes the STS-1 data and the meteorologial profile, the April mean model and the January median and 10% low models. Note that the AF Reference Atmospheres only contain the extreme percentiles for January and July. The January median model fits the Shuttle data better than the April mean model, suggesting that winter conditions existed at the time of reentry. The meteorological profile, on the other hand, lies between these two models.

Figures 8 and 10 show data from the STS-2 and STS-5 flights. They also contain the November mean model and the January median, 10% and 1% low and 10% high (Figure 10) models. The STS-5 data are close to the meteorological profile, but the STS-2 data deviate sharply above 68 km. The latter suggests unusual atmospheric conditions at the location of STS-2 reentry. it should be noted, however, that most of these data lie near the 10% low curve and only one point touches the 1% low curve. Thus the occurrence of these results is not statistically significant. The same conclusion applies to the data from STS-5.

Data from STS-4 are given in Figure 9. The data are close to the meteorological profile and models up to about 70 km. Above that altitude there are rapid fluctuations of up to ±20% in magnitude. Some of the peaks pass below the 1% low values. At that time the Shuttle was located near 25° N, 170° W at approximately 1200 hours local time. This means that it was very close to the summer sub-solar point. It is interesting to speculate that the fluctuations may be the result of convective atmospheric activity.

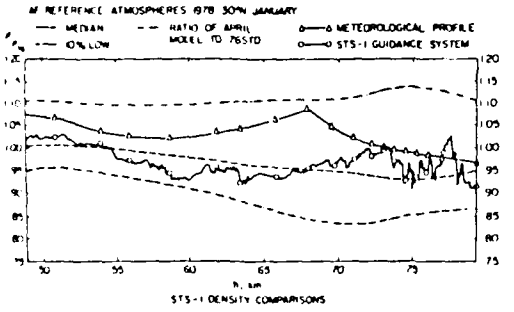

Fig. 7. Density ratios for STS-1, the meteorological profile and models specifying atmospheric variability.

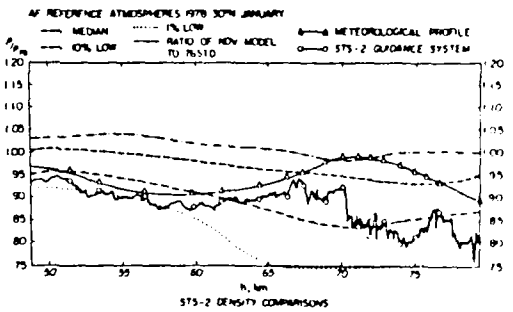

Fig. 8. Density ratios for STS-2 and models of atmospheric variability.

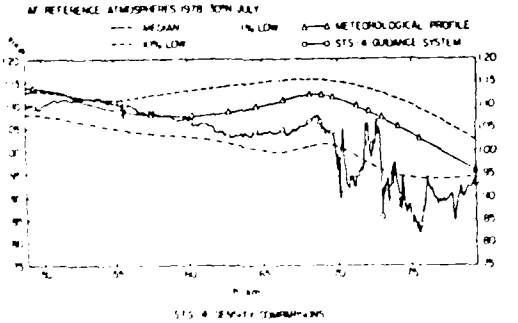

Fig. 9. Density ratios for STS-4 and models of atmospheric variability.

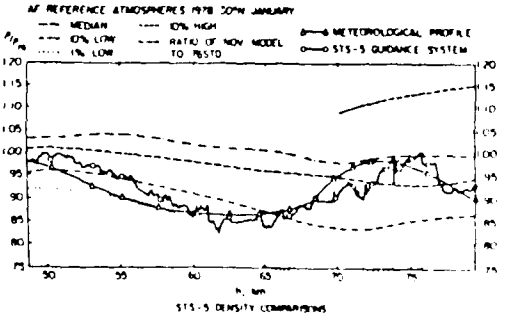

Fig. 10. Density ratios for STS-5 and models of atmospheric variability.

CONCLUSIONS

The available reference atmospheres and climatologically specified atmospheric variability up to 80 km at low and middle latitudes are reasonably accurate. At high latitudes, particularly in the winter, there are large systematic variations and large variability, such as result from sudden stratospheric warmings. Improved models are required for these conditions. This is part of the more general problem of unpredictable variations. These include turbulence, detailed storm effects in real time, and the location, amplitude, phase and velocity of gravity waves.

REFERENCES

1. COSPAR Working Group 4, COSPAR International Reference Atmosphere (CIRA) 1972, Akademie-Verlag,, Berlin (1972)

2. A. E. Cole and A. J. Kantor, Air Force Reference Atmospheres, AFGL-TR-78-0051, ADA 058505 (1978)

3. G. V. Groves, A Global Reference Atmosphere from 10 to 80 km, AFGL-TR-85-0129, ADA 162499 (1985)

4. J. J. Barnett and M. Corney, A Middle Atmosphere Temperature Reference Model from Satellite Measurements, Adv. Space Res. 5, #7, 125 (1985)

5. Yu. P,. Koshelkov, Proposal for a Reference Model of the Middle Atmosphere of the Southern Hemisphere, Adv. Space Res. 3, #1, 3 (1983)

6. J. J. Barnett and M. Corney, Middle Atmosphere Reference Model Derived from Satellite Data, Handbook for MAP, 16, 47, SCOSTEP Secretariat, University of Illinois, Urbana, IL, U.S.A. (1985)

7. J. M. Forbes, Atmospheric Tides between 80 and 120 km, Handbook for MAP, 16, 278, SCOSTEP Secretariat, University of Illinois, Urbana, IL, U. S. A. (1985)

8. COESA, U. S. Standard Atmosphere 1976, U. S. Government Printing Office, Washington, DC (1976)

Adv. Space Res. Vol. 7, No. 10, pp. (10)83–(10)96, 1987
Printed in Great Britain. All rights reserved.

0273-1177/87 $0.00 + .50
Copyright © 1987 COSPAR

SOUTHERN HEMISPHERE REFERENCE MIDDLE ATMOSPHERE

Yu. P. Koshelkov

Central Aerological Observatory, State Committee of the U.S.S.R. for Hydrometeorology and Control of Natural Environment, 123376 Moscow, U.S.S.R.

ABSTRACT

The wind part of the rocket-based empirical model of the middle atmosphere of the Southern Hemisphere is revised on the basis of new rocket and radar data. Wind and temperature values from this empirical model are compared with corresponding values from the satellite-based reference atmosphere compiled by Barnett and Corney. General similarity of the two models is confirmed, though marked discrepancies are sometimes revealed.

An empirical model for the Southern Hemisphere middle atmosphere based on rocketsonde information was published earlier /1,2/. The wind part of the model is now revised using greater amount of rocketsonde data (table 1), rawin results at the 20 km level /3/ and MF radar winds in the mesosphere at Adelaide, Townsville, Christchuch and in the Antarctic /4–8/. As a result, rather significant changes are obtained in the wind model values above 60 km and only minor alterations below. The revised reference wind values are presented in the Appendix and fig.1.

TABLE 1 The Number of Wind Measurements for Main Rocketsonde Sites in the Southern Hemisphere up to September 1985 Used for Compiling the Reference Atmosphere

Site	Period of obs.	Altitude, km		
		40	60	80
Vessels:	1961–1985			
5°N–5°S		535	210	--
5°S–15°S		118	28	—
15°S–25°S		190	12	--
25°S–35°S		141	17	—
35°S–45°S		109	13	--
45°S–55°S		126	9	—
Kerguelen Is.	1973–1981	171	156	72
Molodezhnaya	1969–1985	887	711	391
Woomera	1962–1974	111	78	43
Mar Chiquita	1966–1979	164	64	--
Ascension Is.	1964–1985	1750	857	44

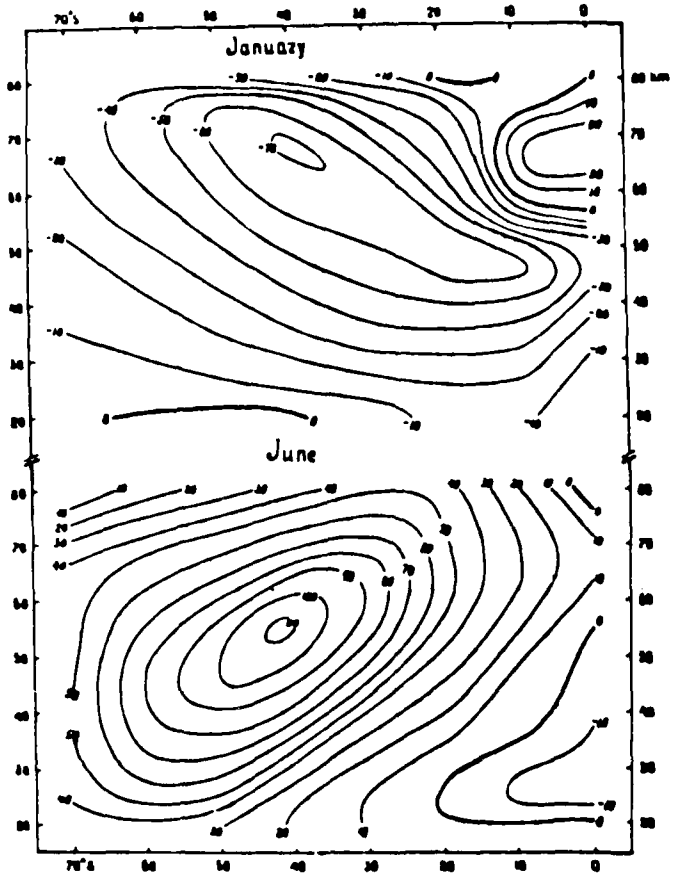

Fig.1. Cross sections of mean zonal wind (m/s) according to the S.H. reference model (based mainly on rockets and allowing for the MF radar data); upper part- January ;lower part - June.

Tables 2-4 give results of the comparison made for the Southern Hemisphere region between existing reference models- the one based mainly on rocketsondes (presented above, also in /1,2/) and that based on satellites /9/.

Significant systematic discrepancies in temperature (table 2, fig.2)between the two reference models at all latitudes of the Southern Hemisphere are only observed at altitudes 75 and 80 km (the rocketsonde are about 10°C colder than the satellites). For other altitudes, mean annual discrepancies exceeding 5°C are found at 35-40 km over the Antarctic.
The nature of the discrepancy encountered in summer is not clear while in the winter stratosphere it may be a result of different duration of the observational period for rocket sounding and satellites. Temperatures from an analytical presentation of the climatic distribution /10/ in which the MLR data have been correlated with atmospheric temperatures recorded by means of Soviet rocketsondes are also shown and reveal lowest temperatures.

Annual density differences between the models (table 3) are small. It is only in the upper mesosphere of low and middle latitudes that the density values from the rocket-based model are consistently higher than the satellite-based values (the roverse is true for the Antarctic mesosphere). As for

TABLE 2 Differences in Temperature (°C) between the Rocket-based and Satellite-based Reference Atmospheres

Height (km)	Month J	F	M	A	M	J	J	A	S	O	N	D	Year
						70°S							
80	-I	-5	-II	-I6	-I2	-9	-9	-I5	-I6	-II	-8	-3	-9.7
70	-4	-3	-3	-4	I	I	-2	-3	-5	-II	-9	-3	-3.7
60	0	-3	I	0	I	-3	-6	-2	-I	-I	-I	-I	-I.3
50	I	0	-I	-3	-8	-9	-6	-3	-3	-2	-I	0	-2.9
40	-5	-5	-I	0	-5	-8	-8	-3	-6	-9	-8	-7	-5.4
30	0	-2	2	4	I	I	-3	-5	-4	4	I	0	-0.I
20	0	-I	0	0	2	-2	-2	-I	-I	3	0	0	-0.2
						40°S							
80	-8	-I0	-I2	-I2	-I5	-I3	-I4	-I6	-I5	-I2	-8	-6	-IL8
70	0	-2	-2	-I	-4	-4	-3	-5	-8	-9	-7	-3	-4.0
60	0	2	4	5	5	2	3	7	7	4	3	0	3.5
50	3	0	-3	-3	I	I	-2	2	3	2	-I	I	0.3
40	-2	-3	-2	-I	2	4	0	0	4	I	-5	-5	-0.6
30	-I	0	I	2	3	5	3	0	I	3	3	-I	I.6
20	2	I	0	0	0	I	I	0	0	-I	0	0	0.3
						I0°S							
80	-9	-9	-I4	-I9	-I6	-I3	-I2	-I4	-I5	-I6	-I4	-9	-I33
70	3	I	-2	I	5	5	I	-2	-4	0	I	2	0.9
60	-I	2	4	4	2	I	I	3	4	5	2	0	2.2
50	I	0	0	0	0	2	2	0	I	I	I	I	0.7
40	-I	-3	-3	-I	0	0	2	-I	-I	-2	-2	-2	-I.2
30	I	I	I	I	0	-I	0	I	0	I	2	2	0.7
20	-I	-2	-3	-I	-I	-I	-I	-2	-I	-I	-I	-2	-I.4

TABLE 3 Differences in Density Values (% of the mean) between the Rocket-based and Satellite-based Reference Atmospheres

Height (km)	Month J	F	M	A	M	J	J	A	S	O	N	D	Year
						70° S							
80	-7	-8	-I	I	-2	-8	-I0	-8	-9	-I3	-II	-6	-6.8
70	-2	-6	I	3	-5	-I0	-I0	-8	-6	-5	-3	-2	-4.4
60	-3	-4	0	2	-6	-9	-8	-8	-7	-6	-4	-3	-4.7
50	-3	-4	0	3	-I	-3	-3	-4	-5	-4	-4	-3	-2.6
40	0	-I	I	4	2	I	0	-4	-2	I	I	I	0.3
30	I	I	0	0	I	2	5	2	2	-2	0	I	I.I
20	0	I	0	-I	-I	I	3	-I	-I	-4	-I	0	-0.3

40°S

80	-2	0	I	2	I	4	0	2	4	-I	-5	-6	0.0
70	-I	I	I	2	6	7	2	6	II	7	I	-3	3.5
60	-I	-I	-3	-2	3	6	-I	0	4	3	-3	-3	0.2
50	-3	-2	-I	0	3	5	I	0	3	2	-2	-4	0.2
40	0	0	I	I	2	4	2	0	0	I	2	-I	I.0
30	I	0	-I	-I	0	-I	0	0	0	-I	-I	0	-0.3
20	-I	0	0	I	I	0	0	I	I	I	0	-I	0.2

I0°S

80	3	I	I	4	7	7	3	I	0	4	3	3	3.I
70	I	0	2	2	2	2	2	2	2	3	I	0	I.6
60	I	-I	-2	-2	-I	0	0	-I	-2	-2	0	0	-0.8
50	0	-I	-I	-I	-I	-I	-I	0	-I	-I	-I	0	-0.8
40	0	I	I	0	0	0	-I	I	0	0	0	I	0.2
30	0	I	0	0	0	I	0	0	0	-I	0	0	0.I
20	2	2	2	2	I	I	I	2	I	I	2	I	I.5

TABLE 4 Differences in Zonal Wind Values (m/s) between the Rocket-based and Satellite-based Reference Atmospheres

Height (km)	Month												Year
	J	F	M	A	M	J	J	A	S	O	N	D	
						70°S							
80	-I5	-8	-24	-5	-22	-39	-29	-30	3	-7	-I8	-2I	-I7.9
60	-I0	9	2	8	3	-4	4	-8	3I	I8	-6	-II	3.0
40	-I2	0	I	3	3	-II	-8	-I2	20	-7	-6	-I2	-2.4
20	0	-2	-3	I	-2	-5	-7	-7	-7	-3	-2	0	-3.I
						40° S							
80	I8	20	9	-7	-8	-I0	3	0	2	-4	4	I	2.3
60	-3	-I	3	-8	-I9	-I5	0	I7	0	-I3	0	-9	-4.0
40	0	I	-5	-II	-I8	-I9	-I0	4	-3	-II	I	-2	-0.I
20	0	I	0	-3	-I	-I	-5	-4	-6	-3	-I	I	-I.8
						20°S							
80	3	-4	-20	2	22	37	I3	-2	-I7	II	23	22	7.5
60	-4	-5	-7	-5	-I4	-I0	-I6	-26	-4	2	I5	7	-5.6
40	-2	-4	-I7	-8	-I7	-I7	-I2	-I0	-II	-I	I3	II	-6.2
20	-5	0	-2	-2	-4	-5	-6	-5	-4	-I	0	-4	-3.2

monthly values, discrepancies higher than 5% are registered in the mesosphere and higher than 10% - only in the upper Antarctic mesosphere. The analytical model reveals the lowest density values in the upper mesosphere when compared to other models (fig.3).

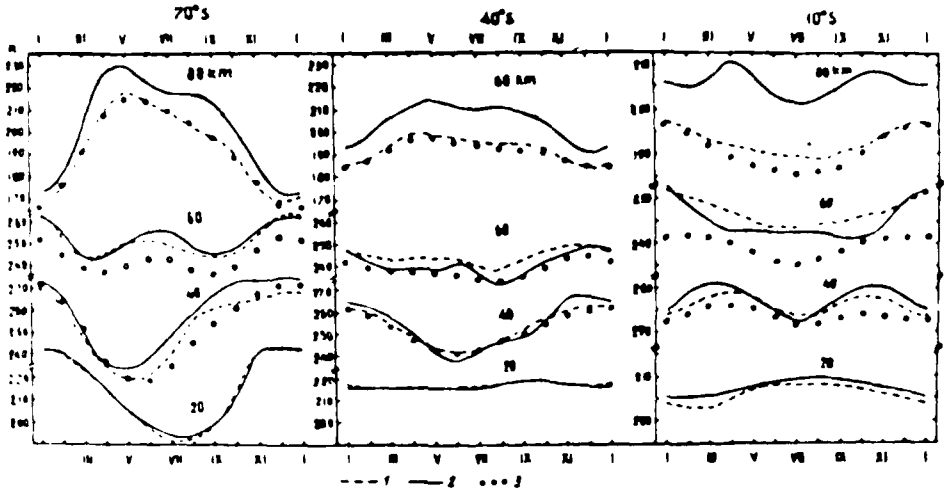

Fig.2. Seasonal temperature variations at latitudes 10°S, 40°S and 70°S. 1-S.H. reference middle atmosphere (based on rocket data); 2- middle atmosphere reference model curves from satellite data (Barnett and Corney, 1985); 3- CAO analytical model (Ivanovsky et al, 1984).

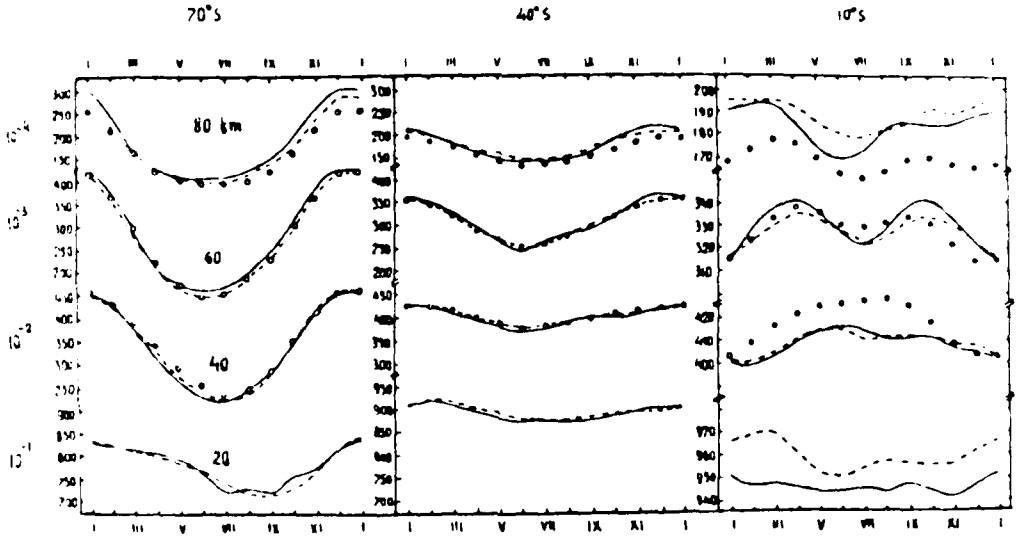

Fig. 3. Seasonal density variations at latitudes 10°S, 40°S and 70°S.(for legend see fig.2).

Seasonal variations of temperature or density revealed by the rocket-based and satellite-based models are similar but sometimes are smoother in the former case than in the latter (e.g.,temperature curves at 40 and 60 km for 40°S, density variation at 20 km for 70°S).Main discrepancies in the seasonal variations between the two models are encountered in the upper equatorial mesosphere.

Latitudinal temperature variations (fig.4) in the Southern Hemisphere revealed by the reference models have much in common. However, at the heights of 40 km and 80 km the magnitude of the gradients in summer is greater in the case of satellite data than in the case of rocketsonde data. The minimum in winter is located 5 to 10° latitude further south when depicted by the rocket data; the minimum is built up above the 55-km level utilising the rocket information and above 50 km in case of the SCR/HMR analysis. (In the Northern Hemisphere, discrepancies between the existing models are great in winter). Density gradients (fig.5) in the Southern Hemisphere in summer are somewhat greater when based on the rocketsonde data; the reverse is true for the winter period.

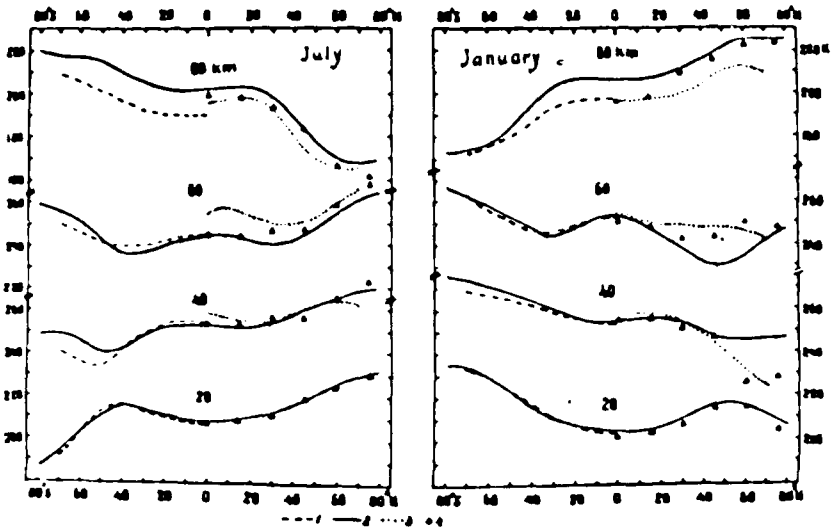

Fig.4. Meridional temperature variations in January and July. 1-S.H. reference middle atmosphere (based on rocket data); 2- middle atmosphere reference model derived from satellite data (Barnett and Corney, 1985); 3- CIRA 1972; 4—Air Force Reference Atmospheres (Cole and Kantor, 1978).

Temperature differences between the hemispheres determined by the satellites (fig.6) indicate higher temperatures occurring in the summer stratosphere in the Southern Hemisphere. A similar result could be seen from the comparison of rocket-based models and an exception in the 55-60 km layer may result from deficiencies of the compilation techniques, e.g., overestimation of temperature by CIRA 1972 in this layer. Both rocket and satellite data confirm relatively high temperature background formed in the Antarctic stratosphere and mesosphere in mid-winter above 30-35 km. Mid-latitudes are colder in the Southern than in the Northern Hemisphere, and this effect is more readily seen from rocketsondes than from SCR/PMR satellites. Density gradients in the Southern Hemisphere from the rocket data in summer are generally smaller and in winter greater than those given by the satellite data.

Hemispheric asymmetries in density values (fig.7) are similar when deduced

from the rocket and satellite-based reference atmospheres. Negative values of hemispheric differences (S.H. lower than N.H.) in winter are greater (and extend to the spring period) when estimated from the rocket data than from the satellites. In summer the density values are a little greater in the Southern than in the Northern Hemisphere, according to both models considered.

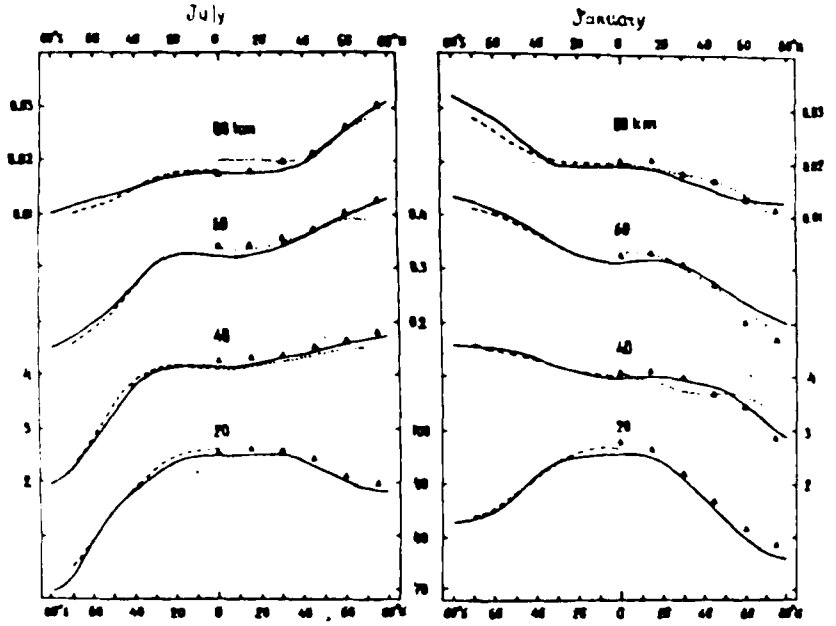

Fig.5. Meridional density variations in January and July (for legend see fig.4).

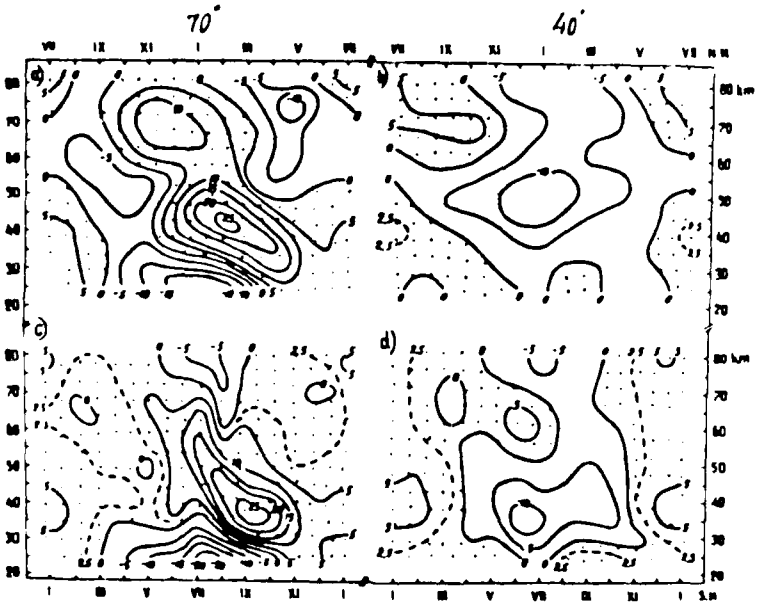

Fig.6. Temperature differences (°C) between the Southern and Northern Hemispheres, at 40° lat. and at 70° lat. a),b)-S.H. reference middle atmosphere (based on rocket data) and CIRA-72(N.H.). c),d)-Middle atmosphere reference model derived from satellite data (Barnett and Corney, 1985).

Values of zonal wind speed as well as the patterns of seasonal variations depicted by the rocket and satellite data analyses do not reveal substantial discrepancies (Table 4, fig. 8).

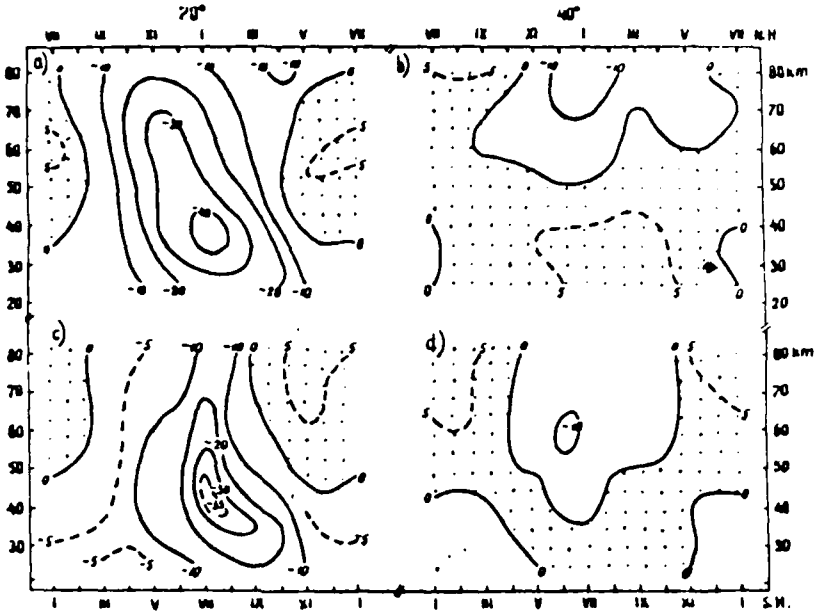

Fig.7. Density differences (%) between the Southern and Northern Hemispheres, at 40°lat. and 70°lat. (for legend see fig.6).

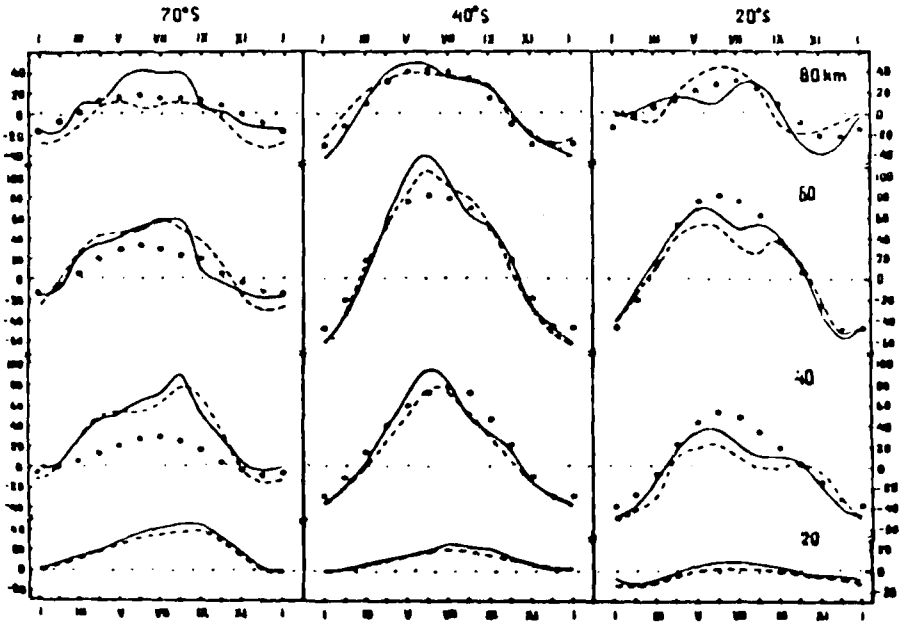

Fig.8. Seasonal variations of zonal wind (m/s) at 20°S, 40°S, and 70°S (for legend see fig.2).

However, the westerly flow in winter estimated from the rockets is 5 to

15 m/s weaker than that from the satellites; in high latitudes, this is valid during the whole winter; in low latitudes - only in early winter and not at all altitudes. It cannot be ruled out that a rapid attenuation of the westerly geostrophic wind over the Antarctic in September-October seen from the satellite data (fig.8) is a specific feature of the years considered. A small but systematic discrepancy could also be traced in winter between the radiosonde-based winds of the two models at the 20-km level. Greatest discrepancies between the models are found in the upper mesosphere.

Summer easterlies in the two models are of nearly equal intensity in middle latitudes, while the rocket winds over the Antarctic are greater (by 5 to 12 m/s) than the satellite winds; in the latter, puzzling is the appearance of zero wind values at 30-40 km at 70°S distorting latitudinal wind sections /9/ in December and January. The satellite-based sections also reveal development of two separate cores in the westerlies (near 60-70°S and 30°S) in the period from August to October and two cores in the easterlies (at 40-45°S and 15°S) from December to February which are not readily seen in the rocket-based winds. At specified altitude levels, the meridional distribution of zonal wind (fig.9) is rather smooth and reveals general similarity between the satellite and rocket analyses, particularly in summer.

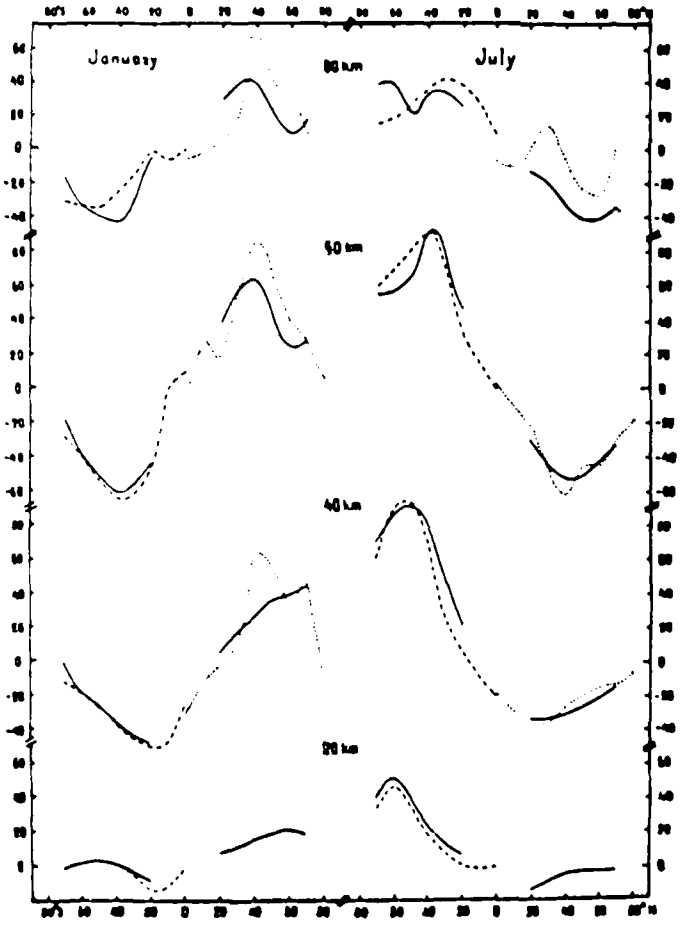

Fig.9. Meridional variations of zonal wind speed (m/s), in January and July (for legend see fig.4).

The main maximum of westerly speeds in winter reaches its northern-most position ($\sim 40^{\circ}$S) in May (rocket data) or June (satellite data). Its height, as the two models agree, should be about 55 km from April to June, 50 km in July and decreases with time afterwards- more rapidly according to the satellite data. The satellite-based model confirms the fact noted earlier /12/ that the altitude position of the westerly maximum is by several kilometers lower in the Southern than in the Northern Hemisphere.

Hemispheric asymmetry in zonal wind speeds (table 5) analysed separately from rocket and satellite data, proves to be of the same nature: both easterly flow in summer (with the exception of the polar region) and westerly flow in winter are more intensive in the Southern than in the Northern Hemisphere. The magnitude of the hemispheric differences, however, in winter is greater for the satellite than for the rocket data. In summer, satellite-based differences at 70°lat. also seem to be exaggerated.

TABLE 5 Differences in Zonal Wind Speed (m/s) between the Southern and Northern Hemispheres. Top - comparison of rocket-based models (the present model, S.H., and CIRA-1972, N.H.); bottom - the satellite-based model /9/.

Height (km)	Latitude					
	20	40	70	20	40	70
	Summer (Jan. S.H.-July N.H.)			Winter (July S.H.-Jan. N.H.)		
80	- /9	-22/-12	-31/18	- /-2	-38/-6	0 /20
60	-26/-14	-3/-9	3/16	12/9	6/29	30/27
40	-14/-15	-10/-6	1/14	11/16	9/56	16/25
25	5/0	0/2	2/4	0/0	13/18	40/17

In general, the rocket-based and the satellite-based reference atmospheres in a similar manner reflect main features of the structure and circulation in the stratosphere and mesosphere of the Southern Hemisphere. There are, however, some discrepancies between the results of the two models the origin of which should be resolved.

REFERENCES

1. Yu.P.Koshelkov, Adv.Space Res. 3, 3-16 (1983).
2. Yu.P.Koshelkov, Handbook for MAP 16, 15-35 (1985).
3. Yu.P.Koshelkov, Antarctica 25, 13-14 (1986).
4. G. J.Fraser, J. Atmos.Terr.Phys. 46, 143-146 (1984).
5. R. MacLeod and R.A.Vincent, J.Atmos. Terr.Phys. 47, 567-574 (1985).
6. A.H. Manson, C.E.Meek, R.A.Vincent and M.J.Smith, Handbook for MAP 16, 36-46 (1985).
7. A.Phillips and R.A.Vincent, private communication (1986).

8. R.A.Vincent, J.Atmos. Terr. Phys. 46, 961-974 (1984).

9. J.J.Barnett and M.Corney, Handbook for MAP 16, 47-85 (1985).

10. A.I.Ivanovsky, V.V.Fedorov, V.N. Glazkov, I.N.Ivanova, L.M. Kolomiitseva, Yu.P.Koshelkov, E.N.Kovshova, K.E. Speransky, and L.V. Sherbakova, preprint to XXV COSPAR Meeting, Graz, Austria (1984).

11. A.E.Cole and A.J.Kantor, Air Force Reference Atmospheres, Air Force Surv. in Geophys. 382, AFGL-TR-78-0051.

12. Yu.P.Koshelkov, Space Research XV, 167-172 (1975).

APPENDIX Southern Hemisphere Reference Middle Atmosphere. Zonal winds (m/s).

Height (km)	Month J	F	M	A	M	J	J	A	S	O	N	D
						0°S						
80	0	-34	-40	-34	-20	-7	9	-10	-25	-35	-11	3
75	12	-8	-14	-17	-10	1	10	1	-12	-22	-15	11
70	25	23	18	7	4	11	10	12	-6	9	4	15
65	24	27	30	22	12	12	8	13	15	23	21	11
60	10	22	28	32	13	6	-1	7	15	25	15	0
55	-5	15	25	29	13	0	-11	-2	10	22	7	-15
50	-34	0	18	23	13	-3	-22	-10	4	17	5	-26
45	-38	-22	4	16	12	-4	-24	-18	-3	12	5	-21
40	-26	-32	-16	-1	4	-7	-20	-21	-11	2	2	-15
35	-16	-22	-22	-13	-10	-11	-17	-19	-14	-7	-5	-14
30	-9	-12	-12	-12	-15	-15	-15	-16	-15	-12	-11	-11
25	-6	-7	-7	-10	-12	-17	-15	-15	-15	-15	-13	-8
20	-2	-1	0	1	1	1	0	-1	-3	-3	-3	-3
						10°S						
80	-6	-40	-35	-12	9	20	29	8	-22	-29	-13	6
75	-3	-10	-13	-3	18	26	30	22	-5	-20	-18	6
70	11	20	11	19	26	30	28	31	23	2	-11	-3
65	10	22	23	37	34	31	24	23	30	16	-2	-12
60	1	14	24	40	32	28	16	14	20	19	-11	-22
55	-22	0	21	34	27	18	0	5	12	15	-11	-42
50	-56	-22	10	28	20	11	-11	-4	5	14	-6	-49
45	-63	-43	-9	20	16	7	-11	-7	-1	10	-3	-36
40	-49	-44	-28	7	12	4	-8	-6	-4	3	-4	-22
35	-35	-36	-31	-10	-1	0	-6	-8	-7	-3	-8	-18
30	-27	-25	-21	-15	-11	-8	-8	-9	-9	-9	-12	-17
25	-18	-17	-16	-14	-12	-12	-10	-11	-12	-13	-14	-16
20	-12	-12	-10	-5	-1	0	- 1	-2	-4	-6	-8	-10
						20°S						
80	-1	-5	-10	16	34	44	39	27	-12	-20	-18	-9
75	-20	2	3	26	42	49	43	39	5	-11	-30	-25
70	-30	0	13	40	53	52	43	41	30	2	-32	-35
65	-36	-8	17	45	57	55	40	36	38	10	-25	-45
60	-47	-16	11	42	53	53	31	26	35	14	-21	-52
55	-60	-31	0	36	46	46	23	16	23	14	-18	-53
50	-65	-42	-11	30	37	38	14	9	13	13	-12	-50
45	-61	-48	-22	20	28	30	10	4	5	9	-7	-39
40	-56	-43	-30	10	18	21	9	0	-1	4	-5	-30
35	-32	-30	-30	-3	5	11	7	0	-3	0	-5	-20
30	-27	-28	-25	-9	-3	3	4	-1	-4	-5	-7	-17
25	-19	-20	-18	-11	-5	-2	0	-3	-5	-6	-10	-14
20	-14	-14	-12	-6	-1	1	1	0	-2	-4	-6	-9

Height (km)	Month											
	J	F	M	A	M	J	J	A	S	O	N	D
						30°S						
80	-16	2	16	33	45	49	42	38	18	-7	-20	-18
75	-36	-11	18	41	55	60	57	51	34	0	-31	-38
70	-52	-20	17	47	70	73	68	61	45	4	-33	-51
65	-63	-28	11	50	76	86	72	63	47	7	-29	-55
60	-63	-35	5	45	74	88	68	56	44	11	-25	-54
55	-63	-41	-1	39	67	84	60	48	38	14	-20	-52
50	-59	-42	-3	32	57	73	51	36	30	13	-15	-46
45	-53	-39	-11	24	43	58	39	28	20	9	-11	-37
40	-45	-32	-13	15	30	38	26	19	12	4	-9	-29
35	-35	-27	-13	7	20	24	18	14	8	1	-6	-21
30	-24	-22	-12	1	9	16	13	11	6	-1	-7	-15
25	-14	-16	-11	-2	4	9	9	8	3	-2	-5	-10
20	-5	-6	-4	2	6	9	9	6	4	1	-1	-2
						40° S						
80	-26	0	21	33	40	38	37	30	26	-2	-21	-33
75	-54	-19	22	41	50	54	52	45	37	2	-32	-53
70	-70	-31	19	50	60	66	66	58	46	4	-32	-62
65	-78	-35	12	52	73	87	81	70	52	6	-30	-59
60	-64	-36	7	49	83	104	92	76	52	7	-27	-54
55	-59	-35	2	44	84	110	97	76	48	7	-24	-49
50	-52	-32	0	39	73	101	91	70	43	7	-19	-43
45	-43	-27	-1	32	64	89	83	61	39	6	-16	-35
40	-36	-21	-2	24	50	74	72	51	30	5	-14	-28
35	-29	-17	-2	17	36	56	59	41	22	5	-10	-20
30	-19	-12	-3	12	25	37	42	33	18	6	-7	-14
25	-10	-7	-2	8	16	23	30	25	15	7	-3	-8
20	1	2	5	9	13	18	20	18	15	10	5	3
						50°S						
80	-35	-8	13	20	26	25	27	23	20	-2	-21	-43
75	-66	-21	17	32	38	42	43	37	31	1	-32	-56
70	-81	-27	16	41	49	55	56	46	40	2	-32	-66
65	-87	-27	16	45	59	69	68	61	47	3	-29	-68
60	-81	-25	17	47	70	82	81	72	54	3	-27	-61
55	-76	-22	16	46	77	93	93	81	56	5	-23	-54
50	-68	-18	13	48	77	100	101	84	56	8	-19	-52
45	-61	-15	11	42	71	98	101	82	54	10	-16	-31
40	-55	-12	10	34	60	87	93	76	51	13	-13	-25
35	-22	-8	9	27	49	76	84	71	49	17	-9	-19
30	-14	-5	7	20	38	66	72	64	43	22	-4	-13
25	-7	-2	7	17	30	43	56	52	44	26	1	-7
20	3	7	11	16	22	30	36	37	32	24	9	4

Height (km)	Month											
	J	F	M	A	M	J	J	A	S	O	N	D
						60° S						
80	-34	-20	-4	I2	I9	I5	I9	I6	I3	-3	-26	-43
75	-45	-26	5	22	28	30	34	28	2I	I	-32	-50
70	-46	-26	I3	3I	39	46	48	40	3I	2	-32	-50
65	-43	-20	23	4I	49	56	60	53	40	4	-26	-47
60	-38	-I5	27	48	57	64	70	64	49	9	-23	-4I
55	-33	-II	32	54	62	7I	78	74	58	I3	-I9	-36
50	-28	-9	3I	55	67	79	86	83	66	I8	-I3	-30
45	-22	-7	27	54	68	80	92	9I	72	24	-II	-25
40	-I8	-6	2I	47	64	79	88	90	75	30	-8	-20
35	-I4	-4	I7	38	58	75	82	84	76	39	-3	-I5
30	-9	-2	I4	30	50	65	74	76	73	46	I	-II
25	-4	2	I2	25	42	54	64	66	66	5I	8	-5
20	I	6	I3	I9	28	37	47	52	49	4I	I3	2
						70°S						
80	-3I	-25	-I4	7	I2	3	I0	I0	7	-5	-29	-36
75	-34	-25	-9	I3	20	I5	23	I9	II	I	-33	-4I
70	-32	-I7	3	25	3I	34	36	30	I8	3	-30	-39
65	-30	-I0	I8	37	39	44	52	4I	29	9	-27	-36
60	-27	-3	25	42	44	47	59	50	37	I5	-20	-3I
55	-23	-I	29	46	46	47	62	6I	45	2I	-I4	-28
50	-I8	0	30	49	48	49	64	69	55	25	-8	-23
45	-I4	0	29	52	5I	5I	64	76	64	30	-6	-I9
40	-I2	0	25	48	53	5I	6I	77	70	37	-4	-I6
35	-I0	0	20	42	50	5I	56	72	72	44	0	-I3
30	-7	I	I6	33	45	47	50	65	69	50	5	-9
25	-4	2	I2	26	37	43	43	53	57	44	I0	-5
20	-I	4	9	I7	24	29	33	36	37	28	I3	0

Adv. Space Res. Vol. 7, No. 10, pp. (10)97–(10)104, 1987
Printed in Great Britain. All rights reserved

0273-1177/87 $0.00 + .50
Copyright © 1987 COSPAR

MIDDLE ATMOSPHERE TEMPERATURE MEASUREMENTS AS COMPARED TO ATMOSPHERIC MODELS

D. Offermann, R. Gerndt and R. Küchler

Physics Department, University of Wuppertal, 5600 Wuppertal 1, F.R.G.

ABSTRACT

Two large sets of temperature data measured in Europe are compared to atmospheric models that were prepared for the NEW CIRA. The data were taken by rocket flights during the Energy Budget and MAP/Wine Campaigns, and during several years of operation of ground based OH* spectrometers. Monthly mean temperature profiles from 20 - 85 km are available for November, December, and January. They are in very good agreement with the new models. Seasonal and latitudinal variations of upper mesosphere temperatures are obtained from the OH* data. They are also in fair agreement with the new models. These are therefore found a definite improvement as compared to the older ones. On the basis of this general agreement it is concluded that finer details as variations with solar cycle, magnetic activity, etc. could come into reach of future models.

INTRODUCTION

Current reference atmospheres like CIRA 1972 /1/ or the Air Force Reference Atmospheres /2/ contain middle atmosphere temperature models that are mostly based on rocket measurements. It is well known that these are biased towards the American continent. Recently Barnett and Corney /3/ proposed a temperature model derived from several years of satellite infrared measurements, that is more global in nature. Groves combined previous rocket data and this recent satellite model /4/. As it is planned to replace CIRA 1972 by a new version (1986) including more recent measurements, it is interesting to compare the various models to independent data, that have not been used in any of the temperature models, and that were not taken in America.

There are two respective sets of data that were measured by different techniques in Europe since 1980. The first set was obtained by 21 meteorological rockets launched from ESRANGE (68° N, 21° E) in November 1980 during the Energy Budget Campaign /5/, and by 64 meteorological rockets launched from Andoya (69° N, 16° E) in December 1983 and January/February 1984 as part of the MAP/Wine Campaign /6/. It covers the altitude regime 20 - 85 km, and represents a very substantial fraction of all rocket temperature measurements taken in northern Scandinavia. The second set was derived from several years of ground based measurements of near infrared emissions of the OH* layer near the mesopause. These were mostly performed by spectrometers located at Wuppertal (51° N, 7° E) and Oslo (60° N, 11° E), and to a lesser degree by spectrometers at Andoya, ESRANGE, and Longyearbyen (78° N, 15° E). Hence all of these data stem from a narrow sector in geographic longitude while covering quite a range of latitudes and an extended time period.

The meteorological rockets employed Datasondes or passive falling spheres. These techniques, their accuracy and the data obtained during the two campaigns were described in detail in various papers /7 - 10/. The OH emissions originate from a layer centered at about 86 km and 8 km thick /11/. Temperatures derived thus represent weighted means over the emission layer. They are nevertheless useful data because the temperature gradient at this altitude is generally small. Comparison of OH* temperatures with simultaneous rocket or lidar measurements have been made as much as possible /13, 17/. In ten cases analysed no systematic differences were found. It is therefore believed that OH* temperatures are reliable at the level of 4 - 5 K at least. As a consequence the temperatures gained by rocket measurements during the MAP/Wine Campaign have been normalized to the OH* temperatures /10/. As these temperature profiles are obtained by downward integration of the measured atmospheric densities, the normalization affects the temperatures to about one scale height below the normalization level. During the discussion of rocket data given below, it must therefore be kept in mind that the MAP/Wine temperatures above 80 km cannot be considered independent data. OH* data obtained and their analysis for the time period of the two campaigns

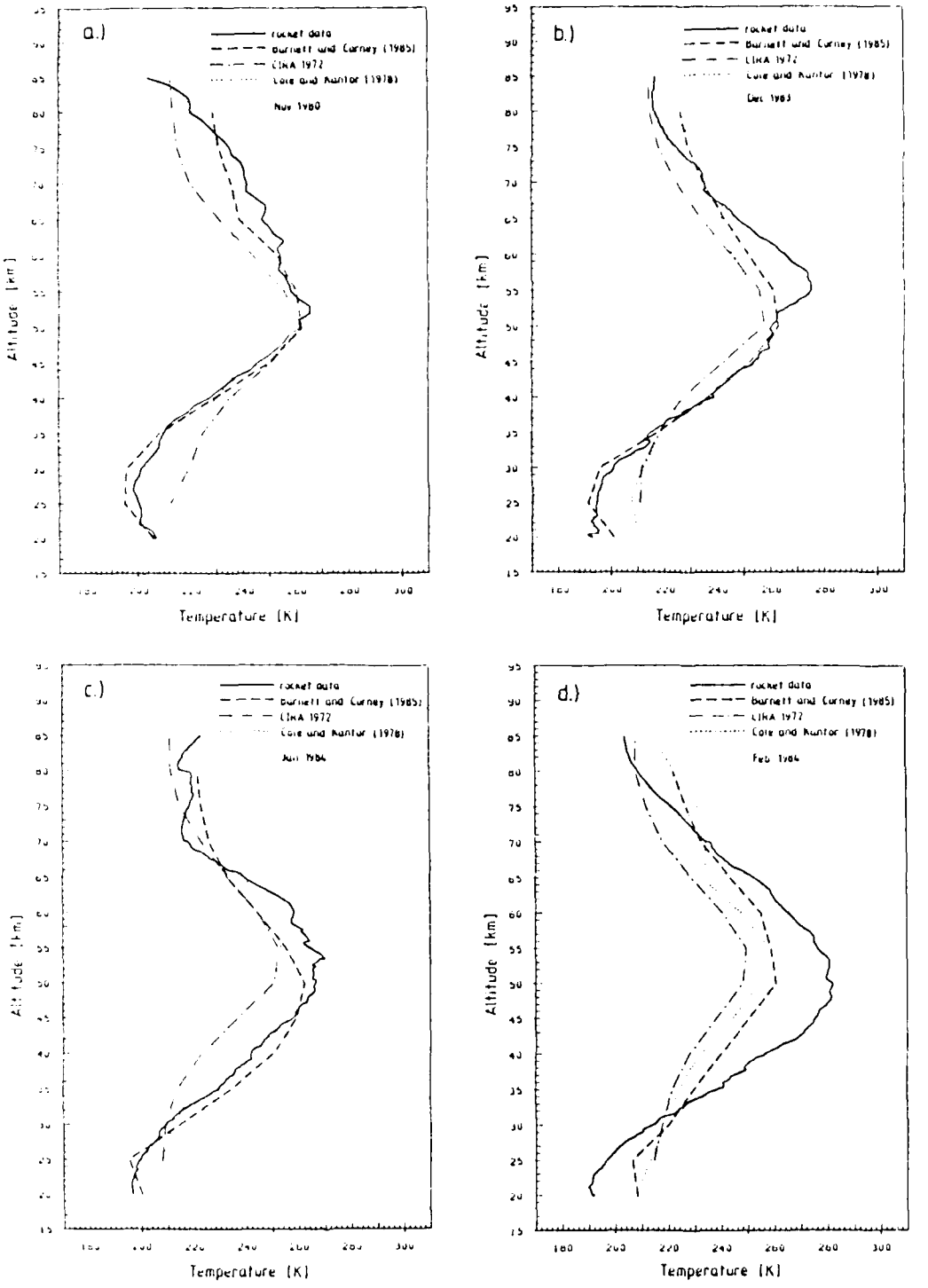

Fig. 1. Monthly mean temperature profiles as measured by rockets: a) Energy Budget Campaign (Nov. 1980), b,c,d) MAP/Wine Campaign (Dec. 1983 to Feb. 1984). Model profiles from reference atmospheres are given for comparison.

are described in detail elsewhere /12 - 14/. There are many additional data taken at other times /13, 15, 16/ that will be discussed together with the campaign data below.

MONTHLY TEMPERATURE PROFILES

Rocket temperatures measured during the Energy Budget Campaign (November and 1st December 1980) were averaged at altitude steps of 1 km, and are shown in Fig. 1a. The resulting altitude profile is taken as a mean November profile, though one must bear in mind the possibility of individual differences from one winter to another. The mean profile is not smooth, but shows some small scale structure including a number of kinks. This is mostly attributed to short period waves (gravity waves etc.) that were present. The kinks are due to the fact that the various rockets covered different altitude ranges. Hence it occurs that mean temperatures at two adjacent altitude levels are calculated from different numbers of measurements and that a kink may arise. The number of data points (rockets) available for averaging is largest in the middle of the altitude regime covered (for instance 23 at 50 km). It decreases at the highest and lowest levels and is about 7 at 80 - 85 km and 7 at 20 - 25 km. The mean temperature values are therefore less significant here. As the small scale structures would disappear if the number of rocket flights available for the mean would go towards infinity, these structures in Fig. 1a give an indication of the quality of the measured monthly mean profile.

From the rocket data measured during the MAP/Wine Campaign respective mean profiles are obtained for the months of December, January, and February (at altitude steps of 0.2 km). They are shown in Fig. 1b, c, d. The following numbers of rocket flights were available in the regimes of the uppermost five kilometers, the stratopause, and the lowest five kilometers: 4, 10, 3 in December 1983; 19, 10, 5 in January 1984; and 17, 26, 5 in February 1984. It should be noted that several minor stratospheric warmings (and respective mesospheric coolings) were present during the MAP/Wine and Energy Budget campaigns /14/. These may have contributed to the residual wavy structures in the monthly mean profiles. By end of February 1984 a major (final) warming occurred /18/. This is easily seen in the high stratopause temperatures of Fig. 1d, though the rocket flights covered only the build-up phase, and not the decay phase of the major warming. The profile given in Fig. 1d therefore cannot be considered a reliable mean representative for the month of February.

To compare the measured data with reference atmospheres, respective profiles were taken from CIRA 1972 (Part 2) and from the model of Cole and Kantor /2/ for the latitude in question, and are shown in Fig. 1. The data presented are seen to be consistently higher than CIRA 1972 in the mesosphere in all four months. In the upper part of the stratosphere they are somewhat lower than CIRA 1972 in November, turning to be higher (with increasing tendency) in December, January, and February. In the lower stratosphere they are considerably lower than CIRA 1972 in all four months. The differences between the present data and the Cole and Kantor model are less pronounced. They are, however, clearly visible and follow a systematic pattern at least in the stratosphere, too. As these deviations are so systematic, it is concluded that individual features of the winters in question were relatively small compared to the deviations discussed.

Also included in Fig. 1 are profiles of Barnett and Corney /3/. They show a very encouraging agreement with the rocket data at all altitudes and months with the exception of February 1984. (This month quite obviously is too strongly biased by the major stratospheric warming). The deviations of the present data from this new model are - on the mean - much smaller than from any of the two other models discussed. Thus on the basis of our data the model of Barnett and Corney must be considered a real improvement in the middle atmosphere for high latitude winter.

In Fig. 2a, b the monthly means of December 1983 and January 1984 are given again. In this case the model profiles of Barnett and Corney and of Groves /4/ are included for comparison. It is seen that the Groves curves are somewhat below the Barnett and Corney profiles in the upper mesosphere, whereas they tend to be above them in the lower mesosphere. The same is found for the November and February profiles not shown here. Comparison to the measured profiles presented here shows that there is a systematic difference, the measured data being lower than the models in the upper mesosphere, and higher in the lower mesosphere. It thus appears that the Groves profiles are even somewhat better a fit to the data than the Barnett and Corney profiles. This conclusion is, however, not really safe because the systematic deviations could be precursors of the major warming in February 1984. This event is namely characterized by the same type of deviations from the model profiles, which are, however, much larger (see Fig. 1d). Such deviations are typical for stratospheric warmings /2/. The argument is supported by the November 1980 data where the Groves model is not a better fit to the data than the Barnett and Corney model.

As the difference between the two models (shaded area in Fig. 2) is small for the conditions discussed one may take them together as "undisturbed" mean profiles of the mesosphere. The deviation of the measured profiles from them is considerable and systematic, as said above.

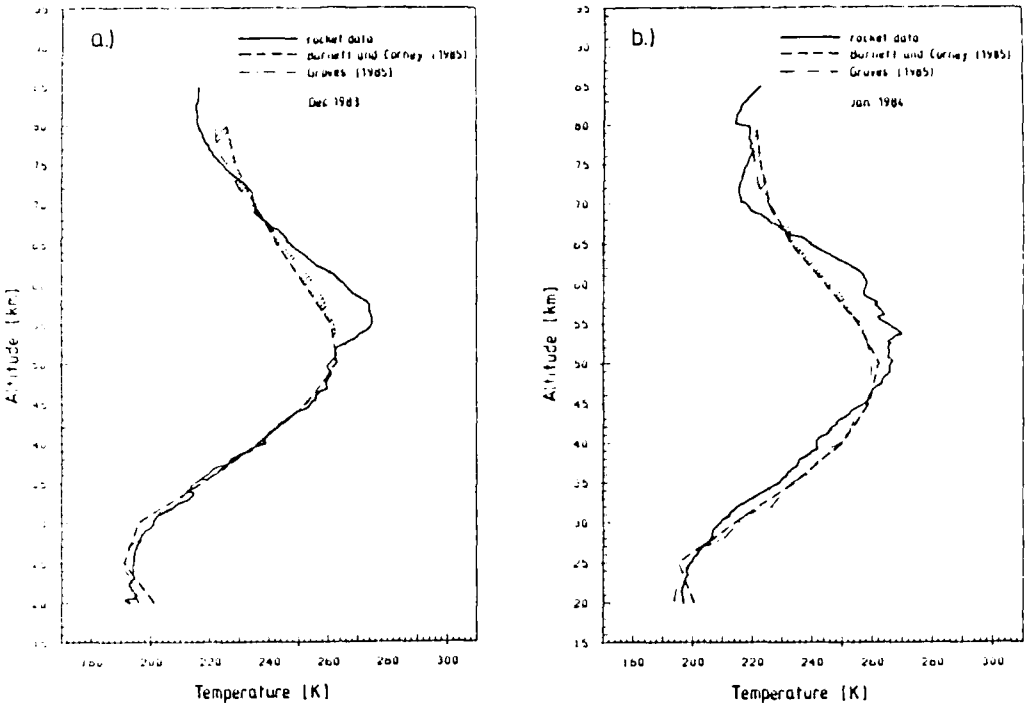

Fig. 2. Comparison of rocket temperatures to the models of Barnett and Corney /3/ and Groves /4/. a) December 1983; b) January 1984

If it is justified to adopt these profiles as being undisturbed, one is faced with the peculiar feature of a build-up phase of the major (final) warming which starts more than two months before the peak of the warming occurs! This "precursor structure" is less pronounced if the Groves profiles are adopted as references. One might thereby be led to prefer this model.

UPPER MESOSPHERE TEMPERATURES

Seasonal Variations

Two near infrared spectrometers of the University of Wuppertal for determination of OH* temperatures were operated since 1980 at Wuppertal and since 1982 at Oslo, respectively. During the campaigns described one of the instruments was taken to the rocket ranges (ESRANGE or Andoya). The spectrometers measured continuously every night as much as weather and instrumentation allowed. One temperature value was taken every two to five minutes. From these data nightly mean values were calculated. Typically 15 good nights were available each month. Nightly means were averaged and yielded the monthly means used in this analysis. Hence a very large number of temperature determinations enters a monthly mean, the statistical error of which is therefore rather small (<1 K). The total error of the mean values is $\leq \pm$ 2.5 K /13/. The monthly means obtained at Wuppertal and Oslo since 1980 are given in Fig. 3. (If less than five daily mean values were available for a monthly mean, it is labelled by "1".) Temperatures could not be measured at Oslo around summer solstice, as solar elevation remains too high during night.

Seasonal variation as measured above Wuppertal (51° N) is shown in Fig. 4. Several years of data were averaged to obtain the curve. It is compared to three atmospheric models. There are large differences with respect to the Cole and Kantor model /2/. Agreement with the Groves model /4/ is much better. Best agreement is obtained with Barnett and Corney /3/, if this model curve is slightly shifted in time (by 9 days to earlier times). The agreement is

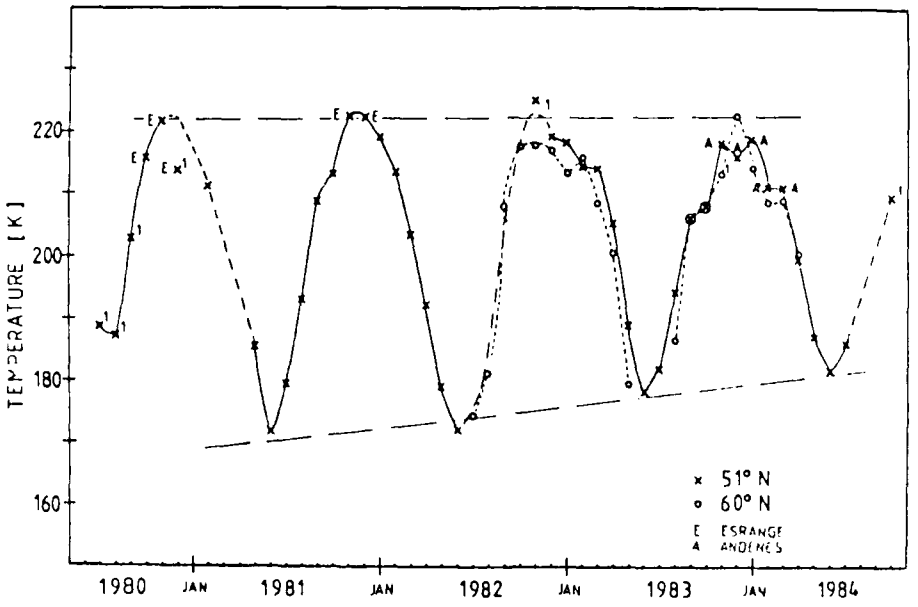

Fig. 3. Monthly mean OH* temperatures (86 km) measured at Wuppertal (51° N) and Oslo (60° N). Measurements during rocket campaigns at ESRANGE or Andoya are indicated by E and A, respectively. Dashed line connecting the summer minima has a gradient of 3 K/year.

very good in winter. In summer there appears to be a slight discrepancy. It should be noted here, that the Barnett and Corney model does not extend to 86 km. Its uppermost level (at 81.7 km) was used in Fig. 4 instead. (The same applies to the Groves model.) Hence if there is a temperature gradient in this altitude regime, it will affect the agreement. The data shown in Fig. 3 appear to indicate a longterm trend especially of the summer temperatures, as will be discussed below. The range of change of summer minimum temperatures is given in Fig. 4 as a bar together with the June temperature value. If one goes into these finer details one should note that the Barnett and Corney model is based on data taken from 1973 - 1978 (ascending part of the solar cycle), whereas the OH* temperatures were measured from 1980 - 1984 (descending part of solar cycle).

The seasonal variation measured at Oslo (60° N) is shown in Fig. 5. The Barnett and Corney model is shifted by 3 days (to earlier times) in this picture. Agreement of this model with data is again good, although the summer differences are somewhat larger. In winter the model appears to be slightly too high. A similar result was indicated by the rocket data taken at even higher latitudes, as discussed above. However, the difference in altitude of measured and model curves has to be taken into account, before conclusions can be drawn.

Latitudinal Variations

Fig. 3 shows that two OH* spectrometers of the University of Wuppertal were operated simultaneously at Wuppertal and Oslo for a time period of about two years. Also one of the two instruments was operated once in a while at even higher latitudes (68° - 69° N). These two instruments were carefully calibrated by a standard procedure to make the measured data comparable. They were also operated at the same place (Oslo) for a while, and proved to yield the same temperatures /13/. Latitudinal dependence of 86 km temperatures during the course of the year can therefore be derived from these data /13/. As an example the latitudinal differences during two winter and two summer months are shown in Fig. 6. They are compared to respective atmospheric models. Model data are for 10° E, and vary by less than 0.2 K when the exact longitudes of the measurement sites are used. The slight differences between measurements and models as discussed above (and largest in summer) are of course reproduced in this picture. The essential result obtained from Fig. 6 is, however, that the relative latitudinal variation of temperature is small (especially in winter), and fairly similar in models and measured data. Three additional data points are included to Fig. 6, which were measured by two other instruments. The data points at 78° N (Svalbard, /16/) are about in

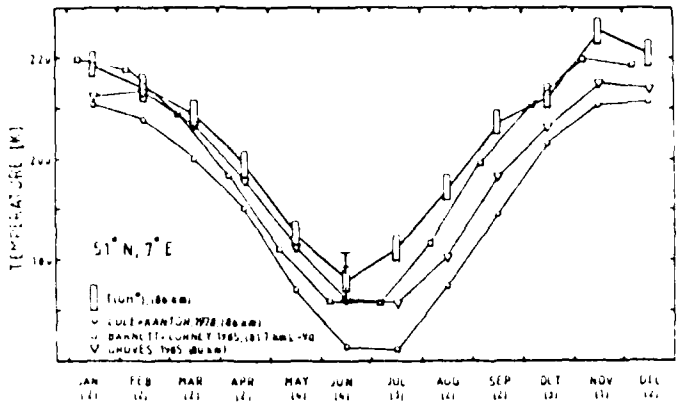

Fig. 4. Seasonal variation of Qff* temperature (86 km) above Wuppertal. The figure below the month gives the number of years available for calculating the mean. Size of the symbol indicates error of measured data. Profiles from reference atmospheres are given for comparison.

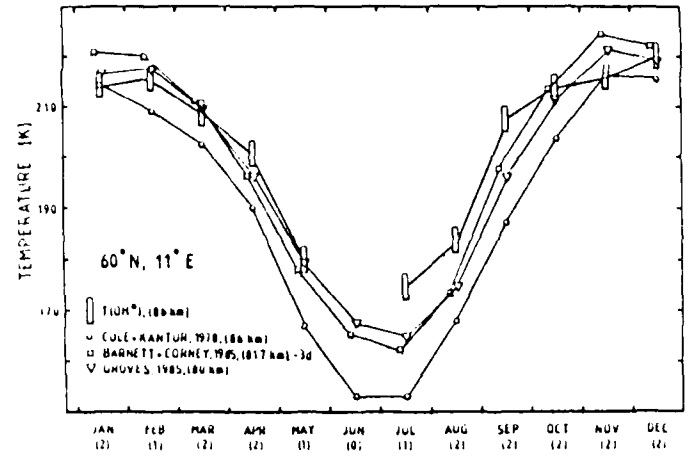

Fig. 5. As Fig. 4, but above Oslo.

line with the models, taking into account that the December value may have been affected by a stratospheric warming/mesospheric cooling. The August value at 68° N was taken under conditions of noctilucent clouds /15/. It is therefore not surprising that it strongly deviates from the models.

Other Variations

As mentioned above the Qff* temperatures shown in Fig. 3 indicate a long term trend of seasonal variations. It is seen that winter maximum values are relatively constant, whereas summer minimum values appear to increase from 1980 to 1984 by roughly 3 K per year. This coincides with the beginning descent of solar cycle 21. An anticorrelation of temperatures with solar cycle of comparable magnitude was also obtained previously from 5577 Å atomic oxygen green line emissions originating about 10 km higher in the atmosphere /19/.

The temperature differences remaining between the data presented in this paper and the recent atmospheric models are of the order of 10 K, and frequently much smaller. It thus

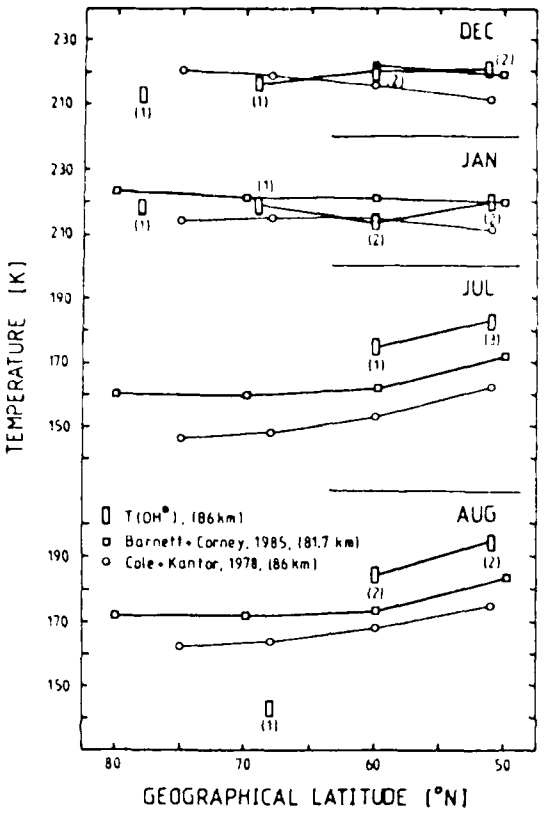

Fig. 6. Latitudinal variations of OH* temperatures in winter and summer as compared to atmospheric models. Measured data points connected by straight lines are from instruments of University of Wuppertal. Size of symbols indicates error of these data. Figures near the data points give the number of years available for calculating the mean. Barnett and Corney model values are for 10° E longitude.

appears that finer details of upper mesosphere temperature variations as with solar cycle, nametic activity, etc. could come into reach of modeling efforts in the near future.

Acknowledgement

The ground based spectrometer measurements were supported by Deutsche Forschungsgemeinschaft, Bonn. The cooperation of E.V. Thrane and T. Blix during the Oslo measurements is gratefully acknowledged. For the rocket data we are indepted to W. Meyer, C.R. Philbrick, F.J. Schmidlin, and U. von Zahn.

References

1. COSPAR International Reference Atmosphere, Akademie Verlag, Berlin, GDR, 1972.

2. A.E. Cole and A.J. Kantor, Air Force Reference Atmospheres, AFCL-TR-78-0051, A.F. Geophys. Lab., Hanscom AFB, Ma 01731, USA (Feb. 1978)

3. J.J. Barnett and M. Corney, Middle atmosphere reference model derived from satellite data, in: Handbook for MAP 16, eds. K. Labitzke, J.J. Barnett, B. Edwards, Univ. Illinois, Urbana, 1985, p. 47.

4. G.V. Groves, A global reference atmosphere from 18 to 80 km, AFGL-TR-85-0129, A.F. Geophys. Lab., Hanscom AFB, Ma 01731, USA (May 1985)

5. D. Offermann, The Energy Budget Campaign 1980: introductory review, J. Atmos. Terr. Phys. 47, 1-26 (1985)

6. U. von Zahn, The project MAP/WINE: an introduction, J. Atmos. Terr. Phys., submitted (1986)

7. F.J. Schmidlin, Repeatability and measurement uncertainty of the United States meteorological rocketsonde, J. Geophys. Res. 86, 9599-9603 (1981)

8. F.J. Schmidlin, C.R. Philbrick, and D. Offermann, Atmospheric density, temperature, and wind measurement techniques during the 1980 Energy Budget Campaign, in:Sounding Rocket Program Aeronomy, Project: Energy Budget Campaign 1980, Experiment Summary, eds. D. Offermann and E.V. Thrane, Bundesministerium fur Forschung und Technologie, BMFT-FB-W 81-032, Bonn, FRG, 1981, p. 362.

9. C. R. Philbrick, F.J. Schmidlin, K.U. Grossmann, G. Lange, D. Offermann, K.D. Baker, D. Krankowsky, and U. von Zahn, Density and temperature structure over northern Europe, J. Atmos. Terr. Phys. 47, 159-172 (1985)

10. W. Meyer, R. Gerndt, C.R. Philbrick, and F.J. Schmidlin, The middle atmosphere above Andoya, Norway, during the winter 1983/84 as derived from metrockets and OH nightglow observations, in: Proc. 7th ESA Symposium on European rocket and balloon programmes, ed. T.D. Guyenne and J. Hunt, ESTEC, Noordwijk, The Netherlands, 1985, p. 41.

11. D.J. Baker and A.T. Stair, Rocket measurements of the altitude distributions of the hydroxyl airglow, this issue.

12. D.J. Baker, A.J. Steed, G.A. Ware, D. Offermann, G. Lange, and H. Lauche, Ground-based atmospheric infrared and visible emission measurements, J. Atmos. Terr. Phys. 47, 133-145 (1985)

13. R. Gerndt, Untersuchung der Temperaturvariationen in der oberen Mesosphare mit Infrarot-Spektrometern, Ph. D. thesis, University of Wuppertal, FRG, 1986.

14. D. Offermann, R. Gerndt, R. Küchler, K. Baker, W.R. Pendleton, W. Meyer, U. von Zahn, C.R. Philbrick, and F.J. Schmidlin, Mean state and long term variations of temperature in the winter middle atmosphere above northern Scandinavia, J. Atmos. Terr. Phys., submitted (1986).

15. C.R. Philbrick, J. Barnett, R. Gerndt, D. Offermann, W.R. Pendleton, P. Schlyter, F.J. Schmidlin, and G. Witt, Temperature measurements during the CAMP program, Adv. Space Res. 4, 153-156 (1984)

16. H.K. Myrabø, Temperature variation at mesopause levels during winter solstice at 78° N, Planet. Space Sci. 32, 249-255 (1984)

17. U. von Zahn, K.H. Fricke, R. Gerndt, and T. Blix, Mesospheric temperatures and the OH layer height as derived from ground based LIDAR and OH^* spectrometry, J. Atmos. Terr. Phys., submitted (1986).

18. K. Labitzke, A.H. Manson, and E.R. Williams, Hemispheric synoptic analysis of 95 km winds during the winter of 1983/84 and comparison with stratospheric parameters, J. Atmos. Terr. Phys., submitted (1986).

19. G. Hernandez, Lower-thermosphere temperatures determined from line profiles of OI 17,924-K (5577 Å) emission in the night sky, 1. Longterm behavior, J. Geophys. Res. 81, 5165-5172 (1976)

Adv. Space Res. Vol. 7, No. 10, pp. (10)105–(10)115, 1987
Printed in Great Britain. All rights reserved.

0273-1177/87 $0.00 + .50
Copyright © 1987 COSPAR

OZONE REFERENCE MODELS FOR CIRA

G. M. Keating,* D. F. Young** and M. C. Pitts***

*NASA Langley Research Center, Hampton, VA 23665, U.S.A.
**PRC Kentron Corporation, Hampton, VA 23666, U.S.A.
***ST Systems Corporation, Hampton, VA 23666, U.S.A.

ABSTRACT

The ozone reference model which is to be incorporated in the COSPAR International Reference Atmosphere (CIRA) is described and compared with other measurements of the Earth's ozone distribution. Ozone vertical structure models from approximately 25 to 90 km are provided combining data from five recent satellite experiments (Nimbus-7 LIMS, Nimbus-7 SBUV, AE-2 SAGE, Solar Mesosphere Explorer (SME) UVS, and SME IR). The results include the latest improvements in the SBUV algorithms using the most recent estimates of ozone cross sections. Also, the latest refinements in SME algorithms are incorporated. These algorithm improvements have improved agreement between the satellite data sets. Standard deviations are provided of monthly zonal means, and an estimate of the interannual variability is given. The models based on satellite data compare well with the Krueger and Minzner mid-latitude model incorporated into the U. S. Standard Atmosphere which is based on rocket and balloon measurements. Other comparisons are shown with Umkehr and more recent balloon data. Models are also provided of total columnar ozone reflecting recent improved estimates of ozone cross section. Information is provided on *semi*annual and annual variations. Other systematic variations including estimates of diurnal variations in the mesosphere will be included in the CIRA document.

INTRODUCTION

Since the ozone chapter in the "Draft Reference Middle Atmosphere" was published in MAP Handbook number 16 in 1985 (Keating and Young, /1/), a number of results have been obtained concerning ozone in the middle atmosphere. The Nimbus 7 SBUV data have been reprocessed and archived taking into account improved ozone cross sections of Paur and Bass /2/, climatological variations in temperatures which affect ozone cross sections, and other factors /3/. Refinements have also been made on the Solar Mesosphere Explorer (SME) 1.27 μm and UV ozone data. The refinements from the SBUV and SME data have been incorporated here in updated ozone reference models. We have chosen to use the same six satellite experiments and same time intervals which we used previously. Therefore the satellite measurements are restricted to the late 1970's and early 1980's during primarily a period of relatively high solar activity.

We have also incorporated various improvements recommended by the COSPAR Task Group on Reference Middle Atmospheres, by the Ad Hoc Group on Ozone Reference Models for CIRA, and by others. Before the final submission of the manuscript for incorporation in the new CIRA, it is planned that members of these groups as well as members of the IAMAP International Ozone Commission will be provided the revised document for review and comment.

Over the last 50 years, a number of measurements of ozone in the middle atmosphere have been obtained from the ground and from balloons, rockets and satellites. Numerous models have been developed to summarize various portions of these measurements since detailed knowledge of the global distribution of ozone is important for studies of atmospheric circulation, dynamic processes, and the radiation balance and photochemistry of the atmosphere. Space does not allow an enumeration of these models here, but a brief description of many of these models as well as of various satellite measurements of ozone are provided by Keating and Young /1,4/.

The satellite measurements used in developing these models are enumerated in Table 1. Also shown in Table 1 is the pressure range and time interval incorporated for each of the data sets. A description of these measurements, including an assessment of the accuracy and precision of the various instruments, is given by Keating and Young /1/.

We briefly present here updated figures of the ozone reference models, examples of the annual and semiannual components of these models, and comparisons of the updated models with the Krueger and Minzner model /5/ as well as with long-term balloon and Umkehr measurements.

MODELS OF TOTAL COLUMN OZONE

Monthly latitudinal models of total column ozone are based on the archived first 4 years of data from the Nimbus 7 TOMS experiment. The total column ozone values given in Figure 1 are 5.5% higher than the TOMS archived data (as of June 1986) (Bhartia, private communication, 1986) to be in fair accord with the improved ozone cross sections of Paur and Bass /2/ and with Dobson measurements /6/. Note the high values in mid and high latitudes in spring in the Northern Hemisphere and at mid latitudes in local spring in the Southern Hemisphere. Also note the low values in September - October near 80°S. These low values reflect the recently discovered "ozone hole" in the Antarctic /7/. The corresponding standard deviation in percent of individual ozone measurements relative to the zonal mean as well as a measure of interannual variability of total column ozone are provided by Keating and Young /1/. Largest standard deviations and largest interannual variability are seen to occur in the "ozone hole." Farman et al. /7/ give evidence that ozone values in the vicinity of the "ozone hole" may have been closer to 300 Dobson units prior to the Nimbus 7 measurements.

MODELS OF OZONE VERTICAL STRUCTURE

The ozone vertical structure models of monthly zonal latitudinal variations (10° resolution) are based on the SBUV, LIMS, SAGE, SME-UVS and SME-IR data indicated in Table 1. The 4-year mean of the SBUV data was given a weight of 2 due to the combination of extensive temporal and spatial coverage, while the other shorter data sets were each given a weight of 1.

Although there is interannual variability, comparsion of the SBUV data over the 4-year period of measurements shows a remarkable similarity of structure from year to year. For example, shown in Figure 2 is the vertical structure at 0°, 20°N, 40°N and 60°N for November of 1978, 1979, 1980 and 1981. Note how the 0° and 20°N profiles come together near 4 mb. The 60°N profiles changes in each case from the lowest profile at 4 mb to the highest at 1.5 mb.

Shown in Figure 3 is the interannual variability of zonal mean ozone expressed as standard deviation (in percent) relative to the mean of 4 years of SBUV data as a function of pressure and latitude for the months of November and July. As indicated in the previous figure, the interannual variability of zonal means in November is very low, generally less than 4%. In contrast, the month of July gave the largest variability over this 4-year period with the maximum variability occurring at high winter latitudes. The interannual variability appears to be strongly related to quasibiennial oscillations.

Shown in Figure 4 is the average standard deviation (in percent) of the individual data points making up the monthly zonal means based on the 4 years of SBUV data. The standard deviations are shown as a function of latitude and pressure and appear considerably different from the interannual variability displayed in Figure 3. Minimum standard deviations occur near the equator and in the summer hemisphere. Standard deviations can exceed 15% at high latitudes and result from substantial longitudinal variations in ozone as well as changes in the zonal means during the month. The patterns for individual years look very similar to these mean patterns.

Shown in Figure 5 is an example of the agreement between the five data sets used to generate models of the ozone vertical structure from 20 mb to 0.003 mb (~25 to 90 km). Note that the mixing ratio is displayed on a log scale to allow accurate representation of the two orders of magnitude variation over this altitude range. It should be recognized that each data set represents entirely different techniques of measuring the vertical structure of ozone. The agreement shown here is fairly representative. Generally the SBUV ozone values redetermined with the improved ozone cross section give better agreement with the LIMS and SAGE data sets than the earlier version.

Monthly updated tables, including the data refinements as a function of pressure and altitude with 10° resolution in latitude, are provided by Keating and Pitts /8/. Shown in Figure 6 are the resulting ozone distributions for the equinox and solstice months. From the tables, detailed information concerning the annual and semiannual variations of ozone are available. For example, Figure 7 shows the annual variation at 50°S and 50°N over the entire range of altitudes from 25 to 90 km. Notice the asymmetries between the two hemispheres. Shown in Figure 8 is the semiannual variation at 30°S and 30°N for the entire range of altitudes. Note the symmetry in the low latitude variations in the two hemispheres and the evidence of wave propagation from the mesosphere down into the stratosphere.

Shown in Figure 9 is the vertical structure of global mean ozone (weighted by cosine of latitude) and the maximum and minimum extremes of the values tabulated in Keating and Pitts.

COMPARISON OF MODEL WITH BALLOON, ROCKET, AND UMKEHR MEASUREMENTS

It is of interest to compare the ozone vertical structure model provided here, which is based on satellite measurements, with ozone measurements obtained by other techniques. The Krueger and Minzner annual mean ozone reference model of 45°N /5/ based on balloon and rocket data has proven to be very useful and is included in the U. S. Standard Atmosphere, 1976. Data from rocket soundings in the latitude range of 45°N ± 15°, results of balloon soundings at latitudes from 41°N to 47°N, and latitude gradients from Nimbus 4 BUV observations have been taken into account to estimate the annual mean concentration and its variability up to heights of 74 km for an effective latitude of 45°N. Shown in Figure 10a is a comparison of the vertical structure of the annual mean volume mixing ratio given by Krueger and Minzner with that of the annual mean determined by averaging the monthly values at 40° and 50°N based on the model given here which is tabulated in Keating and Pitts /8/. As may be detected, there is good agreement between the balloon and rocket measurement model and the satellite measurement model. The satellite-derived volume mixing ratios are slightly lower below 0.5 mb than given in the earlier satellite model [/1,4/] due to the improved absorption coefficients. Shown in Figure 10b are the percent differences of the Krueger and Minzner model from the satellite measurement model. Below altitudes of 0.2 mb, the agreement is generally within 10%. Above 0.2 mb, differences as large as 45% occur, but all differences at all levels are within the error bars indicated in the Krueger and Minzner model. Both models give maximum mixing ratios near 5 mb.

Shown in Figure 11 is a comparison of the annual mean vertical ozone distribution from ozonesonde data from Hohenpeissenberg (FRG) (48°N, 11°E) over the period 1967-1985 and from Thalwil-Payerne (Switzerland) (47°N, 7°E) over the period 1967-1982 with the 47.3°N zonal average annual mean based on the satellite data. Also, the annual mean vertical structure of Umkehr data from Arosa (Switzerland) (47°N, 10°E) 1955-1983 is compared. These data were generously provided by R. D. Bojkov (1986). Considering that the ozonesonde and Umkehr data do not represent a zonal average but do represent conditions over a period of many years, the agreement is very good. Comparisons month by month of the ozonesonde data show better than 10% agreement with the zonal mean mixing ratios, but show evidence of local phase shifts relative to the zonal mean annual variations.

CONCLUSIONS

Incorporating data based on improved algorithms has improved agreement between the satellite data sets used to develop the ozone models described here. Good agreement is also shown between these models based on satellite data and various sets of rocket, balloon, and Umkehr data. Because of space limitations, only a portion of the material to be included in the CIRA ozone reference model is presented here. Updated tables may be found in /8/.

REFERENCES

1. G. M. Keating and D. F. Young, Interim reference ozone models for the middle atmosphere, Handbook of Map 16, 205-230 (ed. K. Labitzke, J. J. Barnett, and B. Edwards) (1985).

2. R. J. Paur and A. M. Bass, The ultraviolet cross-sections of ozone: II. Results and temperature dependence, in: Atmospheric Ozone, ed. C. S. Zerefos and A. Ghazi; D. Reidel Publishing Co., Dordrecht 1985, pp. 611-616.

3. Nimbus Project, The Nimbus 7 User's Guide, SBUV ozone data set (Version 5), to be published as NASA Reference Publication (1986).

4. G. M. Keating and D. F. Young, Proposed ozone reference models for the middle atmosphere, Adv. Space Res. 5, No. 7, 155-166 (1985).

5. A. J. Krueger and R. A. Minzner, A mid-latitude ozone model for the 1976 U. S. Standard Atmosphere, J. Geophys. Res., 81, 4477-4481 (1976).

6. P. K. Bhartia, K. F. Klenk, A. J. Fleig, C. G. Wellemeyer, and D. Gordon, Intercomparison of Nimbus 7 Solar Backscattered Ultraviolet ozone profiles with rocket, balloon and Umkehr profiles, J. Geophys. Res. 89, 5227-5238 (1984).

7. J. C. Farman, B. G. Gardiner, and J. D. Shanklin, Large losses of total ozone in Antarctica reveal seasonal ClO_x/NO_x interaction, Nature 315, 207-210 (1985).

8. G. M. Keating and M. C. Pitts, Proposed reference models for ozone, Adv. Space Res. (in press) (1987).

Table 1. Satellite data used for interim reference ozone models.

Instrument	Incorporated Pressure Range	Incorporated Time Interval
NIMBUS 7 LIMS	0.5 - 20 mb	11/78 - 5/79
NIMBUS 7 SBUV	0.5 - 20 mb	11/78 - 9/82
AE -2 SAGE	5 - 20 mb	2/79 - 12/79
SME UVS	0.07 - 0.5 mb	1/82 - 12/83
SME IR	0.003 - 0.5 mb	1/82 - 12/83
NIMBUS 7 TOMS	TOTAL	11/78 - 9/82

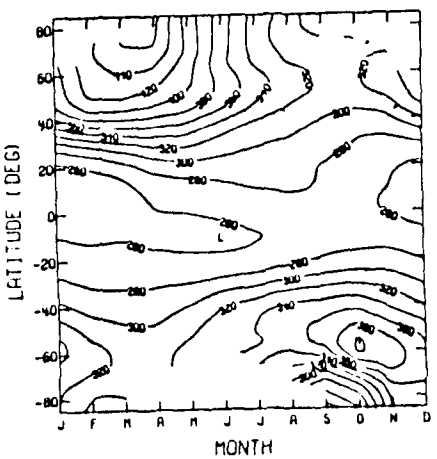

Figure 1. Zonal mean of total column ozone (Dobson units) as a function of latitude and month.

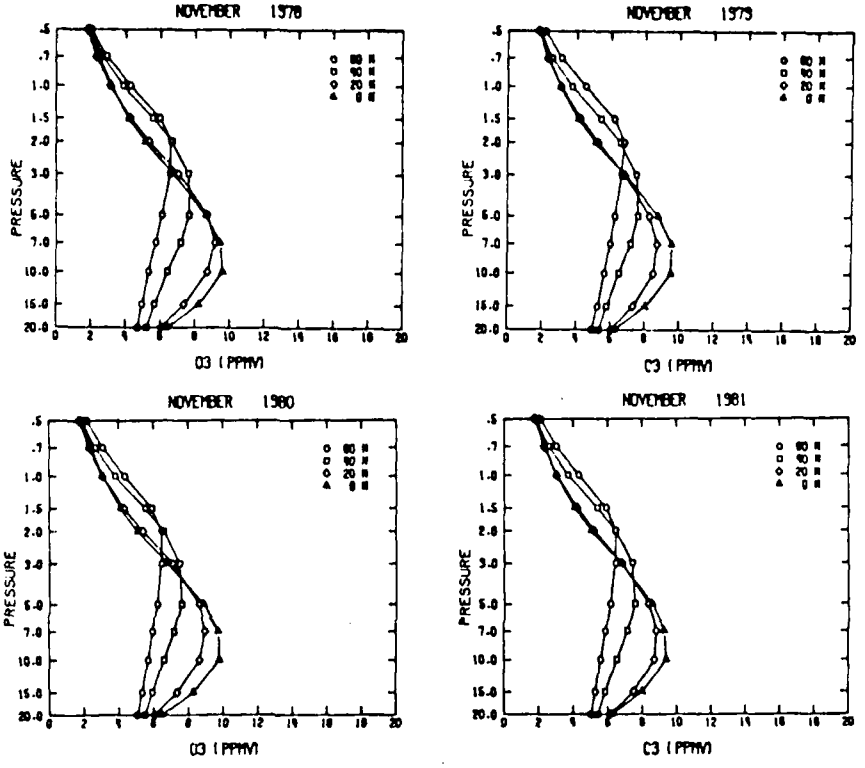

Figure 2. Similarity of ozone vertical structure in November from year to year (Nimbus 7 SBUV data).

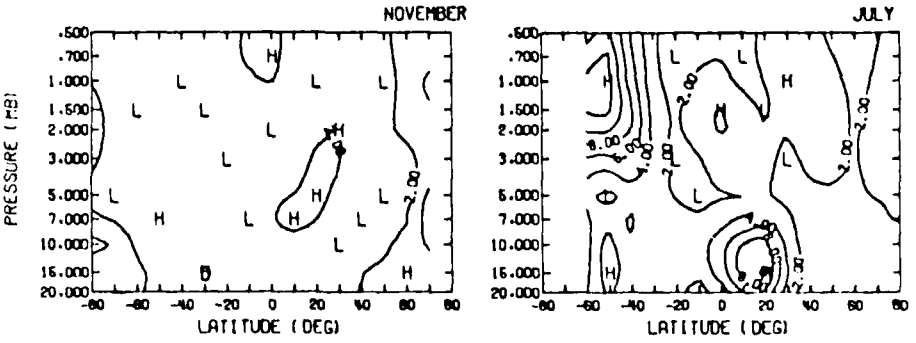

Figure 3. Interannual variability of ozone vertical structure expressed as yearly standard deviation (percent) from 4-year zonal means for the months of November and July (Nimbus 7 SBUV data).

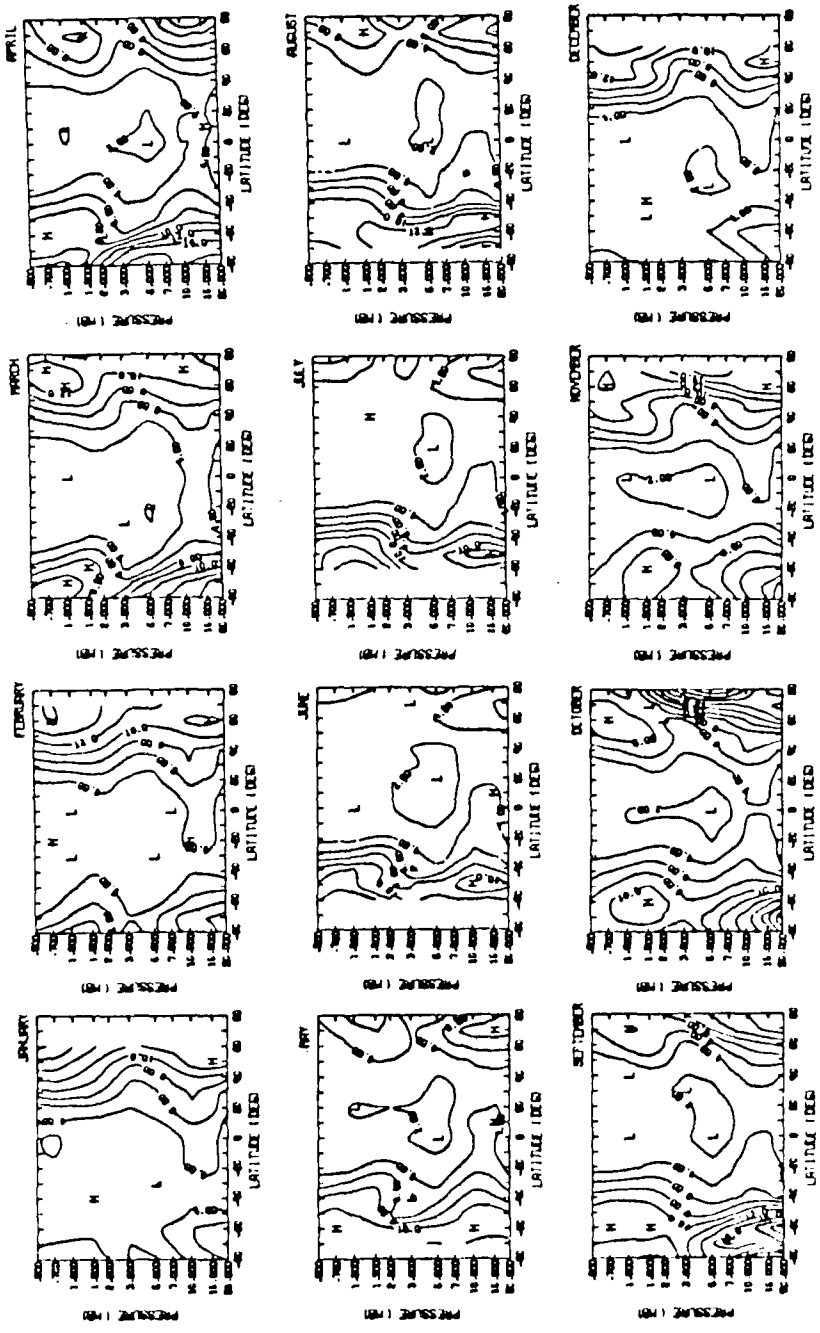

Figure 4. Average monthly standard deviation (percent) from zonal mean ozone (Nimbus 7 SBUV data).

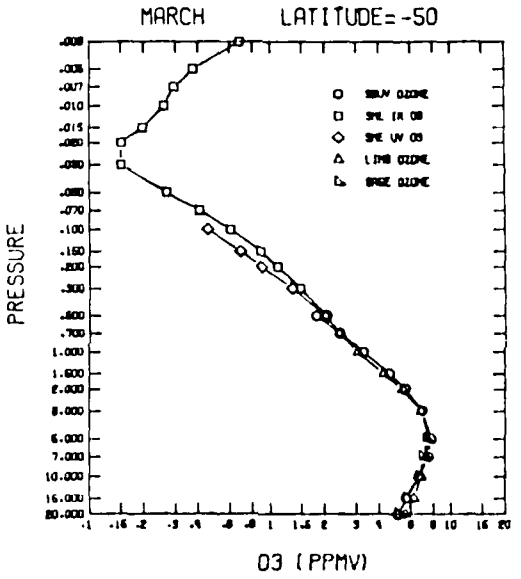

Figure 5. Comparison of measurements from five satellite experiments of zonal mean ozone volume mixing ratios for March, 50°S.

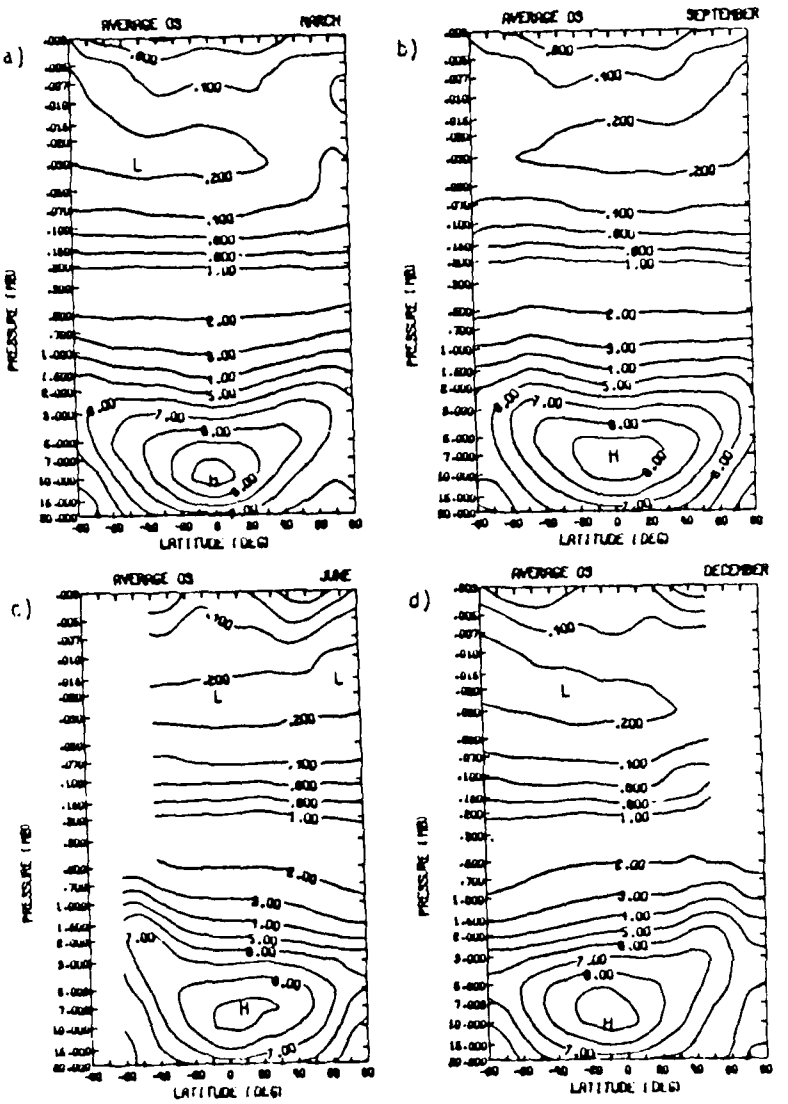

Figure 6. Monthly zonal mean ozone volume mixing ratios (ppmv) as function of latitude (deg) and pressure (mb) for (a) March, (b) September, (c) June, and (d) December.

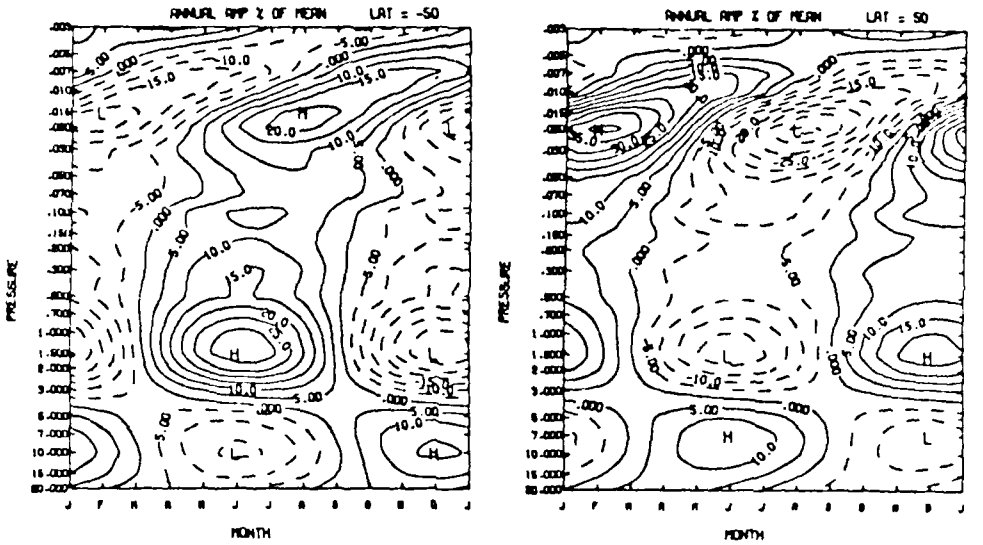

Figure 7. Annual variability expressed as percent of mean at 50 °S and 50 °N as functions of month and pressure.

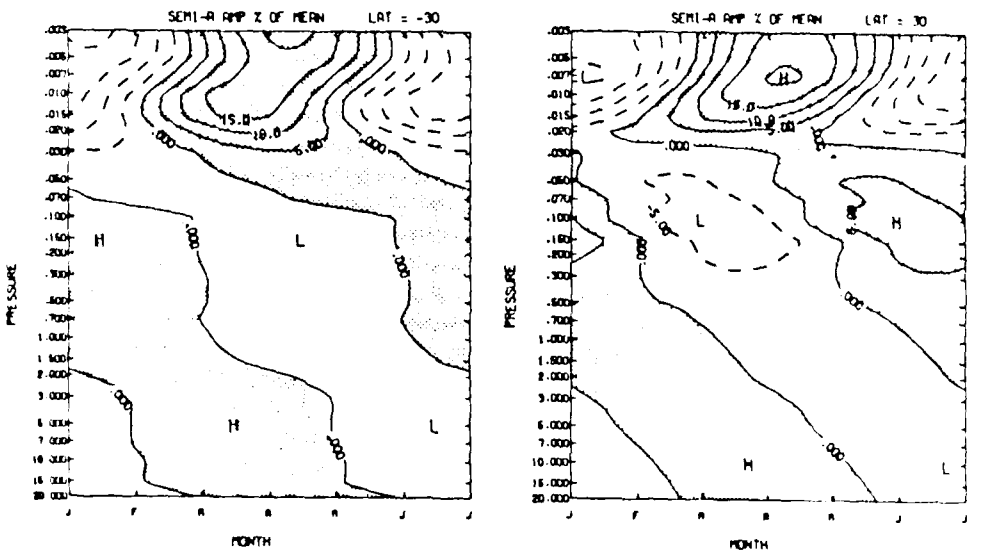

Figure 8. Semiannual variability expressed as percent of mean at 30 °S and 30 °N as function of month and pressure.

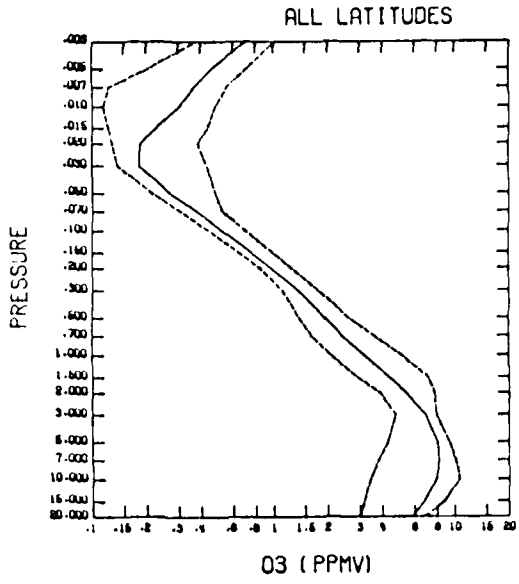

Figure 9. Global mean vertical structure of ozone volume mixing ratio (ppmv) (weighted by cosine of latitude) and the maxima and minima of Table 4 monthly latitudinal profiles.

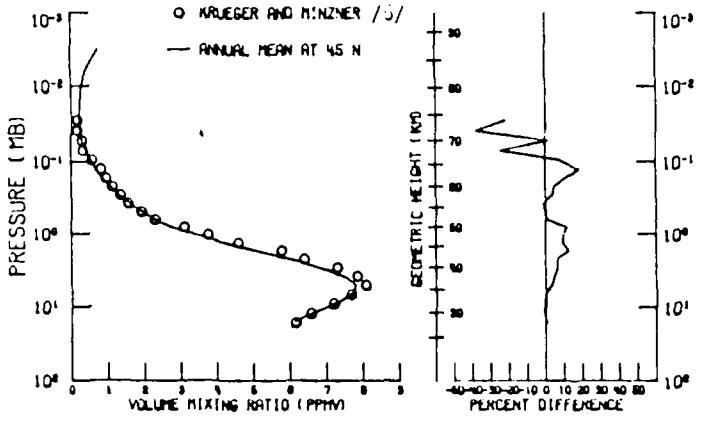

Figure 10. Comparison of annual mean ozone volume mixing ratio (ppmv) at 45°N based on the satellite data model of Table 4 and based on the balloon and rocket data model of KRUEGER and MINZNER /5/ . On the left (a) is shown the vertical structure in the two models and on the right (b) the percent difference from the satellite data model of the Krueger and Minzner model.

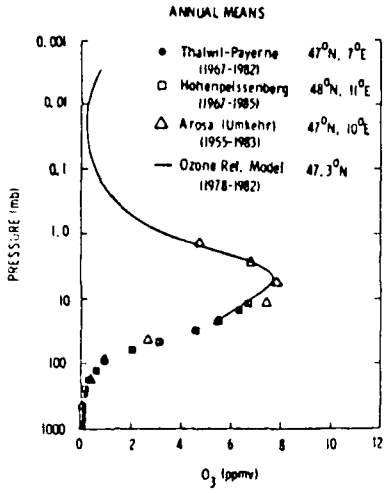

Figure 11. Long-term balloon and Umkehr measurements of ozone compared with ozone reference model based on satellite data.

Adv. Space Res. Vol. 7, No. 10, pp. (10)117–(10)131, 1987
Printed in Great Britain. All rights reserved

0273-1177/87 $0.00 + .50
Copyright © 1987 COSPAR

A PROPOSED INTERNATIONAL TROPICAL REFERENCE ATMOSPHERE UP TO 1000 km

M. R. Ananthasayanam and R. Narasimha*

Department of Aerospace Engineering, Indian Institute of Science, Bangalore 560 012, India
**Also National Aeronautical Laboratory, Bangalore 560 017, India*

ABSTRACT

Motivated by the need in many aerospace applications for a meaningful reference atmosphere characteristic of the whole of the tropics in both the northern and southern hemispheres of the globe, a proposal was made earlier by the authors for altitudes up to 80 km. This proposal is here extended up to an altitude of 1000 km. The proposal is based on balloonsonde, rocketsonde, grenade, falling sphere and satellite data in the range 0 to 100 km, and on the MSIS- 83 model from 100 to 1000 km. The proposal consists of linear segments in the temperature distribution with values in degrees Celsius of 27, -9, -74, -5,-5, -74 and -80.4 at geopotential altitudes of 0, 6, 16, 46, 51, 74 and 84.69 km (= 86 km geometric altitude) respectively, beyond which the description is in terms of geometric altitude. A linear segment between 86 and 97 km with a lapse rate of 0.6°C/km is followed by an elliptic variation commencing with a temperature gradient of zero at 97 km to reach at 110 km a temperature of -45°C with a gradient of 15°C/km. This gradient remains constant up to 120 km where the temperature is 105°C. Beyond 120 km the temperature distribution follows a Bates type of profile up to 1000 km to reach a value there of 760°C. A sea level pressure of 1010 mb and an acceleration due to gravity of 9.78852 ms^{-2} corresponding to the Tropic of Cancer are used in the preparation of the atmospheric tables.

INTRODUCTION

With the presently available meteorological data it is now possible to characterise atmospheric conditions typical of a season, month or even a day. However, a standard atmosphere representative of the mean annual conditions is still essential for many aerospace applications. An International Standard Atmosphere (ISA: see /1,2/) valid for mid-northern latitudes specified upto 32 km, and its proposed extension to higher altitudes (such as in /3/), have been formulated for meeting these needs.

The authors have previously discussed at length /4 to 7/ the problems of defining atmospheric standards for India and the tropics, and have shown that it is possible to specify a suitable Indian Standard Tropical Atmosphere (ISTA) and an International Tropical Reference Atmosphere (ITRA), valid up to 80 km and about 30°N in latitude. None of the standard or reference atmospheres formulated earlier /8 to 15/ for the tropics has covered the above latitude and altitude range. In the present work ITRA is extended to an altitude of 1000 km. The subsequent sections discuss the accuracy and consistency of the data available for use in formulating the present proposal.

DATA BASE FOR ITRA UP TO 1000 KM

The present reference atmosphere is developed in four parts, namely,

(i) in the troposphere and lower stratosphere, using balloonsonde data,

(ii) in the upper stratosphere, utilising rocketsonde data,

(iii) in the mesosphere, considering grenade, falling sphere and the Nimbus satellite data, and

(iv) in the thermosphere, based mainly on the MSIS-83 model.

Table 1 shows the details of the available data and their sources.

REMARKS ON THE QUALITY AND CONSISTENCY OF DATA

Troposphere and Stratosphere

As discussed in /7,16/ the post-1970 balloonsonde data of the India Meteorological Department as also the Monthly Climatic Data for the World /17/ for the American stations up to 20 km are consistent. Further the rocketsonde data up to about 50 km from various countries, in particular the USSR and USA which have provided the data for a large number of stations /14,18,19/ over the globe, are consistent and thus can be used for proposing the reference atmosphere. Beyond about 50 km there are unresolved differences /20,21,22/ among the above rocketsonde data, perhaps due to the exposure of the thermistor probes to the free-molecular conditions around 50 km and above.

Mesosphere

For the higher altitude range of about 50 to 100 km we have used the falling sphere and grenade data /23 to 26/. These data are generally consistent among themselves and possess an accuracy of about 2 to 3°C. Smith et al /23/ report pitot data as well, but these lead to temperature values which are about 5°C higher on an average from the grenade data for the low latitude stations such as Ascension & Natal (see Table 1); as the reason for this discrepancy is not clear we have not considered the pitot data. Data in this altitude range are not as extensive as one would wish but are nevertheless just adequate to propose a reasonable reference for describing the mean annual conditions. The most recent Nimbus data /27/, worked out from the radiance values, are quite consistent with the present proposal from about 50 to 70 km as shown in Figure 1. However, beyond this altitude the satellite values are higher than the falling sphere and the grenade data, and the reason for this is not yet clear.

Thermosphere

In this region, most grenade or falling sphere data are available up to about 100 km. Beyond this altitude the number of soundings is very small. Further beyond about 80 km one has to specify in any reference atmosphere the varying concentration of the various species, which have to match with the conditions that may be specified at about 120 km by a suitable thermospheric model such as in /28 to 31/. These problems are discussed in greater detail later. For the present work we have used the MSIS-83 model /30/ for the above purpose.

THE PHYSICAL CONDITION OF THE ATMOSPHERE FROM SEA LEVEL TO 1000 KM

From sea level up to an altitude of about 85-86 km, air is known to be in a thoroughly mixed condition and thus the relative concentrations of the various constituents do not change. Up to this height the atmosphere can be described in terms of the molecular scale temperature T_M, versus the geopotential altitude H. Using the relation between temperature and altitude one can work out the pressure, density and other atmospheric properties.

Beyond about 85 km molecular dissociation commences, and above 100 km molecular diffusion predominates, and so air can no longer be treated as a perfect gas. It is then necessary to specify at each level the varying concentrations of the different species constituting air. As in /3/, the description at and beyond 86 km is in terms of the kinetic temperature T, versus the geometric altitude Z. In this region the vertical density profile $n_i(Z)$ of the atmospheric constituent i as given in /3,32/ is

$$n_i(Z) = n_i(Z_o)\{T(Z_o)/T(Z)\}I(K/(D_i+K),H)I(D_i/(D_i+K),H_i)$$
$$.I(\alpha_i.d\ lnT/dZ.D_i/(D_i+K),1)I(V_i/(D_i+K),1) \quad ...(1)$$

$$\text{where } I(x,y) = \exp\left(-\int_{Z_o}^{Z}(x/y)dZ\right) \quad ...(2)$$

and Z_o is taken to be 86 km as in /3/. The K and D are respectively the height-dependent eddy and molecular diffusion coefficients; H and H_i are the scale heights for air and each of its constituents and α_i is the species thermal diffusion coefficient. The first three integrals in Eqn(1) refer to mixing and diffusive processes. The so-called flow term denoted by the fourth integral has to account for the complex chemical and transport processes which occur in the above region of the atmosphere /33 to 35/. However, in developing a reference atmosphere that should be capable of being generated easily for comparison with experiment and be useful for analytical studies, one has to look for reasonable assumptions which simplify the approach. For this we assume that the turbopause level for the various species terminates sharply at a height of Z_{ti}. The flow term is more complicated than the mixing and diffusion terms. For this we propose a simple form such as

$$V_i/(D_i+K) = a_i\{(120-Z)(Z-86)\}^2 \quad ...(3)$$

where the a_i are adjustable parameters to be so chosen that the particular species concentration values at 120 km are close to the average values for low latitudes from the MSIS-83 model. The major constituent N_2 is assumed to be in complete diffusive equilibrium above its turbopause height. Thus once the temperature distribution is specified the N_2 number density distribution can be worked out. In fact we adjust T(Z) such that the value for the number density of nitrogen at 120 km matches as closely as possible with the value from the MSIS-83 data. Thus the value of its a_i = 0. The atomic oxygen is strongly governed by the chemical and transport processes, but as we shall discuss below its distribution is dealt with differently. Thus the a_i need to be chosen only for Molecular Oxygen, Argon and Helium.

Beyond an altitude of 120 km the various species constituting air are assumed to be in diffusive equilibrium. The MSIS-83 model in fact specifies the conditions of the temperature, its gradient at this altitude as also the temperature profile from 85 km up to an exospheric altitude of 1000 km for varying latitude and longitude, and solar, magnetic, seasonal, daily and hourly

conditions; this is used to extend ITRA up to 1000 km.

If the temperature distribution known as the Bates profile /36/ is written as

$$T(Z) = T_E - (T_E - T_{120}) \exp(-sz') \qquad ...(4)$$

where T_E, T_{120} are respectively the temperatures at 1000 km and at 120 km, with

$$z' = (Z - 120)(R_e + 120) / (R_e + Z),$$

$$s = (dT/dZ)_{Z=120} / (T_E - T_{120}),$$

and R_e = the radius of the Earth,

then the number density can be expressed in closed form /36/ as

$$n_i(Z) = n_i(120)\{T_{120}/T(Z)\}^{(1+\alpha_i+1/sH_i')}.\exp(-sz') \qquad ...(5)$$

with $H_i' = (R_e T_E)/(m_i g(120))$,

the argument of g(.) referring to the altitude.

PROPOSED INTERNATIONAL TROPICAL REFERENCE ATMOSPHERE (ITRA) UP TO 1000 KM

The philosophy adopted by the authors /4,5,6/ in proposing the reference has been that it should

(a) be reasonably close to mean conditions,

(b) within the range of variation inherent in the atmosphere over the space and time which it describes and the uncertainty in the data, be as simple as possible,

(c) adopt, where no physical principles are violated, as many of the parameters in the ISA as possible, and

(d) be dynamically consistent.

Temperature distribution with altitude

Usually straight line temperature distribution with altitude is used. This is done since a closed form integration for obtaining the atmospheric properties is then possible.

As indicated in /6,7/, the proposed standard has a sea level temperature of 27°C and a lapse rate of 6°C/km up to 6 km (which is lower than the ISA value but is characteristic of the humid tropics) and 6.5°C/km (as in ISA) from 6 to 16 km, the tropopause height where the temperature is -74°C. In the stratosphere, a single lapse rate of -2.3°C/km all the way up to a stratopause height of 46 km, with a temperature of -5°C, was found to fit the data very well /6/. Though this temperature is somewhat higher than indicated by the Thumba value, we consider it appropriate because of the fact that the stratopause temperature increases with increasing latitudes. The available data in the mesosphere indicate that the constant temperature stratopause extends up to 51 km. Considering the differences between the geopotential and geometric height which is of the order of about 1 km, it turns out that the above level for the end of stratopause is more appropriate than the value of 52 km in our earlier proposal /7/.

In the mesosphere it should be noted that inversions occur during some months and there are also well known double mesopauses with different temperature values as well. However the mean annual conditions can be specified in a simple way as shown in Figure 1. Due to the sparsity of the data, we have considered stations at both low and high latitudes, which indicate the latitudinal variation and thus help in formulating the present reference atmosphere for the tropics. In the present proposal a constant lapse rate of 3°C/km from 51 km to 74 km leads to a temperature of -74°C (as at the tropopause!). The Wallops Island and the Churchill data /23/ indicate that the latitudinal variation is weak (atleast between 50 and 85 km). Further, up to an altitude of 70 km, excellent agreement exists for the present proposal with the Nimbus data /27/ averaged over 30 S to 30 N in latitude. Also the present proposal up to about 75 km is consistent with the various monthly reference atmospheres for the northern and southern hemispheres as proposed in /14/,/15/ respectively.

Between 80 and 100 km it is once again expedient to go by the variations between low latitude and mid-latitude station data. From Figure 1 one may note that the Ascension Island data indicate some kinks but the Kwajalein data are smooth, but beyond 100 km these are based on only three soundings. The MSIS-83 model data show much higher values than the Kwajalein data around 85 km. Thus, considering the latitudinal variations between the station data of Kwajalein, Wallops and Churchill we find that it is best to have from 74 km altitude a lapse rate of 0.6°C/km (geopotential) up to a geopotential altitude of 84.69 km (= 86 km geometric height) and later once again a lapse rate of 0.6°C/km (geometrical) between 86 and 97 km of geometric altitude.

In the altitude from about 100 to 120 km we noticed that the MSIS - 83 data averaged over the range of magnetic index A_p = 0 to 10 and solar activity index $F_{10.7}$ = 75 to 225, is close to its value for A_p = 4.0 and $F_{10.7}$ = 150. Further the above is averaged over 30 S to 30 N. These averaged model data are also given in Table 1. In the present proposal the temperature variation has been chosen close to such latitudinally averaged MSIS data which leads to a value for the number density of nitrogen close to MSIS - 83 value at 120 km. Thus the minimum temperature in the present proposal in the mesosphere is -80.4°C at 97 km and the subsequent rise in the temperature in the lower thermosphere is described by an elliptical distribution which has a temperature of -45°C at 110 km where the gradient reaches the value 15°C/km. Subsequently the temperature increases at the same rate up to 120 km where it reaches a value of 105°C. Figure 2 shows ITRA between 0 and 120 km. A similar procedure indicates a choice of 760°C (=1033.15°K) at 1000 km.

Distribution of nitrogen

This is obvious as explained in the previous section since the temperature distribution from about 74 km up to 120 km has been so chosen as to match the value of the species number density at 120 km. The assumed turbopause height is at 105 km for this constituent.

Distribution of atomic oxygen

A perusal of the data in the literature /37,38,39/ shows two things very clearly regarding this constituent. The first is that it follows very closely the Chapman distribution whose form is

$$[O] = [O]_m . \exp 1/2\ [1-(Z-Z_m)/SH - \exp\{(Z-Z_m)/SH\}] \quad ...(6)$$

where $[O]_m$ is the value of the peak concentration located at Z_m, and SH is the shape factor. Offerman et al /37/ have shown for a large number of experimental data that the above peak atomic oxygen concentration correlates with the total column density of atomic oxygen up to an altitude of 110 km. From their correlation plot we have inferred that the value for the shape factor should be 5. It may be mentioned that the value from /3/ shown in their Figure (somewhat away from the correlation relation) would require a shape factor of 5.5. Further the above body of data also indicates Z_m to be around 97 km, so we choose this value. Within the limits of the variability of the atomic oxygen as noted in the various experiments the above choices for SH and Z_m seem reasonable to describe the variation of the atomic oxygen between 86 and 120 km.

Distribution of molecular Oxygen, Argon and Helium

These are calculated by choosing suitable values for the various a_j in Eqn (1) so that their concentrations match with the MSIS-83 model values at 120 km. The assumed levels of the turbopause for these species are respectively 105, 105 and 95 km as in the MSIS-83 model. With a given value of the concentration at 120 km it has been noticed by us that any choice of the turbopause height for the first two species between 95 and 105 km does not substantially affect their distribution between 86 and 120 km. But for helium which is very light it seems more appropriate to use the lower value namely 95 km for getting a suitable description. Figure 3 shows the distribution of the various species in ITRA from 80 to 120 km.

Mean sea level pressure

As discussed in the earlier paper /7/ a sea level pressure of 1010 mb has been chosen based on the southern and northern hemisphere tropical data from /40/ for the years 1951 to 1960 for nearly 200 stations. This value of the sea level pressure is somewhat lower than the mid-latitude value of 1013.25 mb in ISA.

Acceleration due to gravity (g)

For this we suggest a value corresponding to the Tropic of Cancer, which from Lambert's formula in /41/ is 9.78852 ms^{-2} (truncated to five decimal places).

TABLE 2: DEFINING PARAMETERS AND CONSTANTS FOR THE PROPOSED ITRA

Geop Alt (km)	0	6	16	46	51	74	84.69
Temp (^oC)	27	(6.0)	-9	(6.5)	-74	(-2.3)	-5 (0.0) -5 (3.0) -74 (0.6) -80.40

Geom Alt(km)	86	97	110	120	1000	
Temp (^oC)	-80.4	(0.6)	-87 *	-45	(-15)	105 ** 760

The bracketed quantities denote lapse rate in ^oC/km. The (*) denotes an elliptical variation of temperature distribution, commencing with zero gradient at 97 km and ending with a gradient of 15^oC/km at 110 km, and (**) indicates a Bates type of profile commencing with a gradient of 15^oC/km at 120 km and ending with 1000 km.

Sea level pressure = 1010 mb ;

Acceleration due to gravity = 9.78852 ms^{-2}

Constituent	N_2	O	O_2	Ar	He
z_{ti}	105.0	-	105.0	105.0	95.0
$n(120)/m^3$	3.261+17	8.80+16	2.90+16	1.10+15	2.40+13

The molecular weight, the ratio of the specific heats of air, the gas constant, and the other constants for the transport properties are assumed to be the same as in /3/. The atmospheric properties for the proposed ITRA are provided in an abridged form in Tables 3 to 6.

ACKNOWLEDGEMENTS

The authors sincerely thank the Aeronautics Research and Development Board for having supported this study through a grant for the project 'SITA'. Thanks are also due to Mr.K.L. Diwakara Murthy, Mr.B. Narasimhan, Mr.T.V. Adinarayana and Mr.R.S. Ravindra Kumar for their help at various periods in developing the computer program and in the preparation and checking of the Atmospheric Tables.

REFERENCES

1. US Standard Atmosphere, NASA and USAF, U.S. Government Printing Offices, Washington. D.C. (1962)

2. Manual of the ICAO Standard Atmosphere, Doc 7488/2, Second Edition (1964)

3. US Standard Atmosphere, NOAA, NASA and USAF, U.S. Government Printing Offices, Washington. D.C. (1976)

4. M.R. Ananthasayanam and R. Narasimha, Standard Atmospheres for Aerospace Applications in India, Report 79 FM 5, Dept. of Aeronautical Engineering, Indian Institute of Science, Bangalore (1979)

5. M.R. Ananthasayanam and R. Narasimha, Standards for the Tropical Indian Atmosphere, Space Research XX, 25 (1980)

6. M.R. Ananthasayanam and R. Narasimha, Proposals for an Indian Tropical Atmosphere upto 50 km, Adv.Space Research, Vol. 3, No. 1, 17 (1983)

7. M.R. Ananthasayanam and R. Narasimha, A Proposed International Tropical Reference Atmosphere up to 80 km, MAP Handbook, Vol 16, 197-204 (1985)

8. A.E. Cole and A.J. Kantor, Air Force Reference Atmospheres, AFGL-TR-78-0051 (1978)

9. P.R. Pisharoty, A Standard Atmosphere for the Tropics (msl to 20 km), Indian Jour. of Met. and Geophysics 10, 243 (1959)

10. Air Registration Board, BCAR (1966)

11. US Standard Atmosphere Supplements, Environ. Sci. Surv. Admin., NASA and US Air Force (1966)

12. COSPAR International Reference Atmosphere, Academie Verlag, Berlin (1972)

13. M.N. Sasi and K. Sen Gupta, A Model Equatorial Atmosphere

over the Indian Zone from 0 to 80 km, VSSC TR 46-157-79, Trivandrum, India (1979)

14. A.E. Cole, A.J. Kantor and C.R. Philbrick, Kwajalein Reference Atmospheres, AFGL-TR-79-0241 (1979)

15. Yu.P. Koshelkov, An Empirical Temperature Model of the Middle Atmosphere of the Southern Hemisphere, Space Research XX, 41 (1980)

16. H. Van de Boogard, The Mean Circulation of the Tropical and Subtropical Atmospheres - July, NCAR/TN-118+STR, Boulder, Colorado (1977)

17. National Climatic Data Center, Monthly Climatic Data for the World (1973-78)

18. World Data Center, High Altitude Meteorological Data, Quarterly Issues, NOAA, Ashville, North Carolina, USA (1976)

19. India Meteorological Department, Climatology of the Stratosphere in the Equatorial Region over India, Meteorological Monograph, Climatology No.9 (1976)

20. F.G. Finger, M.E. Gelman, F.J. Schmidlin, R. Leviton and B.W. Kennedy, Compatibility of Meteorological Rocketsonde Data as Indicated by International Comparison Tests, J. Atmos. Sci. Vol 32, 1705 (1975)

21. A.I. Ivanovsky, L.M. Kolomitseva, E.V. Licenko, Yu.N. Rybin, K.E. Speransky and Yu.M. Tshermishenko, Preliminary Results of the Intercomparison Test of US and USSR Meteorological System at Wallops Island, Space Research XIX, 127 (1979)

22. F.J. Schmidlin, J.R. Duke, A.I. Ivanovsky and Y.M. Chernyshenko, Results of the August 1977 Soviet and American Meteorlogical Rocketsonde Intercomparison held at Wallops Island, Virginia, NASA RP-1053 (1980)

23. W. Smith, J.S. Theon, D.W. Wright Jr., J.P. Casey and J.J.Horvarth, Measurements of the Structure and Circulation of the Stratosphere and Mesosphere,1970, NASA TR R-391 (1972)

24. P.H.O. Pearson, Annual Variations of Density, Temperature and Wind between 30 and 97 km at Woomera shortly after dusk, 1962-1972, Space Research XIV, 67 (1974)

25. G.V. Groves, Seasonal Variations of Temperature, Pressure, Density and Winds to 80 km Altitude at Woomera, 1957-1963, Space Research VII, 1111 (1966)

26. A.C. Faire and K.S.W. Champion, Upper Atmospheric Parameters Obtained from Recent Falling Sphere Measurements at Elgin, Florida, Space Research IX, 343 (1969)

27. J.J. Barnett and M. Corney, Middle Atmosphere Reference Model Derived from Satellite Data, MAP Handbook Vol. 16, 47-85 (1985)

28. A.E. Hedin, J.E. Salah, J.V. Evans, C.A. Reber, G.P. Newton, N.W. Spencer, D.C. Kayser, D. Alcayde, P. Pauer, L. Cogger and J.P. McClure, A Global Thermospheric Model based on Mass Spectrometer and Incoherent Scatter Data, MSIS 1, N_2 Density and Temperature, J. Geophy. Res., Vol 82, No. 16, 2139-2147 (1977)

29. A.E. Hedin, C.A. Reber, G.P. Newton, N.W. Spencer, H.C. Brinton and H.G. Mayr, A Global Thermospheric Model based on Mass Spectrometer and Incoherent Scatter Data, MSIS 2, Composition, J. Geophy. Res., Vol 82, No. 16, 2148-2156 (1977)

30. A.E. Hedin, A Revised Thermospheric Model based on Mass Spectrometer and Incoherent Scatter Data, MSIS-83, J. Geophy. Res., Vol 88, 10170 (1983)

31. J.M. Forbes, Thermal Structure of the 80 km to 120 km Region, MAP Handbook, Vol 16, 231 - 238 (1985)

32. P.W. Blum and K.G.H. Schuchardt, Principles of a Global Wind-Turbulence Model of the Seasonal Latitudinal Variation of the Thermosphere as Deduced from Satellite Data, Space Research, Vol XX, 97-100 (1980)

33. F.D. Colegrove, W.B. Hanson and F.S. Johnson, Eddy diffusion and Oxygen Transport in the lower thermosphere, J. Geophy. Res., Vol 70, 4931-4941 (1965)

34. T.J. Shimazaki, Dynamic Effects an Atomic and Molecular Oxygen Distribution in the Upper Atmosphere, A Numerical Solution of Equations of Motion and Continuity, J. Atmos. Terr. Phy., Vol 29, 723-741 (1967)

35. T.J. Keneshea and S.P. Zimmermann, The Effect of Mixing upon Atomic and Molecular Oxygen in the 70-170 Region of the Atmosphere, J. Atmos. Sc., Vol 27, 831-840 (1970)

36. W.L. Oliver, A Procedure for the Efficient Calculation of Atmospheric Density, presented at the COSPAR meeting held at Ottawa, May-June (1982)

37. D. Offermann, V. Friendrich, P. Ross and U. Von Zahn, Neutral Gas Composition Measurements between 80 and 120 km, Planet Space Sci., Vol. 29, 747 (1981)

38. M.N.M. Rao and G.S.N. Murty, Deduction of lower thermospheric atomic oxygen density profiles from ground-based night airglow measurements, RSD-110, NPL, New Delhi-12

39. G.S.N. Murty and M.N.M. Rao, Deduction of the height profile of the vertical eddy diffusion coefficient in the lower thermosphere from the ground-based night airglow measurements, NPL, New Delhi-12

40. World Weather Records, US Department of Commerce, NOAA, National Climate Centre, Ashville, N.C. (1967)

41. R.J. List, Smithsonian Meteorological Tables, Sixth Revised Edition, Fourth Reprint, Smithsonian Institute, Washington D.C. (1968)

TABLE 1: KINETIC TEMPERATURE DATA IN ^{o}K CONSIDERED FOR PROPOSING ITRA

STATION / MODEL SATELLITE	LAT	LONG	PERIOD	DATA TYPE	ALT IN KM 50	55	60	65	70	75	80	85	90	95	100	Z/H	REF NO
Kwajalein	9 N	168 W	1956-78	S	270	261	246	230	213	200	196	194	191	186	179	Z	14
Asc & Natal	8 S		1960-70	G	267	261	248	228	211	201	197	200	189	185		Z	23
Thumba	9 N	77 E	1971-77	T	269	256	242	227	213	205	193					Z	19
Woomera	31 S	137 E	1957-63	S	267	259	249	232	218	204	191					Z	24
Wallops Is	38 N	75 W	1960-70	G		258	245	231	217	208	198	194	193	169	180	Z	23
Churchill	59 N	94 W	1960-70	G		258	251	236	226	216	201	193	194	194		Z	23
Cole & Kantor	Avg of 0		- 30 N	TPS	270	261	246	230	213	201	198	197				H	14
Koshelkov	Avg of 0		- 30 S	TPS	268	260	247	231	214	203	197					H	15
Cole & Kantor			45 N	TPS	269	259	246	234	222	211	202	194				H	14
Koshelkov	Avg of 40 S		- 50 S	TPS		255	242	229	215	203	195					H	15
Asc & Natal	8 S		1960-70	P		261	248	237	220	207	207	210	215	215	200	Z	23
Wallops Is	38 N	75 W	1960-70	P		258	245	230	216	208	209	204	203	199	196	Z	23
Churchill	59 N	94 W	1960-70	P		241	239	236	228	213	213	207	199	203	205	Z	23
Alt in km	-- >				52.7	56.5	60.1	63.5	66.7	70.0	73.1	76.1	79.1	82.2			
Nimbus	Avg of 30 S		- 30 N	R	262	251	241	230	220	213	212	208	206	205		H	27
Nimbus	Avg of 45 S		& 45 N	R	259	249	240	232	226	220	215	209	204	199		H	27
MSIS-83 data: A_p = 4.0; $F_{10.7}$ = 150	Alt(km)				85	90	95	100	105	110	115	120					
	Avg of 30 S		- 30 N		199	187	185	187	196	228	300	379				Z	30
	Avg of 45 N		& 45 S		195	181	178	185	206	243	303	376				Z	30

T = Thermistor; G = Grenade; S = Sphere; P = Pitot; R = Radiance; H = Geopotential; Z = Geometrical

TABLE 3: ATMOSPHERIC PROPERTIES OF ITRA (SI UNITS)

GEOPT ALT (m)	PRES ALT (m)	TEMP (°K)	PRESSURE (mb)	PRESSURE RATIO	DENSITY (kg/m³)	DENSITY RATIO	SONIC VELCTY (m/s)	UNIT REY NUMBER (s/m²)
-2000	-1890	312.15	1.262 3	1.250 0	1.408 0	1.202 0	354.18	7.402 0
00	30	300.15	1.010 3	1.000 0	1.172 0	1.000 0	347.31	6.348 0
2000	1940	288.15	8.010 2	7.930-1	9.684-1	8.261-1	340.29	5.412 0
4000	3840	276.15	6.290 2	6.227-1	7.934-1	6.769-1	333.13	4.584 0
6000	5740	264.15	4.886 2	4.838-1	6.444-1	5.497-1	325.81	3.856 0
8000	7640	251.15	3.750 2	3.712-1	5.201-1	4.437-1	317.70	3.240 0
10000	9540	238.15	2.837 2	2.809-1	4.150-1	3.540-1	309.36	2.700 0
12000	11430	225.15	2.113 2	2.093-1	3.270-1	2.790-1	300.80	2.228 0
14000	13410	212.15	1.547 2	1.532-1	2.540-1	2.167-1	291.99	1.819 0
16000	15520	199.15	1.110 2	1.099-1	1.942-1	1.657-1	282.90	1.467 0
18000	17660	203.75	7.914 1	7.836-2	1.353-1	1.154-1	286.15	1.002 0
20000	19760	208.35	5.684 1	5.628-2	9.503-2	8.107-2	289.36	6.908-1
22000	21820	212.95	4.112 1	4.071-2	6.726-2	5.738-2	292.54	4.800-1
24000	23860	217.55	2.995 1	2.965-2	4.796-2	4.091-2	295.68	3.362-1
26000	25870	222.15	2.196 1	2.175-2	3.444-2	2.938-2	298.79	2.373-1
28000	27860	226.75	1.621 1	1.605-2	2.490-2	2.124-2	301.87	1.686-1
30000	29820	231.35	1.203 1	1.192-2	1.812-2	1.546-2	304.92	1.207-1
32000	31770	235.95	8.988 0	8.899-3	1.327-2	1.132-2	307.93	8.697-2
34000	33700	240.55	6.750 0	6.683-3	9.776-3	8.339-3	310.92	6.307-2
36000	35640	245.15	5.097 0	5.047-3	7.244-3	6.179-3	313.88	4.602-2
38000	37590	249.75	3.869 0	3.831-3	5.397-3	4.604-3	316.81	3.378-2
40000	39550	254.35	2.952 0	2.923-3	4.043-3	3.449-3	319.71	2.494-2
42000	41510	258.95	2.263 0	2.241-3	3.045-3	2.597-3	322.59	1.851-2
44000	43480	263.55	1.743 0	1.726-3	2.304-3	1.966-3	325.44	1.381-2
46000	45460	268.15	1.349 0	1.335-3	1.752-3	1.495-3	328.27	1.036-2
48000	47470	268.15	1.046 0	1.035-3	1.359-3	1.159-3	328.27	8.034-3
50000	49480	268.15	8.110-1	8.030-4	1.054-3	8.988-4	328.27	6.230-3
52000	51500	265.15	6.284-1	6.222-4	8.256-4	7.043-4	326.43	4.926-3
54000	53530	259.15	4.845-1	4.797-4	6.512-4	5.556-4	322.72	3.957-3
56000	55560	253.15	3.712-1	3.675-4	5.108-4	4.358-4	318.96	3.162-3
58000	57600	247.15	2.826-1	2.798-4	3.984-4	3.398-4	315.16	2.514-3
60000	59630	241.15	2.137-1	2.116-4	3.088-4	2.634-4	311.31	1.988-3
62000	61680	235.15	1.605-1	1.589-4	2.378-4	2.029-4	307.41	1.563-3
64000	63720	229.15	1.197-1	1.185-4	1.819-4	1.552-4	303.46	1.221-3
66000	65770	223.15	8.850-2	8.762-5	1.382-4	1.179-4	299.46	9.482-4
68000	67820	217.15	6.492-2	6.428-5	1.042-4	8.885-5	295.41	7.312-4
70000	69880	211.15	4.721-2	4.675-5	7.790-5	6.645-5	291.30	5.599-4
72000	71940	205.15	3.402-2	3.369-5	5.777-5	4.929-5	287.13	4.255-4
74000	74030	199.15	2.428-2	2.404-5	4.247-5	3.623-5	282.90	3.208-4
76000	76100	197.95	1.722-2	1.705-5	3.031-5	2.585-5	282.05	2.301-4
78000	78150	196.75	1.219-2	1.207-5	2.158-5	1.841-5	281.19	1.647-4
80000	80170	195.55	8.609-3	8.524-6	1.534-5	1.308-5	280.33	1.177-4
82000	82160	194.35	6.068-3	6.008-6	1.088-5	9.278-6	279.47	8.391-5
84000	84120	193.15	4.267-3	4.225-6	7.697-6	6.566-6	278.61	5.969-5
84690	84790	192.73	3.776-3	3.738-6	6.824-6	5.822-6	278.31	5.303-5

TABLE 4: ATMOSPHERIC PROPERTIES OF ITRA (SI UNITS)

PRESSURE (mb)	GEOPT ALT (m)	NUMBER DENSITY (m^{-3})	MEAN PARTICLE SPEED (ms^{-1})	MEAN COLLSN FREQ (s^{-1})	MEAN FREE PATH (m)	DYNAMIC VISCTY kg/(m.s)	KINMATIC VISCTY (m^2/s)	THERMAL CONDVTY W/(m.K)
1.010 3	00	2.437 25	4.684 2	6.758 9	6.931-8	1.847-5	1.575-5	2.626-2
8.500 2	1500	2.114 25	4.614 2	5.774 9	7.990-8	1.804-5	1.774-5	2.556-2
7.000 2	3130	1.802 25	4.535 2	4.837 9	9.376-8	1.757-5	2.027-5	2.479-2
5.000 2	5820	1.366 25	4.403 2	3.559 9	1.237-7	1.677-5	2.553-5	2.350-2
3.000 2	9610	9.029 24	4.195 2	2.242 9	1.871-7	1.551-5	3.571-5	2.151-2
2.000 2	12360	6.502 24	4.036 2	1.553 9	2.598-7	1.455-5	4.653-5	2.002-2
1.500 2	14190	5.152 24	3.926 2	1.197 9	3.279-7	1.390-5	5.609-5	1.902-2
1.000 2	16610	3.612 24	3.829 2	8.186 8	4.678-7	1.332-5	7.666-5	1.814-2
5.000 1	20790	1.723 24	3.919 2	3.998 8	9.803-7	1.386-5	1.672-4	1.896-2
3.000 1	23990	9.990 23	3.988 2	2.358 8	1.691-6	1.426-5	2.969-4	1.958-2
2.000 1	26610	6.481 23	4.042 2	1.551 8	2.607-6	1.459-5	4.682-4	2.008-2
1.000 1	31260	3.092 23	4.138 2	7.574 7	5.464-6	1.517-5	1.020-3	2.098-2
5.000 0	36140	1.475 23	4.236 2	3.699 7	1.145-5	1.576-5	2.221-3	2.190-2
2.000 0	42940	5.548 22	4.369 2	1.435 7	3.045-5	1.656-5	6.206-3	2.317-2
1.000 0	48350	2.701 22	4.427 2	7.078 6	6.255-5	1.691-5	1.302-2	2.374-2
5.000-1	53760	1.394 22	4.358 2	3.596 6	1.212-4	1.650-5	2.461-2	2.307-2
2.000-1	60470	6.043 21	4.186 2	1.497 6	2.796-4	1.546-5	5.318-2	2.143-2
1.000-1	65200	3.212 21	4.061 2	7.719 5	5.261-4	1.470-5	9.518-2	2.025-2
5.000-2	69640	1.707 21	3.939 2	3.979 5	9.899-4	1.397-5	1.702-1	1.913-2
2.000-2	75130	7.300 20	3.809 2	1.646 5	2.314-3	1.320-5	3.759-1	1.796-2
1.000-2	79140	3.695 20	3.786 2	8.279 4	4.573-3	1.306-5	7.350-1	1.775-2
5.000-3	83100	1.870 20	3.763 2	4.165 4	9.034-3	1.292-5	1.437 0	1.755-2
3.776-3	84690	1.419 20	3.753 2	3.153 4	1.190-2	1.287-5	1.885 0	1.747-2

TABLE 5: VARIATION OF SPECIES CONCENTRATIONS (m^{-3}) WITH ALTITUDE

ALT (km)	TEMP (^{o}K)	NITROGEN	ATOMIC OXYGEN	MOLECULAR OXYGEN	ARGON	HELIUM
86.00	192.73	1.108 20	2.907 16	2.972 19	1.325 18	7.435 14
87.00	192.13	9.353 19	5.961 16	2.509 19	1.119 18	6.267 14
88.00	191.53	7.893 19	1.054 17	2.114 19	9.432 17	5.274 14
89.00	190.93	6.657 19	1.650 17	1.777 19	7.939 17	4.425 14
90.00	190.33	5.612 19	2.339 17	1.488 19	6.668 17	3.699 14
91.00	189.73	4.728 19	3.056 17	1.242 19	5.586 17	3.079 14
92.00	189.13	3.982 19	3.736 17	1.031 19	4.668 17	2.551 14
93.00	188.53	3.352 19	4.325 17	8.529 18	3.889 17	2.102 14
94.00	187.93	2.820 19	4.788 17	7.020 18	3.230 17	1.723 14
95.00	187.33	2.372 19	5.110 17	5.750 18	2.675 17	1.406 14
96.00	186.73	1.993 19	5.294 17	4.689 18	2.210 17	1.312 14
97.00	186.13	1.675 19	5.351 17	3.808 18	1.820 17	1.235 14
98.00	186.29	1.401 19	5.301 17	3.069 18	1.490 17	1.155 14
99.00	186.77	1.170 19	5.166 17	2.462 18	1.216 17	1.076 14
100.00	187.58	9.766 18	4.967 17	1.969 18	9.900 16	9.989 13
101.00	188.73	8.143 18	4.723 17	1.570 18	8.044 16	9.242 13
102.00	190.24	6.785 18	4.452 17	1.250 18	6.528 16	8.531 13
103.00	192.15	5.652 18	4.165 17	9.937 17	5.293 16	7.862 13
104.00	194.50	4.707 18	3.873 17	7.900 17	4.291 16	7.238 13
105.00	197.36	3.920 18	3.583 17	6.283 17	3.479 16	6.660 13
106.00	200.83	3.280 18	3.302 17	4.924 17	2.665 16	6.129 13
107.00	205.08	2.745 18	3.033 17	3.861 17	2.035 16	5.643 13
108.00	210.38	2.294 18	2.778 17	3.033 17	1.556 16	5.197 13
109.00	217.38	1.913 18	2.539 17	2.385 17	1.192 16	4.785 13
110.00	228.15	1.579 18	2.317 17	1.865 17	9.073 15	4.385 13
111.00	243.15	1.294 18	2.110 17	1.454 17	6.898 15	4.003 13
112.00	258.15	1.073 18	1.920 17	1.154 17	5.338 15	3.683 13
113.00	273.15	8.999 17	1.745 17	9.304 16	4.198 15	3.415 13
114.00	288.15	7.615 17	1.585 17	7.611 16	3.351 15	3.190 13
115.00	303.15	6.500 17	1.438 17	6.310 16	2.710 15	3.000 13
116.00	318.15	5.590 17	1.305 17	5.296 16	2.219 15	2.841 13
117.00	333.15	4.842 17	1.183 17	4.495 16	1.836 15	2.706 13
118.00	348.15	4.220 17	1.072 17	3.853 16	1.535 15	2.590 13
119.00	363.15	3.700 17	9.715 16	3.331 16	1.295 15	2.490 13
120.00	378.15	3.261 17	8.800 16	2.900 16	1.100 15	2.400 13
200.00	925.92	3.525 15	4.515 15	1.869 14	2.530 12	8.346 12
300.00	1021.28	1.459 14	7.023 14	4.988 12	2.812 10	5.063 12
400.00	1031.75	8.101 12	1.341 14	1.838 11	4.576 8	3.334 12
500.00	1032.97	4.995 11	2.731 13	7.626 9	8.613 6	2.238 12
600.00	1033.13	3.345 10	5.830 12	3.476 8	1.823 5	1.521 12
700.00	1033.15	2.420 9	1.301 12	1.731 7	4.308 3	1.045 12
800.00	1033.15	1.884 8	3.027 11	9.371 5	1.130 2	7.255 11
900.00	1033.15	1.574 7	7.332 10	5.500 4	3.280 0	5.089 11
1000.00	1033.15	1.407 6	1.846 10	3.487 3	1.048 -1	3.604 11

TABLE 6: ATMOSPHERIC PROPERTIES OF ITRA FROM 86 TO 1000 KM

ALT (km)	TEMP (^{o}K)	ACCN GRAV (ms^{-2})	PRES SCALE HT (km)	NUMBER DENSITY (m^{-3})	MEAN PARTCLE SPEED (ms^{-1})	MEAN COLL FREQ (s^{-1})	MEAN FREE PATH (m)	MEAN MOL WT
86.0	192.73	9.528	5.81	1.419 20	375.4	3.152 4	1.191-2	28.96
87.0	192.13	9.525	5.79	1.198 20	374.8	2.658 4	1.410-2	28.95
88.0	191.53	9.522	5.78	1.011 20	374.3	2.240 4	1.671-2	28.95
89.0	190.93	9.519	5.76	8.529 19	373.8	1.887 4	1.981-2	28.93
90.0	190.33	9.516	5.75	7.190 19	373.4	1.589 4	2.350-2	28.91
91.0	189.73	9.514	5.74	6.056 19	373.0	1.337 4	2.790-2	28.88
92.0	189.13	9.511	5.73	5.098 19	372.6	1.124 4	3.314-2	28.84
93.0	188.53	9.508	5.73	4.287 19	372.3	9.448 3	3.941-2	28.79
94.0	187.93	9.505	5.72	3.602 19	372.1	7.934 3	4.690-2	28.74
95.0	187.33	9.502	5.72	3.025 19	371.9	6.658 3	5.586-2	28.67
96.0	186.73	9.499	5.71	2.537 19	371.8	5.584 3	6.658-2	28.60
97.0	186.13	9.496	5.71	2.127 19	371.7	4.680 3	7.942-2	28.53
98.0	186.29	9.493	5.74	1.776 19	372.4	3.914 3	9.515-2	28.44
99.0	186.77	9.490	5.77	1.480 19	373.4	3.272 3	1.141-1	28.35
100.0	187.58	9.487	5.82	1.233 19	374.9	2.736 3	1.370-1	28.26
101.0	188.73	9.484	5.87	1.027 19	376.7	2.289 3	1.646-1	28.16
102.0	190.24	9.481	5.95	8.546 18	378.9	1.916 3	1.977-1	28.06
103.0	192.15	9.478	6.03	7.115 18	381.5	1.607 3	2.374-1	27.96
104.0	194.50	9.475	6.13	5.927 18	384.6	1.349 3	2.850-1	27.85
105.0	197.36	9.472	6.25	4.941 18	388.2	1.135 3	3.419-1	27.73
106.0	200.83	9.469	6.39	4.129 18	392.5	9.592 2	4.092-1	27.60
107.0	205.08	9.466	6.56	3.454 18	397.5	8.128 2	4.891-1	27.47
108.0	210.38	9.463	6.76	2.891 18	403.6	6.907 2	5.844-1	27.34
109.0	217.38	9.461	7.02	2.417 18	411.3	5.885 2	6.989-1	27.20
110.0	228.15	9.458	7.41	2.006 18	422.6	5.018 2	8.421-1	27.05
111.0	243.15	9.455	7.95	1.658 18	437.6	4.293 2	1.019 0	26.88
112.0	258.15	9.452	8.50	1.386 18	452.2	3.710 2	1.219 0	26.73
113.0	273.15	9.449	9.04	1.172 18	466.4	3.235 2	1.442 0	26.58
114.0	288.15	9.446	9.59	9.995 17	480.3	2.841 2	1.690 0	26.45
115.0	303.15	9.443	10.14	8.597 17	493.7	2.512 2	1.965 0	26.33
116.0	318.15	9.440	10.68	7.447 17	506.8	2.234 2	2.269 0	26.23
117.0	333.15	9.437	11.23	6.493 17	519.5	1.997 2	2.602 0	26.13
118.0	348.15	9.434	11.78	5.693 17	531.9	1.793 2	2.967 0	26.05
119.0	363.15	9.431	12.32	5.018 17	544.0	1.616 2	3.367 0	25.98
120.0	378.15	9.428	12.86	4.443 17	555.8	1.461 2	3.803 0	25.92
200.0	925.92	9.199	38.93	8.238 15	954.9	4.656 0	2.051 2	21.50
300.0	1021.28	8.924	52.67	8.583 14	1094.1	5.558-1	1.968	18.06
400.0	1031.75	8.661	60.34	1.458 14	1153.7	9.953-2	1.159	16.41
500.0	1032.97	8.410	66.70	3.005 13	1195.2	2.126-2	5.622 4	15.31
600.0	1033.13	8.170	77.40	7.384 12	1269.0	5.546-3	2.288 5	13.58
700.0	1033.15	7.939	101.37	2.348 12	1431.6	1.990-3	7.195 5	10.67
800.0	1033.15	7.718	147.65	1.028 12	1703.5	1.037-3	1.643 6	7.54
900.0	1033.15	7.507	207.53	5.822 11	1991.7	6.864-4	2.902 6	5.51
1000.0	1033.15	7.304	256.39	3.789 11	2183.7	4.897-4	4.459 6	4.59

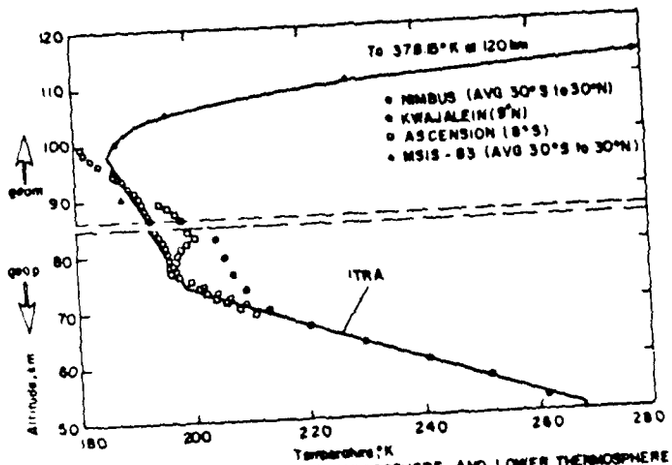

FIG 1 COMPARISON OF DATA IN THE MESOSPHERE AND LOWER THERMOSPHERE WITH THE PROPOSED ITRA

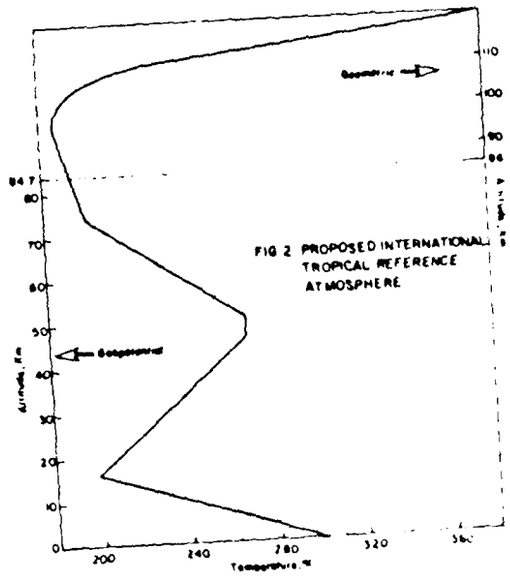

FIG 2 PROPOSED INTERNATIONAL TROPICAL REFERENCE ATMOSPHERE

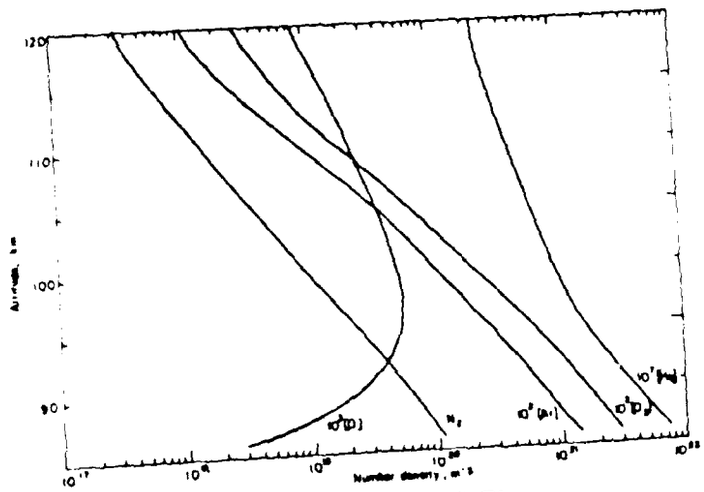

FIG 3 VARIATION OF SPECIES CONCENTRATION IN ITRA

Section 2

Upper Middle Atmosphere Properties

Adv. Space Res. Vol. 7, No. 10, pp. (10)135–(10)141, 1987
Printed in Great Britain. All rights reserved

0273-1177/87 $0.00 + .50
Copyright © 1987 COSPAR

ATMOSPHERIC STRUCTURE BETWEEN 80 AND 120 km

J. M. Forbes and G. V. Groves

*Department of Electrical Computer, and Systems Engineering, Boston University, Boston, MA 02215, U.S.A.
**Department of Physics and Astronomy, University College London, London WC1E 6BT, U.K.

ABSTRACT

Recent progress in modelling the temperature, density, and pressure specifications between 80 and 100 km is reported. The data base consists primarily of rocket and incoherent scatter measurements of temperature. An analytic polynomial scheme is described whereby smooth transitions with tabulations below 80 km and the MSIS-83 model above 120 km are obtained. Evaluations of the quality of fit to the data and possible directions for future work are also presented.

INTRODUCTION

Specific recommendations for the new CIRA made in 1984 were that /1/:

(i) Tabulations between 80 and 120 km should represent zonally- averaged values, and

(ii) The temperature, density and pressure specifications between 80 and 100 km should provide a smooth transition with zonally-averaged satellite data below and MSIS-83 /2/ above.

This paper reviews work in progress to meet these recommendations.

METHOD OF TEMPERATURE MODELLING

Monthly temperature cross-sections in height and latitude have been determined that meet the following conditions (Fig. 1):

(1) A smooth transition at 130 km to the temperature profile of MSIS-83 for mid-month dates and mean solar activity of F10.7 = 120 units, Ap = 10, longitudinal and diurnal (also semi-diurnal and terdiurnal) dependences being neglected.

(2) A smooth transition at 70 km to the zonal mean temperatures of the monthly mean models to 80 km previously prepared /3/. The models to 80 km are taken to represent mesospheric structure for mean solar conditions (F10.7 = 120 units) as their database extends over years for which solar activity averages to about this level.

(3) A constrained least-squares fit to observed temperature differences (from an initial temperature model), the imposed constraint being that the ratio (partial pressure of N_2 at 130 km)/(partial pressure of N_2 at 70 km) that is calculated for a fitted temperature profile should equal the same ratio as calculated from the pressure values provided by the upper and lower matching models.

The analytical procedure is to express the reciprocal of temperature T (or more precisely g/T, g being the gravity acceleration) as a polynomial in height, then by integration the ln(N_2 - pressure ratio) may also be expressed as a polynomial in height and the coefficients chosen to satisfy (3) above. Temperature data (70 to 130 km) that have been utilized for (3) above are:

(a) The temperature data previously utilized in the construction of CIRA 1972 /4/, and

(b) Subsequent data, reviewed in /1/, which have been obtained either by rocket techniques or incoherent scatter (I.S.) measurements, the latter being the main source of data above 100 km.

The incoherent scatter data utilized were from:

(a) The Millstone Hill model (/5/, Table 1) for F10.7 = 120 units, A = 10.

(b) The St. Santin model (/6/, Table 1) which is applicable for Kp = 2, i.e. Ap = 7, and which was evaluated for F10.7 = 120 units.

(c) An Arecibo model based on observations for 1970-1975, i.e. from solar maximum to solar minimum, which could be taken to represent mean solar conditions.

Individual temperature profiles that were utilized were from rocket launchings extending over a wide range of years and solar conditions. These values were processed without making any correction to mean solar conditions to individual profiles on the assumption that this dependence would average out in the overall analysis.

The monthly tabulations of observed temperature differences have been prepared from the above sources of data at each 5 km height interval from 70 to 130 km and each 10° latitude interval from pole to pole. In the absence of data, values are used from the MSIS-83 model which extends down to 85 km. Very little southern hemisphere data are available but if an observed temperature difference were available at a N. latitude for the same season it would be taken to apply at the same S. latitude in the absence of any data there.

As a consequence of the polynomial fitting procedure, each monthly temperature cross-section has an analytical representation and mean zonal temperature may be readily calculated for any height and latitude, and also for any date by interpolating between consecutive months.

COMPARISONS BETWEEN MODELS AND DATA

At Low Latitudes

Above 100 km the main sources of data are (1) the incoherent scatter measurements over Arecibo, Puerto Rico (18°N, 67°W) and (2) the Kwajalein (9°N, 168°E) Reference Atmospheres, 1979 /7/ which are based on rocket data. The open and filled-in circles in Fig. 1 show April data from these sources when corrected to 10°N latitude. The point of interest is that the profile satisfactorily fits the data while simultaneously satisfying the N2-pressure constraint. The same can also be said of the data below 100 km, most of which are single temperature profiles. Differences between temperature data and the calculated profiles have been averaged over 11 months at 5 km height intervals as shown in Fig. 1. (Symbols may be plotted just above or below the height to which they refer for reasons of clarity). On averaging these means with weights according to the number of observations on which they are based the line profile shown in Fig. 1 is obtained for their weighted average, which does not generally differ significantly from zero. This leads to the conclusion that the introduction of the N2-pressure constraint has not biased the fit to the temperature data, or in other words that the upper and lower models can be matched in a way that is consistent with the temperature data in the intermediate height region.

A comparison is also made in Fig. 1 between the fitted profile and MSIS-83. At 115-120 km, the profile gives lower temperatures than MSIS-83 in all months, the difference being greatest in April and reaching 40 K as shown in Fig. 1. A comparison between MSIS-83 and observed values is shown in Fig. 2 and MSIS-83 exceeds observed values in most months, whereas the new profile for 9°N lies much closer than MSIS-83 to the Kwajalein data for all months and the new 18°N profile lies closer to the Arecibo data than MSIS-83 on average. There are however considerations that tell against the ready acceptance of the new profiles whereas MSIS-83 temperatures 'follow the sun', being 1 or 2K higher at 18°N than at 9°N in summer with small equinox maxima, the new profiles show a consistent equatorwards temperature decrease throughout the year that averages 15K between 18°N and 9°N and has an annual variation with maxima and minima at consecutive equinoxes. Without any clear understanding of the physical origin of such variations at low latitudes, the possibility must remain open that the differences between the Kwajalein and Arecibo data have a dependence other than the latitudinal one which this analysis is set up to model. Consideration is currently being given to the best way to utilize the data from these two low latitude sites.

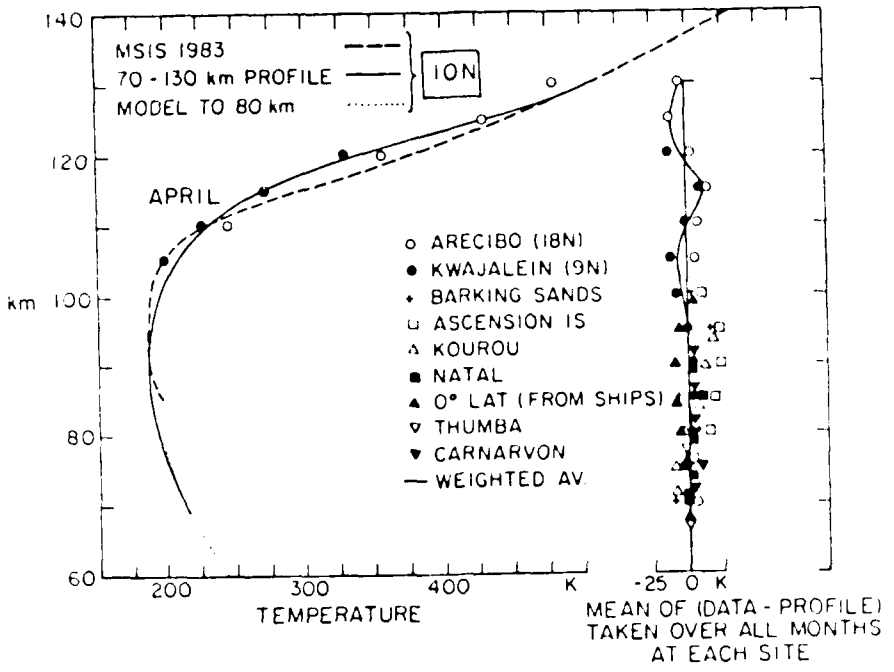

Fig. 1. A 70-130 km temperature profile determined for April at 10°N latitude. Annual mean deviation of observations from calculated profiles for individual low latitude stations.

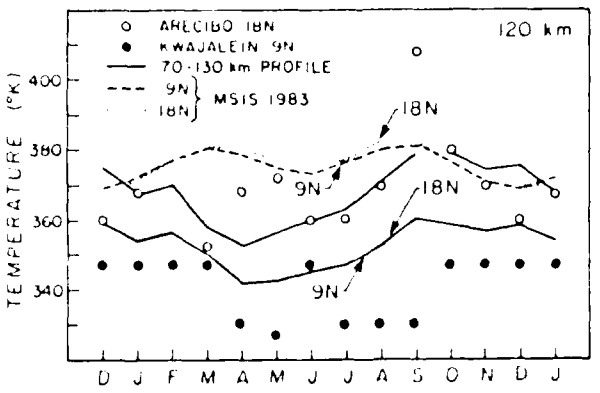

Fig. 2. Monthly mean temperatures observed at Arecibo (18°N) and Kwajalein (9°N) at 120 km compared with (i) MSIS-83 (dashed and dotted lines) and (ii) calculated values (continuous lines).

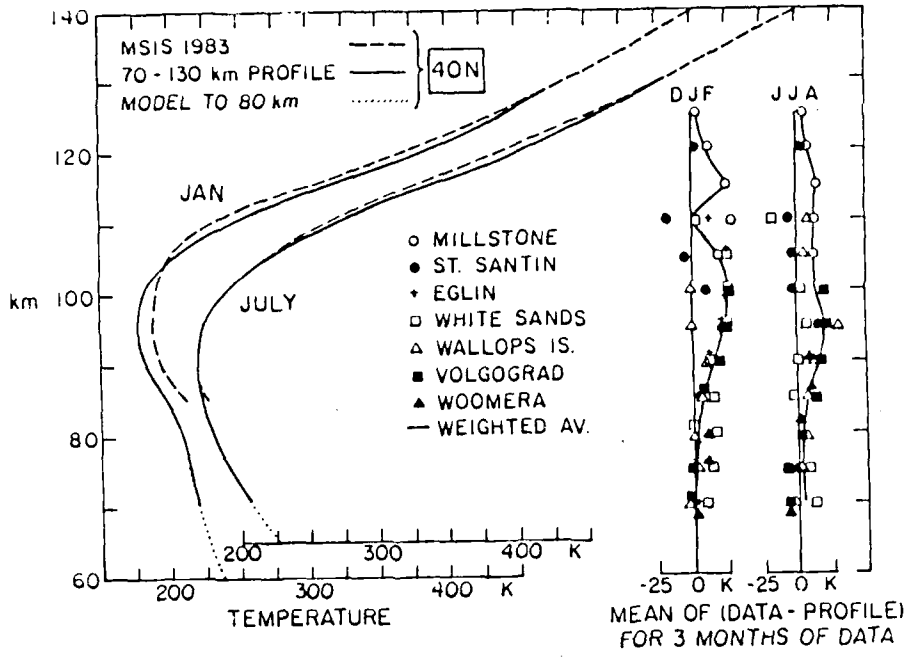

Fig. 3. January and July 70-130 km temperature profiles at 40°N latitude. Mean deviation of observations from calculated profiles for winter months (DJF) and summer months (JJA) at individual middle latitude sites.

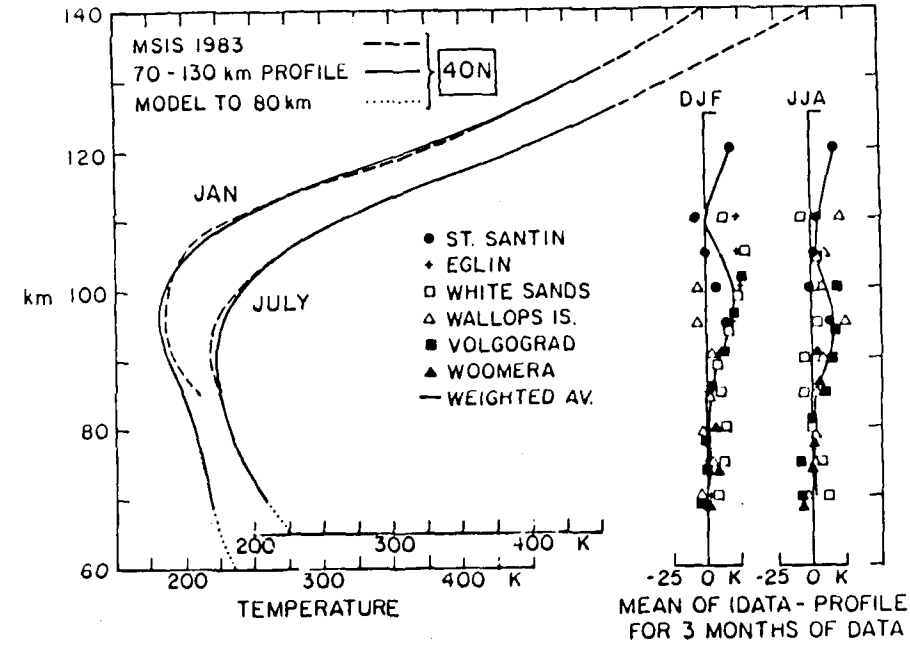

Fig. 4. The same as Fig. 3 without the inclusion of Millstone Hill data.

At Middle Latitudes

Fig. 3 is for 40°N and shows both January and July profiles and mean deviations of the data from the model for each site averaged over winter months (DJF) and summer months (JJA). The main result to be noted is that for both seasons (and also for other times of the year), observed values are consistently higher than those of the profiles calculated. This bias arises from the imposed N2-pressure constraint, the fall off in pressure between the 70 km value of the lower model and the 130 km value of MSIS-83 being greater than that implied by the temperature observations at the intermediate heights. It should however also be noted that MSIS-83 values between 105 and 125 km are even lower than the new profiles and are therefore still lower than the observed values.

Consideration is being given to possible revisions in the modelling technique that might lead to a reduction in the bias that is apparent at all heights in the mean deviations (Fig. 3).

One possible revision would be to exclude the Millstone Hill I.S. data as these values are noticeably high. Fig. 4 shows the results obtained when Fig. 3 is reworked without the Millstone Hill values; and it is seen that although the biases are reduced they are still significant, particularly from 85 to 105 km, and the matter warrants futher consideration.

At High Latitudes

Fig. 5 shows the January and July profiles determined for 70°N and also the mean deviations of the data from the new profiles for each of the three high latitude sites averaged over winter months (DJF) and summer months (JJA). In this case the mean deviations do not show any consistent bias, but no definite conclusion is possible with the limited data samples available.

It is of interest to note that a July mesopause is obtained at 88 km with a temperature of 155K (Fig. 5), which agrees with the discussion of McKay /8/ who states: 'Moderately low mesopause temperatures (150-160K) are a consistent feature at 60N during summer. These temperatures are the result of adiabatic cooling associated with rising motions in the general circulation. There is an additional cooling effect which can occasionally lower the mesopause temperature to 130-240K. This effect persists over timescales of weeks and during this time NLC will be seen'. It therefore follows that if observations are biased to the time of NLC, the lower values of close to 142K which are shown by CIRA 1972 /4/ and Air Force Reference Atmospheres /9/ are more representative of these times of additional cooling, whereas the present profiles which match upper and lower models represent mesopause conditions without the addtional cooling.

TEMPERATURE VARIABILITY

In addition to the mean deviations of observed temperatures from the calculated profiles that have been shown in Figs. 1,3,4 and 5, the RMS deviations from these means have been calculated with averaging over all months and these are shown in Fig. 6 for low, middle and high latitude grouping of sites. Fig. 6 shows that at all latitudes the RMS deviations increase with height except possible at 100-105 km at middle and high latitudes where values may decrease slightly before increasing again more rapidly up to 130 km. At low latitudes data are lacking above 95 km but there is an indication that a more rapid increase begins at 85 km. A likely origin of these variations is the upward propagation of tides and gravity waves. Theoretical tidal amplitudes (/10/, Fig. 14 and /11/, Fig. 11) indicate that the increase above 85 km at low latitudes might be associated with the diurnal tide, that above 105 km at middle latitudes with the sime-diurnal tide plus a possible smaller contribution from the diurnal tide and that above 105 km at high latitudes with the semi-diurnal tide alone. At lower heights, the variations are likely to arise from a spectrum of gravity waves and the slow rate of increase of amlitude with height would be indicative of wave breaking with the possible extinction of most of the energy of these waves at 100-105 km. In this 'gravity wave' region RMS values increase noticeably from low to high latitudes. At 80 km, for example, RMS values are 8, 12 and 16 K for the low, middle and high latitude data.

DENSITIES AND PRESSURES

At the present stage of this work, profiles have been constructed for temperatures and partial N_2 pressures. The calculation of the latter is based on the equation of state and the barometric law and accoount is taken of the transition from a mixing region at 70 km to diffusive conditions at 130 km using the relations from MSIS-83. The effect of this transition in the case of N2 is particularly small as its molecular weight of 28 lies very close to that of air in the mixing region (28.96).

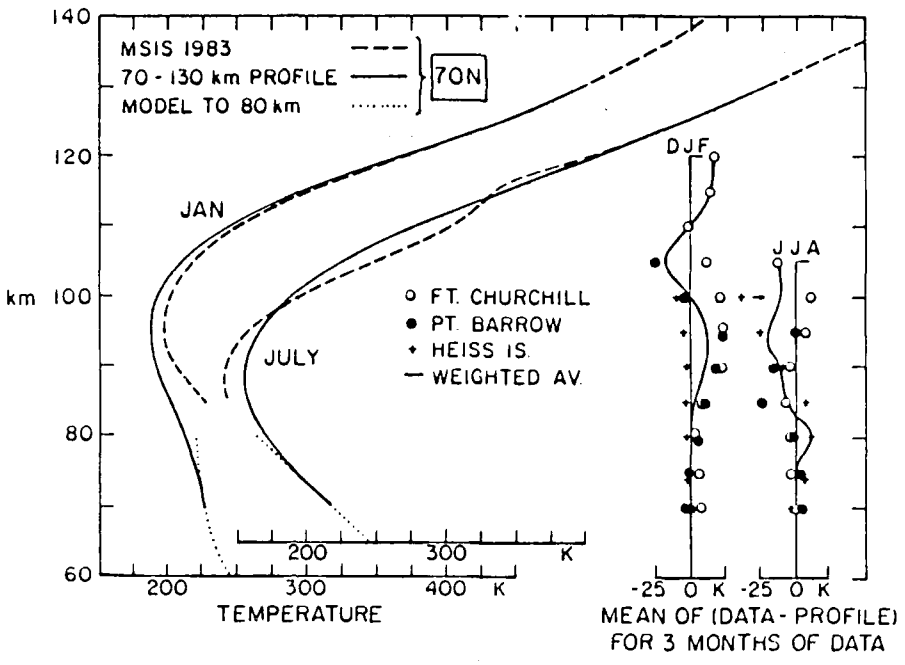

Fig. 5. January and July 70-130 km temperature profiles at 70°N latitude. Mean deviation of observations from calculated profiles for winter months (DJF) and summer months (JJA) at individual high latitude sites.

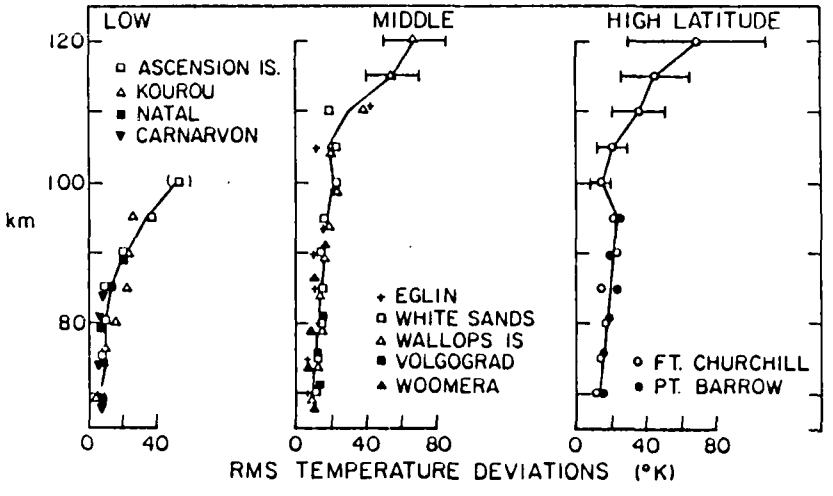

Fig. 6. Annual RMS deviation of obsrved temperature differences (from calculated profiles) with respect to their mean deviation for each site.

Attention has yet to be given to the vertical distribution of other gas constituents and to the possiblity of making these continuous with the upper and lower models at 130 and 70 km respectively. The final step to the modelling of total densities and pressures would then be a relatively simple one.

It may be recorded that mean pressure distributions have now been extended upwards to the 0.005 mb (83 km) and 0.001 mb (91 km) levels by Koshelkov /12/ and are in the height range of interest.

DISCUSSION

A theoretical and numerical anlysis is being developed for modelling atmospheric structure between 70 and 130 km for mean solar conditions. Monthly profiles have been analytically generated for all latitudes and heights from 70 to 130 km in temperature and partial N_2 pressure which have a smooth transition to MSIS-83 at 130 km and an 18-80 km model at 70 km. Attention will be given to the modelling of other gas constituents and to the possibility of combining the three models for the height regions 18-70, 70-130 and above 130 km to provide an analytical model for all heights above 18 km. Treatment of the 70-130 km region is however limited by available data and there are important variations that have yet to be considered. These are with (i) solar activity, (ii) longitude, (iii) time of day and (iv) seasonal asymmetry between N. and S. hemispheres. Although the present analysis extends over both hemispheres, the small seasonal asymmetry generated via the upper and lower matching models at 70 and 130 km lacks direct observational support on account of the lack of S. hemisphere data.

Acknowledgements. GVG gratefully acknowledges support to University College London for this work from the Air Force Office of Scientific Research under Grant No. AFOSR - 84-0045.

REFERENCES

1. J.M. Forbes, Temperature Structure of the 80 km to 120 km Region, *presented at the XXV COSPAR Meeting, Graz, Austria*, June 1984.

2. A. Hedin, A Revised Thermospheric Model based on Mass Spectrometer and in Incoherent Scatter Data: MSIS-83, *J. Geophys. Res.*, *88*, 1017) (1983).

3. G.V. Groves, A Global Reference Atmosphere From 18 to 80 km, *Air Force Surveys in Geophysics, No., 448, AFGL-TR-85-0129*, Air Force Geophysics Laboratory, Hanscom AFB, MA 01731. (1986)

4. COSPAR Working Group 4, *COSPAR International Reference Atmosphere, CIRA 1972*, Akademic Verlag, Berlin (1972).

5. R.H. Wand, Lower Thermospheric Structure From Millstone Hill Incoherent Scatter Radar Measurements 2. Semidiurnal Temperature Component, *J. Geophys. Res.*, *88*, 7211 (1983).

6. D. Alcayde, Temperature, molecular nitrogen concentration and turbulence in the lower thermosphere inferred from incoherent scatter data, *Ann. Geophys.*, *35*, 41 (1979).

7. A.E. Cole, A.J. Kantor, and C. Philbrick, *Kwajalein Reference Atmospheres, 1979, Environmental Research Papers, No.677, AFGL-79-0241*, Air Force Geophysics Laboratory, Hanscom AFB, MA 01731

8. C.P. McKay, Noctilucent cloud formation and the effects of water vapor variability on temperatures in the middle atmosphere, *Planet. Space Sci.* *33*, 761 (1985).

9. A.E. Cole and A.J. Kantor, Air Force Reference Atmospheres, *Air Force Survey in Geophysics, No. 382, AFGL-TR-78-0051*, Air Force Geophysics Laboratory, Hanscom AFB, MA 01731. (1978)

10. J.M. Forbes, Atmospheric Tides 1. Model Description and Results for the Solar Diurnal Component, *J. Geophys. Res.*, *87*, 5222 (1982).

11. J.M. Forbes, Atmospheric Tides 2. The Solar and Lunar Semidiurnal Components, *J. Geophys. Res.*, *87*, 5241 (1982).

12. Y.P. Koshelkov and E.N. Kovshova. *Antarctica*, *24*, 29 (1985).

Adv. Space Res. Vol. 7, No. 10, pp. (10)143–(10)153, 1987
Printed in Great Britain. All rights reserved.

0273-1177/87 $0.00 + .50
Copyright © 1987 COSPAR

MEAN WINDS OF THE UPPER MIDDLE ATMOSPHERE (~70–110 km) FROM THE GLOBAL RADAR NETWORK: COMPARISONS WITH CIRA 72, AND NEW ROCKET AND SATELLITE DATA

A. H. Manson,[1] C. E. Meek,[1] M. Massebeuf,[2] J. L. Fellous,[2] W. G. Elford,[2] R. A. Vincent,[3] R. L. Craig,[3] R. G. Roper,[4] S. Avery,[5] B. B. Balsley,[5] G. J. Fraser,[6] M. J. Smith,[6] R. R. Clark,[7] S. Kato[8] and T. Tsuda[8]

[1]*I.S.A.S., University of Saskatchewan, Canada*
[2]*CNRS/CRPE and CNES, France*
[3]*University of Adelaide, Australia*
[4]*Georgia Institute of Technology, U.S.A.*
[5]*CIRES and NOAA, Boulder, U.S.A.*
[6]*University of Canterbury, New Zealand*
[7]*University of New Hampshire, U.S.A.*
[8]*Kyoto University, Japan*

ABSTRACT

A substantial quantity of wind data have been assembled from radar systems since CIRA-72 was formed: most of these radars include height ranging, and operate on a regular and even continuous basis. Systems include meteor and MF (medium frequency) *Radars: an* MST (mesosphere-stratosphere-troposphere) Radar (meteor mode); and an LF (low frequency) drift system. Latitudes represented are near 20° N/S, 35° N/S, 45° N/S, 50°N, 65° N/S. In all cases tidal oscillations were calculated so that corrected mean winds (zonal, meridional) are available - the meridional was not included in CIRA-72. Means for groups of years near 1980 are available, as well as individual recent years (1983, 1984) to allow assessment of secular trends: revised and improved analysis has been completed for several stations.

Height-time cross-sections have been formed for each observatory: heights are typically ~75-110 km, with time resolution of 7-30 days. Such detailed cross-sections were almost unknown before 1972. *Comparisons with* CIRA-72 are shown, and these emphasize the differences between hemispheres (NH, SH) in the radar winds. Other new winds from rockets and satellite radiances are contrasted with the radar set. There are important differences with the satellite-derived geostrophic winds (1973-78): possible explanations involve secular trends, longitudinal variations, and ageostrophy.

INTRODUCTION

The number of radars providing winds in the upper middle atmosphere has increased significantly in the last decade. Depending on the technique, these systems fill the data gap between 60 km or 80 km and ~110 km. Below 60/80 km small rockets have provided wind data directly /1/, and since ~1973 satellite radiance measurements have been made, enabling geostrophic winds to be calculated /2/. Above 110 km larger rockets and incoherent-scatter radars provide temperatures and winds. The radars include MF radars or partial reflection systems giving data from 60/70-100/110 km; and meteor radars (and MST radars operating as meteor radars) 80-110 km. We show or discuss here data from 14 locations, which represent a good Northern Hemispheric (N.H.) North American chain (18-65°N, ~90°W), an Oceanian chain (78°S-35°N, ~140°E) which is mainly in the southern hemisphere (S.H.), and some Western European data (44-68°N, ~0°E): data are still being obtained at 9 of these locations, including two new Antarctic stations. The methods of data analyses are discussed in detail elsewhere /3,4,5,6,7,8,9,10/. Generally tidal oscillations have been removed from days or groups of days, and the remaining mean winds and longer period oscillations plotted as height-time contours. Time resolution varies from 10-15 days to seasonal.

In earlier papers involving this global radar set /11,12/ composite cross-sections from the years 1978-1982 were formed so that only the major temporal features remained. However, here more recent individual years are also shown, in several cases using refined analysis. This is to demonstrate the reliability of our earlier conclusions /11,12/, and illustrate interannual variability. The wind contours from MF radars are compared with satellite-derived geostrophic wind contours, because of the considerable overlap (10-20 km) between the two types of data. Latitudinal cross-sections for two solstitial months are then shown that enable comparisons between zonal winds from CIRA-72, the radars and satellite-derived geostrophic winds; and also meridional winds from a compilation of G.V. Groves /13/ and the radar set. Tabulations of monthly mean values for most stations appear elsewhere /12/. The sign convention is as follows: for the zonal winds, positive winds are from the west (west or westerly winds, called by some "eastward") and negative winds are from the east (easterly winds, or "westward"). For the meridional winds, positive winds are from the south (south or southerly winds), and negative winds are north or northerly winds. It is also convenient to describe these latter as poleward or equatorward winds. The figures are consistent for the

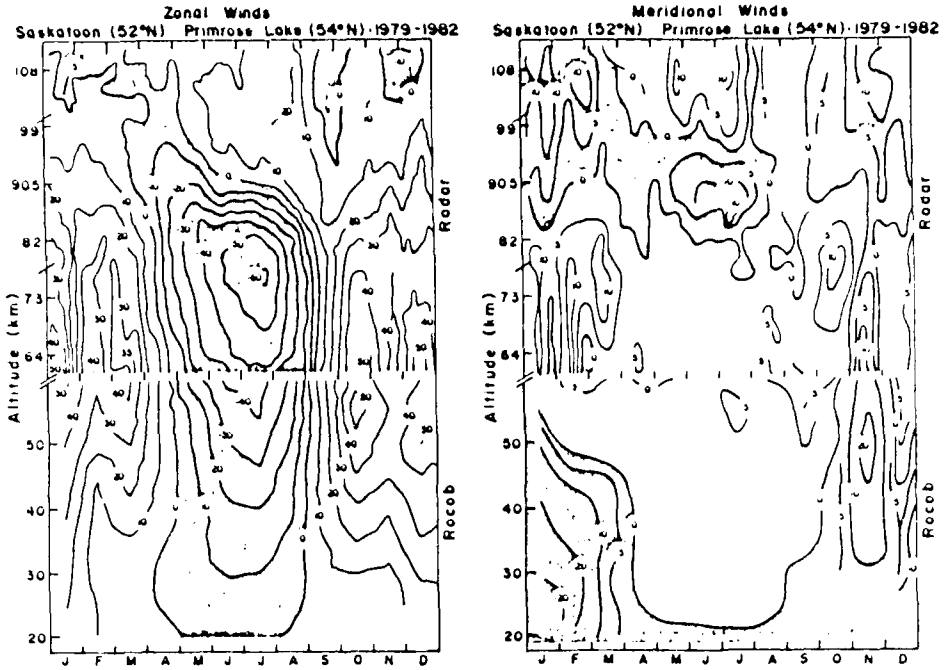

Fig. 1 Saskatoon, 1979-82, 52°N, 107°W: 10d means; s.d. 5 ms^{-1} at 90 km.

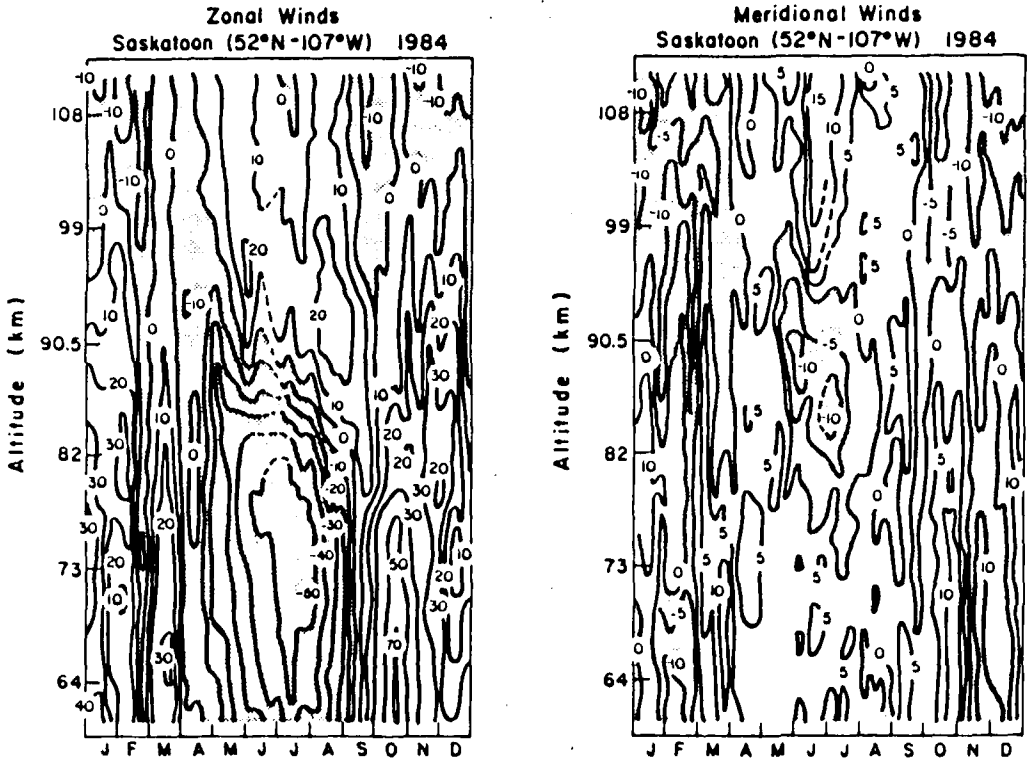

Fig. 2 Saskatoon, 1984.

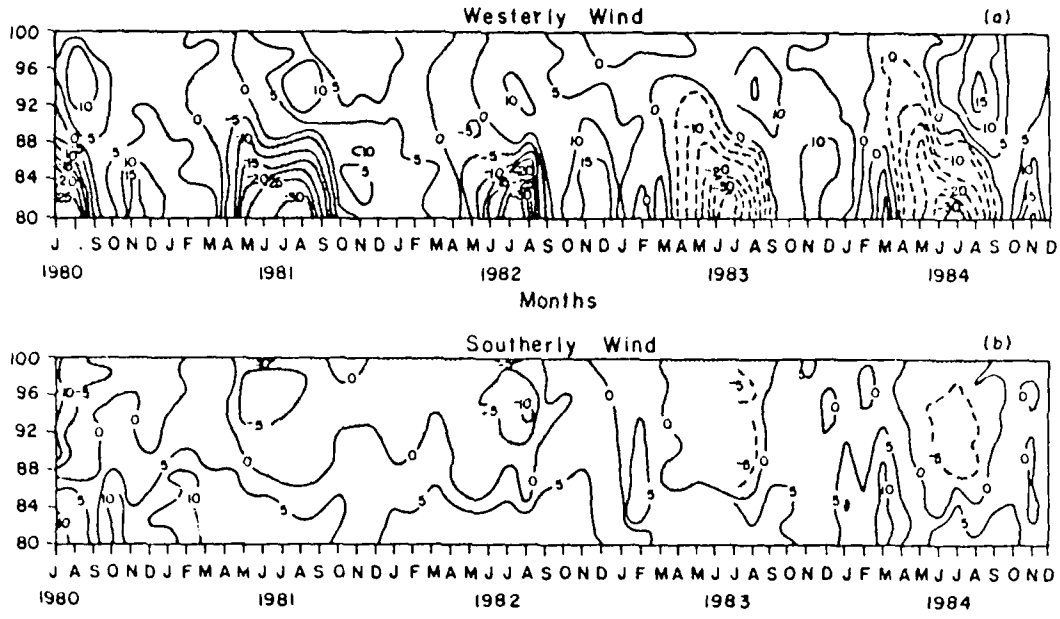

Fig. 3 Poker Flat, 1980-84, 65°N, 147°W: 30d means.

most part, but any differences are mentioned in the captions.

GENERAL MIDDLE-, HIGH-LATITUDE (35-65°) CHARACTERISTICS

The main features of zonal (EW) and meridional (NS) flows are evident in the 4 year compilation (1979-82) for Saskatoon (52°N, Figure 1): rocket data from Primrose Lake (54°) have been added. Time resolution is 10 days and 30 days respectively /14/. The summer-centred months are dominated by a strong, smoothly contoured easterly flow from 20-90 km. The 50° contour from CIRA-72 /15/ is very similar, although its easterly maximum and zero line are ~5 km lower; and its westerly flow near 100 km is stronger due to tidal contamination /16/. During winter-centred months the westerly flow is weaker than CIRA, and there is much more structured, repeatable variability, due to planetary waves, stratospheric warmings (STRATWARMS) /13/, and long period (12-, 6-mth) oscillations /14,16/. CIRA-72 winds were almost discontinuous at 60 km, due to STRATWARMS in different years in each set of data, and winds above 60 km in February were quite unrealistic. The summer meridional winds (Fig. 1) demonstrate poleward flow 20-80 km and above 95 km, with equatorward flow between: this latter has been identified at all longitudes near 50/60°N /18/, at lower latitudes, and both hemispheres /12,15/. For

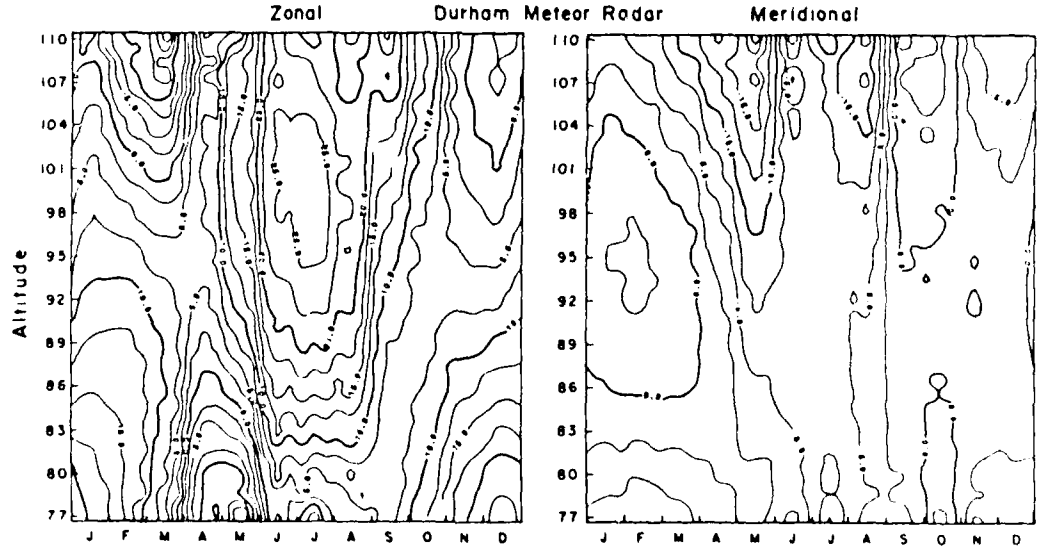

Fig. 4 Durham, 1978/79/84, 43°N, 71°W.

December-March there is poleward flow from ~50-85 km, with reverse flow above and below. The contours of Groves /15/ differs significantly, as they are dominated by a larger and stronger (-25 m/s) summer-centred equatorward flow. This difference will be discussed in more detail later, when all stations are discussed. To demonstrate the small interannual variability, and for comparison with other new contours, Saskatoon radar winds for 1984 are also shown in Figure 2 /19,20/.

A long series of EW/NS contours from Poker Flat (65°N) are shown in Figure 3: these are from an MST radar (meteor detection mode), /8/. Only contours for 1980-1982 data were shown before /11,21/. The zonal features are similar each year to Saskatoon, but the strengths of solstitial cells near 80 km are about half as large. The summer zero line is also near 90 km. There is much more variability in the NS flow, but 95 km summer flow is always strongest and equatorward; below it is usually poleward - very similar to Saskatoon.

An important re-analysis of meteor winds from Durham (43°N) has been completed (Figure 4), which allows EW wind shears and reversals to be accurately represented (earlier a linear wind variation was assumed /11/). Data from 1978/79/84 are included. The summer shears from 80-90 km are now higher (20 m/s) than earlier (10 ms^{-1}), and more comparable to those at Saskatoon (50 ms^{-1}) and Poker Flat (35 ms^{-1}). The Durham zonal wind reversal height is now at 78 km. Overall the contours are more realistic, and now quite similar to the French data from Garchy /11/, which also had a large easterly spring tongue and a low reversal height (~82 km). There is much less difference in the new NS contour, and as before, the summer flow is equatorward but not strong or focussed in a cell.

A new analysis has also been completed for Kyoto (35°N): contours for 1983-1985 are shown in Figure 5. The analysis is now quite similar to that used by MF radars, with harmonics being fitted to time series of hourly mean winds at each height. The changes are actually small, most obviously the summer westerly flow is stronger than before /11/. Comparisons between the new Kyoto MST radar, the Kyoto meteor radar and the Adelaide MF radar (35°S) are proceeding. At this point however, it appears that the summer easterly flow reversal occurs below 82 km (Figure 5), by extrapolation near 80 km; in contrast Adelaide's is near 85 km and the flow is more mid-latitude in form /11,15,21/. Near 35°N, Atlanta /11/ and Kyoto may both show negative easterly flow in fall and early winter, with strong westerly flow in late summer - features quite similar to CIRA-72 at 20° /11/. Stratwarm effects are evident at both locations /6/. Meridional flow at Kyoto (Figure 5) is mainly equatorward, with maxima

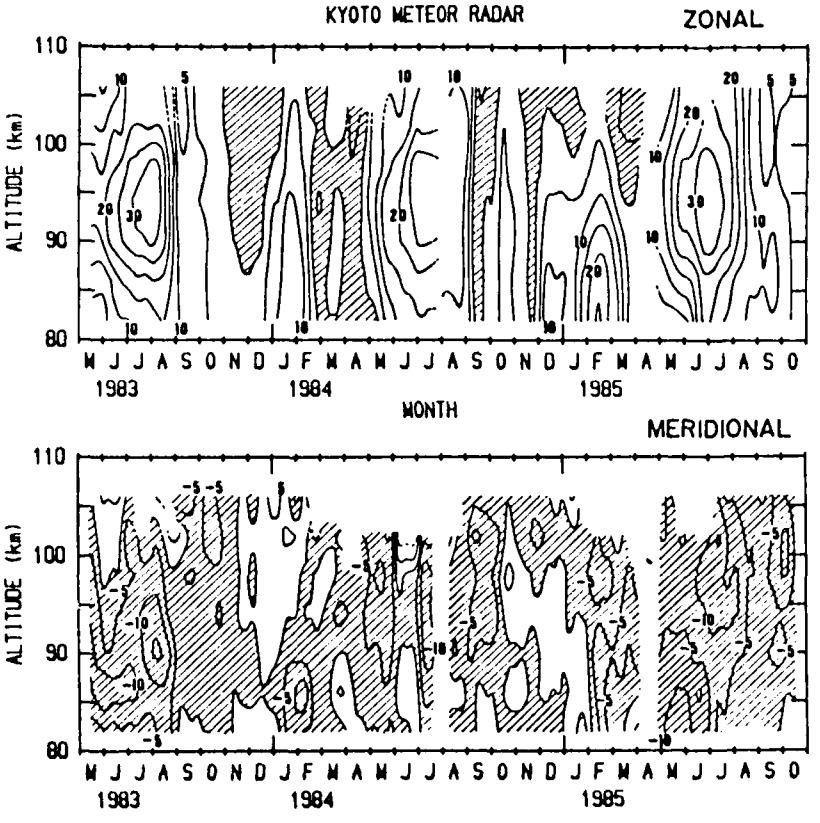

Fig. 5 Kyoto, 1983-85, 35°N, 136°E: periods <25d removed.

in summer centred near 92 km: quite similar to Atlanta and other northern hemisphere stations.

Finally, new data from Kürschner and Schminder for central Europe (52°N) are shown. The new method involves the use of modulation on low frequency radio signals to obtain height from the LF drift method /22/. Contours for two years, 85-110 km, are in Figure 6, and should be

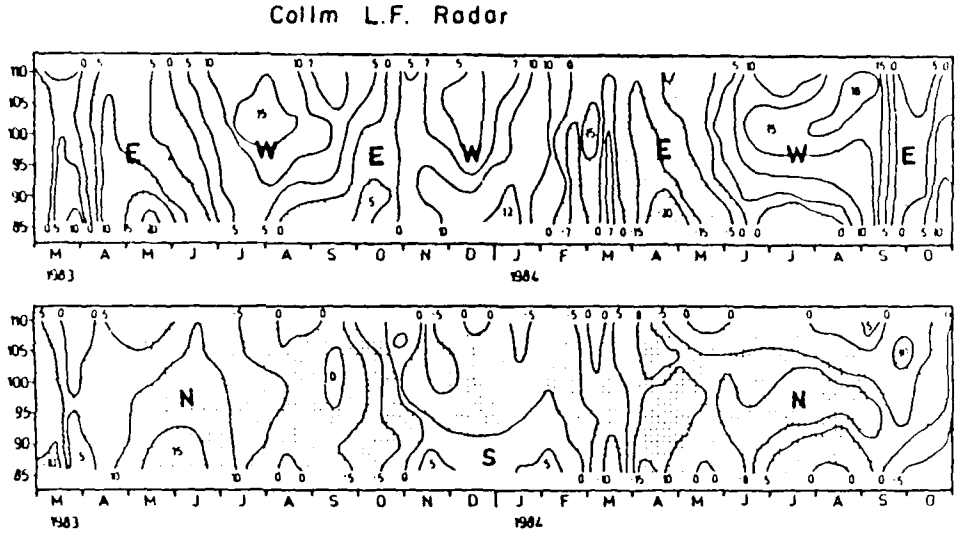

Fig. 6 Collm, 1983-84, 52°N, 15°E.

compared with Saskatoon (52°N) (Figures 1,2). Similarities dominate: the summer westerlies above ~90 km, winter westerlies; and easterly flows in fall (September-November) and the spring. The latter, however, demonstrates the largest differences: the tongue is wider both years, including June in 1983, and February and March in 1984. The meridional flow is very similar in positions and strengths. Longitudinal differences appear quite small on the basis of this comparison.

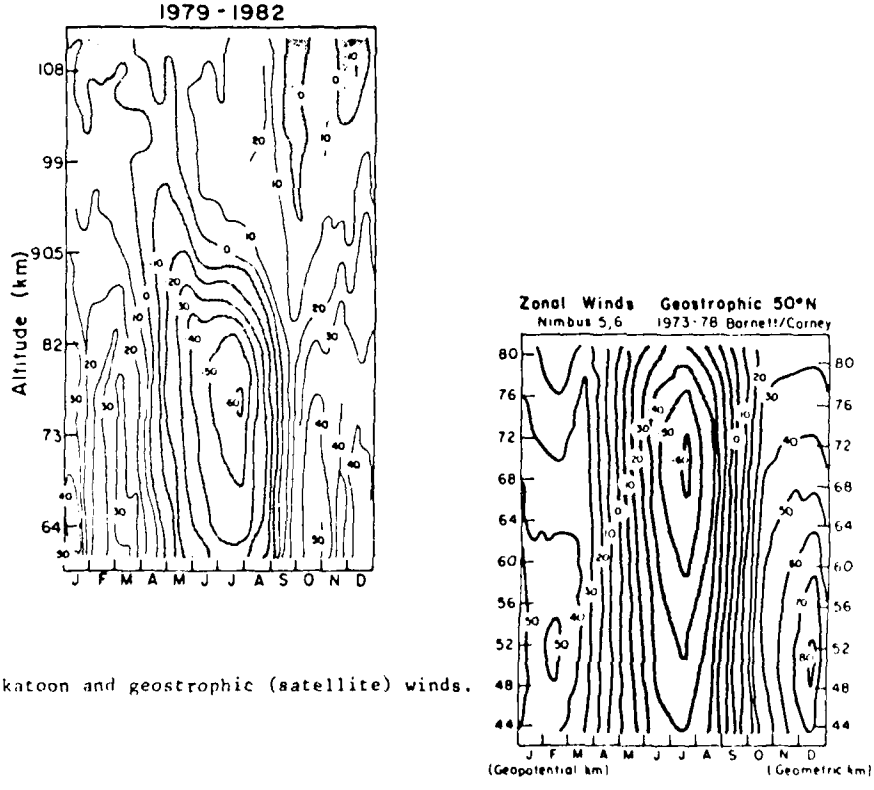

Fig. 7 Saskatoon and geostrophic (satellite) winds.

COMPARISONS BETWEEN MF RADARS AND SATELLITE DATA

In Figures 7-9 we show zonal wind contours from Saskatoon (52°S; 1979-1982), Christchurch (44°S, 1978-1980), and Adelaide (35°S, 1978-1983) each compared with satellite-derived geostrophic winds /2/. Wind shears (75-80 km) and heights of summer maxima are compared in Figure 10. In these figures individual locations are being compared with zonal means; however the amplitudes of standing waves 60-80 km are quite small, especially in summer /2/, so this should not be an important factor /23/. At Saskatoon, the geostrophic summer cell is 5 km lower in altitude, while winter values are similar; shears are similar (Figure 10). However the years do not completely overlap, and while no obvious trend is evident at Saskatoon 1978-

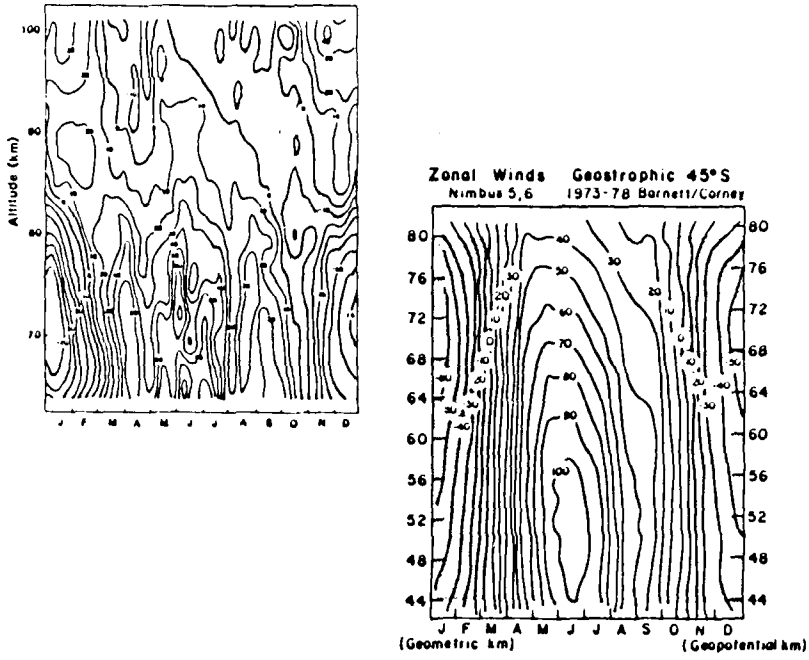

Fig. 8 Christchurch (1978-80, 44°S, 173°E) and geostrophic (satellite) winds.

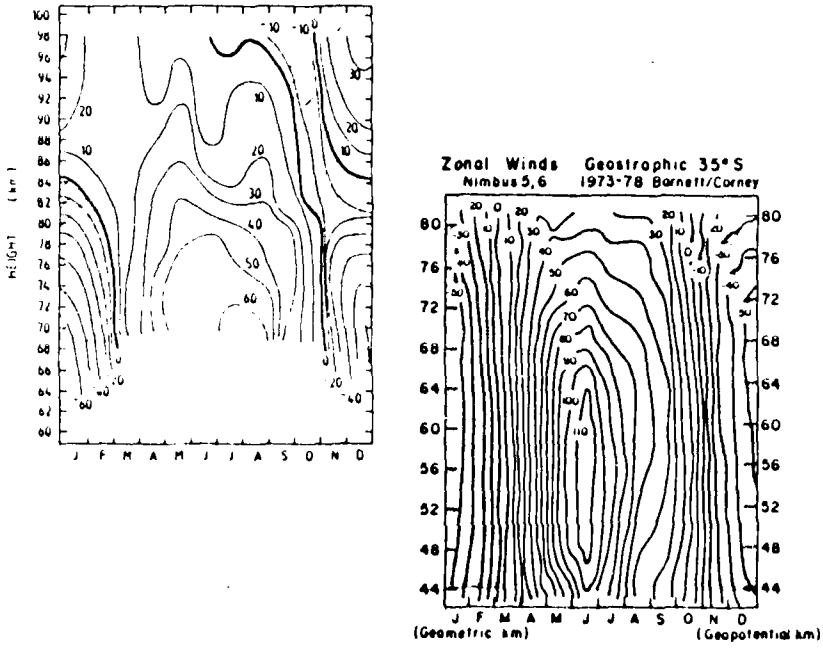

Fig. 9 Adelaide (1978-83, 35°S, 138°E) and geostrophic (satellite) winds.

1984 (/14/, Figure 2) significantly weaker flow was observed near 1975 /24/ using a limited data sample. At Christchurch (Figure 8) the geostrophic summer cell is at a similar height, but slightly weaker, and the shear (75-80 km) is much weaker; winter is similar in general strengths, but again the geostrophic wind (based on months) lacks planetary wave or even annual/semi-annual influences /15/. The slope of the zero line is quite different in fall and spring, and the radar winds show much greater wind shear, especially in the latter half of February. These results are consistent with stronger latitudinal temperature gradients. Averaging intervals partially overlap. Finally at Adelaide (Figures 9,10), with some averaging interval overlap, the agreement is quite good, although the height of the radar summer maximum cannot be seen. However Adelaide contours for 1973-77, /21/, based upon a more limited data sample from Meteor and MF radars (80-100 km), indicate secular trends, and markedly poorer agreement with the geostrophic winds (1973-78) e.g. the summer 80 km radar values were near 0 ms^{-1} and not -30 ms^{-1}. Thus putting aside temporarily the possibility of ageostrophy, there is some evidence at Saskatoon and Adelaide for secular trends, so that identifying years for contours may be important.

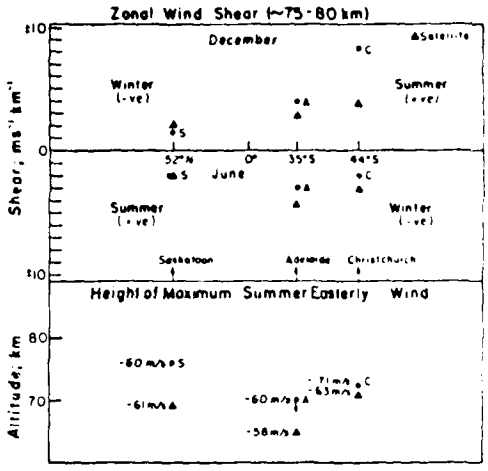

Fig. 10 Radar and geostrophic wind comparisons.

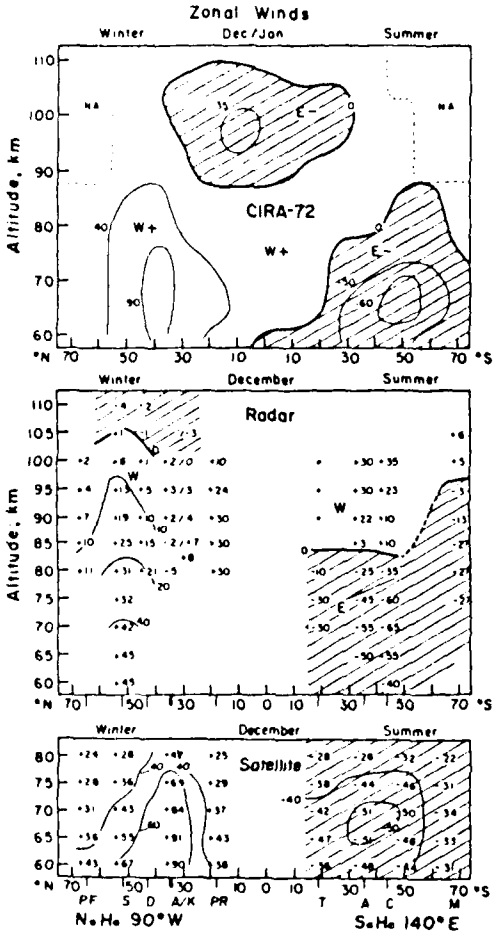

Fig. 11 Radar, CIRA-72, satellite zonal wind comparisons: December.

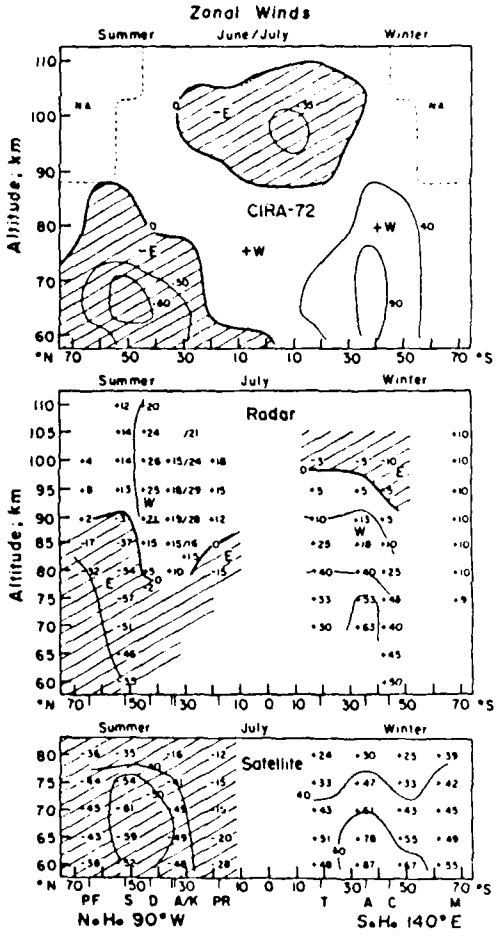

Fig. 12 Radar, CIRA-72, satellite zonal wind comparisons; July.

LATITUDINAL CROSS-SECTIONS

The comparison between CIRA-72, the radar winds and satellite geostrophic winds is well illustrated in height-latitude cross-sections (Figures 11,12); and we show here December (an early solstice month, clear of N.H. stratospheric warmings, but early summer in the S.H.) and July, for ~90°W in the N.H., and ~140°E in the S.H. However Kyoto (136°E) has also been included with N.H. data. From CIRA-72, July (June 15 - July 15) and January (December 15 - January 15) are shown. The time rates of change are quite small in mid-season, so that conclusions drawn here are usually typical of the entire solstitial seasons. Only the zero contours, and maximum of cells are shown for CIRA-72. All data are updated since 1965 /12/. The lack of hemispheric symmetry is immediately obvious from the radar winds: the winters are most alike and even then the N.H. zero line is ~5 km higher (allowing for the comparison between early winter (December) and mid-winter (July)), reflecting smaller poleward temperature gradients there. Comparing with CIRA-72, two other points emerge: the upper zero lines were not available for that model; and there is an easterly tropical cell above 87 km which is not evident at our four low latitude stations. For the summers, these stations again do not have the easterly flow above 87 km, which is shown in CIRA. The other main summer differences between the S.H. and N.H. at these longitudes, are due to the consistent westerly flow at and above 80 km revealed at Durham (43°N), Atlanta (34°N) and Kyoto (35°N), and the higher reversal heights in Oceania. Note that in the N.H. near 90°W, the systematic reduction in the height of the zero line with decreasing latitude (65-35°N) is now quite similar to that shown by CIRA-72. Over France /11,12/ the zero line varied from ~83 km (Carchy, 47°N, 1970-76) to ~87 km (Monpazier, 44°N, 1975-80) indicating some possible secular and longitudinal variations. These values and differences between the stations are confirmed by recent analysis.

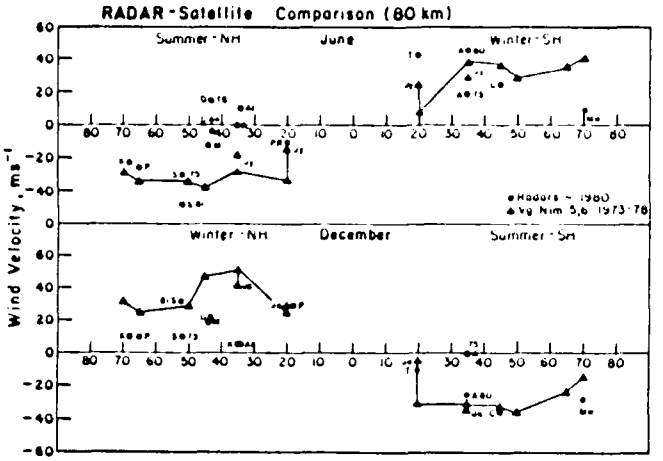

Fig. 13 Radar and geostrophic 80 km wind comparisons: other stations, K, Kiruna; M, Monpazier; PR, Puerto Rico; T, Townsville /21/.

Winds from the Antarctic summer mesosphere (Mawson, 68°S; Scott Base, 78°S; MF radars) /25, 26,15/ and for the winter (Mawson) have recently become available, and Mawson values have been added to Figures 11,12. These summer data and other S.H. MF radar data were compared elsewhere with CIRA-72 and a new S.H. model by Koshelkov based on rocket data /26,15,27/. From Figure 11, and considering Scott Base (78°S) and Poker Flat (65°N, Figure 12) also, CIRA-72 had the high latitude summer maximum and zero lines as much as 20 km too low. Koshelkov's model is in better agreement, showing the upward tilt with increasing latitude of the easterly peak and the zero line, but they are ~10 km lower in height than radar winds from 20-78°S. There are also important differences between Koshelkov's model and the radar winds in winter at medium latitudes /15/. An updated model due to Koshelkov has recently been produced and compares with the radar winds more satisfactorily.

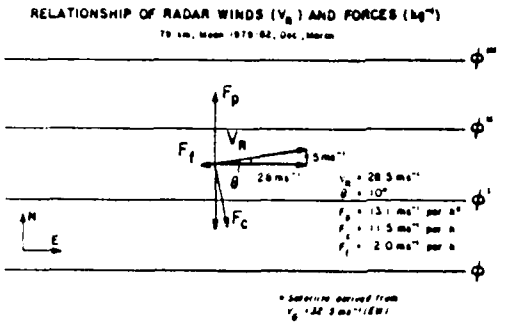

Fig. 14 Saskatoon radar and satellite wind comparisons /23/; V_R, radar wind. Forces: Fp, pressure term balancing coriolis torque on geostrophic wind (V_G); F_C, due to coriolis torque on V_R; F_f, friction component.

Now comparing with the geostrophic winds, overlap occurs at 80 km for Meteor radars, and 60-80 km for MF radars. S.H. values are quite similar for both seasons although there are some differences at Townsville (20°S), and much stronger geostrophic winds at 68°S in winter. For the N.H. there are also significant differences, e.g. in winter there is a geostrophic wind maximum near 35° which is not seen at all by the radars; and in summer the geostrophic wind is easterly at all latitudes, whereas westerly flow is seen at 3 radar stations (34-43°N) having substantial data. This comparison is summarized in Figure 13 for 80 km data, where European data have been added. In the S.H. agreement is quite good for

recent radar data apart from the 20°, 68° differences just mentioned; but an earlier more limited data sample which overlaps better in time (Adelaide -1975), does not agree well. For the N.H. most radar stations have smaller westerly values (~50%) in winter (Saskatoon showing a trend (1975-1981)), while in summer stations equatorward of 50° have much lower easterly values, which may even become westerly.

There are many possible reasons for the differences between the measured and geostrophic winds: a) There is some evidence for secular trends in the winds, so that intervals involved should always be stated. Unfortunately increasing the overlap does not always help the comparison. b) There is evidence for some longitudinal differences (above, and /2/). However, these are small and suggest that comparisons such as Figures 11/12 probably indicate real differences. c) There may be height and temperature errors or biases in the satellite data. d) The winds from 60-80 km may be significantly ageostrophic.

The last possibility has been discussed in detail recently /28/, and significant ageostrophy was found up to 80 km. Studies of mean winds, EW and NS, and gravity wave (GW) intensities and fluxes at Saskatoon /29/ and Adelaide /30/ have shown that there is significant GW momentum deposition in the region 60-90 km. At Saskatoon near 90 km in summer (Figure 1,2) this acceleration balances the coriolis torque on the NS flow (~100 ms^{-1} per day). Near 80 km the acceleration in summer is small or insignificant, while in winter quite large accelerations occur from 70-90 km (50-100 ms^{-1} per day). Recent comparisons of satellite geostrophic and radar winds, both at Saskatoon (1978-1982), have confirmed this /23/, and also shown that standing planetary waves lead to considerable ageostrophy in fall and winter. The "friction"

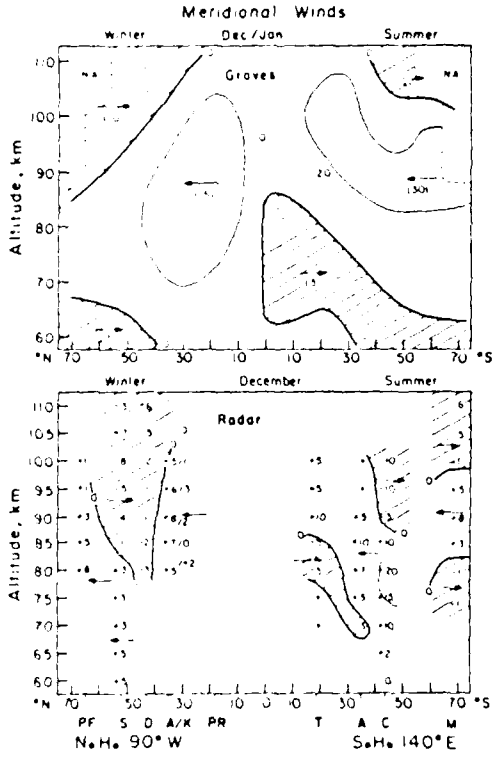

Fig. 15 Radar and Groves /13/ meridional wind comparisons: December.

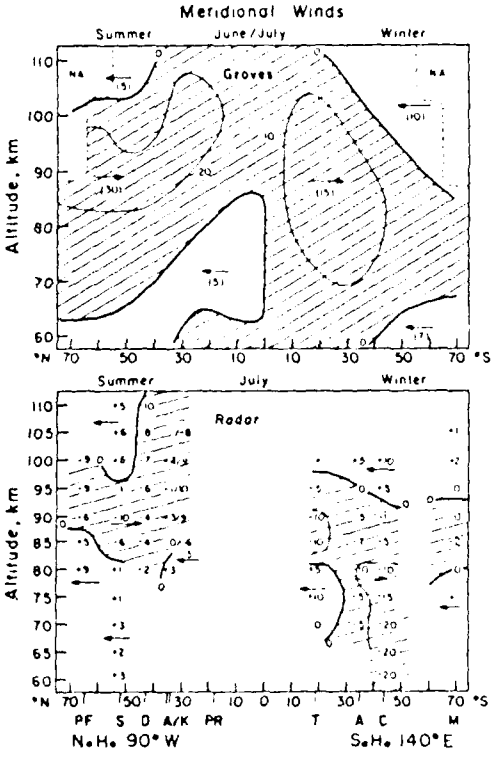

Fig. 16 Radar and Groves /13/ meridional wind comparisons: July.

term due to GW interactions effectively turns the wind vector into the low or out of the high pressure region just as in the troposphere near the ground (Fig. 14), and reduces the zonal component of the wind when compared to the geostropic value. The heights at which this ageostrophy occurs will vary with latitude, depending on GW characteristics and mean winds 0-60 km. This effect could explain some of the differences seen in Figs. 7-13, e.g. the large winter geostrophic winds at 80 km. Possible errors in the calculated geostrophic wind are evident from a perusal of an analysis by Groves /31/. Using alternate tropospheric data and methods based on rocket calibrations, Groves produced values which differed from Barnett and Corney /2/ by 5-60% from 76-80 km.

Finally we show meridional height-latitude cross-sections (Figures 15,16) as for the zonal wind, but compare here with Groves' data /13/. For July, the general agreement is quite good, apart for the fact already noted, i.e. the N.H. summer equatorward flow is weaker and

more restricted in height than Groves. December's patterns illustrate some hemispheric asymmetry, although the S.H. summer flow is again more restricted than Groves. The contours of the N.H. winter flow are quite different from Groves, although overall there is considerable poleward flow within the mesosphere.

CONCLUSION

Winds from the Global Radar Network for recent years have confirmed the basic climatological patterns shown in earlier radar studies. In addition the winds reveal some secular trends over the last decade, as well as small longitudinal variations and hemispheric asymmetries. Comparisons between radar winds and satellite-derived geostrophic winds reveal substantial similarities. However significant differences do exist near 80 km, especially during the NH winter, and in the NH summer equatorward of 50°N. In the SH differences exist near 20°, and at high latitudes (68°) especially in winter. Possible causes include errors or uncertainties in the analysis of radiance data, winter planetary wave activity and ageostrophy due to planetary and gravity waves. This latter was demonstrated by a particular study at Saskatoon.

REFERENCES

1. F.J. Schmidlin, Handbook for Middle Atmosphere Program (MAP), SCOSTEP Secretariat, University of Illinois, Urbana, Illinois, U.S.A. 61801, 16, 12 (1985).

2. J.J. Barnett and M. Corney, Handbook for Middle Atmosphere Program (MAP), SCOSTEP Secretariat, University of Illinois, Urbana, Illinois, U.S.A. 61801, 16, 47 (1985).

3. A.H. Manson, C.E. Meek and J.B. Gregory, J. Geophys. Res. 86, 9615 (1981).

4. M. Massebeuf, R. Bernard, J.L. Fellous, and M. Glass, J. Atmos. Terr. Phys. 41, 647 (1979).

5. R.A. Vincent and T.J. Stubbs, Planet. Space Sci. 25, 441 (1979).

6. M. Salby and R.G. Roper, J. Atmos. Sci. 37, 237 (1980).

7. M.J. Smith, Ph.D. thesis, University of Canterbury, Christchurch, New Zealand. (1981).

8. S.K. Avery, A.R. Riddle, and B.B. Balsley, Radio Sci. 18, 1021 (1983).

9. R.R. Clark, J. Atmos. Terr. Phys. 45, 621 (1983).

10. T. Aso and R.A. Vincent, J. Atmos. Terr. Phys. 44, 267 (1982).

11. A.H. Manson, C.E. Meek, M. Massebeuf, J.L. Fellous, W.G. Elford, R.A. Vincent, R.L. Craig, R.G. Roper, S. Avery, B.B. Balsley, G.J. Fraser, M.J. Smith, R.R. Clark, S. Kato, T. Tsuda and A. Ebel, Adv. Space Res. 5, 135 (1985).

12. A.H. Manson, C.E. Meek, M. Massebeuf, J.L. Fellous, W.G. Elford, R.A. Vincent, R.L. Craig, R.G. Roper, S. Avery, B.B. Balsley, G.J. Fraser, M.J. Smith, R.R. Clark, S. Kato, T. Tsuda and A. Ebel, Handbook for Middle Atmosphere Program (MAP), SCOSTEP Secretariat, University of Illinois, Urbana, Illinois, U.S.A. 61801, 16, 239 (1985).

13. G.V. Groves, J. Brit. Interplanet. Soc. 22, 285 (1969).

14. C.E. Meek and A.H. Manson, J. Atmos. Terr. Phys. 47, 477 (1985).

15. A.H. Manson, C.E. Meek, R.A. Vincent, and M.J. Smith, Handbook for Middle Atmosphere Program (MAP) 16, 36 (1985).

16. A.H. Manson, C.E. Meek, and J.B. Gregory, J. Geomag. & Geoelectr. 33, 613 (1981).

17. A.H. Manson and C.E. Meek, Planet. Space Sci. 32, 1087 (1984).

18. G.D. Nastrom, B.B. Balsley, and D.A. Carter, Geophys. Res. Lett. 9, [illegible]

19. A.H. Manson, C.E. Meek, and S.K. Avery. Physica Scripta (In Press)

20. A.H. Manson and C.E. Meek, Radio Sci. 20, 1441 (1985).

21. A.H. Manson, C.E. Meek, M. Massebeuf, J.L. Fellous, W.G. Elford, R.A. Vincent, R.L. Craig, R.G. Roper, S. Avery, B.B. Balsley, G.J. Fraser, M.J. Smith, R.R. Clark, S. Kato, T. Tsuda and A. Ebel, Rept. No. 4, Atmospheric Dynamics Group, Atmospheric Studies, University of Saskatchewan, Saskatoon.

AD-A190 685 PROCEEDINGS OF WORKSHOP 15 OF THE COSPAR MEETINGS HELD 2/2
IN TOULOUSE FRANCE (U) AIR FORCE GEOPHYSICS LAB
HANSCOM AFB MA K S CHAMPION 21 JAN 88 AFGL-TR-88-0016
UNCLASSIFIED F/G 4/1 NL

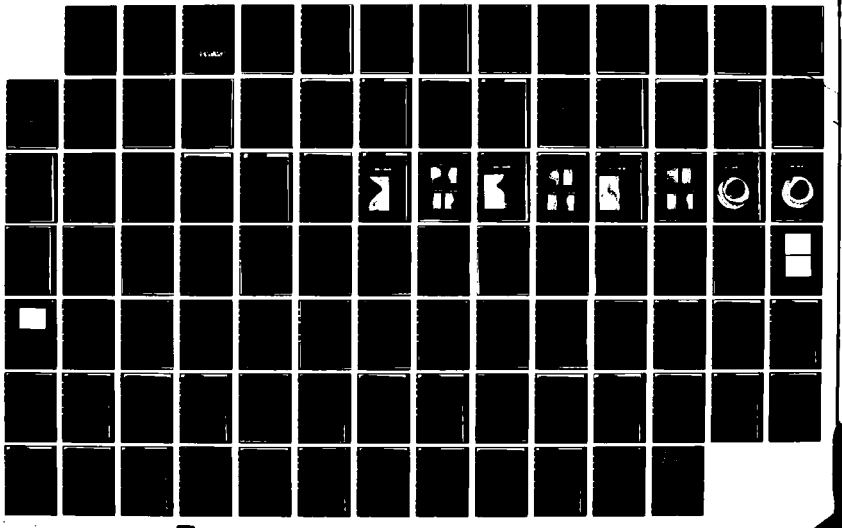

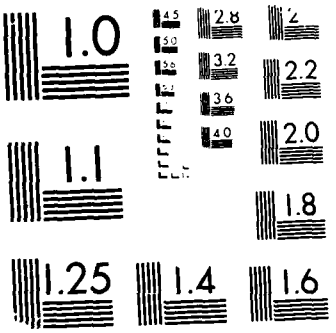

MICROCOPY RESOLUTION TEST CHART
NATIONAL BUREAU OF STANDARDS 1963-A

22. R. Schminder and D. Kurschner, Handbook for Middle Atmosphere Program (MAP), SCOSTEP Secretariat, University of Illinois, Urbana, Illinois, U.S.A. 61801, 13, 248 (1984).

23. K. Labitzke and A.H. Manson, Physica Scripta (In Press).

24. J.B. Gregory, C.E. Meek, and A.H. Manson, Weather and Climate Responses to Solar Variations, ed. B.M. McCormac, Colorado Assoc. Univ. Press 1983, p. 626.

25. G.J. Fraser, J. Atmos. Terr. Phys. 46, 1049 (1984).

26. R. Macleod and R.A. Vincent, J. Atmos. Terr. Phys. 47, 567 (1985).

27. Yu. P. Koshelkov, Handbook for Middle Atmosphere Program (MAP), SCOSTEP Secretariat, University of Illinois, Urbana, Illinois, U.S.A. 61801, 16, 15 (1985).

28. L.S. Elson, J. Atmos. Sci. 43, 409 (1986).

29. C.E. Meek, I.M. Reid, and A.H. Manson, Radio Sci. 20, 1383 (1985).

30. R.A. Vincent and I.M. Reid, J. Atmos. Sci. 40, 1321 (1983).

31. G.V. Groves, Air Force Surveys in Geophysics No. 448, AFGL-TR-85-0129 (1985).

Adv. Space Res. Vol. 7, No. 10, pp. (10)155–(10)158, 1987
Printed in Great Britain. All rights reserved.

0273-1177/87 $0.00 + .50
Copyright © 1987 COSPAR

LONG PERIOD WIND OSCILLATIONS IN THE 80–110 km ALTITUDES OBSERVED BY THE KYOTO METEOR RADAR IN 1983–1985

T. Tsuda,* S. Kato* and R. A. Vincent**

*Radio Atmospheric Science Center, Kyoto University, Kyoto, Uji 611, Japan
**Physics Department, University of Adelaide, Adelaide, South Australia 5001

ABSTRACT

During the MAP period, the Kyoto meteor radar has almost continuously monitored the wind fields in the 80–110 km altitudes. Wind oscillations with various periods ranging from 2 to 20 days are detected. The period of the quasi 2-day wave in 1983 was 2.2 days in summer months but became as short as about 2.0 days in autumn. Antisymmetry in phase profiles is detected by comparing the behavior of the quasi 2-day wave simultaneously observed at Adelaide and Kyoto.

RESULTS

Using 60 days of data, we have determined an autocorrelation function with a maximum time lag of 30 days. By shifting periods of the analyses, a moving spectrum of eastward wind oscillations with periods longer than 1 day is calculated as shown in Fig. 1. An oscillation with a period of 1.4 days is regularky recognized in summer months such as in July-September 1983, June-July 1984, and June-August 1985. The quasi 2-day wave is dominant in summer in 1983 and 1984. Its amplitude in 1985 is smaller than in the preceding two years. In 1983 and 1984, the periods of the quasi 2-day oscillation are longer than 2 days in summer and tend to become shorter than 2 days in September. Oscillations with periods of about 3 days are enhanced in August-September, 1983 and April-August, 1984, and their periods tend to increase in autumn. In 1985, an oscillation with a period of 4 days is recognized, and it seems to split into two oscillations with different periods. Longer period oscillations with periods ranging from 6 to 8 days do not seem to have regular seasonal variations.

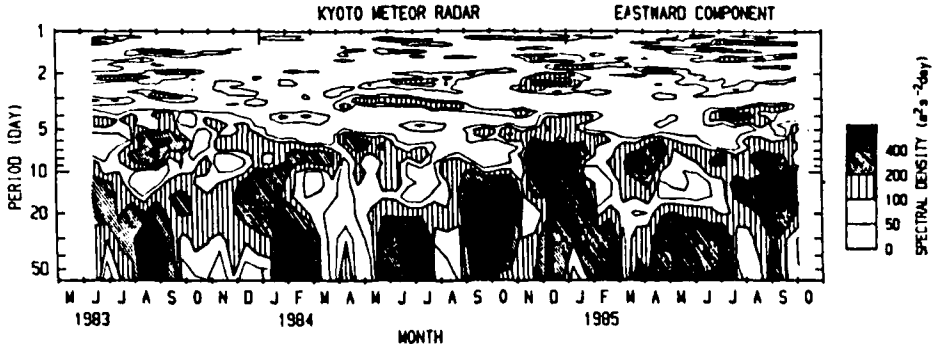

Fig. 1. A moving power spectrum of the eastward wind component observed in 1983–1985 by the Kyoto meteor radar. Each spectrum is determined by calculating an autocorrelation function with a maximum time lag of 30 days.

The quasi 2-day oscillation has been extensively studied both experimentally /1,2/, and theoretically /3,4/. The wave becomes dominant in summer months /5/, and has various periods

such as 51 hrs /3/ or 48 hrs /6/. Fig. 1 suggests that the period of the quasi 2-day wave ranges 2.1-2.5 days in summer, and becomes as small as 2 days in other seasons, although there is relatively large year-by-year variation.

Fig. 2 shows the frequency spectra determined every 15 days using 60 days of data observed in 1983. The frequency resolution of this analysis is 0.017 day^{-1}, corresponding to 1.6 hrs at around 2-day period. The wave period was 52 hrs in June-August, then rapidly changed to 47.5 hrs in September. This change in the period of the quasi 2-day oscillation might be attributed to variation of the background condition.

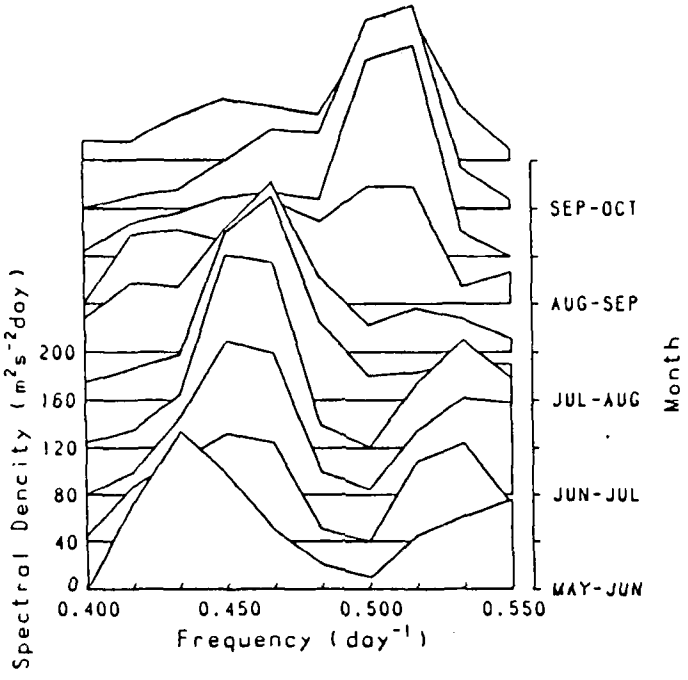

Fig. 2. Power spectra of the eastward component of the quasi 2-day wave. Each spectrum is calculated every 15 days by using 60 days of data.

The quasi 2-day oscillation has been theoretically explained by assuming a fundamental Rossby mode with a zonal wavenumber of three, and determined its period as 53 hrs (2.25 days) /3/. Another theoretical study has shown that a jet stream in the lower atmosphere can excite the quasi 2-day wave /4/. By assuming either mechanism, the wave period is affected by variation of the background atmosphere. Therefore, the observed evidence of the change of the periods in summer and autumn is not inconsistent with the models, but is interesting in clarifying the behavior of free oscillations.

Because the quasi 2-day oscillation becomes dominant in summer in each hemisphere, simultaneous observations of the wave in both hemispheres are rare. Simultaneous observations of the quasi 2-day wave at Scheffield (53°N) and Townsville (19°S) in August, 1980 have been reported /7/, although the enhancement of the wave was not detected at Adelaide (35°S). This phenomenon has been explained as leakage of the intense quasi 2-day wave excited in the northern hemisphere into the southern hemisphere /7/.

Fig. 3 shows height profiles of amplitudes and phases observed in the period of January 18-31, 1984, when large amplitudes of the quasi 2-day wave were observed at Adelaide /8/. The amplitude and phase are determined at each altitude by using a least squares fitting of sinusoidal curves with a period of 48 hrs. The amplitudes observed at Kyoto are roughly 1/4 of those at Adelaide. Although the amplitude of the zonal component detected at Adelaide is larger than the meridional one by a factor of two, there is not a large difference in amplitudes at Kyoto. Phase profiles agree well between the Adelaide and Kyoto results, although the zonal and meridional ones are out of phase and in phase, respectively, suggesting dominance of an antisymmetric mode.

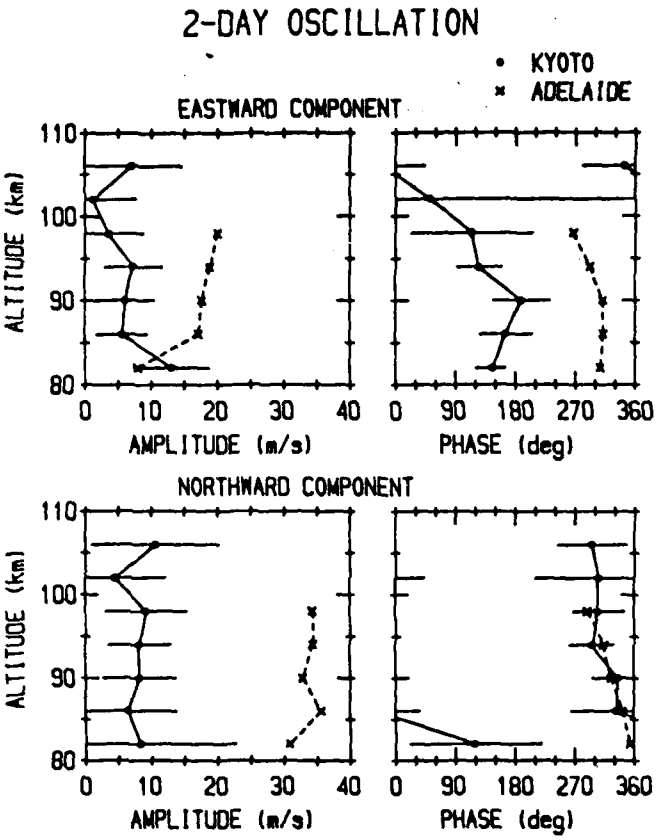

Fig. 3. Amplitude and phase profiles of an oscillation with a period of 48 hrs observed by the Kyoto meteor radar on January 18-31, 1984. Simultaneous observations at Adelaide are also shown (from /8/). Phase values of 0° and 180° correspond to 0 LT on even and odd days in January, respectively.

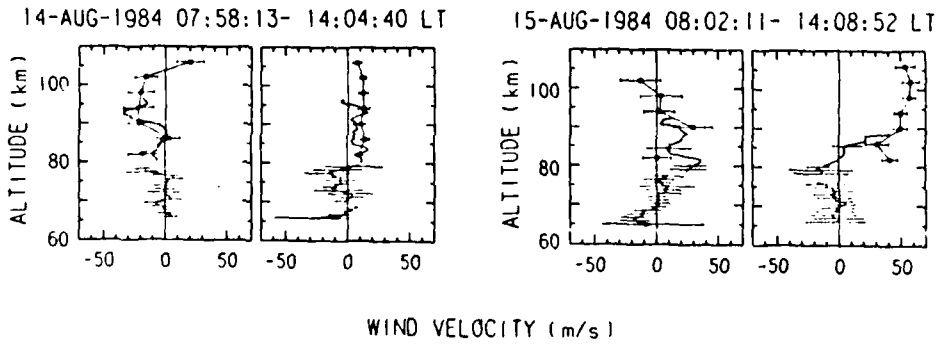

Fig. 4. Wind profiles in daytime observed on (a) August 14, 1984, and (b) August 15, 1984, respectively. Thin and thick curves correspond to the MU radar measurements using turbulent scattering and meteor echoes. Square symbols correspond to the Kyoto meteor radar observations.

Fig. 4 shows daytime mean wind profiles observed on two successive days in August, 1984 /9/. The meridional winds have opposite directions, and the zonal ones show large difference between the two days. Fig. 5 shows time variation of the zonal wind component after filtering shorter variations than 32 hrs at several altitudes observed by the Kyoto meteor radar. The quasi 2-day oscillation was dominant in the middle of August. Comparison of wind profiles in Fig. 4 is accidentally done on two periods corresponding to the minimum and maximum of the oscillation, which gives a large difference in mean wind profiles. It is suggested that the wind fields in the upper mesosphere and lower thermosphere are affected by the long period oscillations which have neither definite oscillation periods like tides nor a regular seasonal variation. Therefore, it seems inappropriate to determine the mean wind profiles using less frequent sounding of the wind fields.

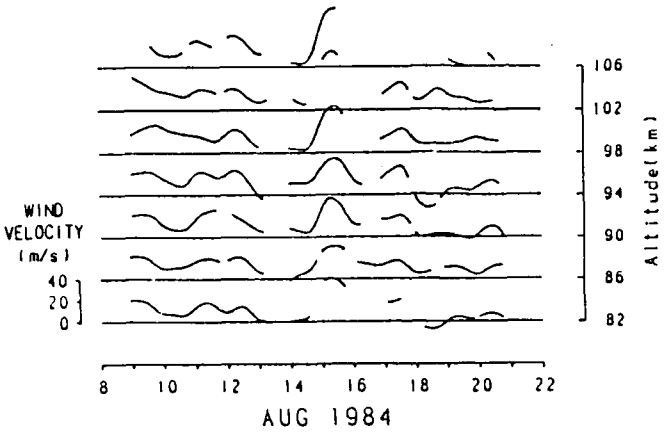

Fig. 5. Eastward wind velocities observed in August 1984 by the Kyoto meteor radar after filtering out short period components less than 32 hrs.

REFERENCES

1. Müller, H. G. and L. Nelson, A travelling quasi 2-day wave in the meteor region, J. Atmos. Terr. Phys., 40, 761-766 (1978).

2. Craig, R. L., R. A. Vincent, G. J. Fraser and M. J. Smith, The quasi 2-day wave in the southern hemisphere mesosphere, Nature, 287, 319 (1980).

3. Salby, M. L., The 2-day wave in the middle atmosphere: Observation and theory, J. Geophys. Res., 86, 9654-9660 (1981).

4. Plumb, R. A., Baroclinic instability of the summer mesoshpere: A mechanism for the quasi-two-day wave, J. Atmos. Sci., 40, 262-270 (1983).

5. Vincent, R. A., MF/HF radar measurements of the dynamics of the mesopause region -A review, J. Atmos. Terr. Phys., 46, 961-976 (1984)

6. Craig, R. L. and W. G. Elford, Observations of the 2-day wave near 90 km altitude at Adelaide (35°S), J. Atmos. Terr. Phys., 16, 344-356 (1981).

7. Craig, R. L., R. A. Vincent, S. P. Kingsley and H. G. Müller, Simultaneous observations of the quasi 2-day wave in the northern and southern hemispheres, J. Atmos. Terr. Phys., 45, 539-541 (1983).

8. Vincent, R. A., private communication (1985).

9. Tsuda, T., M. Yamamoto, T. Sato, S. Kato and S. Fukao, Comparison observations between the MU radar and the Kyoto meteor radar, Radio Sci., 20, 1241-1246 (1985).

Adv. Space Res. Vol. 7, No. 10, pp. (10)159–(10)162, 1987
Printed in Great Britain. All rights reserved.

0273-1177/87 $0.00 + .50
Copyright © 1987 COSPAR

A GLOBAL MODEL OF CIRCULATION AND TEMPERATURE FOR THE UPPER MESOSPHERE – LOWER THERMOSPHERE REGION

Yu. I. Portnyagin and T. V. Solovjeva

The U.S.S.R. State Committee for Hydrometeorology and Control of the Natural Environment, U.S.S.R.

ABSTRACT

The zonal mean model of zonal and meridional wind for the Northern and Southern Hemisphere based the analysis of meteor radar wind and partial reflection drift data for the 70-110-km height interval is constructed. The height-latitudinal cross-sections of vertical wind are calculated from data on the latitudinal structure of a meridional wind field using the continuity equation. The temperature field cross-sections from the zonal wind model using the thermal wind equation are derived.

For some three decades ground-based techniques: meteor-, partial reflection-, and, more recently MST-radars have produced a considerable body of experimental data on the atmospheric parameters (wind data especially) at 70-110-km. These data ultimately provide the basis for the development of more detailed global wind and temperature model than previous models like CIRA-72 and others.

We have tried to construct a revised version of a zonal circulation model at upper mesosphere-lower thermosphere heights using data measured at twenty seven meteor radar stations and at six station which carry out measurements by the partial reflection method. General list of references can be found in /1,2/.

The two-dimensional zonally averaged wind model includes height-latitude cross-sections of the wind field for all seasons of the year and covers practically all latitudes of the Northern and Southern Hemispheres. The method of constructing these models is described in /1/. The cross-sections are shown in Fig.1. When analysing these we can deduce that for different seasons there are characteristic global circulation structures. The description of their main features are available from /1/.

The height-latitude cross-sections of the zonal wind field permit the construction of the detailed height-latitude cross-section of temperature fields using thermal wind equation. Fig.2 present the temprerature cross-sections calculated for some months of the year.

Assuming that the meridional wind field is formed due to processes providing vertical momentum transfer, the eddy meridional wind field is proposed to be parametrized in the following way

$$u_* = -\frac{1}{\rho}\left(\frac{\partial}{\partial z} k_z \rho \frac{\partial v_a}{\partial z}\right)\left(2\Omega\cos\theta\right)^{-1} + k_t \quad , \qquad (1)$$

where u_* is the coefficient of the vertical macroturbulent momentum exchange; k_z is depend on height, latitude and time (i.e. the month of the year) and k_t is a parameter depending on height and time.

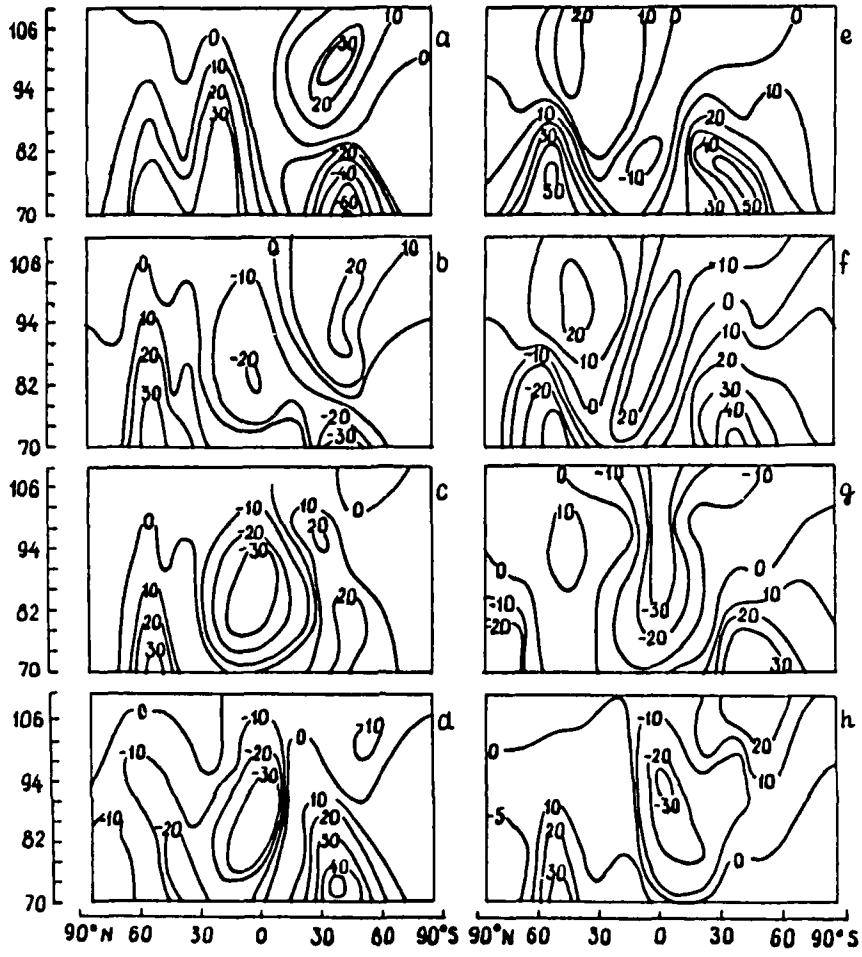

Fig. 1. The height-latitude structure of the zonal wind field (m s^{-1}). a) December, b) February, c) March, d) April, e) June, f) August, g) September, h) October (positive values are westerly wind).

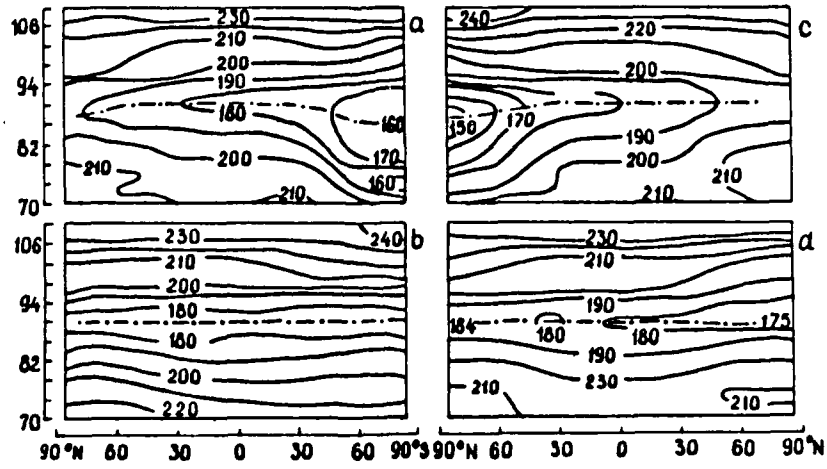

Fig. 2. The height-latitude structure of the temperature field. a) January, b) March, c) July, d) October.

When choosing the form of k_z and k_t we used the meridional wind obtained for many years by the meteor radar and partial reflection methods at the following sites of the Northern and Southern Hemispheres: Heiss Island (80.5°N), Obninsk (55°N), Saskatoon (52°N), Poker Flat (65°N), Durham (43°N), Christchurch (44°S), Atlanta (34°N), Kyoto (35°N), Adelaide (35°S), Townsville (20°S), Mogadishu (2°N) and Molodezhnaya station (67°S). k_z and k_t have maximum values at 95-100-km. k_z maximises in middle latitudes and decreases toward the poles and the equator with the k_z values twice as large in summer as winter. As far as the seasonal variations of k_z are concerned in the periods of stable circulation (winter, summer) k_z is approximately twice as large as it is in the reconstruction periods. With allowance for there estimates k_z and k_t proposed to be parametrized in the following way

$$k_z(t,z,\theta) = \begin{cases} k_m(\theta,t)\exp[-a_1(z-z_{max})^2] & \text{at } z \geq z_{max} \\ k_m(\theta,t)\exp[-a_2(z-z_{max})^2] & \text{at } z < z_{max} \end{cases} \quad (m^2 s^{-1})$$

$$k_m(\theta,t) = \begin{cases} 1/2\ k_{m_1}(t)(1-\cos 4\theta) & \text{at } 0° < \theta \leq 90°, \\ 1/2\ k_{m_2}(t)(1-\cos 4\theta) & \text{at } 90° < \theta < 180°, \end{cases} \quad (2)$$

$$k_{m_1}(t) = b_1(c_1(t-7) + d_1 + \cos(\tfrac{\pi}{3}(t-1)) \cdot 10^3 ,$$

$$k_{m_2}(t) = b_2(c_2(t-7) + d_2 + \cos(\tfrac{\pi}{3}(t-1)) \cdot 10^3 ,$$

$$k_t(z,t) = f\cos(\tfrac{\pi}{6}(t-5))\exp(-f_1(z-z_{max})^2) . \quad (m\,s^{-1})$$

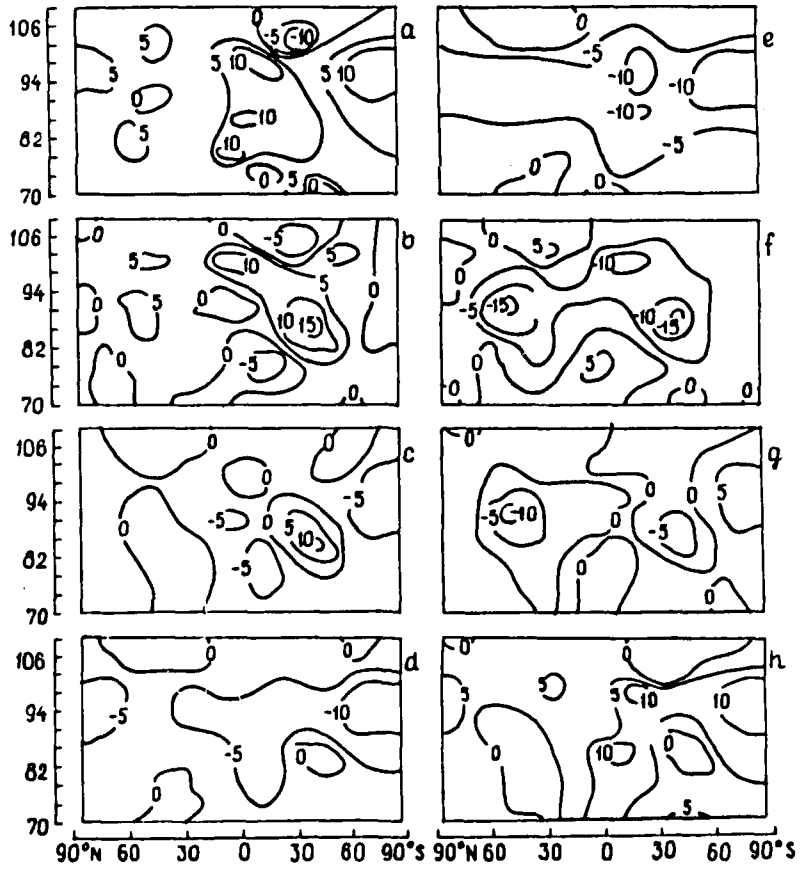

Fig. 3. The height-latitude structure of the meridional wind field (m s^{-1}). a) December, b) February, c) March, d) April, e) June, f) August, g) September, h) October (positive values are southerly wind).

Where t is the month order number (January - t=1, February - t=2 etc.); z_{max} is the height of the maximum values of k_z and k_t. Our model uses the following coefficient values: a_1 =0.2 10^{-1}, a_2 =0.01 10^{-1}, b_1 =1.1, b_2 =1.0, c_1 =-0.02, c_2 =0.03, d_1 =2.5, d_2 =2.4, f_0 =8 at $0° < \theta < 90°$, f_0 =15 at $90° < \theta < 180°$, f_1 =0.04 at $z > z_{max}$, f_1 =0.003 at $z \leq z_{max}$, z_{max}=98 km.

In equation (1) the first term on the righthandside seems to describe the contribution of large-scale inhomogeneties connected with baroclinic instability in the ageostrophic meridional wind. The second term parametrizes the contribution of smale-scale turbulence caused by destruction of internal gravity waves in the region where their saturation is observed.

Using the above parametrizations we calculated ageostrophic meridional wind fields. For the equatorial (15°N-15°S) latitude region the equation (1) is not true, therefore to estimate the meridional wind velocities in this region we used polynomial interpolation. Fig. 3 shows the height-latitude cross-section of the ageostrophic meridional wind field for some months of the year obtained by the above method.

The values of the vertical wind velocity component w_0 were estimated from the calculated results of a meridional wind using the standart numerical integration of the continuity equation. Calculated results for the vertical wind field w_0 are given in Fig. 4. As seen from the figure, in the meteor zone there are large-scale structures of ascending and descending flows which can significantly influence the temperature structure of the mesopause-lower thermosphere. The zones of ascending and descending wind, alternating in latitude, are indicative of global circulation cells in the considered height region.

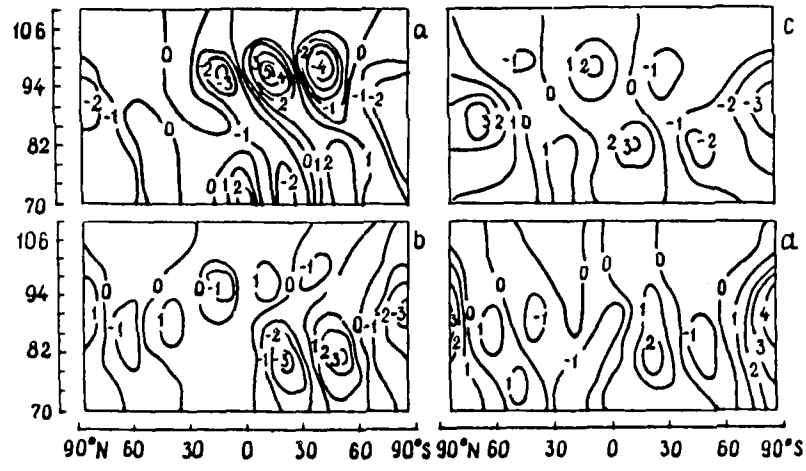

Fig. 4. The height-latitude structure of the vertical wind field (cm s^{-1}). a) January, b) March, c) July, d) October.

REFERENCES

1. Yu.I. Portnyagin, Basic features of global circulation in the mesopause-lower thermosphere region, Handbook for MAP 10, 134 (1984)

2. A.H. Manson, C.E. Meek, M. Massebeuf, J.L. Fellous, W.G. Elford, R.A. Vincent, R.L. Craig, R.G. Roper, S. Avery, B.B. Balsley, G.J. Fraser, M.J. Smith, R.R. Clark, S. Kato, N. Tsuda and A. Ebel, Wind of the upper middle atmosphere (60-110 km): a global distribution from radar systems (M.F., Meteor, VHF). Handbook for MAP 16, 239 (1985)

Adv. Space Res. Vol. 7, No. 10, pp. (10)163–(10)169, 1987
Printed in Great Britain. All rights reserved.

0273-1177/87 $0.00 + .50
Copyright © 1987 COSPAR

PLANETARY AND GRAVITY WAVES IN THE MESOSPHERE AND LOWER THERMOSPHERE

R. A. Vincent

Department of Physics, University of Adelaide, Adelaide, South Australia 5001

ABSTRACT

Planetary and gravity waves contribute significantly to the variability of atmospheric parameters in the middle atmosphere. In the mesosphere and lower thermosphere the wave fluctuations are sufficiently large to often mask the prevailing or mean state of the atmosphere. This review summarizes current knowledge about the motion, temperature and density fields associated with both large and small scale waves and stresses improved understanding that has come from recent ground based, rocket and satellite investigations.

INTRODUCTION

Rocket, ground based and theoretical studies of the mesosphere and lower thermosphere show that waves play an important role in the dynamics of the mesosphere and lower thermosphere. It is now believed that the level of gravity wave activity in particular, determines the mean state of the mesosphere. The waves manifest themselves in wind, temperature, density, pressure, ionization and airglow fluctuations in the 80 - 120 km height range and the amplitudes are so large that they can dominate at these altitudes so that the basic state can be extracted only after considerable averaging. Rockets have enabled the density and temperature structure to be measured with excellent height resolution, while long term studies of wind motions using MST, partial reflection and meteor radars and, more recently, lidar investigations of temperature and density, have enabled the temporal behaviour of the waves to be better understood.

To illustrate the spectral range of motions evident near the mesopause Fig. 1 shows a composite of power spectra of wind motions measured at widely separated locations and illustrates how wave energy is distributed as a function of frequency. The spectra show three distinct parts, viz. (i) a long period section corresponding to periods longer than 24 hr, and associated with planetary scale waves, (ii) a section between peaks associated with the semidiurnal and diurnal tides and (iii) a section at periods less than 12 hr where the spectral density decreases monotonically (except for the 8 hr tidal peak).

The purpose of this paper is to summarise the salient features of wave activity in the mesosphere and lower thermosphere, with particular emphasis on wave amplitudes and spatial scales and where possible to provide information on the seasonal and latitudinal variations in these quantities.

PLANETARY WAVES

Tropospherically forced planetary waves are confined primarily to the winter hemisphere. Satellite observations show that the waves reach their maximum amplitudes at or just above the stratopause, with maximum temperature fluctuations of the order of 6 K reached at latitudes near 60° /47/. Radar observations at Adelaide give maximum wind variations of about 25-30 ms^{-1} in mid to late winter at heights near 65-70 km. The amplitudes decay to 15 ms^{-1} above 80 km. Amplitudes may be larger in the northern hemisphere. Under favourable conditions in the northern hemisphere, planetary waves with periods between 5 and 30 days have been observed to penetrate up to heights near 110 km, producing oscillations with vertical amplitudes of between 2 and 10 km /42,43,44/. In summer, forced planetary waves are excluded from the upper atmosphere by the stratospheric easterlies but it is possible for planetary scale transient motions associated with normal modes or with baroclinic instabilities of the stratospheric jets, to be observed in the mesosphere. The narrow spectral peak located near 48 hr in the Adelaide data in Fig. 1 is a manifestation of the quasi 2-day wave, which is one of a series of travelling global scale waves which have been discovered by long-term wind measurements made by ground based radars. Spectral analyses of long data sets suggest that the transient wave energy tends to maximize in local summer /3,5/. A range of wave periods has been identified, but the most commonly reported periods

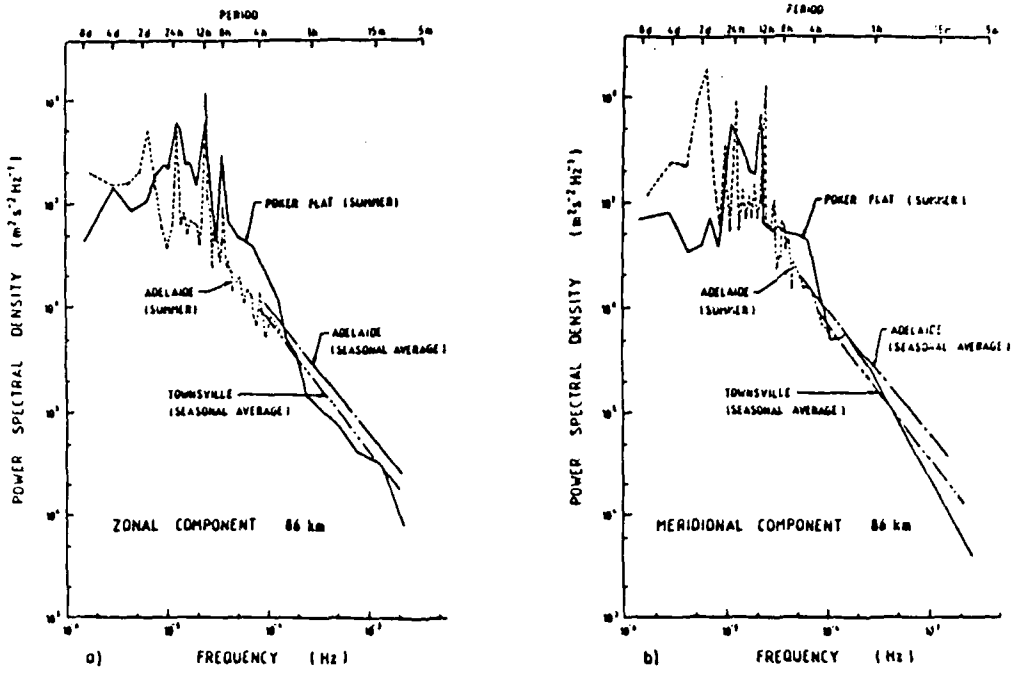

Fig. 1. Power spectra of the meridional and zonal wind components observed at Poker Flat (65° N), Adelaide (35°S, 138°E) and Townsville (19°S, 147°E). The Poker Flat data are is after Carter and Balsley /1/.

fall into three well defined intervals which are, 10 - 20 days, 4 to 7 days and 1.9 to 2.2 days. These are often referred to as the "16-day", "5-day" and "2-day" oscillations respectively, although precise determination of the periods involved is often not possible. Comparative studies made at different longitudes indicate the waves are westward travelling, with the best determinations of wavenumber being made for the 2- and 5- day waves. The inadequate length of many data sets have necessarily restricted studies of the "16-day" wave although, as continuous radar observations become available, this situation will improve. Table 1 summarizes some of the features of those waves which have been extensively reported but it should be noted that waves of other periods (e.g. 1.6 to 1.7 days) have been reported /15,16/.

TABLE 1 Characteristics of Transient Planetary Waves

Period (days)	Amplitude (ms^{-1})	Vertical Wavelength (km)	Zonal Wavenumber
10-20	5-10	> 100	1 (?)
4- 7	5-30	25 to > 100	1
1.9-2.2	10-50	50 to > 100	3

It is usually assumed that these transient oscillations are caused by Rossby-gravity normal modes generated in the lower atmosphere. These modes are evanescent in the vertical except in height regions with westward winds (easterlies) and equatorward temperature gradients when the waves can be locally propogating. Salby /19/ has recently reviewed the characteristics of normal modes.

Each mode has a well defined structure with respect to latitude and longtitude but, in practice, it has not always been possible to make a positive identification from observations in the 80 - 120 km region because of inadequate geographic coverage. However, an association has been reported between a 5-day wind oscillations in the mesosphere and a westward travelling wavenumber-one wave in the stratosphere /8/. Satellite radiance studies show evidence for both 5-day and 2-day waves with temperature amplitudes tending to maximize in the lower mesosphere /17,18/ with values of about 0.5-0.8 K.

The most extensively studied oscillation is the '2 day' wave and the seasonal and spatial behaviour is now well established. The wave is usually observed in the summer hemisphere reaching maximum amplitudes at about 90 km in July/August in the northern hemisphere /11,12/ and in January in the southern hemisphere /9/. Both radar wind

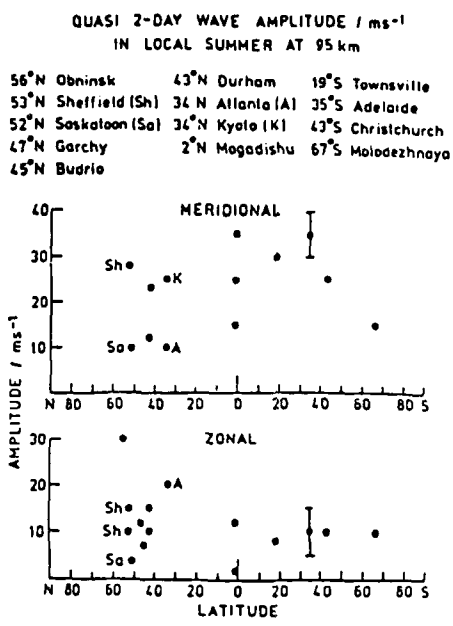

Fig. 2. Amplitudes of 2 day-wave as a function latitude, (after /5/).

measurements and satellite observations show that the wave amplitudes are maximum in the southern hemisphere /5,12/. This is illustrated in Fig. 2 which shows the mean meridional and zonal wind amplitudes plotted as a funcion of latitude; it is evident that the maximum response is in the meridional component at southern low-to-mid-latitudes. The wave amplitudes can be so large (50 ms^{-1}) that the wave appears to be non-linear /48/. A hemispheric difference in wave period has also been noted, /5/ with northern hemisphere observations giving periods near 51 hr /11,13/ while periods nearer 48 hr are reported for the southern hemisphere /9,10/.

GRAVITY WAVES

Wave Amplitudes Figure 1 shows that at a given location, the gravity wave amplitudes have about the same magnitude in both the zonal (u') and meridional (v') wind components although some anistotropy has been observed at Adelaide /49/ with v' greater than u' by about 20%. The spectra show that the energy density (proportional to $V'^2 = u'^2 + v'^2$) follows a power relationship f^{-k} as a function of frequency, f. The exponent k, lies in the range 1.5 to 2.0 /1,2/ but may change with latitude and season /20/. Averaged over the period range between 12 hr and the Vaisala-Brunt period (about 5 min) the rms amplitudes are about 15-20 ms^{-1} in each component /2/ although if the spectrum is assumed to extend out to the inertial frequency (the theoretical lowest frequency for gravity waves) then the rms amplitudes are about 25 ms^{-1}.

Vertical velocity motions are not as easy to measure as the horizontal components but measurements made over a range of latitudes with vertically pointing narrow beam radars give rms amplitudes of the order 1-2 ms^{-1} /5,20,22/. Vertical oscillations near the buoyancy frequency are particularly evident (periods ~ 5 - 15 min).

Temperature and density fluctuations induced by gravity waves have been extensively studied by rockets /23,26,27/ and recently by lidars /28/. Figure 3 shows vertical profiles of temperature and density. Amplitudes are of the order of 0.05 to 0.1 in fractional density, values which are consistent with those inferred from the gravity wave motions /2/. The figure indicates the very wide range of temperature variations which can be observed at high latitudes with the greatest wave activity occurring in winter /45/ with amplitudes as large as 30 K; at mid-latitudes the temperature fluctuations are about 10 K.

Seasonal and geographical variations in wave activity are not well known in the 80-120 km height region but what observations are available indicate an annual variation in temperature fluctuations at high latitudes (Fig. 3), with maximum amplitudes occurring in winter, and a smaller variation at mid-to-low latitudes with a semi-annual variation

[illegible] of Figure 3. The Brunt-Vaisala [illegible]
the right assumes [illegible]

occuring in the tropics /5,6,20,23,24/. These observations are in general accord with studies of wave activity in the stratosphere /25/.

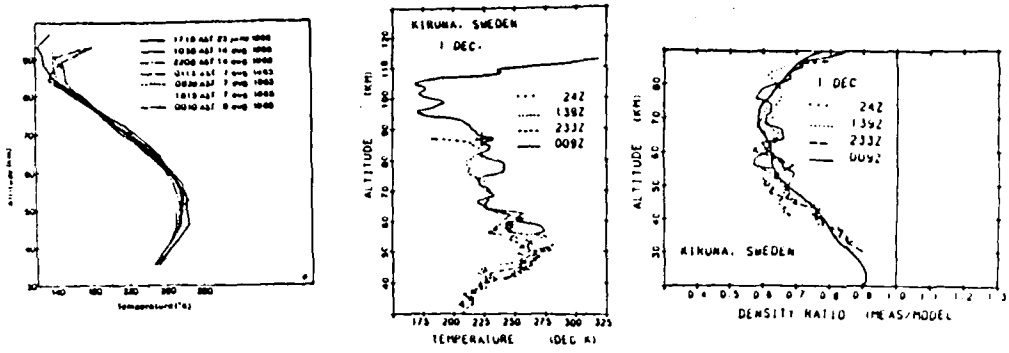

Fig. 3. Rocket measurements of temperature in Summer (a) at Barrow, Alaska (71°N) after /45/, and (b) Winter at Kiruna (68°N) after /26/. (c) Vertical profile of neutral density fluctuations /26/.

Recent radar wind measurements at a few sites are producing a better understanding of the variability of mesospheric wave activity. At Saskatoon and Adelaide, clear minima in wave intensities are found at times around the Spring and Fall reversals in zonal wind direction, as shown in Fig. 4.

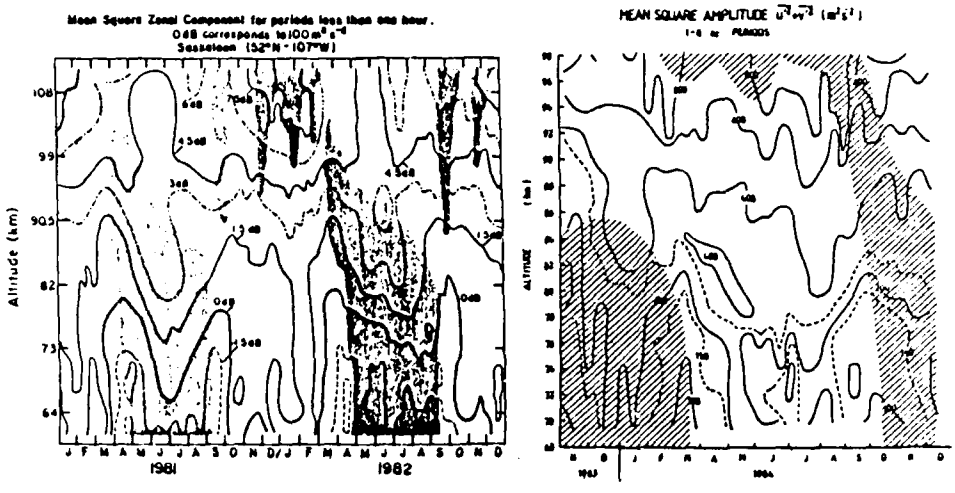

Fig. 4. Mean square zonal amplitudes of gravity waves with periods, less than 1 hr observed at Saskatoon /51/ and (b) total mean square amplitudes of gravity waves in the 1-8 hr period range measured at Adelaide /49/. The shading indicates regions of westward (easterly) winds.

It is emphasised that the amplitudes quoted above are long term averages. On a time scale of a few hours or so there can be quite significant changes in wave amplitude in the mesosphere /26,29/.

Wavelengths and Phase Velocities. The profiles shown in Fig. 3 indicate that the vertical wavelengths (λ_z) of gravity waves in the mesosphere are greater than a few km. Philbrick /27/ using rocket techniques found that the minimum vertical scale increases from about 1.5 km near 60 km to about 3 km near 100 km despite the fact that scales smaller than 0.5 km could be resolved. This increase in the minimum vertical wavelength is also ilustrated in Fig. 5a, where values scaled from rocket vapour trails and temperature probes are plotted as a function of height; the change in λ_z with height is ascribed to eddy and molecular damping effects /30/. Typical values for λ_z range from about 3 km to about 40 km in the 80 - 120 km region; mean values are about 10 to 12 km /2,4,26/.

There are relatively few direct measurements of the horizontal wavelengths (λ_h) and phase velocity (c). What information is available comes from photographs of noctilucent clouds and air-glow emissions /31-34/. Indirect estimates have also been made with radars /2,21,29,35,36/. Figure 5b is a composite of wavelength observations measured by

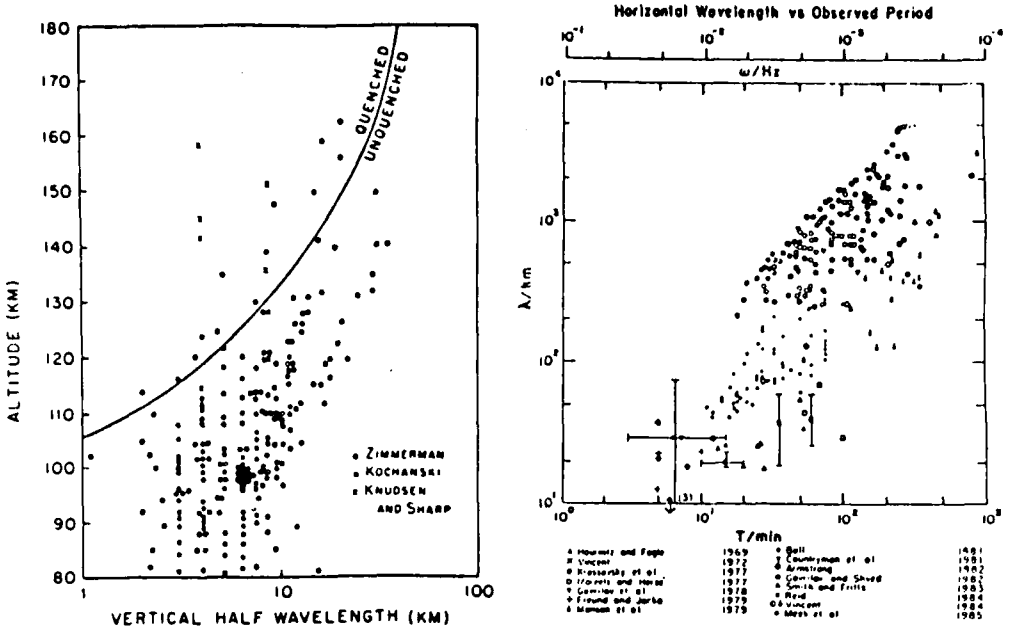

Fig. 5.(a) Vertical half wavelengths observed in small scale wind fluctuations /30/. (b) A plot of horizontal wavelength versus period 50/.

a number of techniques, summarized by Reid /5/. The diagram shows a systematic increase in the mean λ_h with increasing period. The inferred phase velocities do not show any significant change with period but typically lie within the range 10-100 ms^{-1}. These results should be treated with some caution for at least two reasons : (i) for the longer periods only indirect estimates are so far possible and, (ii) most values of λ_h and c are derived from observations of quasi-monochromatic wave motions which may not be representative of the mesospheric wave-field as a whole, which often appears to consist of a random superposition of waves.

Finally, it is important to note that it is the phase speed of the waves relative to the mean flow ($|c - \bar{u}|$), that is the important quantity rather than he velocity relative to the ground, c. Estimates of this instrinsic phase speed can be made by using the gravity wave dispersion relation, which for this purpose, can be approximated as: $\lambda_z \approx 2\pi |c - \bar{u}|/N$ where N is the Vasiala-Brunt frequency. Since λ_z typically lies in the range 5-20 km in the mesosphere, this means that $|c - \bar{u}|$ is probably in the range 15 to 60 ms^{-1}

Energy and Momentum Fluxes. It is frequently found that the gravity wave amplitudes do not grow significantly with height, which means that the wave kinetic energy density, given by $\rho_o \overline{v^2}$ decreases with increasing height /2,6,21,24,40,41/. Here ρ_o is the atmospheric density and $\overline{v^2}$ the mean-square perturbation velocity. The energy decay is of the form $\exp(-z/h_o)$ where the height scale h_o, is typically 5 to 12 km although there may be some seasonal variation /6/.

The energy-density decay with height is usually taken to indicate either that the waves are saturating (breaking) and/or that they are being externally damped by eddy and molecular processes. Evidence for wave breaking may be seen in Fig. 3b which shows temperature gradients approaching the adiabatic lapse rate. Whatever the situation, the dissipating waves contribute to the energy and momentum budgets of the upper atmosphere. Estimates of the energy dissipation rates of the order of 0.01 to 0.2Wkg^{-1} have been given /2,6,40,41/ but more knowledge is required of the energy fluxes into the mesosphere and lower thermosphere before the full contribution to the energy budget can be established. An analysis of 50-60 min period waves observed in noctilucent clouds gave fluxes ~ 7.10^{-4} Wm^{-2} /37/ and an estimate of about 10^{-2} Wm^{-2} was derived from radar measurements averaged over all seasons and wave periods /5/.

Dissipating and saturating gravity waves also contribute to the momentum budget of the mesosphere. Recent theory has stressed the role that gravity waves play in balancing the Coriolis torques induced by the mean meridional circulation; gravity waves are now believed to drive the mesospheric circulation. The theory and observational requirements are summarized in /38,39/. Radar techniques have been developed to measure

the upward flux of zonal momentum ($\overline{u'w'}$) and the few results to date show that fluxes are in the correct sense and of the right magnitude (~ 1-5 $m^2 s^{-2}$) for the wave 'drag' to act in the manner suggested by theory /29,35,39,51,52/. Observations suggest that quite short period waves (less than 1 hr) carry a significant fraction of the energy and the momentum fluxes despite the fact that, as Fig. 1. shows, it is long period waves which have the largest energy densities /2,39/. To date, there have been few reported measurements and other potentially important fluxes such as u'v' but observations at Adelaide give magnitudes of up to 50 $m^2 s^{-2}$ /49/.

DISCUSSION

Considerably more observations are required before the structure and the roles played by atmospheric waves in the 80-100 km region can be fully elucidated. Further information is needed before the modal structure of transient planetary waves can be determined and compared with theory. Similarly, more information is required about internal gravity waves and especially about the zonal components of wavelength and phase velocity and momentum fluxes /38/. At present there is an inadequate geographical coverage with most observations coming from the mid-to-high latitudes in the northern hemisphere. There is a need for a wider coverage in the southern hemisphere and especially in equatorial regions where waves may play a very important role in determining the mean state of the atmosphere.

REFERENCES

1. D.A. Carter and B. Balsley, J. Atmos. Sci. **39**, 2905, (1982)
2. R.A. Vincent, J. Atmos. Terr. Phys. **46**, 119, (1984)
3. M.I. Smith, Upper Atmos. Circulation and Wave Motion Ph.D thesis, University of Canterbury, N.Z. (1981)
4. A.H. Manson, C.E. Meek, J.B. Gregory and D.J. Chakrabarty, Planet Space. Sci. **30**, 1283, (1982)
5. R.A. Vincent. J. Atmos. Terr. Phys. **46**, 961, (1984)
6. A.H. Manson,, C.E. Meek and J.B. Gregory, J. Geophys. Res. **86**, 9615, (1981)
7. M. Massebeuf, R. Bernard, S.L. Fellous and M. Glass, J. Atmos. Terr. Phys, **43**, 535, (1981)
8. I. Horota, Y. Mackawa, S. Fukao, K. Fuykuyama, M.P. Saltzer, J.L. Fellous, T. Tsuda and S. Kato, J. Geophys. Res. **88**, 6835, (1983)
9. R.L. Graig and W.G. Elford, J. Atmos. Terr. Phys. **43**, 1051, (1981)
10. R.L. Craig, R.A. Vincent, G.J. Fraser and M.J. Smith Nature **287**, 339,(1980)
11. H.G. Muller and L. Nelson, J. Atmos. Terr. Phys. **40**, 761, (1978)
12. C.D. Rodgers and A.J. Prata, J. Geophys. Res. **86**, 9661 (1981)
13. R.L. Craig, R.A. Vincent, S.P. Kingsley and H.G. Muller, J. Atmos. Terr. Phys. **45**, 529, (1983)
14. R.R. Clark, J. Atmos. Terr. Phys. **45**, 621, (1983)
15. G. Cevolani, S.P. Kingsley and H.G. Muller. J. Atmos. Terr. Phys. **45**, 275, (1983)
16. M.L. Salby and R.G. Roper, J. Atmos. Sci. **38**, 1827, (1980)
17. C.D. Rodgers and A.J. Prata, J. Geophys. Res. **86**, 961, (1981)
18. C.D. Rodgers, J. Atmos. Sci. **33**, 710, (1976)
19. M.L. Salby, Rev. Geophys. Space Phys. **22**, 209 (1984)
20. M.E. Fezal, M. Glass, J.L. Fellous, and M. Massebeuf J. Atmos. Terr. Phys. **43**, 543, (1981)
21. I.D. Countryman, P.K. Rastogi, S.A. Bowhill and P.M. Dolas, Handbook for MAP, **2**, 301, (1981).

22. R.F. Woodman and A. Guillen, J. Atmos. Sci. 3, 493, (1974)

23. J.S. Theon, I.N. Nordberg, C.B. Katchen and J.J. Horvarth J. Atmos. Sci. 24, 428, (1967)

24. B.B. Balsley, W.L. Ecklund and D.C. Fritts, J. Atmos. Sci. 40, 2451 (1983)

25. I Hirota, Dynamics of the Middle Atmosphere, D. Reidel, Tokyo65,(1984)

26. C.R. Philbrick, K.U. Grossman, R. Hennig, G. Lange, D. Krankowsky, D. Offerman, F.J. Schmidlin, and A. von Zahn, Adv. Space Res, 2 121, (1983)

27. C.R. Philbrick, Handbook for MAP, 2, 333, (1981)

28. M.L. Chanin and A Hauchecorne, J. Geophys. Res. 86 9715, (1981).

29 R.A. Vincent and I.M. Reid, J. Atmos. Sci.,40, 1321, (1983).

30. C.O. Hines, The Upper Atmosphere in Motion Am. Geophys. Union Washington, DC, 433, (1974)

31. E.B. Armstrong, J. Atmos. Terr. Phys. 44, 325, (1982)

32. G. Moreels and H. Herse, Planet Space Sci, 25, 265, (1977)

33. B. Haurwitz and B. Fogle, Deep Sea Res. 16, 85, (1969)

34. J.T. Freund and F. Jacka, J. Atmos. Terr. Phys. 41, 25, (1979)

35. I.M. Reid, Radar Studies of Atmospheric Gravity Waves Ph.D Thesis, University of Adelaide, Australia (1984)

36. S.A. Smith and D.C. Fritts, Proc. 21st Conf. on Radar Meteorology, Edmonton, Canada, 104 (1983)

37. C.O. Hines, J. Atmos. Sci. 25, 937, (1968)

38. D.C. Fritts, M.A. Geller, B.B. Balsley, M.L. Chanin, I. Hirota, J.R. Holton, S. Kato, R.S. Lindzen, M.R. Schoeberl, R.A. Vincent and R.F. Woodman, Bulletin of the Am. Met. Spc. 149, (1984)

39. D.C. Fritts, Rev. Geophys. and Space Phys. 22, 275, (1984)

40. R.A. Vincent and T.J. Stubbs, Planet Space Sci. 25, 441, (1977)

41. C.O. Hines, J. Geophys. Res. 70, 177, (1965)

42. G.M. Brown and J.I. John, J. Atmos. Terr. Phys. 41 379, (1979)

43. D.J. Cavalieri, R.J. Deland, T.A. Plemra and R.F. Gavin, J. Atmos. Terr. Phys. 36, 561, (1974)

44. G.J. Fraser, J. Atmos. Terr. Phys. 39, 12, (1977)

45. D.F. Heath, E. Hilsenrath, A.J. Krueger, W. Nordberg, C. Prabhakara, and J.S. Theon, Developments in Atmospheric Science Elsevier, Amsterdam.

46. R.A. Vincent, J. Atmos. Terr. Phys. 34, 1881, (1972)

47. J.J. Barnett, Phil Trans. Roy. Soc. London, A296, 41, (1980)

48. R.A. Plumb, R.A. Vincent and R.L. Craig, J. Atmos. Sci, In press (1986)

49. R.A. Vincent and D.C. Fritts, J. Atmos. Sci, In press (1986)

50. I.M. Reid, J. Atmos. Terr. Phys. In press, (1986)

51. C.E. Meek, I.M. Reid and A.H. Manson, Radio Sci, 20, 1383 (1985)

52. D.C. Fritts and R.A. Vincent, J. Atmos. Sci, In press (1986)

Adv. Space Res. Vol. 7, No. 10, pp. (10)171–(10)181, 1987
Printed in Great Britain. All rights reserved.

0273-1177/87 $0.00 + .50
Copyright © 1987 COSPAR

TURBULENCE IN THE REGION 80–120 km

W. K. Hocking

Department of Physics, University of Adelaide, Adelaide, South Australia 5000

ABSTRACT

Measurements of turbulent energy dissipation rates and eddy diffusion coefficients have been collated, and mean height profiles of fundamental turbulence parameters in the region 80–120 km are presented.

INTRODUCTION

It is generally agreed that there is significant turbulence in the region 80–120 km, although there is still some debate as to its temporal and spatial morphology. The main sources of turbulence are probably gravity waves and tides, and these generate turbulence by processes such as non-linear breaking, shear instabilities, convective overturning and critical-level interactions /1,2,3,4,5/. Measurements of turbulence have often shown turbulence to appear in horizontal laminae of thicknesses of a few kilometres, interspersed with non-turbulent regions /6/, and it appears that turbulence is both spatially and temporally intermittent. Turbulence appears to occur in patches /7,88/, and /8/ have presented data to suggest that turbulence occurs between 30% and 80% of the time, with the lower percentage occurring at lower heights. Generally though, turbulence is important to an upper altitude of somewhere between 95 and 110 km (the exact limit varies with time within this range), whereupon the atmospheric viscosity becomes so large that it quickly damps any tendency for turbulence to form. This transition region is called the "turbopause".

Turbulence Parameters

Turbulence affects its environment in two main ways; it may heat the fluid in which it exists, and it causes diffusion of momentum, heat, and matter. Turbulence occurs on a wide range of scales, but in this work most discussion will be concentrated on small scale turbulence; that is, scales less than about 5 km in size, where turbulence is at least quasi-isotropic, and can truly be called three-dimensional turbulence.

Energy dissipation A general feature of three-dimensional turbulence is the energy transfer direction. Some large-scale feature such as a wind shear or a temperature gradient becomes unstable, and generates smaller scale cyclic motions. These new motions generate smaller rotational random motions, and these in turn cause others. Eventually extremely small scales are reached, at which the small scale shears are so large that molecular viscous forces become important and energy is deposited as heat into the atmosphere. The rate at which heat is deposited per unit mass will be donated by "ε" here. In fact energy is lost at all scales, although the majority of the heat loss does occur at the smallest scales. Some energy can also be lost at larger scales by the weak radiation of buoyancy waves. This process will not be parameterised here, but it is important to note that it does occur /9,10,11/.

Turbulent diffusion Diffusion occurs in both laminar and turbulent flows, but is much more rapid in the latter. In laminar flow, the rate of diffusion of momentum is represented by the viscosity ν, and the rate of transfer of heat by the thermal diffusivity κ_t. In that case, diffusion occurs due to random molecular motions. In the case of flow involving fluctuating fluid motions, the momentum and continuity equations can be written in terms of mean and fluctuating components. After suitable rearrangement, a set of equations which involve terms like $\overline{u'w'}$ occur, where u' represents the fluctuating component of the zonal wind, w' represents the fluctuating vertical component, and the overbar represents a suitable average /12/. The term $\overline{u'w'}$ represents vertical flux of horizontal momentum, and this term multiplied by the density ρ represents a so called "Reynolds's stress". In

molecular flow, the kinematic viscosity is defined by the relation $\tau = -\rho \nu.(d\bar{u}/dz)$ where τ is a drag force per unit area. In the case of flow with fluctuating motions, the Reynold's stress acts like the viscous drag, and a "turbulent coefficient of eddy viscosity" is defined through the relation

$$\rho.\overline{u'w'} = -\rho.K_m.(\frac{d\bar{u}}{dz}) \quad (1)$$

by analogy with the definition of molecular viscosity. K_m is also called the "turbulent momentum diffusion coefficient". Likewise the analog of the thermal diffusivity, κ_t, is the turbulent heat diffusion coefficient, K_t. The rate of diffusion of minor (inert) constituents is also controlled by K_t.

One must be careful, however, not to carry the analogy with molecular processes too far. As an example, if a cloud of gas is released in air, and expands by molecular diffusion, then the mean square radius of this cloud expands according to a law of the type $r^2 = 2\nu t$, where t represents time. However, this is not true for turbulent diffusion, for in that case the cloud expands according to a law of the type $r^2 \alpha t^3$. This occurs because as the cloud expands, large scale eddies become important in the diffusion process /13/.

The ratio of the molecular viscosity to the thermal diffusivity, ν/κ_t, is called the Prandtl number, and for air is about 0.7. Similarly, a "turbulent Prandtl number", $P_r = K_m/K_t$ is defined for turbulent processes, and often it is assumed that the value of this turbulent Prandtl number is also 0.7, although this is not always justified. For example, /9/ has made rocket measurements which suggest that P_r may have a numerical value of 2 or 3. Recently, physical reasons have been advanced to explain why P_r might be quite large when considered over long time scales /94/. Often, K_t and K_m are treated as a similar parameter, usually denoted by K, despite the fact that $P_r \neq 1$, and given the accuracy with which these parameters have been measured in the mesosphere, this has not been entirely unreasonable. Recently demands for greater accuracy in the measurements of K_t and K_m have arisen, and the need to consider these parameters as distinct parameters may be more important in the future.

There is an assymmetry in the rate of diffusion as a function of the direction being considered. The vertical diffusion coefficient, which parameterizes the vertical diffusion rate, is often denoted by K_{zz} to distinguish it from the horizontal diffusion coefficients, K_{xx} and K_{yy}. In most of this paper, the effects of turbulence at scales less than about 5 km (small scale) will be examined. At such scales, the rate of diffusion is approximately independent of direction; the rates of diffusion in the vertical and horizontal are at least similar to within a factor of 2 or 3. The eddy diffusion coefficients obtained at these scales are also appropriate for calculation of vertical diffusion rates at larger scales, since buoyancy effects limit the vertical extent of eddies, and most of the energy of turbulence occurs in eddies with vertical scales less than about 5 km. Horizontal diffusion rates, however, can become quite large at larger scales. Some very preliminary estimates of horizontal diffusion coefficients have been made by /14/. As mentioned earlier, in this work it is primarily the vertical and small scale diffusion coefficients which are of interest.

There is one more analogy with molecular processes of note. For the molecular case, the viscosity and thermal diffusivity are proportional to the product of the molecular mean free path and the mean molecular speed. It is usual to also regard K_m and K_t as a product of a typical scale and typical velocity, and for approximate calculations it is common to write

$$K_{m,t} \sim L_B . v_L \quad (2)$$

where L_B is a "typical" scale, and v_L is the eddy velocity associated with this scale. More will be said of these "typical" scales later.

Finally, although equation (1) represents perhaps the best formal definition of K, other less formal formulae are often used in practice. For example, equations like (2) are often applied in experimental situations, whilst in numerical modelling "K" is often a term introduced to simply close the equations (e.g. /95/). Some of the various estimates of K have been compared by /46/.

Kolmogoroff Theory

Many of the measurements of K and ε presented in this paper were deduced under the assumption that the turbulence being observed obeyed the classical Kolmogoroff theory of inertial-range turbulence /15,16/. Many authors who used this theory commented on the possible inappropriateness of it to the lower thermosphere, but due to lack of alternative theories were forced to use it.

Indeed, it would be surprising if the Kolmogoroff theory did rigorously apply in the lower thermosphere. For example, the upper part of the region generally has a very stable temperature profile, something like that of the stratosphere, so buoyancy forces could well

be important in producing anisotropic turbulence. However, high resolution measurements in the stratosphere /17/ have shown that in any turbulent layer, there is some part of the spatial spectum which obeys the $k^{-5}/^3$ spectrum predicted by Kolmogoroff, and the smallest and largest scales which obey this relation also agree nicely with theory.

A more serious difficulty for the thermospheric case is the separation of the smallest and largest scales, or, equivalently, the value of the Reynold's number. For Kolmogoroff's theory to apply, it is necessary that the Reynold's number be very large /18/. The Reynold's number for the atmosphere is defined as

$$Re = \frac{L_B v_L}{\nu} = \frac{K}{\nu}, \qquad (3)$$

in analogy with flow in pipes, where L_B is a typical "outer scale", and v_L is the velocity associated with scale L_B. In the troposphere, $\nu \sim 10^{-6}$ m^2 s^{-1}, $L_B \sim$ 100m - 1 km and $v_L \sim$ 1-10ms^{-1}. Hence Re $\sim 10^7 - 10^9$, which is satisfactorily large. However, in the lower thermosphere $\nu \sim 1$ m^2 s^{-1}, (e.g. Fig 3a) whilst L_B and v_L are similar to the tropospheric values. Hence Re can be less than 100, and this may not be large enough to maintain an inertial subrange.

Nevertheless, the little experimental data available suggests that the turbulence at least tries to tend to an $k^{-5}/^3$ structure /19,20/, at least in conditions of weak to moderate wind shear. For stronger wind shears, other theories (e.g. /21/) have occasionally been invoked.

The region 80-120 km is a difficult region to study. It is too low for insitu satellite measurements and too high for balloons. Measurements of ε and K must be made by somewhat indirect means, and are therefore difficult. Given the apparent tendency for the atmosphere to at least try and approach an "inertial" spectrum, it will be assumed in this article that the Kolmogoroff theory may be approximately applied. This may mean some systematic errors in some of the profiles presented, but certainly the profiles should be accurate to at worst a factor of 3. It is freely admitted that the Kolmogoroff theory may not be an exact description of thermospheric turbulence.

RELATIONS BETWEEN K, ε AND THE SCALES OF TURBULENCE

The inertial range theory of Kolmogoroff applies between two scales, L_B and ℓ_0. The first (larger) is called the outer scale of turbulence, the second the inner scale. Within this range, viscosity has negligible effect. However, at scales less than ℓ_0, energy dissipation due to viscous forces becomes important. The so-called "Kolmogoroff microscale", η, is a scale well within this range of viscous dissipation, and is defined by

$$\eta = (\nu^3/\varepsilon)^{1/4}. \qquad (4)$$

It can be shown that $\ell_0 = 7.2\eta$ /22/. It can also be shown that the outer scale is a function of ε, and is given by /11/

$$L_B = c_1 \varepsilon^{1/2} \omega_B^{-3/2}. \qquad (5)$$

Here ω_B is the Brunt-Vaisala angular frequency, and /11/ has suggested that $c_1 = 2\pi/0.62$. Plots of L_B and ℓ_0 as a function of altitude have been presented by /23/. Finally within a turbulent region K and ε can be shown to be related by the expression

$$K = c_2 \varepsilon/\omega_B^2 \qquad (6)$$

and various authors have suggested values for c_2. While /11/ suggested that $c_2 = 0.8$, /24/ suggested $c_2 = 0.33$, and /25/ took $c_2 = 0.6$. It appears that c_2 lies between 0.2 and 1.0. Both equations (5) and (6) only apply in conditions of static stability, where $\omega_B > 0$.

The three equations (4), (5) and (6) together with the expression $\ell_0 = 7.2\eta$ form the main relation to be used in this article. However, it is also useful to note that

$$L_B/\eta = (R_e)^{3/4}, \qquad (7)$$

where R_e is the Reynold's number (see (2)). Thus the separation of the inner and outer scales is a very simple function of R_e.

THE TURBOPAUSE

The molecular kinematic viscosity ν increases exponentially with the increasing height in the atmosphere, and at some height it becomes greater than the eddy viscosity K. The height at which $K = \nu$ (or equivalently, the Reynold's number Re = 1) is the turbopause. When this occurs, it may be seen from equation (7) that $L_B = \eta$. Hence near the turbopause, there can be no inertial range of turbulence whatsoever. The scales at which turbulence generation

could occur are comparable to those at which viscous forces are important, and any mechanism which attempts to induce turbulence is very quickly damped. The height of the turbopause varies because ε varies. At the turbopause $\nu = K$, so that $\varepsilon \sim \nu \omega_B^2$. Larger values of ε allow larger ν values, pushing the turbopause height up.

The turbopause was first observed experimentally with rocket vapour trail measurements. The trails appeared turbulent up to the turbopause, and then quite suddenly became laminar above that height. The reason for the rapid change lies largely in the exponential increase in ν with height. When a vapour trail forms, it first diffuses by molecular processes, until a time $t_\eta \sim (\frac{\nu}{\varepsilon})^{1/2}$ after release. Then the trail begins to appear turbulent. The kinematic viscosity increases exponentially with height, and near the turbopause, this transition time may typically increase from less than a minute to greater than 2 minutes in less than about 5 km. Thus the trail appears laminar for considerable time at the higher heights. This, coupled with higher damping which turbulence experiences due to the larger viscosity, results in the appearance of a rapid transition to laminar flow in the vapour trails. Careful observation has shown that there can be evidence of weak turbulence up to altitudes as high as ~ 130 km /26/. Nevertheless, the turbopause does truly represent a level above which turbulence plays only a minor role.

The turbopause shows a large degree of fluctuation in height, both in day to day variation and seasonal variation, and /27/ has collated a large set of measurements of this height, largely acquired with rocket measurements. There is large scatter, and no clear trend as a function of season is apparent. However,/27/ did find a negative correlation between the turbopause height and the temperature at 120 km altitude. Because of this large scatter, and the lack of any clear seasonal trend, this parameter will not be discussed any more extensively in this article.

METHODS OF DETERMINATION OF ε AND K

Determination of ε and K values can be broadly classified into two types:-

i) measurements of small scale motions ($\lesssim$ 5 km) by direct observation, and

ii) large scale studies of the balance of heat and inert chemical species in the atmosphere.

DIRECT DETERMINATION OF ε.

Most direct measurements of ε in the height range 80-120 km have been made either by rocket measurements or radar, with one or two measurements by airglow techniques.

Rocket Techniques

Most measurements of ε via rocket techniques have involved release of chemo-luminescent compounds from a rocket, and then watching these evolve with time. These have either taken the form of explosions which produced luminescent clouds, or 'slow burns' which released the reactive components slowly as the rocket progressed, resulting in a long trail of luminescence. High resolution photographs of these clouds or trails were then recorded for several minutes after the release. The mean drift of the cloud gave the wind velocity, and the growth of the cloud gave information concerning the turbulence. Generally, the trails grew first in a laminar way, with the trail "radius" r (see shortly for more concerning the definition r) increasing approximately in the manner

$$(r-r_0)^2 = 2\nu t, \tag{8}$$

t=0 being the time at which molecular diffusion begins and r_0 the radius at time t=0. Then, after a characteristic time $\tau_\eta \sim (\frac{\nu}{\varepsilon})^{1/2}$, turbulence sets in, and the trail expands more rapidly. Theory suggests that the relation

$$r^2 = \beta \varepsilon t^3 \tag{9}$$

should be obeyed /13/, at least over distances r which are less that L_B. The constant β is known from theory, so one method by which ε can be obtained is by examining the expansion of the trail according to equation (9) and thus finding ε. Notice that it is not possible to define a "diffusion coefficient" at scales less than L_B, because a law of the type (8) does not apply. At scales beyond L_B, $(r-r_0)^2$ is again proportional to t, and a vertical diffusion coefficient can indeed be defined.

There are problems with this method. One such problem occurs in defining zero time; the trails and clouds expand initially by non-diffusive mechanisms, such as heat gradients and explosive motions /28/. Problems also exist in defining the trail "radius". The most rigorous definition of r would be to use the trail autocorrelation half width, but this was often difficult to find and was not always used.

Rather than use equation (9), /26/ examined the trail expansion to find the time τ_η when the trail expansion changed from molecular to turbulent diffusion, and used equations (8) and (9) to determine when the cloud was in each state. They then found ε via the relation $\varepsilon = \nu \tau_\eta^{-2}$. Nevertheless there are uncertainties in taking this as an equality.

Rather than using either of these methods, /19/ used a more precise formulation similar to equation (1) which required detailed knowledge of all three components of velocity and their spatial gradients. It is not clear whether adequate accuracy of these velocity components was actually attained.

By measuring both winds by cloud releases and temperature profiles by grenade experiments, /8/ were able to calculate the Richardson number as a function of altitude. Tropospheric observations of relations between Richardson number, wind speed, and turbulence intensity were applied to estimate the mean square eddy velocity, $\langle w^2 \rangle$. Then use was made of the relation

$$\varepsilon = \frac{1}{3.4} \langle w^2 \rangle \omega_B \qquad (10)$$

to estimate ε. Later /29/ suggested that the relation should more appropriately be

$$\varepsilon = 0.4 \langle w^2 \rangle \omega_B \qquad (11)$$

and all the values of /8/ have been corrected to suit equation (11) in this text. /65/ used theoretical relations between viscosity and the minimum vertical wavelength of gravity waves /19/ to help extract turbulence parameters, and another method used involved calculations of structure functions from high resolution winds /81/. More recently /96/ have made high resolution measurements of electron density to infer turbulent energy dissipation rates.

It has at times been claimed that rocket measurements of turbulence are unreliable, because the rocket itself could induce the turbulence /82/. This does not appear to be the case, since rocket results show good agreement with remote sensing measurements such as radar observations, which do not suffer from this possibility.

Radar Techniques

The main two radar techniques involve (i) observations of meteor trails and (ii) observations of radar fading times. The former method was originally implemented by /30/, and involves firstly measurement of velocities transverse to the meteor trail alignment, and thence formation of the structure function

$$D_{tt}^2 = \langle | v_t(\underline{x}) - v_t (\underline{x} + \underline{r}) |^2 \rangle, \qquad (12)$$

v_t being the velocity perpendicular to $\underline{r}$.

According to theory,

$$D_{tt}^2 = \frac{4}{3} C_v^2 \varepsilon^{2/3} r^{2/3} \qquad (13)$$

in the inertial range, and recent measurements give $C_v^2 = 2.0$ /31/. However, /30/ assumed

$$D_{tt}^2 = 4.82 \varepsilon^{2/3} r^{2/3}. \qquad (14)$$

For this paper, values presented by /30/ have been corrected to satisfy the former formula. /32/ also applied this method and ε values obtained from there have been similarly adjusted. More recently /33/ have also applied a similar meteor method.

When a backscatter radar with a narrow beam is used, it is possible to measure the mean square fluctuating velocity of the scatterers by utilizing the spectral-width of the received signal. Both /34,35/ and /36,37/ have applied this technique, and have used a formula similar to equation (11) to obtain ε. It is important to remove other contaminating effects such as "beam-broadening" when applying this method, and these authors did this. However, /36,37/ used a very wide polar diagram, and as pointed out by /34,35/, this can lead to contamination from larger scale horizontal fluctuating motions (e.g. gravity waves), particularly in conditions of weak turbulence. Thus the values recorded by /36,37/ are at best upper limits on ε, and must be treated with caution. In this paper, the results of /34,35,36,37/ have been adjusted so that equation (11) is obeyed.

Another way by which energy dissipation rates can be obtained is to examine the decay of gravity wave energy with height and this has been done by /36,37,38,39/.

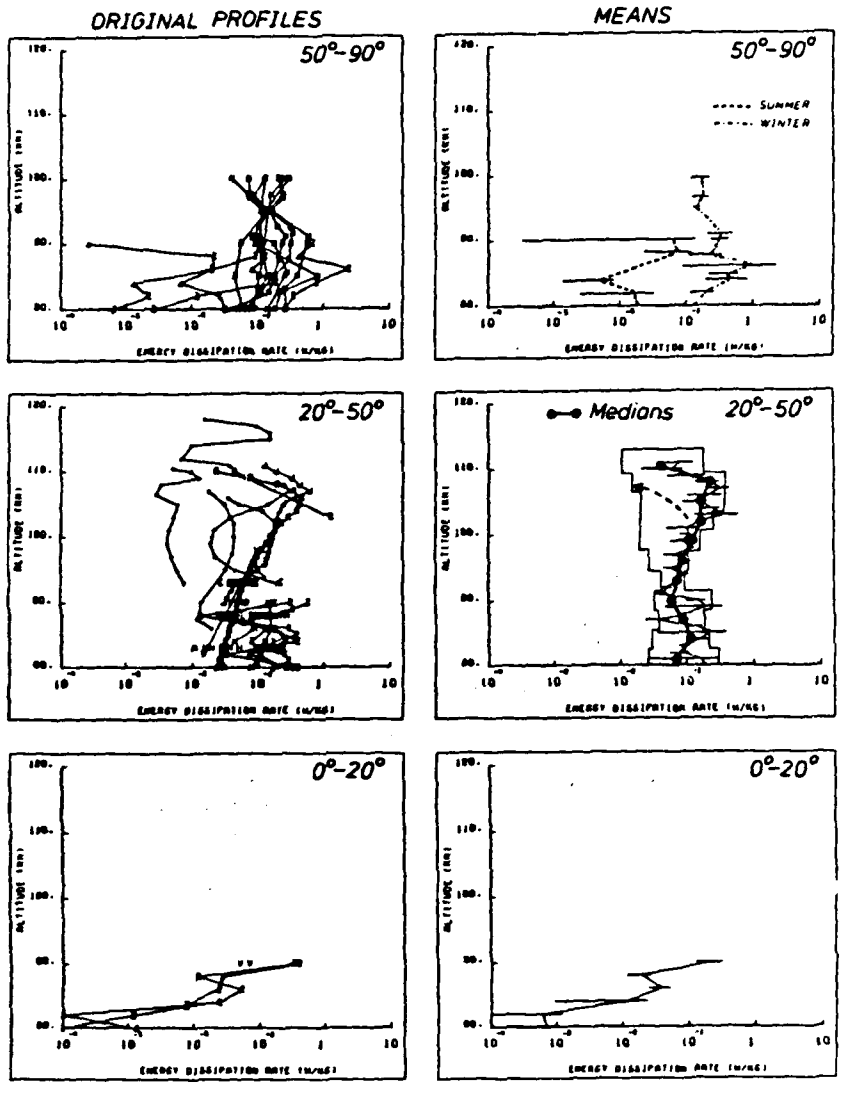

Fig.1. Energy dissipation rates for latitude bands 0-20°, 20-50° and 50-90°. On the left are shown all profiles as extracted from the relevant references, and on the right are the means (($\pm \sigma/\sqrt{n}$ and the medians (heavier lines). Symbols used: Z is used for all profiles involving Zimmerman /8,19,28,40,60,61,62,63,64,65,66,50,67/, M for profiles involving Manson /36,37/, H for Hocking /35/, R for Roper /30,68/, J for Justus /69,70,71,72/, + for Lloyd et al /73/ and Rees et al /26/, V for profiles involving Vincent, /38,39,44/ B for Blamont /6,74,75/ and C for McAvaney /32/.

TYPICAL ENERGY DISSIPATION RATES

All techniques discussed above have some form of possible errors, be they resolution problems, contamination by gravity waves or uncertainty as to the values of certain constants. Nevertheless, most methods are moderately sound in principle, and all results obtained by such methods are shown in Figure 1, together with plots of the mean and medians (where possible) for the latitude bands 0°-20°, 21°-50° and 51°-90°. The means were taken at 1 km intervals, whilst medians refer to 3 km bands. The horizontal lines represent ± one standard deviation for the mean. Originally, the data were also divided into three seasons; summer, winter and equinox. At 21°-50°, ε appeared to be largely independent of season, and below 20° ,there were insufficient data to consider each season separately. Thus the three seasons for these latitude belts have been merged. If there was any trend for 21°-50°, it was that summer values were greater than winter which were greater than equinox at 85-90 km,

but the total variation was less than a factor of 3. This is a different seasonal trend from that found by /30/, and it is felt that there is too little data to place any emphasis on it. It is possible that the seasonal trend found by /30/ was unique to that year of observation. Using a very similar technique,/32/ found no seasonal trend.

Notice that medians have also been plotted for the band 21°-50°, since there were sufficient data to do this. The mean may not be the best way to describe these data, as one large value of ε can seriously affect the mean. The straight edges surrounding the medians represent the lines below which 16% and 84% of the data lie, respectively (i.e. 66%-67% of the data lay within the outlined region). Notice that at times ε values as large as 1-2W kg^{-1} have been observed, but generally ε is of the order of 0.1Wkg. Above ~ 95 km the means and medians agree fairly well, but below this height there are some discrepancies. The median is probably a better measure of typical ε at these heights.

In the 51°-90° region, all the data were due to /8/ for two stations at 60°N and 70°N, and /36,37/. The two extreme left profiles in Figure 1 are those due to /8/ for summer. In the extreme left profile, these values get very low in value, although it should be noted that below 80 km (at 75 - 80 km), the values recorded by /8/ rose somewhat to values of the order of .01 Wkg^{-1}. Hence all that can be said is that the typical values at 80 km are ~ .005 - .02 Wkg^{-1} in summer.

The values due to /36,37/ for summer were $\geq$ 0.1 Wkg^{-1}. If the values due to /8/ are taken as a reference, then it appears that the values from /36,37/ may be contaminated by horizontal gravity wave motion as discussed by /34,35/. Thus they have been ignored in forming the summer means. However, during winter, turbulence is much stronger (according to /8/) so that values due to /36,37/ are therefore probably more reliable, and have been included. It appears that there are larger seasonal fluctuations at high latitudes.

It should also be noted that the 'means' above ~ 100 km are almost certainly an overestimate. Much of the time this region is above the turbopause, and so is laminar, but only ε values corresponding to turbulent conditions have been included in these means. Thus the profile above ~ 100 km only represents occasions when the turbopause is high.

Figure 2 shows the median values of ε for all data collectively, together with 16th and 84th percentiles. The broken arrows on Figure 1 (20°-50°) and Figure 2 are meant to indicate that often the turbopause exists at heights as low as 95-100 km, and often ε profiles actually follow the broken lines rather than continue up to ~ 115 km. The diagonal line in Figure 2 represents the line $\varepsilon = \nu\omega_B^2$. If ε lies to the left of this curve, it means that turbulence cannot develop (or at best can develop only weakly) as this means that the molecular diffusion coefficient is greater than the turbulent diffusion coefficient (see equation (6)).

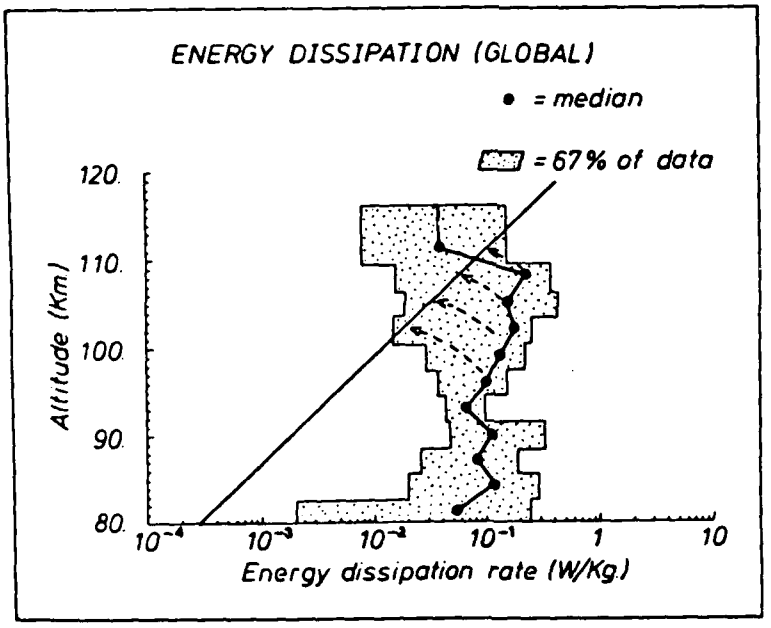

Fig 2. Median profiles for all data. The dotted region represents the region between 16th and 84th percentile. The dashed lines at the top emphasize that often a turbopause exists lower down, and the diagonal line represents $\varepsilon = \nu\omega_B$.

DETERMINATIONS OF K

Whilst a few attempts have been made to determine K from experimental observations, they have not been frequent. /9/ tried to obtain K_R and K_t separately from detailed measurements of wind velocity, and from observing the oscillation amplitude of eddies. Another attempt to determine K directly was tried by /40/ who used rocket measurements of temperature to solve the equation

$$K_t = -\overline{w'\theta'} \Big/ \frac{d\bar{\theta}}{dz}, \qquad (15)$$

θ being potential temperature and w' the vertical fluctuating velocity. Additionally /38/ have looked at gravity wave decay with height, although this method has large inaccuracies due to uncertainties in determining "typical" vertical wavelengths for gravity waves. /41/ also made rocket estimates of K, and /42/ used studies of the transport of water vapour to give estimates of K.

More recently, /43/ has proposed a formula which relates the vertical diffusion coefficient to the mean square fluctuating velocities of gravity waves. This formula has arisen from his work on non-linearity in saturating gravity waves, and takes the form

$$K = \sum_m \frac{\overline{w^2}(m)}{2H\, k\omega_B} \qquad (16)$$

where $\overline{w^2}(m)$ is the mean square fluctuating vertical velocity of gravity waves with vertical wavenumber m, H is the scale height, and ω_B is the Brunt-Vaisala frequency. The parameter k is a "typical" horizontal wavenumber for waves of vertical wavenumber m. Preliminary estimates of K using variations of this formula have been made by /44,45/. It should be noted that the formula does require the existence of a saturated gravity wave spectrum. The gravity wave approach for estimation of K has been compared to the eddy diffusion approach in a recent review by /46/.

Some early estimates of K made by observing the rate of expansion of clouds of vapour release have not been included in the data used in this paper. These are those data which *were calculated under the mistaken belief that turbulent diffusion should give a rate of* expansion as a function of time like that described in equation (8). As has already been noted, a cloud spreading under turbulent processes will follow an expansion as a function of time described by equation (9), and by assuming an expansion like the molecular case, an over-estimation of K will result.

Direct measurements of K do not represent the major means by which K has been determined. More commonly, estimates of K have been made from global temperature and density profile considerations. It was noted /14/ that the temperature gradient at 85-110km is not as steep as it should be if only molecular diffusion acted, and so /14/ concluded that turbulence must be acting to transfer the heat down from the regions where photodissociation (and therefore heating) takes place to the lower regions where CO_2 radiation can occur. Working from this premise they were then able to obtain approximate estimates of the expected eddy diffusion coefficient. In a somewhat similar vein, /48/ noted that observed ratios of the concentration of O_2 to that of O at 120km were higher than might be expected. They postulated that eddy diffusion could mix the O down from 120 km to ~ 90 km, where the mean free path is less, and so allow greater O_2 concentrations in the 90-120 km region. These authors also made estimates of K.

These last two techniques form the basis of many subsequent estimates of K. Successive authors have included temporal variations /49,50/, and have looked at latitudinal and seasonal variations /51,52,92/. It was also pointed out /50/ that some of the earlier papers had assumed that turbulence existed above the turbopause and therefore were in error.

An interesting question arises from this work on energy and oxygen balance. Turbulence produces both heating and diffusion, and it is not at all obvious which process dominates. The rate of diffusion of heat depends on both the turbulent diffusion coefficient K and the vertical temperature gradient, the latter being caused initially by solar heating. Both /52/ and /54/ pointed out that the rates of diffusion and heating are very similar. The question arises as to which is most effective - is diffusion more effective, so that turbulence actually diffuses heat across the heat gradients formed by solar effects faster than it causes heating itself (and thus cooling the mesophere), or is it more efficient at depositing heat, thus heating the mesophere? It turns out that the answer to this question lies in the value of the constant c_2 in equation (6).

The reason for the dependence on c_2 can be seen by examining the Richardson number R_i. This is given by

$$R_i = \omega_B^2 / \langle \left[\frac{d\bar{u}}{dz} \right]^2 \rangle = \omega_B^2 / \left[\varepsilon / K_m \right], \qquad (17)$$

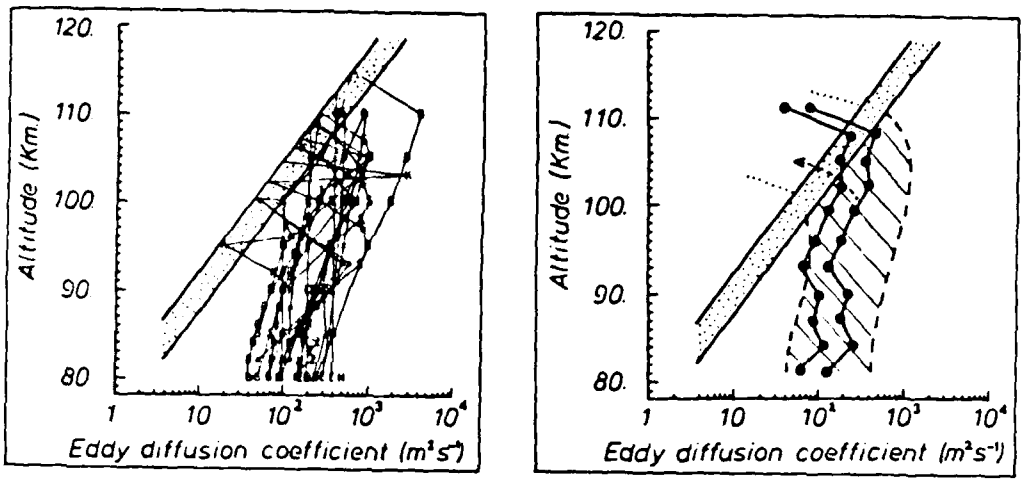

Fig 3a Collective of all eddy diffusion coefficient profiles from all relevant references. No distinction has been made concerning latitude and season. The dotted region represents K = ν, ν being molecular viscosity. Symbols used are: K for Keneshea et al /67/ and Kenesha and Zimmerman /50/, J for Johnson and Wilkins /47/, C for papers involving Colgrove /48,76,/ O for Johnson and Gottlieb /52/, S for Shimazaki /49/, H for Hesstvedt /51/, W for Wofsy and McElroy /77/, T for Teitelbaum and Blamont /41/, E for Ebel /14/ , * for Chandra /25/, Z for Zimmerman and Keneshea /40/, + for Gibbins et al /42/, B for Blum and Schuchardt /78,92/, S for Justus /9/.

Fig 3b Envelope of profiles from Fig 3a, together with ε/ω_B^2 and $0.5\ \varepsilon/\omega_B^2$ profiles deduced from Fig 2.

since $\varepsilon = K_m \left[\frac{d\bar{u}}{dz}\right]^2$ /9/. Here $d\bar{u}/dz$ is the vertical shear in the mean wind. Thus $K_m = c_2\ \varepsilon/\omega_B^2$, where $c_2 = \bar{R}_i$ is the mean Richardson number of all turbulent patches. /53/ showed that the rate of transfer of heat through the mesosphere was $F = nH\rho\omega_B^2 K$, (where n = 7/2, H = scale height, ρ = density), whilst the rate of loss of heat over one scale height was $P = \left(\bar{R}_i\right)^{-1} H\rho\omega_B^2 K$. Thus $P/F = (\bar{R}_i n)^{-1}$. Clearly heating dominates if $\bar{R}_i \lesssim 0.28$, and diffusion if $\bar{R}_i \gtrsim 0.28$. /53/ claimed that for turbulence to occur, R_i must be less than 0.25 so heating should dominate, whilst /54/ claimed that whilst R_i must be less than 0.25 to initiate turbulence, turbulence may then persist for values of R_i as high as 1.0. Thus /54/ claimed $\bar{R}_i$ is nearer 1.0. The estimates suggested earlier (equation (6)) would imply diffusion dominates. Recently /25/ has presented a more rigorous treatment of estimation of eddy diffusivities to bring into account c_2, and assumed $c_2 = 0.6$, and /55/ have concluded that the answer to the question *of whether turbulence* heats or cools the atmosphere depends on the height gradient of K, and claimed that turbulence heats below about 105 km and cools above.

One problem with these theoretical estimates of K is that they do not consider the effects of vertical winds. For example, atomic oxygen from 120 km could be brought down to 90 km by vertical winds at one location, and lifted back up by vertical winds at another. The possibility of such "cells" of circulation has not be included in any of these analyses. Thus, in principle, all prior estimates are upper limits of K.

The relation (6) offers a means of converting the ε profile of figures 1 and 2 to K profiles, but a possible problem arises because the lower thermosphere is not always turbulent. This being so, it may be that whilst the relation (6) *controls diffusion across* a turbulent patch, it may not control diffusion across the whole region 80–120 km. Rather, the rate of diffusion might depend partly on the temporal and spatial frequency of occurrence of turbulent patches in a manner similar to that proposed by /56/ and /57/ for the stratosphere. This is a point which needs further examination in the future, but for the present the relation (6) will be utilized.

In Figure 3a all the relevant K profiles due to all the mentioned authors have been presented. These include both theoretical and experimental ones. The approximate molecular viscosity has also been marked, and turbulent viscosities have been stopped when they encounter this region. In Figure 3b, the shaded region represents broadly the range of values in Fig 3a. The solid lines represent K values deduced by applying equation (6) to

the medians of Figure 2. The Brunt-Vaisala periods were taken from /56/. The profile to the right assumes $K = \varepsilon/\omega_B^2$, and that to the left assumes $K = 0.5\varepsilon/\omega_B^2$. Considering all the potential uncertainties in measurement of both K and ε, the agreement between the two data sets is good, and the results suggest a value for α_2 of about 1.0.

SEASONAL AND LATITUDINAL VARIATIONS

Measurements of the ratio of the densities of O_2 to O at 120 km have been used to estimate K as a function of season /59,92/. Both publications show similar profiles and in particular both find a maximum in K in summer at mid to high latitudes. On the other hand, /14/ obtained a maximum in K during winter at ~30-40° latitude. Thus although attempts have been made to obtain seasonal and latitudinal variations, these are at too early a stage to be included in this review.

SCALES OF TURBULENCE

Based on the profiles derived earlier, it is possible to estimate ℓ_1 and L_B at these altitudes. At 80 km, ℓ_0 ~ 10-20m, whilst at 90 km, ℓ_0 ~ 20-40 m. The outer scale L_B is generally between 400 and 2000m at all altitudes. Between these scales, turbulence should be largely isotropic - at larger scales strong anisotropy may set in. These ranges are also consistent with experimental observations of ℓ_0 /20/. More detailed height profiles of L_B and ℓ_0 have been presented by /23/.

CONCLUSION

Curves of ε, and K vs. height have been presented. One point that clearly emerged is that there is a scarcity of experimental data, and more effort in this section is strongly urged, so that a clear global and seasonal picture of turbulence variation can be built up.

REFERENCES

1. R.S. Lindzen, J. Geophys. Res., 86, 9707-9714, (1981)
2. H. Teitelbaum, and C. Sidi, J. Atmos. Terr. Phys., 38, 413-421, (1976)
3. C. Sidi, and H. Teitelbaum, J. Atmos. Terr. Phys., 40, 529-540, (1978)
4. R.R. Hodges, J. Geophys. Res., 72, 3455-3458, (1967)
5. W.L. Jones, and D.D. Houghton, J. Atmos. Sci., 28, 604-608, (1971)
6. J.E. Blamont and J. Barat in Aurora and Airglow, edited by B.M. McCormac, 156-159, Reinhold Pub. Co. (1964)
7. B.G. Anadarao, R Raghavarao, and J.N. Desai, J. Atmos. Terr. Phys, 40, 157-163, (1978)
8. S.P. Zimmerman, and E.A. Murphy in Proc. NATO Advanced Study Institute,Spatind,Norway, April 12-22, eds. B. Grandal and J.A. Hostet, Reidel Publ. Co. (1977)
9. C.G. Justus, J. Geophys. Res., 72, 1035-1039, (1967)
10. J. Weinstock, J. Atmos. Sci., 35, 1022-1027, (1978)
11. J. Weinstock, J. Atmos. Sci., 35, 634-649, (1978)
12. J.T. Houghton, The Physics of Atmospheres, Cambridge University (1977)
13. G.K. Batchelor, J. Roy. Meteorol. Soc., 76, 133-146, (1950)
14. A. Ebel, J Atmos. Terr. Phys., 42, 617-628,(1980)
15. A.N. Kolmogoroff, Doklady Akad. Nauk USSR, 32,16, (1941) (German Translation in "Sammelband zur Statistischen Theorie der Turbulens", Akademi-Verlag, Berlin (1958))
16. V. Tatarski, Wave Propogation in a Turbulent Medium (translated from Russian by Silverman), McGraw-Hill, N.Y., (1961)
17. J. Barat, J. Atmos. Sci., 39, 2553-2564 (1982)
18. G.K. Batchelor, The Theory of Homogeneous Turbulence, Cambridge University Press (1953)
19. S.P. Zimmerman, C.A. Trowbridge, and I.L. Kofsky, Space Res., XI, 907-914, (1971)
20. H.G. Booker, and R. Cohen, J. Geophys. Res., 61, 707-733, (1956)
21. C.M. Tchen, Phys. Rev.,93, 4-14, (1954)
22. R.J. Hill, and S.F. Clifford, J. Opt. Soc. Am., 68, 892-899, (1978)
23. W.K. Hocking, Radio Sci., 20, 1403-1422, (1985)
24. D.K. Lilly, D.E. Waco, and S.I. Aldefang, J. Appl. Meterol., 13, 488-493, (1974)
25. S. Chandra, Planet. Space Sci.,28, 585-593, (1980)
26. D. Rees, R.G. Roper, K. Lloyd and C.H. Low, Phil. Trans. Roy.,Soc., (Lond), A 271, 631-666, (1972)
27. A.D. Danilov, Adv. Space Res.,4, 67-78, (1984)
28. S.P. Zimmerman, J. Geophys. Res., 73, 463-454, (1968)
29. J. Weinstock, J. Atmos. Sci.,38, 880-883, (1981)
30. W.G. Elford, and R.G. Roper, Space Res.,VIII., 42-54, (1967)
31. J.C. Kaimal, J.C. Wyngaard, Y. Izumi, and O.R. Cote, Q.J. Roy Meteorol. Soc., 98, 563-589, (1972)
32. B.J. McAvaney, Small Scale Wind Structure in the Upper Atmosphere, Ph.D Thesis, University of Adelaide, (1970)
33. J.L. Fellous, and M.E. Frezal, MAP Handbook, Vol.2, 323-332, (1981) Scostep Secretariat University of Illinois, U.S.A.
34. W.K. Hocking, J. Atmos. Terr. Phys., 45, 89-102 (1983)

35. W.K. Hocking, J. Atmos. Terr. Phys., 45, 103-114, (1983)
36. A.H. Manson, and C.E. Meek, J. Atmos. Terr. Phys., 42, 103-113, (1980)
37. A.H. Manson, C.E. Meek, and J.B. Gregory, J. Atmos. Terr. Phys., 43, 35-44, (1981)
38. R.A. Vincent, and T.J. Stubbs, Planet. Space Sci.,25, 442-455, (1977)
39. R.A. Vincent, and S.M. Ball, J. Geophys. Res., 86, 9159-9169, (1981)
40. S.P. Zimmerman, and T.J. Keneshea, MAP Handbook, Vol.2, 311-322, (1981) Scostep Secretariat, University of Illinois, U.S.A.
41. H. Teitelbaum, and J. E. Blamont, Planet. Space Sci., 25, 723-734, (1977)
42. O.T. Gibbins, P.R. Schwartz, D.L. Thacker, and R.M. Bevilacqua, Geophys. Res. Lett., 9, 131-134, (1982)
43. J. Weinstock, Geophys. Res. Letts., 9, 863, (1982)
44. R.A. Vincent, J. Atmos. Terr. Phys., 46, 119-128, (1984)
45. C.E. Meek, I.M. Reid, and A.H. Manson, Radio Sci., 20, 1383, (1985)
46. A. Ebel, J. Atmos. Terr. Phys., 46, 727, (1984)
47. F.S. Johnson, and E.M. Wilkins, J. Geophys. Res., 70, 1281-1284, (1965)
48. F.D. Colegrove, W.B. Hanson, and F.S. Johnson, J. Geophys. Res., 70, 4931-4941, (1965)
49. T. Shimazaki, J. Atmos. Terr. Phys., 33, 1383-1401, (1971)
50. T.J. Keneshea, and S.P. Zimmerman, J. Atmos. Sci., 27, 831-849, (1970)
51. E. Hesstvedt, Geofys. Publik., 27, 1-35, (1968)
52. F.S. Johnson, and B. Gottlieb, Planet. Space Sci., 18, 1707-1718, (1970)
53. D.M. Hunten, J. Geophys. Res., 79, 2533-2534, (1974)
54. F.S. Johnson, J. Atmos. Sci., 32, 1658-1662. (1975)
55. B.F. Gordiets, Yu. N. Kulikov, M.N. Markov, and M. Ya Marov, J. Geophys. Res., 87, 4504-4514, (1982)
56. E.M. Dewan, Science, 211, 1041-1042, (1981)
57. R.F. Woodman and P.K. Rastogi, Geophys. Res. Letts., 11, 243-246, (1984)
58. E.D. Gossard, and W.H. Hooke, Waves in the Atmosphere, Elsevier Scientific Publ. Co., Amsterdam, (1975)
59. S.S. Korolev, and A.G. Kolenik, Geomag. Aeron., 19, 47-50, (1979)
60. S.P. Zimmerman, Space Res. VI., 425-437, (1966)
61. S.P. Zimmerman, J. Geophys. Res., 71, 2439-2444, (1966)
62. S.P. Zimmerman, J. Geophys. Res., 78, 3927-3938, (1973)
63. S.P. Zimmerman, and K.S.W. Champion (1963), J. Geophys. Res., 68, 3049-3056, (1963)
64. S.P. Zimmerman, G.P. Pereira, E.A. Murphy, and J. Theon, Space Res., XIII, 209-215 (1973)
65. S.P. Zimmerman, and N.N. Rosenberg, Space Res., XIII, 623-628, (1972)
66. S.P. Zimmerman, and C.A. Trowbridge, Space Res., XVIII, 203-208, (1973)
67. T.J. Keneshea, S.P. Zimmerman, and C.R. Philbrick,Planet. Space Sci.,27, 385-401 (1979)
68. R.G. Roper, J. Geophys. Res., 71, 4427-4428, (1966)
69. C.G. Justus, J. Geophys. Res., 72, 1933-1940, (1967)
70. C.G. Justus, J. Geophys. Res., 73, 455-458, (1968)
71. C.G. Justus, J. Atmos. Sci., 26, 1137-1141, (1969)
72. C.G. Justus, J. Geophys. Res., 71, 3767-3773, (1966)
73. K.G. Lloyd, C.H. Low, B.J. McAvaney, D. Rees, and R.G. Roper, Planet. Space Sci., 20, 761-769, (1971)
74. J.E. Blamont, and C. de Jager, Ann. Geophys., 17, 134-143, (1961)
75. J. Blamont, Planet Space Sci., 10, 89-101, (1963)
76. F.D. Colegrove, F.S. Johnson, and W.B. Hanson, J. Geophys. Res., 71, 2227-2236,(1966)
77. S.C. Wofsy, and M.B. McElroy, J. Geophys. Res., 78, 2619-2624, (1973)
78. P. Blum, K.G.H. Schuchardt, and U. vonZahn, J. Atmos. Terr. Phys.,40,1131-1135, (1978)
79. J.S. Greenhow, and E.L. Neufeld, J. Geophys. Res., 64, 2129-2153, (1959)
80. W.W. Kellogg, Space Science Rev., 3, 275-316, (1964)
81. A.J. Kochanski, J. Geophys. Res., 69, 3651-3662, (1964)
82. D. Layzer, and J.F. Bedinger, Planet. Space Sci., 17, 1891-1911, (1969)
83. S.T. Massie, J. Geophys. Res., 85, 2155-2164, (1980)
84. T.M. Noel, J. Geophys. Res., 68, 2862-2863, (1963)
85. R.G. Roper, Turbulence in the Lower Thermosphere, in The Upper Atmosphere and Magnetosphere Studies in Geophysics, 129, 117. National Research Council U.S.A.(1977)
86. N.W. Rosenberg, D. Golmb, S.P. Zimmerman, W.K. Vickery, and J.S. Theon, Space Res. XIII, 435-439, (1973)
87. J. Rottger, P.K. Rastogi, and R.F. Woodman, Geophys. Res. Lett., 6, 617-620, (1979)
88. H. Teitelbaum, Space. Res., VI, 425-437, (1966)
89. E. Battaner, and A. Molina, J. Geophys. Res., 85, 6803-6810, (1980)
90. J.S. Greehow, J. Geophys Res., 64, 2208-2209, (1959)
91. C.O. Hines, Canadian J. Phys., 38, 1441-1481, (1960)
92. P.W. Blum, and K.G.A. Schuchardt, J. Atmos. Terr. Phys., 40, 1137-1142, (1978)
93. V. Von Zahn, and T. Herwig, Proc. NATO Advanced Study Institute, Spatind, Norway, April 12-22, eds. B. Grandal, and J.A. Holtet, Reidel Publ. Co., (1977)
94. D.C. Fritts, and T.J. Dunkerton, J. Atmos Sci., 42, 549-556, (1985)
95. R.R. Garcia, and S. Solomon, J. Geophys Res., 90, 3850-3868, (1985)
96. E.V. Thrane, O. Andreassen, T. Blix, B. Grandal, A. Brekke, C.R. Philbrick, F.J. Schmidlin, H.V. Widdel, U. von Zahn and F.J. Lubken, J. Atmos. Terr. Phys., 47, 243-956, (1985)

Section 3

Thermosphere Models and Data

Adv. Space Res. Vol. 7, No. 10, pp. (10)185–(10)197, 1987
Printed in Great Britain. All rights reserved.

0273-1177/87 $0.00 + .50
Copyright © 1987 COSPAR

A THEORETICAL THERMOSPHERE MODEL FOR CIRA

D. Rees and T. J. Fuller-Rowell

Department of Physics and Astronomy, University College London, Gower Street, London WC1E 6BT, U.K.

ABSTRACT

Theoretical and semi-empirical descriptions of the solar and geomagnetic driving forces affecting the terrestrial mesosphere and thermosphere have been used to generate a series of representative numerical models of the thermosphere, covering a wide range of solar and geomagnetic activity levels, for all seasons. These numerical models are compared with observations, and with the most recent experimental and semi-empirical models of the thermosphere. The theoretical models thus give a direct record of the magnitude of the major driving forces which affect the thermosphere as a function of solar and geomagnetic activity parameters. These resulting models can thus be used to evaluate, in a self-consistent way, the covariance of thermospheric structure and dynamics, and evaluate the behaviour of regions which have not been widely explored by ground-based or spacecraft techniques, such as the lower thermospheric regions.

INTRODUCTION

Theoretical three dimensional and time-dependent global models of the earth's thermosphere solve numerically the primitive equations of energy and momentum as applied to the thermosphere, with appropriate boundary conditions /1-3/. Global simulations of the structure and dynamics of the thermosphere require realistic values of the energetic input from the UV and EUV components of solar radiation /4/ and of the heating efficiency /5/. A realistic description of the global thermosphere also requires the inclusion of the highly variable energy and momentum inputs from the solar wind via the earth's magnetosphere /6-8/. Model simulations have been tested by comparison with the wind, temperature and neutral composition data sets from spacecraft such as Dynamics Explorer /9-12/, from ground based facilities such as the incoherent scatter radars /13/, and from ground-based optical instruments such as Fabry-Perot interferometers located at several high latitude stations /14,15/. It has also been possible to compare theoretical predictions with empirical models such as the MSIS 83 model /16/.

Comparisons with data and with empirical models show that the major diurnal, latitudinal and seasonal variations of the middle and low latitude thermosphere, in wind velocity, temperature and density of the major species, can be successfully represented in theoretical models for a wide range of solar and geomagnetic activity levels /1,9,11-15/.

The thermospheric response resulting from intense energy and momentum sources associated with geomagnetic forcing can be simulated by the inclusion of a polar convection electric field, and by the self-consistent enhancement of the polar ionosphere and the polar energy input resulting from magnetospheric precipitation /9,11-16,17-20/. The wind, temperature and composition structures of the thermosphere resulting from these simulations are in agreement with both large scale and local observations of the thermosphere, even during its highly time-dependent response to major geomagnetic disturbances /14,15/. In this paper, the seasonal and latitudinal structural variations of the thermosphere will be described at the December and June solstices for geomagnetically quiet ($K_p \sim 1$), average conditions ($K_p \sim 2$) and moderately disturbed geomagnetic ($K_p \sim 4^+$) conditions. Solar EUV input appropriate to average solar maximum conditions (F10.7 cm = 165) will be used.

The polar energy and momentum sources resulting from magnetospheric forcing are complex and are still not well described in the form required by global three dimensional and time-dependent models. During disturbed periods, the local heating rates and momentum transfer rates from magnetospheric sources can be two orders of magnitude greater than those due to the low latitude solar UV and EUV heating, and an order of magnitude greater

in quiet periods. The structure and dynamics of the polar thermosphere is thus strongly modified by the signatures of magnetospheric processes, even during relatively quiet geomagnetic periods. The MSIS 83 empirical model includes longitudinal and UT variations /16/ in thermospheric structure, even during quiet geomagnetic periods, which can be attributed to the signatures of magnetospheric energy and momentum forcing. Theoretical models provide an excellent means of understanding the causes of these signatures. However, since the magnetospheric convection electric field depends on the structure and time-dependence of the IMF /12,15,21/, a-priori modelling of the thermosphere depends on, at best, real-time observations of magnetospheric electric fields and precipitation.

THEORETICAL MODELLING OF THE THERMOSPHERE

The UCL-3D thermospheric model simulates the time-dependent structure of the vector wind, temperature, density and composition of the neutral atmosphere, by numerically solving the non-linear equations of momentum, energy and continuity /1/, and a time-dependent mean mass equation /2/. The global atmosphere is divided into a series of elements in geographic latitude, longitude and pressure. Each grid point rotates with the earth to define a non inertial frame of reference in a spherical polar coordinate system. The latitude resolution is 2 degrees, the longitude 18 degrees, and each longitude slice sweeps through all local times with a 1 min time step. In the vertical direction the atmosphere is divided into 15 levels in log pressure, each layer equivalent to one scale height thickness, from a lower boundary of 1 Pascal at 80km altitude.

The top pressure level varies in altitude with changes in the temperature profile from around 300km during extremely quiet periods at low solar activity to altitudes in excess of 700km during disturbed periods at high solar activity. In all cases the range of pressure levels covers the thermospheric regimes from below the mesopause, up to and including the altitudes where the neutral velocity and temperature cease to have any vertical structure, in the vicinity of the exobase. Similarly, the pressure or altitude range covers the ionospheric E and F regions, although the simulations described here do not model this environment self-consistently, but rely on empirical descriptions of ion density /22/, with appropriate enhancements to effectively simulate periods of disturbed geomagnetic activity.

The time-dependent variables of southward and eastward neutral wind, total energy density, and mean molecular weight are evaluated at each grid point by an explicit time stepping numerical technique. After each iteration the vertical wind is derived, together with temperature, heights of pressure surfaces, density, and atomic oxygen and molecular nitrogen concentrations. Interpolation to a fixed height is possible for comparison with experimental data.

The momentum equation is non-linear and the solutions fully describe the horizontal and vertical advection, i.e. the transport of momentum. The transformation to a non-inertial frame of a rotating spherical atmosphere is complete with the exception that the radial centrifugal component is absorbed within the gravitational acceleration, g, which is assumed constant at 9.5 m s^{-2}. This transformation results in the curvature and coriolis effects which are fundamental in realistic simulations of atmospheric dynamics. The momentum equation also includes horizontal pressure gradients, described exactly by gradients in the heights of the pressure surfaces, horizontal and vertical viscosity, and ion drag. Similarly, the non-linear energy equation is solved self-consistently with the momentum equation and describes the three dimensional advection of energy, and the transfer of energy between internal, kinetic and potential energy. The solutions also describe the horizontal and vertical heat conduction by molecular and turbulent processes, heating by solar UV and EUV radiation, cooling by infrared radiation, and heating due to the ohmic dissipation of ionospheric currents, known as Joule and frictional heating.

The composition equation, which describes the rate of change of mean molecular weight, is solved self-consistently with the momentum and energy equations, and defines uniquely the concentrations of atomic oxygen and molecular nitrogen. The numerical solution describes the transport of these major species and their relative diffusion by molcular and turbulent processes through the three-dimensional atmosphere. Photo-dissociation of molecular oxygen and chemical processes in the lower thermosphere are not treated explicitly. Evaluation of the respective time-constants, and comparison with experimental data, show that these assumptions are generally realistic. Molecular oxygen density follows nearly the same height variation as molecular nitrogen, and is nearly de-coupled from atomic oxygen, due to the relatively long recombination time-constant.

The separation of the geomagnetic poles from the geographic poles causes photoionisation in the polar regions to have a large diurnal (UT) variation in both hemispheres at any season due to the diurnal rotation of each geomagnetic polar region about its respective geographic pole. This causes the ion drag and frictional and Joule heating rates in the

polar regions to have a large UT dependency by modulating the load on the magnetospheric dynamo. The UT modulation is larger in the souther.. nemisphere due to the greater separation between geomagnetic and geographic poles. The seasonal variation of solar photo-ionisation in the polar regions appears to cause a similar seasonal / hemispheric variation of the geomagnetic energy and momentum inputs as, with increasing E region conductivity due to increasing solar illumination, the ionospheric load on the magnetospheric dynamo is increased /12/. Under any conditions other than close to equinox, the asymmetric solar illumination and photo-ionisation between the two hemispheres causes the geomagnetic dissipation rate in the summer hemisphere to exceed that in the winter hemisphere by a considerable factor /12/.

Under steady solar and geomagnetic conditions, a time dependence in the structure and dynamics of the polar thermosphere is induced by the diurnal rotation of the entire geomagnetic polar regions each UT day about the geographic poles. The diameter of the auroral oval also expands and contracts under the influence of the changing conditions in the solar wind, with an associated modulation of the electric potential across the polar cap (which causes higher or lower ion drift velocities, ion drag and frictional and Joule heating). Regions of magnetospheric energetic particle precipitation roughly covary with convection patterns, varying the location and magnitude of the signatures of magnetospheric processes dramatically /9-15/.

In the real thermosphere, tidal and gravity waves propagate from sources within the troposphere, stratosphere and mesosphere /23-25/. The propagation of these tides, and of planetary wave features associated with lower atmospheric metecrology cause significant perturbations within the lower thermosphere, and can be traced at upper thermospheric heights (300 km and above). There are still few observations above about 120 to 140 km, where meteor radar (80 to 110 km) and incoherent scatter radar data have contributed. The energy associated with the dissipation of such tides and waves from the lower atmosphere (of the order of 1 erg cm^{-2}) has a considerable effect (10 - 30K) on the mean temperature as well as on winds within the upper mesosphere and the lower thermosphere. The thermosphere also shows a violent time-dependent response to intense geomagnetic forcing during major disturbances. Some examples of this direct response to, and of the recovery from, intense geomagnetic disturbances are discussed in /20,26-29/.

THEORETICAL SIMULATIONS OF THE THERMOSPHERE FOR STEADY SOLAR AND GEOMAGNETIC INPUTS

The seasonal and geomagnetic variations of thermospheric structure and dynamics are described in this paper with reference to 'steady state' simulations for the June and December solstices. Three levels of geomagnetic activity will be represented in these simulations, in addition to an illustration of the significant effects of the 'Y' component of the Interplanetary Magnetic Field (IMF). In total, some 30 individual global simulations are available as a data base, from which the subset of representative models shown here have been selected. Purely for illustration, the figures shown illustrate structures and variations at Pressure Level 12 of the model. This corresponds roughly to an altitude of about 320 km (average conditions) and is representative of processes in the middle F2 region of the ionosphere. It is also a region which is well sampled by satellite borne observations, by radars, and by ground-based Fabry-Perot interferometers.

Figure 1a, represents the global wind and temperature distribution at the June 21 solstice, Northern hemisphere summer / Southern hemisphere winter, at low solar (F 10.7 cm flux of atout 80) and low geomagnetic ($K_p \sim 1$) activity. In figure 1b, the mean molecular weight, total density, atomic oxygen density and summed molecular oxygen / molecular nitrogen density are shown for the same conditions. The geomagnetic input is represented by a 30 KV cross-cap potential, on a contracted auroral oval, and with no particle precipitation, and the global use of the Chiu ionospheric model.

Figure 2a,b, represent the global wind and temperature distribution and composition (etc) at the Dec. 21 solstice, Northern Hemisphere winter / Southern Hemisphere summer, for a condition of moderately high solar activity (F 10.7 cm flux of about 165) and average geomagnetic activity ($K_p \sim 2$). The E2/A2 polar electric fields /15,21/ have been used, with the global Chiu ionospheric model.

Both these models are illustrated at 18 UT. There are significant geomagnetic signatures in both longitudinal and UT effects, even at the low activity level. For example, the enhancement of thermospheric winds around the auroral oval and polar cap (Figure 1a) is quite clear in both summer and winter hemispheres. The diurnal rotation of the entire geomagnetic polar regions about the geographic poles causes, in addition to the physical translation of the polar regions, a diurnal (UT) modulation of the solar photo-ionisation within the polar and auroral regions of rapid ion convection and of the enhanced magnetospheric particle precipitation. This UT modulation of photo-ionisation throughout

the geomagnetic polar regions causes quite considerable diurnal and seasonal / latitudinal changes in polar conductivities, ion drag and ohmic dissipation at all seasons and activity levels.

To simulate (Figure 3) a level of higher geomagnetic disturbance ($Kp \sim 4^{+}$), the same polar electric field (B2/A2) is used as for the simulation shown in Figure 2 a,b. The ionising and heating properties of magnetospheric energetic electrons /6/ appropriate to moderately disturbed geomagnetic conditions have also now been introduced. There is considerable direct heating caused by these particles, particularly by soft electrons which are introduced into the dayside polar cusp region, and into the polar cap. These particles also enhance plasma densities /14-15,17-19/, ion drag momentum coupling from the polar convective ion flow, and frictional and Joule heating throughout the entire auroral oval and polar cap.

Figures 1, 2 and 3 demonstrate the major changes which result from the seasonal and latitudinal variations of solar insolation. Under both quiet and disturbed geomagnetic conditions, the summer polar region of the upper thermosphere is several hundred degrees K hotter than the winter pole. As the solar activity level increases, the diurnal and hemispheric temperature amplitudes are very close to proportional. As the geomagnetic input increases, the ratio of maximum summer polar temperature to the minimum (winter, high mid-latitudes at 04 L.T.) also increases. In the model, this is due to increasing load on the magnetospheric electric field due to the back-ground E and lower F region plasma densities. The real thermosphere appears to respond in a similar way, although the empirical data base does not provide enough information to confirm whether the increased power demand resulting from the higher plasma densities in the summer, sunlit, polar cap, can be met by magnetosphere capacity. It is thus not clear that the correct mechanism is fully understood.

In the winter polar region, mid latitude and equatorial regions, atomic oxygen is the dominant atmospheric constituent of the F-region. In the summer polar region, however, atomic oxygen and molecular nitrogen are of roughly equal number densities. A detailed analysis of the compositional and temperature variations as a function of Universal Time and geomagnetic activity shows that the enhancement is closely associated with the summer geomagnetic polar region /12/. The light atomic species (O, He) are enhanced in those regions where there is persistent downwelling, such as in the winter polar night region /30/. There is a complementary strong enhancement of heavy species (N_2, Ar, CO_2) in the summer polar region, which is permanently sunlit for some months around the solstice, where there is persistent upswelling. Significant geomagnetic heating enhances this trend. Thus the simulations of more disturbed geomagnetic conditions show the greater enhancements of molecular nitrogen, and complementary depletion of atomic oxygen, in the summer polar region.

The influence and signatures of the high latitude geomagnetic inputs of energy and momentum are relatively easy to identify. Strong anti-sunward winds blow over the geomagnetic polar cap. A cross-polar cap wind of about 200 m/sec would exist due to solar heating in the absence of any high latitude geomagnetic input. This wind is augmented by a combination of ion drag acceleration over the polar cap, and the convergent sunward winds in both the dusk and dawn parts of the auroral oval. The sunward winds in the dusk and dawn parts of the auroral oval, which are stronger in the dusk than dawn part of the oval /9,17,18/, are induced by ion drag. There is an intensification of these sunward winds by a factor of 2 - 4 between the 'quiet' and the 'disturbed' models. At the same time, the cross polar cap winds increase from 250 to more than 500 m/sec.

Geomagnetic heating, increases the high latitude heat inputs for relatively disturbed conditions, which creates increased diurnal mean meridional wind components from the summer to the winter hemisphere, of the order of 30 m/sec at middle latitudes /12/.

The figures which display, respectively, the quiet and disturbed geomagnetic conditions for the June or December solstices, show the enhancement of polar winds, and the intensification of temperature and composition changes with increasing geomagnetic activity. Localised regions of particularly strong temperature and density increase can be associated with the dayside polar cusp. In the summer polar region, under disturbed geomagnetic conditions, the enhancement of heavy species [N2] and depletion of light atomic species [O] is such that atomic oxygen becomes a minor species. This has a major effect causing average plasma densities in the sunlit summer polar region to be rather lower than those in the dayside sunlit winter polar region /31/. This process presumably is caused by the change from atomic ions (O^{+}) in the winter polar region to molecular ions (NO^{+}, O_2^{+}) in the summer polar region, resulting in an increase in the effective recombination coefficient.

Figure 4 a,b shows the significant changes in wind and temperature patterns (which are also seen in composition and density) resulting from a switch of the 'Y' component of the IMF, for otherwise similar levels of geomagnetic and solar activity. Maximum anti-

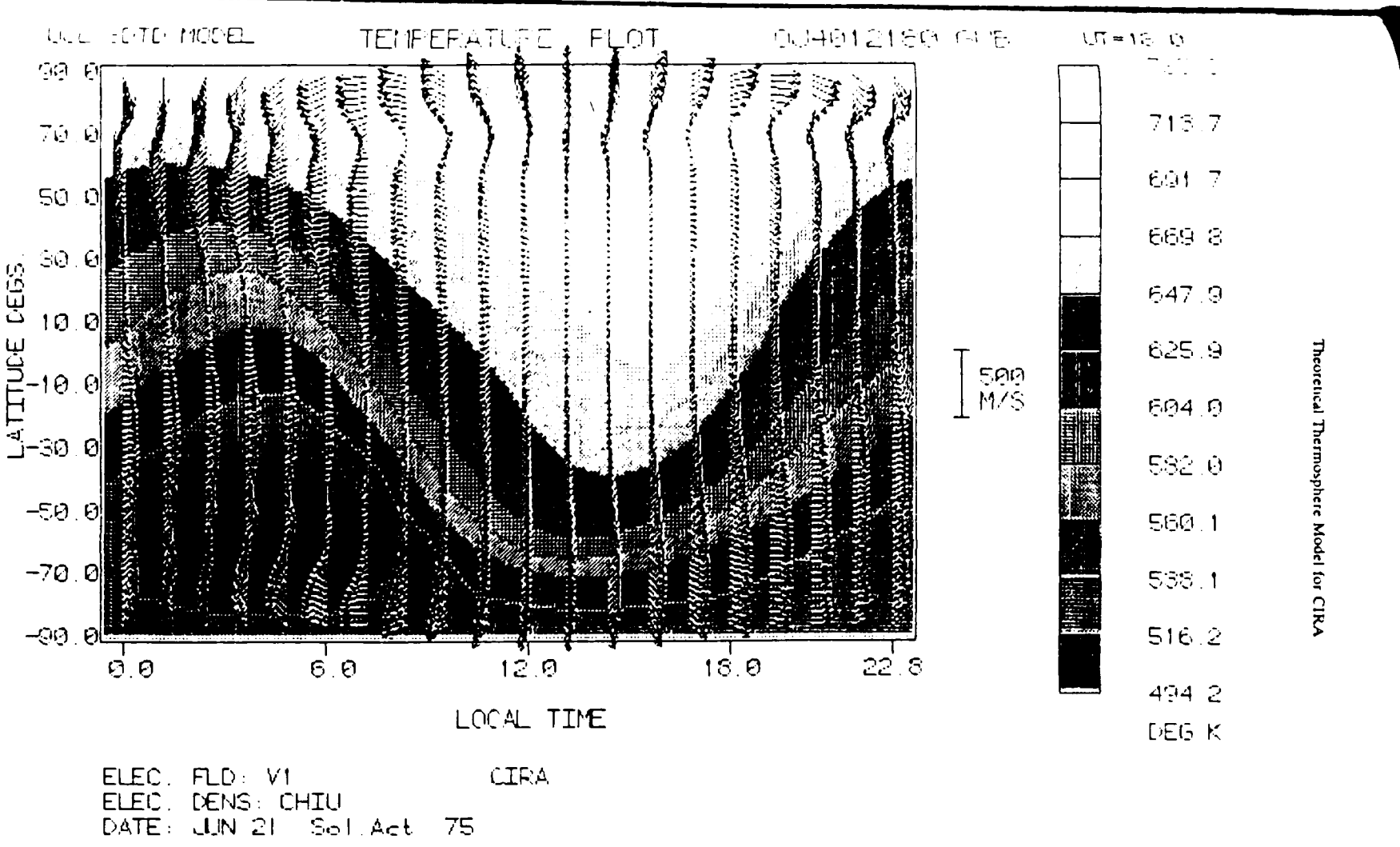

Theoretical Thermosphere Model for CIRA

(10)189

Figure 1 (a) shows the global wind and temperature distribution (320 km) at 18 UT at the June 21 solstice, Northern hemisphere summer/Southern hemisphere winter, at low solar (F10.7 cm flux of 75) and low geomagnetic ($K_p \sim 1$) activity.

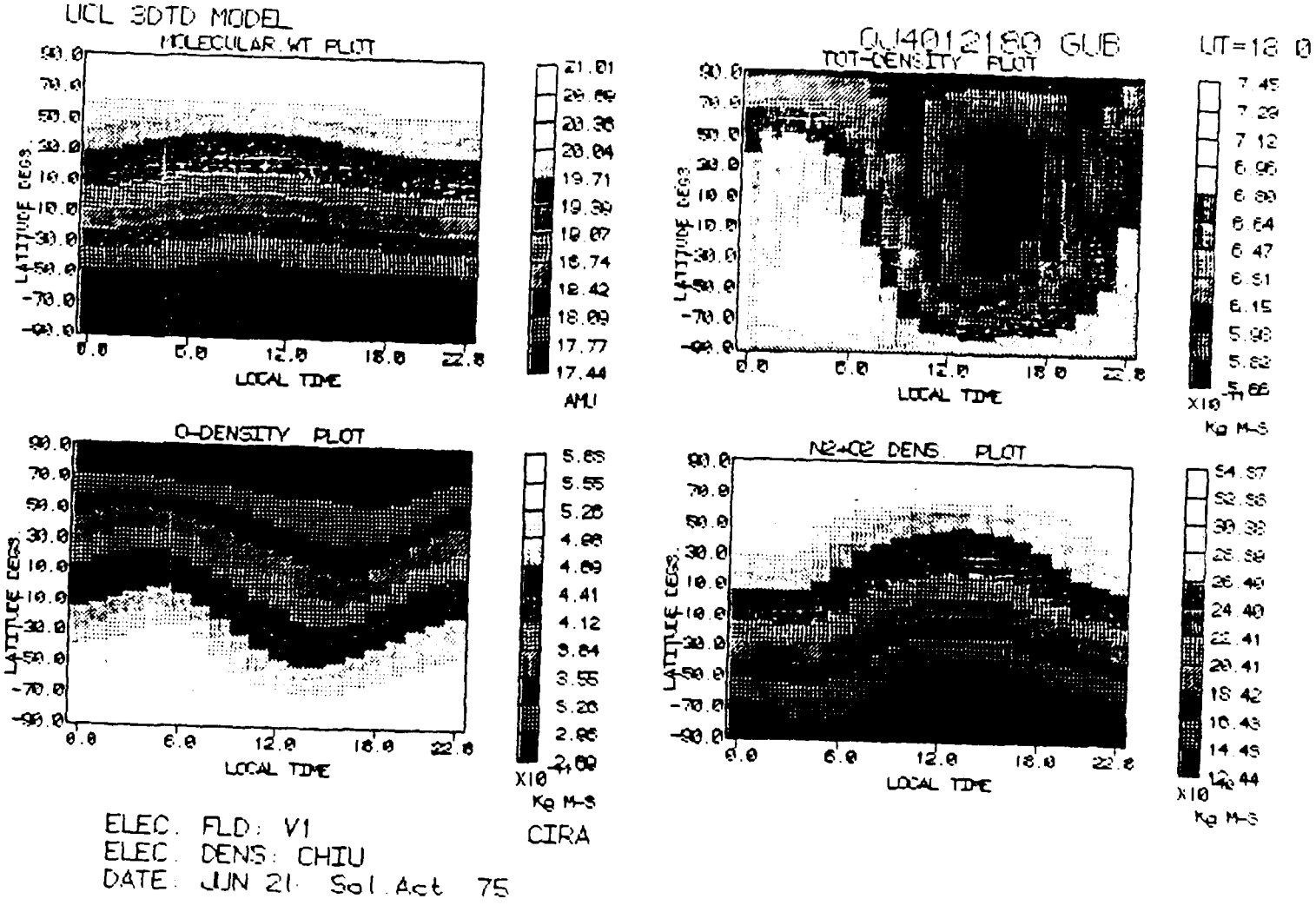

Figure 1 (b) shows the mean molecular weight, total density, atomic oxygen density and summed molecular oxygen/molecular nitrogen density for the same conditions as Figure 1 (a).

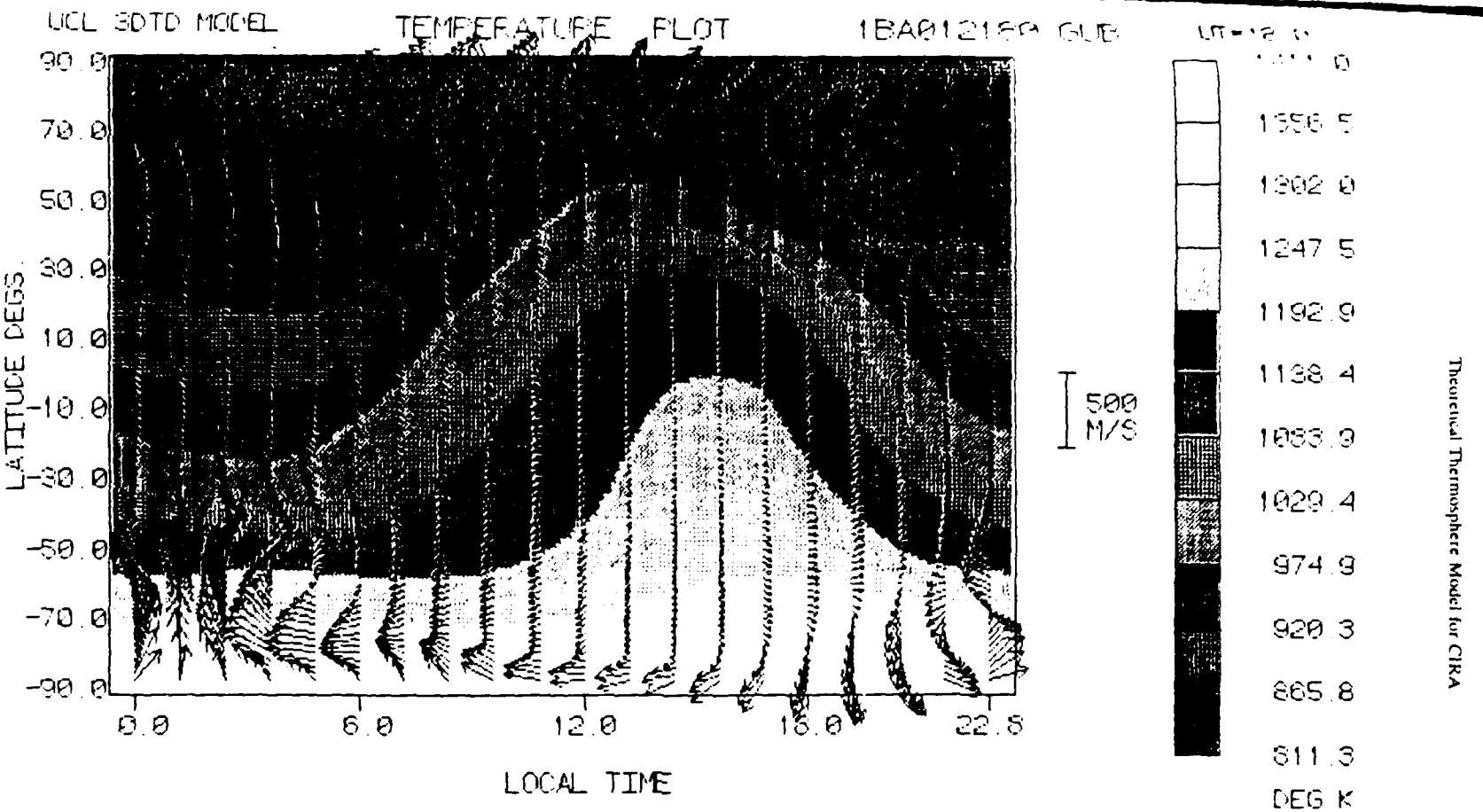

Figure 2 (a) shows the global wind and temperature distribution (320 km) at 18 UT at the Dec. 21 solstice, Northern Hemisphere winter/Southern Hemisphere summer, for a condition of high solar activity (F10.7 cm flux of 165) and slightly disturbed geomagnetic activity ($K_p \sim 2$).

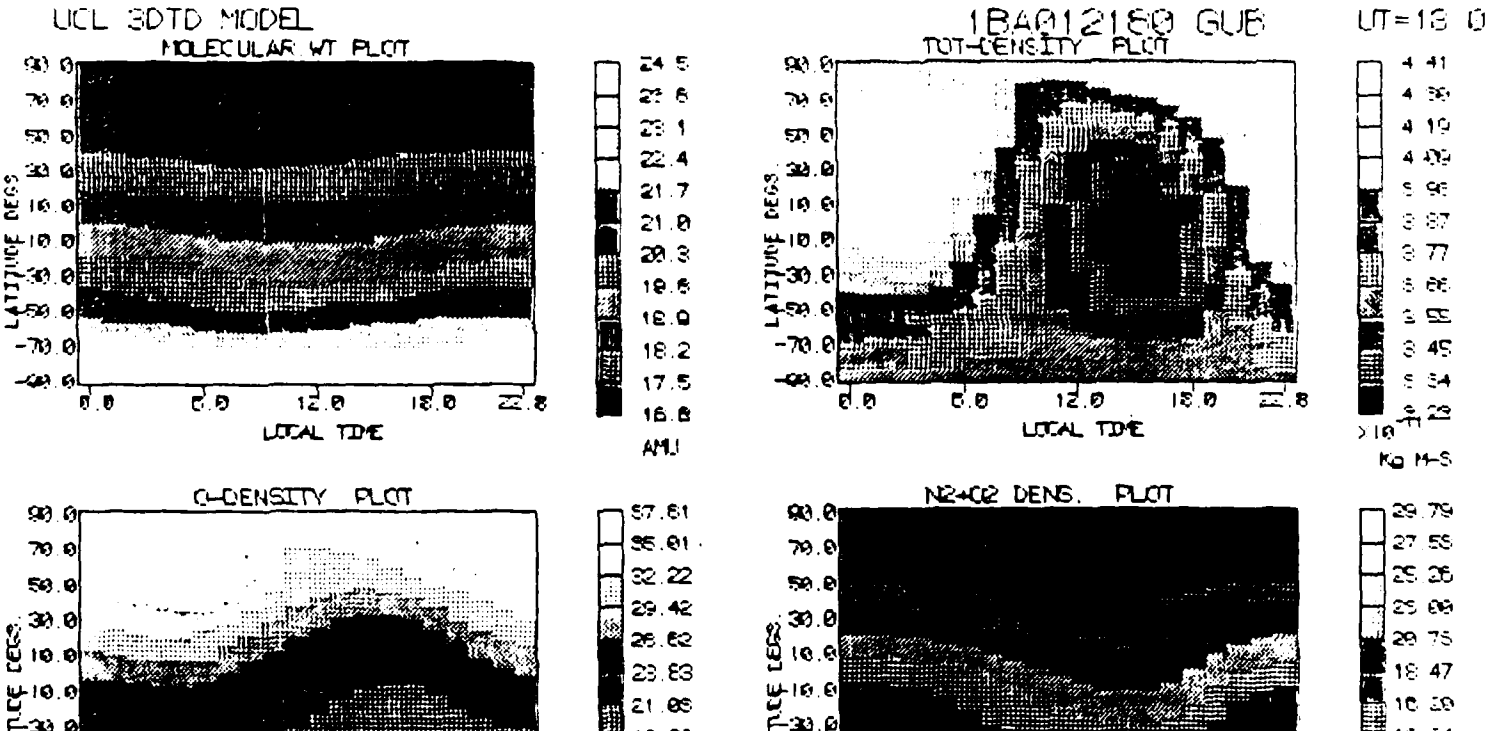

Figure 2 (b) shows the mean molecular weight, total density, atomic oxygen density and summed molecular oxygen/molecular nitrogen density for the same conditions as Figure 2 (a).

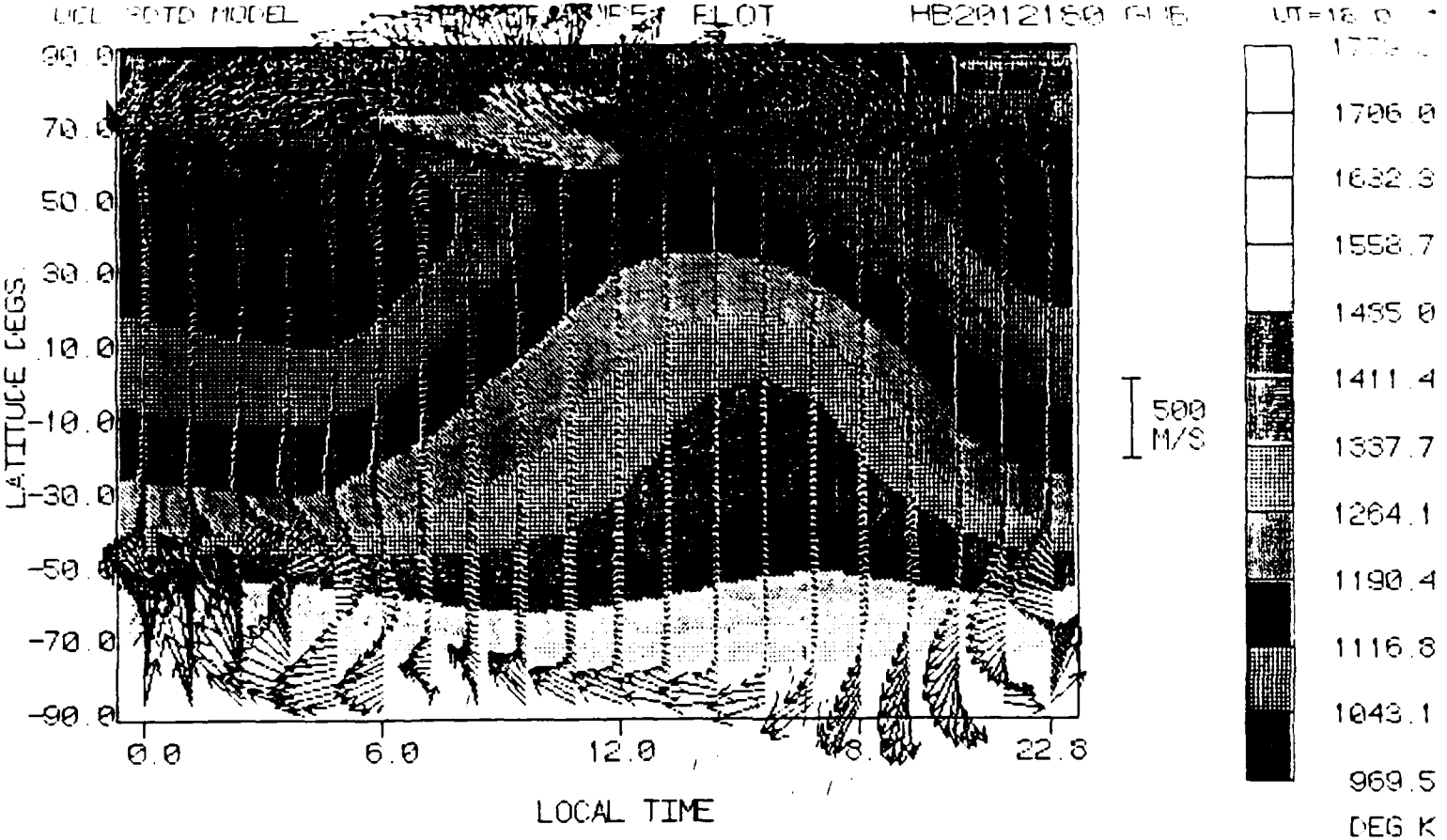

Figure 3 (a) shows the global wind and temperature distribution (320 km) at the Dec. 21 solstice, Northern Hemisphere winter/Southern Hemisphere summer, for condition of high solar activity (F10.7 cm flux of 165) and a higher level of geomagnetic disturbance ($K_p \tilde{} 4^+$).

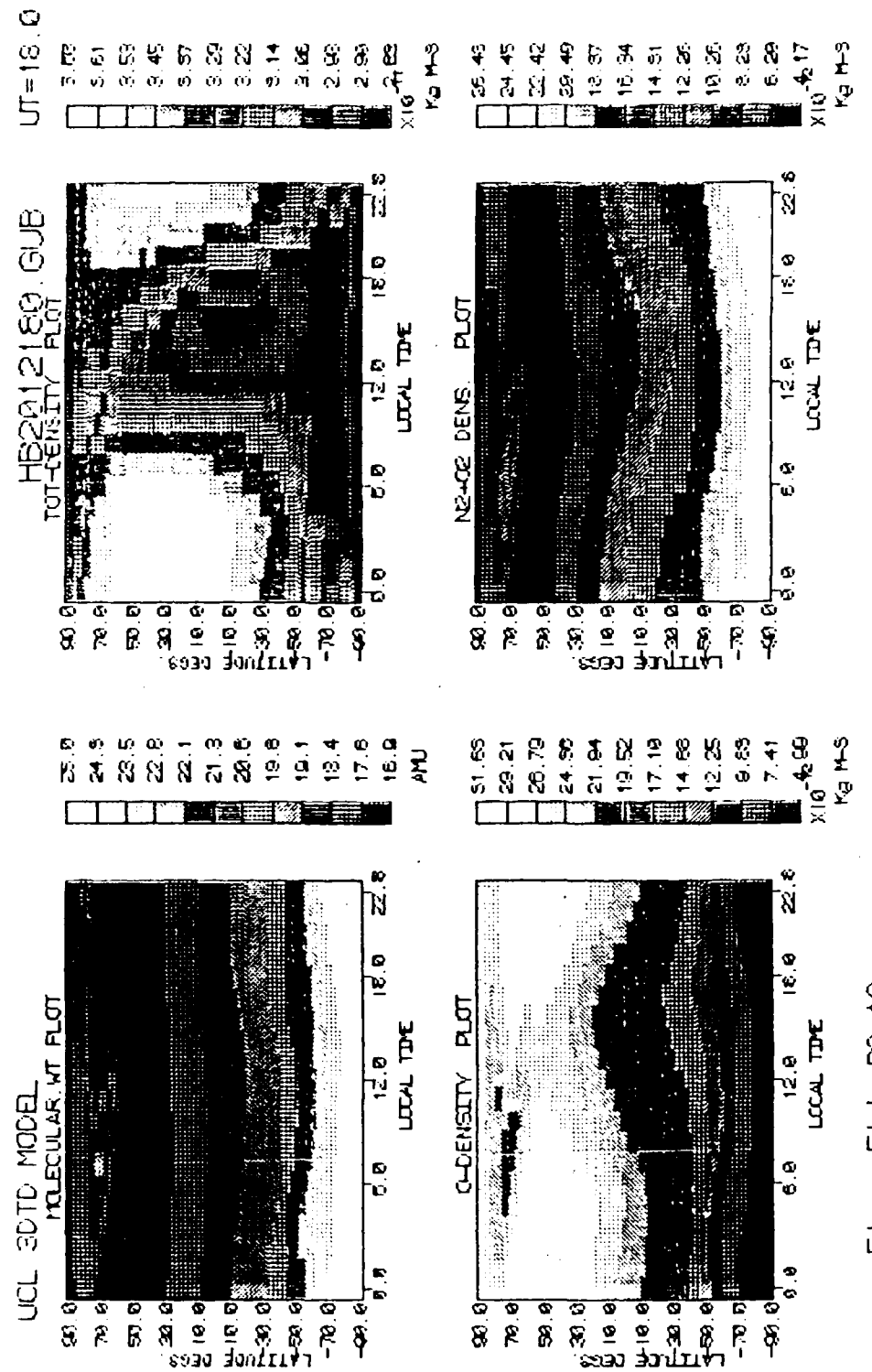

Figure 3 (b) shows the mean molecular weight, total density, atomic oxygen density and summed molecular oxygen/molecular nitrogen density for the same conditions as Figure 3 (a).

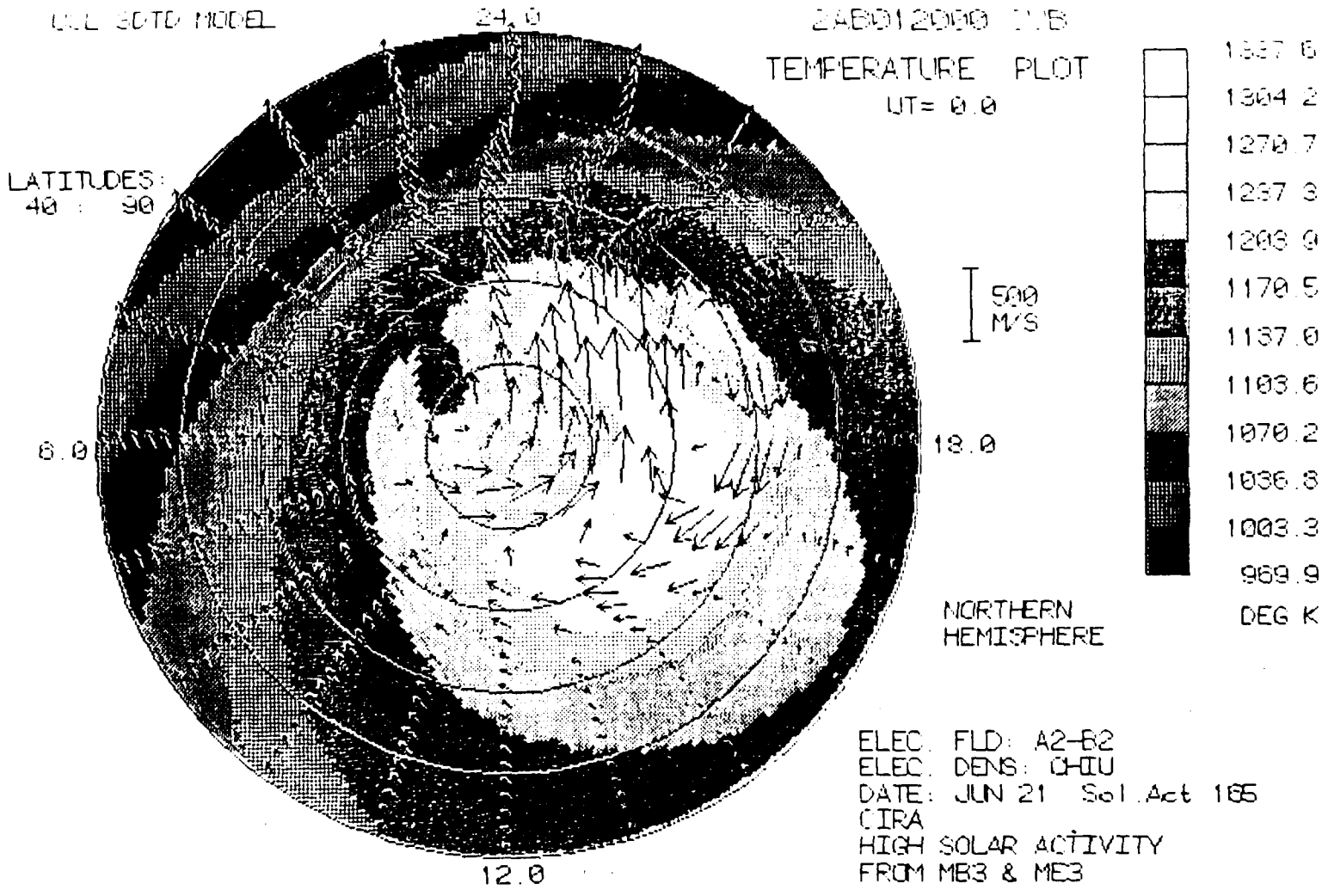

Figure 4 (a) shows the northern polar wind and temperature patterns (320 km, at 00 UT), for a negative IMF BY component, for similar levels of geomagnetic and solar activity to Figure 2 (F10.7 cm flux of 165) and a higher level of geomagnetic disturbance ($K_p \sim 4^+$).

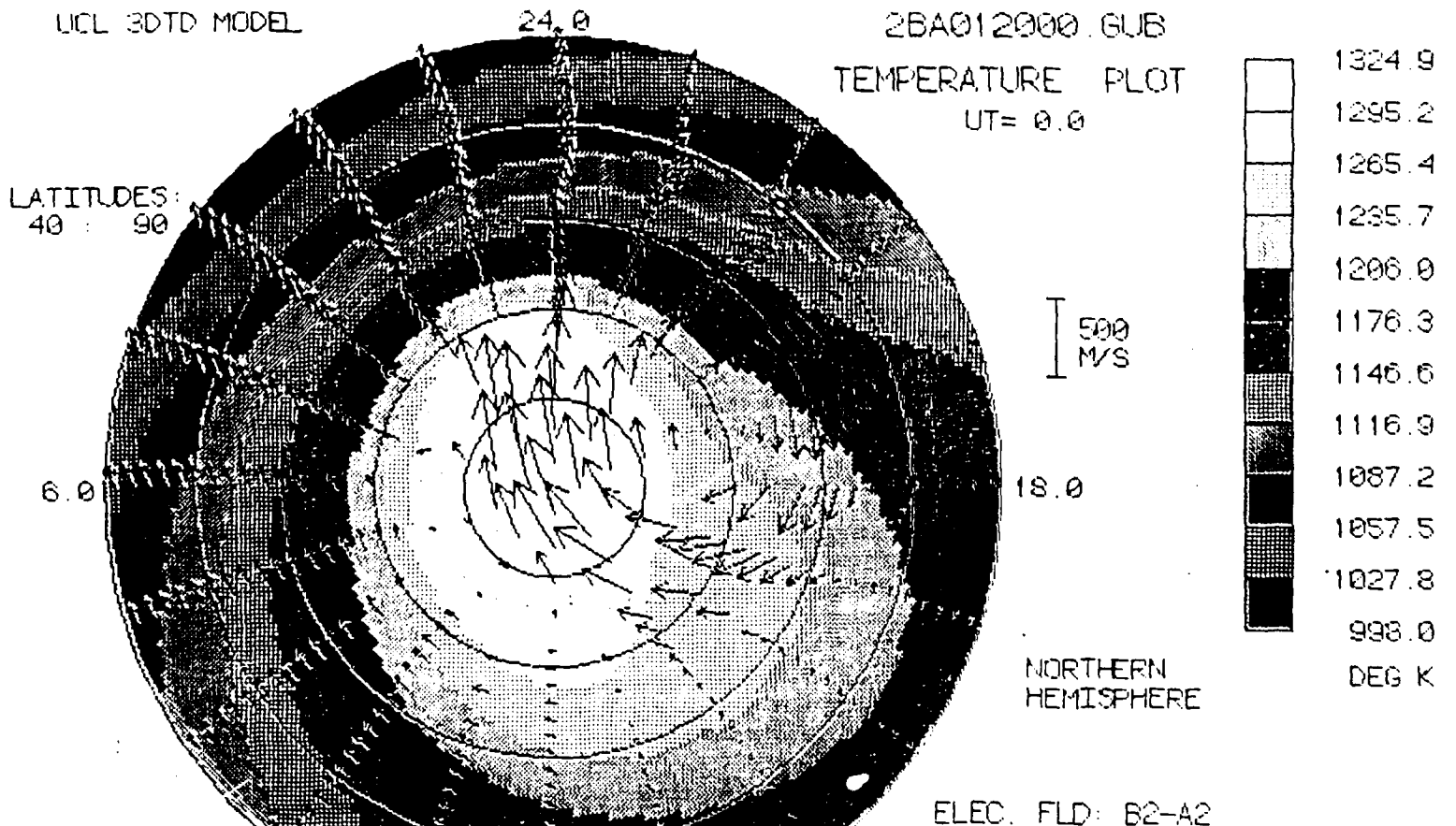

Figure 4 (b) shows the northern polar wind and temperature patterns (at 00 UT), for a positive IMF BY component, for the same levels of geomagnetic and solar activity as Figure 4 (a)

sunward winds are found on the dusk (A2) not dawn (B2) polar cap, while the temperature (and mean molecular weight) maxima have similar changes. Parameterisation of geomagnetic effects requires more than a simple description of the global geomagnetic activity level if the resulting simulation is to be reasonably representative of local as well as global mean thermospheric conditions. Comparing Figure 4 (00 UT) with Figure 2 (18 UT) shows the extent of UT modulation of the polar regions in the intervening six hours.

In the future, using fully coupled self-consistent thermospheric and ionospheric models /32/, if the global geomagnetic input can be described with realism, it will be possible to carry out a moderately accurate prediction of thermospheric conditions. The polar ionosphere/magnetosphere/magnetopause/solar wind coupling has yet to be completed to the level of thermosphere/ionosphere coupling, but some interesting early results are now being obtained. Lastly, thermosphere models are now capable of including terms such as the coupling of tidal, gravity wave and seasonal latitude variations of mesopause. These cause relatively minor effects in the upper thermosphere, but do make significant changes to wind, temperature and density structures within the lower thermosphere /23-35/.

ACKNOWLEDGEMENTS

We would like to express our thanks to Shaun Quegan, Roy Moffett and Graham Bailey for their help in developing the ccupled ionospheric/thermospheric model, and John Harmer and Israel Perla for overseeing the computer runs. Computer time was through the University of London Computer Center; general assistance was by grants from UK Science and Engineering Research Council.

REFERENCES

1. T.J. Fuller-Rowell, and D. Rees, J. Atmos. Sci. 37,2545-2567 (1980)
2. T.J. Fuller-Rowell, and D. Rees, Planet.Space Sci. 31,1209 (1983)
3. R.E. Dickinson, E.C. Ridley, and R.G. Roble, J. Geophys. Res. 87,1599 (1982)
4. H.E. Hinteregger, Adv. Space Res. 1,39 (1981)
5. M.R. Torr, D.G. Torr, and H.E. Hinteregger, J. Geophys. Res. 85,6063 (1980)
6. R.W. Spiro, P.F. Reiff, and L.J. Maher, J. Geophys.Res. 87,8215 (1982)
7. D.S. Evans and L.R. Lyons, J. Geophys. Res. 89,2395 (1984)
8. J.P. Heppner, J. Geophys. Res. 82,1115 (1977)
9. D. Rees, T.J. Fuller-Rowell, R. Gordon, T.L. Killeen, P.B. Hays, L.E. Wharton and N.W. Spencer, Planet. Space Sci. 31,1299 (1983)
10. R.G. Roble, R.E. Dickinson, E.C. Ridley, B.A. Emery, P.B. Hays, T.L. Killeen, and N.W. Spencer, Planet. Space Sci. 31,1479 (1983)
11. P.B. Hays, T.L. Killeen, N.W.Spencer, L.E. Wharton and R.G. Roble, J. Geophys. Res. 89,5597 (1984)
12. D. Rees, R. Gordon, T.J. Fuller-Rowell, M.F. Smith, G.R. Carignan, T.L. Killeen, P.B. Hays and N.W. Spencer, Planet. Space Sci. 33,617 (1985)
13. D. Rees, N.Lloyd, P.J. Charleton, and M. Carlson, J. Murdin, and I. Haggstrom, J. Atm. Terr. Phys. 46,545 (1984)
14. D. Rees, T.J. Fuller-Rowell, M.F. Smith, R. Gordon, T.L. Killeen, P.B. Hays, N.W. Spencer L. Wharton, and N.C. Maynard, Planet. Space Sci. 33,425 (1985)
15. D. Rees, T.J. Fuller-Rowell, R. Gordon, M.F. Smith, J.P. Heppner, N.C. Maynard, N.W. Spencer, L. Wharton, P.B. Hays, and T.L. Killeen, Planet.Space Sci. 34,1 (1986)
16. A.E. Hedin, J. Geophys. Res. 88,10170
17. T.J. Fuller-Rowell, D. Rees, S. Quegan, G.J. Bailey, and R.J. Moffett, Planet. Space Sci. 32,468 (1984)
18. T.J. Fuller-Rowell, and D. Rees, Planet. Space Sci. 32,69 (1984)
19. S. Quegan, G.J. Bailey, R.J. Moffett, R.A. Heelis, T.J. Fuller-Rowell, D. Rees, and R.W. Spiro, J. Atmos. Terr. Phys. 44,619 (1982)
20. D. Rees, Adv. Space Res. 5,4,267 (1985)
21. J.P. Heppner and N.M. Maynard (1983), Paper presented at the Chapman Conference at Irvington Virginia, March, (1983)
22. Y.T. Chiu, J. Atmos. Terr. Phys. 37,1563-1570 (1975)
23. G.V. Groves and J.M. Forbes, Planet Space Sci. 32,447-456 (1984)
24. C. Fesen, R.G. Roble, Ridley, J. Geophys. Res. 91,4471 (1986)
25. T.J. Fuller-Rowell, H. Parish, and D. Rees, Planet. Space Sci., in press (1986)
26. D. Rees, T.J. Fuller-Rowell, and R.W. Smith, Planet. Space Sci. 28,919 (1980)
27. T.J. Fuller-Rowell, and D. Rees, J. Atmos. Terr. Phys. 43,701 (1981)
28. M.F. Smith, D. Rees, and T.J. Fuller-Rowell, Planet. Space Sci. 30,1259 (1982)
29. D. Rees, and T.J. Fuller-Rowell, Adv. Space Res. in press (1986)
30. G.R. Carignan, invited paper COSPAR, Graz, Austria (1984)
31. J.C. Foster, Geophys. Res. 89, A2, P855 (1984)
32. T.J. Fuller-Rowell, S. Quegan, D. Rees, R. Moffett, and E. Bailey, Geophys. Res. Lett. in press (1986)

Adv. Space Res. Vol. 7, No. 10, pp. (10)199–(10)202, 1987
Printed in Great Britain. All rights reserved.

0273–1177/87 $0.00 + .50
Copyright © 1987 COSPAR

SEMI-ANNUAL VARIATION OF THE THERMOSPHERIC DENSITY

L. Sehnal

Astronomical Institute of the Czechoslovak Academy of Sciences, Ondřejov, Czechoslovakia

ABSTRACT

Thermospheric densities were determined from the orbital data of four satellites covering a height range of 266 to 500 km during 1975 to 1982. Using three different thermospheric models (DTM, MSIS, C), the index characterizing the semi-annual density variation was computed and analysed with respect to height and time using a regression by Fourier series. A general formula for the semi-annual density variation was derived. The new formula gives results similar to CIRA 72 at lower heights but displays a greater range of amplitudes at higher altitudes and a shift of extrema with growing height towards later days.

INTRODUCTION

The study of the semi-annual density variation is based usually on the analysis of the ratio of the observed density versus the modelled density corrected for all other known physical effects. The variations of this density index are often fitted by a curve drawn through the values by hand. To avoid the subjectivity in this process we used regression curves given as Fourier series of the second order.

DATA, REDUCTION METHOD AND RESULTS

We had at our disposal the orbital elements of four satellites : ANS (1974 70A), Interkosmos 10 (1973 82A), Interkosmos 11 (1974 34A) and Interkosmos 14 (1975 115A). The densities were determined from the observed drag effect by the formulae of King-Hele /1/. The data covered the period from 1975 to 1982 and the height range from 266 to 500 km. The models used for the determination of the density index were DTM /2/, MSIS /3/ and the C model by Köhnlein /4/.

The semi-annual variation of the density index D was decomposed into the annual and semi-annual component according to

$$D = \sum_{i=1}^{2} A_i \sin\left(i \frac{2\pi}{365} (d - \varphi_i)\right) \quad ,$$

where d is the day count in the year, A_i and φ_i are the amplitudes and phases to be found.

The data gave actually 11 sets of the yearly changes of the density index for each model used. The 33 individual results for A_i and φ_i are given explicitely elsewhere /5/.

The values of A_i and φ_i were then subjected to linear and quadratic regression to find their possible height dependence. The final formula for the semi-annual density variation was found to be

$$\Delta_{SA} \log \rho = (0.01004 + 1.375\times10^{-4}\ h)\ \cos(\bar{\Omega}\ (d + 30.94)) + \\ + (-0.3208 + 1.443\times10^{-4}\ h + 7.714\times10^{-7}\ h^2) \qquad (1) \\ \cos(2\bar{\Omega}\ (d + 101.45 - 0.0927\ h),$$

where $\bar{\Omega} = 2\pi/365$ and the height h is given in km.

The formula includes the height dependence of the amplitudes and also the height variation of the phases of the semi-annual term, which gives rise to the shift of the extrema with height.

COMPARISON WITH OTHER MODELS

The formula (1) can be compared to those by Jacchia /9,10/. First, it is the formula included in the CIRA 72 model and secondly, the formula very similar to ours but having the phases constant in time. Figure (1) shows the changes at 400 km as given by the three expressions.

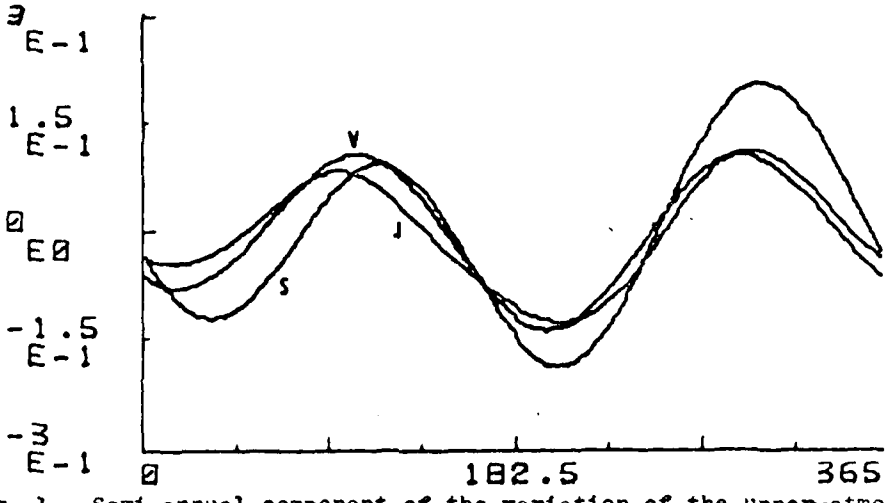

Fig. 1. Semi-annual component of the variation of the upper-atmosphere density at the height of 400 km. The curves given by Jacchia (J) /9/, Jacchia-Volland (V) /10/ and Sehnal (this issue)

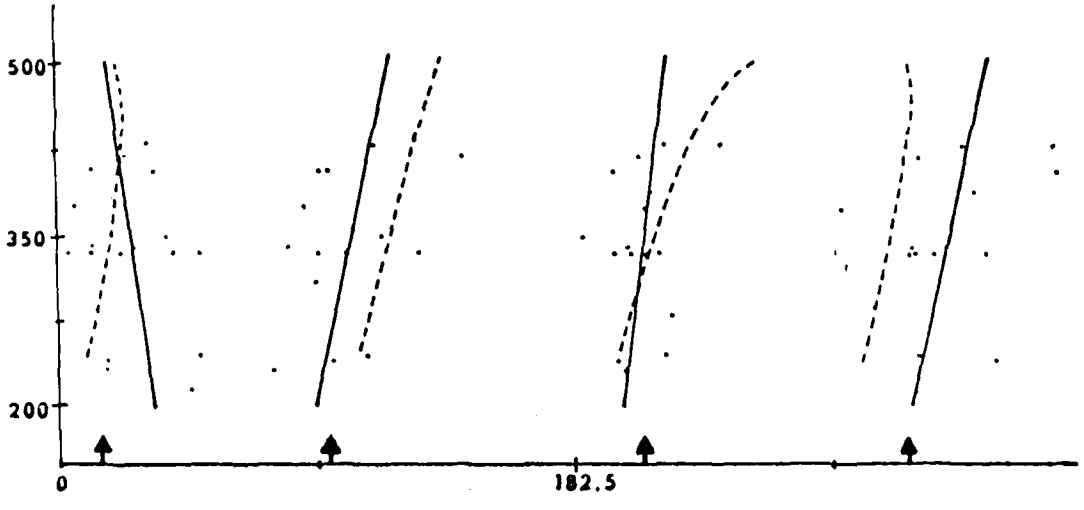

Fig. 2. The shifts of the extreme values of the semi-annual density variation. Individual values (dots) found by Boulton /8/, Walker /6/ and Moore /7/. Full line is the regression line through them, dashed lines correspond to the equation (1) of this issue.

We checked the data as given by some other authors to find a possible shift of extrema with height. Papers by Walker /6/, Moore /7/ and Boulton /8/ give several individual values summarized in Table 1.

Table 1 Dates (in day count) of extrema

Height	Jan. min.	Apr. max.	June min.	Oct. max.	Author
245	51	110	215	304	Walker /6/
240	18	98	198	331	
232	18	77	201		
213	48			303	
335	13	93	203	310	Moore /7/
335	51	128	208	301	
335	23	103	213	303	
335	5	102	197	301	
335	42				
310		92			
280			217		
340				314	
340	28	82	202	302	
340	13				
430			235	352	Boulton /8/
430	33	113	215	320	
420	25	144	206	305	
407	13	96	197	353	
407	35	93			
390			210	324	
375	7	88	208	277	
350	39	115	186		

The above values were then subjected to a linear regression. The situation is shown on Figure (2) where we see the individual data as well as the regression lines. Moreover, the shift as defined by equation (1) is included, too. We can see a good agreement of the slopes of the shifts of the April maxima, June-July minima and of the October-November maxima, too. An interesting situation appears at the January minimum where a decrease of the time with height was found. The times of January minimum as derived by equation (1) would be first growing to a height of about 440 km and then decreasing.

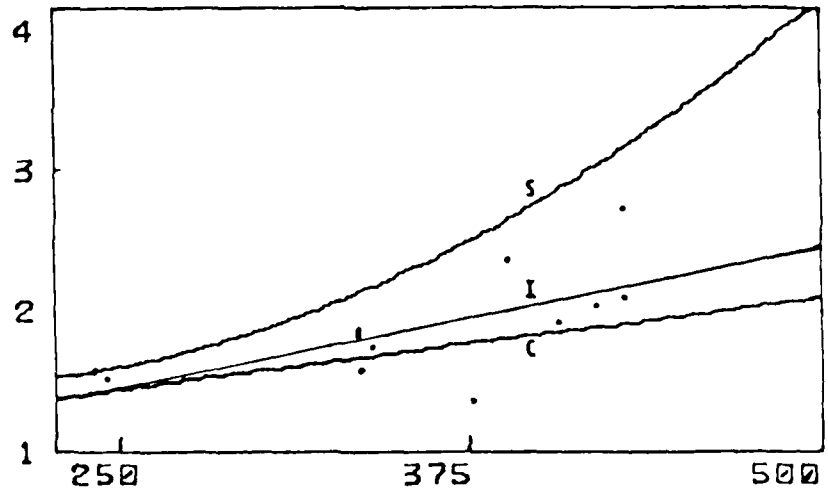

Fig. 3. Rise of the ratio of the October maximum to the June minimum values. Individual values (dots) and the regression curve (I) through them are given. Line C corresponds to CIRA 72 and curve S to the equation (1) of this issue.

The equation (1) defines also a faster rise of the range between the extrema with height. Figure (3) shows the course of the ratio of the density index of the October–November maximum to the June–July minimum with height. The individual values found by the authors quoted are included, too.

REFERENCES

1. D. G. King-Hele, Theory of Satellite Orbits in an Atmosphere, Butterworths, London, 1964

2. F. Barlier, C. Berger, J. P. Falin, G. Kockarts and G. Thuillier, Ann. Geophys., 34, 9, 1978

3. A. E. Hedin, J. E. Salah, J. V. Evans, G. A. Reber, G. P. Newton, N. W. Spencer, D. C. Kayser, D. Alcaydé, P. Bauer, L. Cogger and J. P. McClure, J. Geophys. Res. 82, 2139, 1977

4. W. Köehnlein, Planet. Space Sci., 28, 225, 1980

5. L. Sehnal, Y. E. Helali, M. Y. Tawadrous and B. B. Baghos, Bull. Astr. Inst. Czech., 37, 193, 1986

6. D. M. C. Walker, Planet. Space Sci., 26, 291, 1978

7. P. Moore, Nabl. Issk. Sputnikov Zemli, No. 22, 60, 1983

8. W. J. Boulton, Planet. Space Sci., 33, 1417, 1983

9. L. G. Jacchia, Smithson. Astrophys. Obs. Spec. Rep., No. 375, eq. (40), 1977

10. L. G. Jacchia, Smithson. Astrophys. Obs. Spec. Rep., No. 375, eq. (45), 1977

Adv. Space Res. Vol. 7, No. 10, pp. (10)203–(10)206, 1987
Printed in Great Britain. All rights reserved.

0273-1177/87 $0.00 + .50
Copyright © 1987 COSPAR

MODELS OF THE THERMOSPHERE TOTAL DENSITY FOR SATELLITE DYNAMICS

L. Sehnal

Astronomical Institute of the Czechoslovak Academy of Sciences, Ondřejov, Czechoslovakia

ABSTRACT

Mathematical expressions for models of the upper atmosphere total density distribution and variation, to be used for the analytical determination of drag effects, are developed. The models are computed by a transformation of the other model values of the thermosphere and from the observed data.

INTRODUCTION

The aim of the paper consists in establishing a model of the distribution and variation of the upper atmosphere density which would be suitable for the analytical description of the artificial satellite motion under the drag effects. The model should be simple enough to allow the necessary mathematical treatement and be complex enough to express the density values with sufficient accuracy. Then, if we succeed with the analytical perturbation theory and the changes of the elements will depend on the constans of the atmospherical model, the process may be reversed to determine the constans from the observed perturbations directly.

Basically, such a process is used to construct the models of the Earth gravity field (Earth models). However, since the present drag theories compute the perturbations using just a simple atmospheric models one has to compute the density first and to derive the atmospheric models by adjustment to the density values instead to the perturbations directly

MATHEMATICAL EXPRESSION OF THE DENSITY DISTRIBUTION

First, we express the density distribution over a spherical surface using the spherical harmonics functions. This is essentially the same procedure used in the aeronomic models of the atmosphere (MSIS, DTM, etc.) except that they consider the densities of the individual atmospheric constituents separately. Following that pattern, we shall try to express the density distribution ρ_s over a given surface as

$$\begin{aligned}\rho = {} & A_1 (F-\bar{F}) + A_2 \bar{F} + A_3 K_p + A_4 P_1 + A_5 P_2 + A_6 P_4 + \\ & + A_7 \sin(\bar{\Omega} d + \bar{\Omega}_1) + A_8 \sin(2\bar{\Omega} d + \bar{\Omega}_2) + \\ & + A_9 RW \sin(\bar{\Omega} d + \bar{\Omega}_3) + A_{10} RW \sin)\, 2\bar{\Omega} d + \bar{\Omega}_4) + \qquad (1(\\ & + A_{11} P_1^1 \sin(\bar{\omega} t + \bar{\omega}_1) + A_{12} P_2^2 \sin(2\bar{\omega} t + \bar{\omega}_2) + \\ & + A_{14} RW P_1^1 \sin(\bar{\omega} t + \bar{\omega}_3) + \\ & + A_{15} RW P_2^2 \sin(2\bar{\omega} t + \bar{\omega}_4).\end{aligned}$$

Here, F_2 and $\bar{F}_2$ is the solar flux for day - 1 and mean solar flux, resp. (in 10^{-22} Wm^{-2} Hz^{-1}), A_p is the geomagnetic index and $P_n^m(\varphi)$ are the Legendre polynomials and associated functions of the latitude φ. Also, d is the day count in days ($\bar{\Omega} = 2\pi/365$) and t is the local solar time in hours ($\bar{\omega} = 2\pi/24$.)

RW is a factor of the change of amplitudes of the periodic terms with altitude, $RW = (z_o - z)$.

At this point, the method reminds that of Marcos and Champion /1/, over a certain spherical surface.

Height dependence was chosen with respect to the usual exponential law of density decrease with altitude. Supposing the coeficients of ρ_s change with height in an exponential manner, we selected a series of expressions (1) as

$$\rho = \sum_{k=1}^{K} \exp\left(\frac{z_o - z}{kH}\right) \rho_s^{(k)} , \qquad (2)$$

where $\rho_s^{(k)}$ corresponds to (1) with changing coefficients $A_1^{(k)}$. z_o and z are the altitudes and the constant H should be chosen so that kH would correspond to the values of the real density scale heights within the height interval in question.

PERTURBATION THEORY

The principal question is the transformation of ρ for use in the equation for the changes of the orbital elements; e. g., in case of the semi-major axis a we have

$$\frac{da}{dE} = -a^2 \delta \rho \frac{(1 + e \cos E)^{3/2}}{(1 - e \cos E)^{1/2}} ,$$

where e and E are the excentricity and the excentric anomaly, resp., and δ is the coefficient containing the physival constans of the satellite and the effect of the rotation of the atmosphere.

The transformation is then to be done by formulas known from the celestial mechanics, which change principally the parameters used in the definition of the density ρ, eq. (2), into the orbital elements and time dependent terms. Then, we can integrate over one revolution of the satellite to get the changes of the semi-major axis. Since the definition of ρ contains the coefficients A_1 in linear form, $\rho \sim \rho(A_1)$, we can reverse the procedure to get the changes of a again as a function linear in the coefficients A_1, $\Delta a \sim \Delta a(A_1)$. Using this formulation, we would be able to construct the model of total density directly from the perturbations of the orbital elements without the intermediate determination of the density values. The process of the reverse transformation might be very cumbersome; therefore, the computer algebra minipulation is to be recommended.

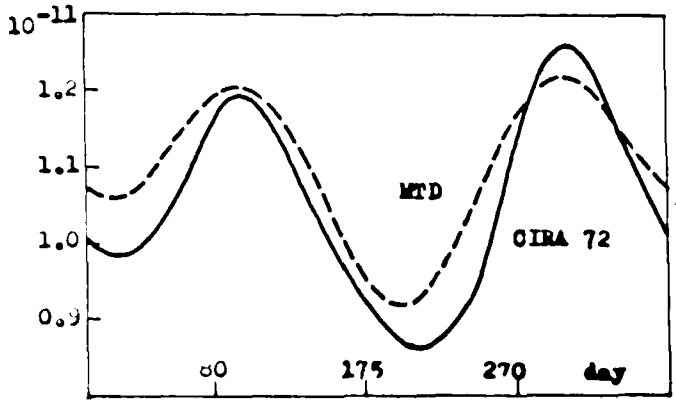

Fig. 1. Annual changes of the thermospheric density (kg/m^3) as given by CIRA 72 and MTD transformation model.

MODELS OF TOTAL DENSITY

First problem of this whole method is to justify the description of the total density by eq. (1) and (2). Therefore, we determined the coefficients A_i by the least squares method, using the data from several known models, e. g., CIRA 72 /1/ and DTM /2/. Examples of the results usinf the CIRA 72 model are plotted on Figures 1 and 2. The agreement of the CIRA values and of our MTD (Model of Total Density) is sufficiently good to approve the usage of eqs. (1) and (2) for observed data. The orbital data od satellites 1973-82 A and 1974-70 A were used to determine the model MTD 2. In this case, however, much greazer differences appeared, due to the imperfection of the initial density data and to their limited number. Nevertheless, the method proved its capability to be used for the determination of the total density model and its use for solving the satellite dynamics problems.

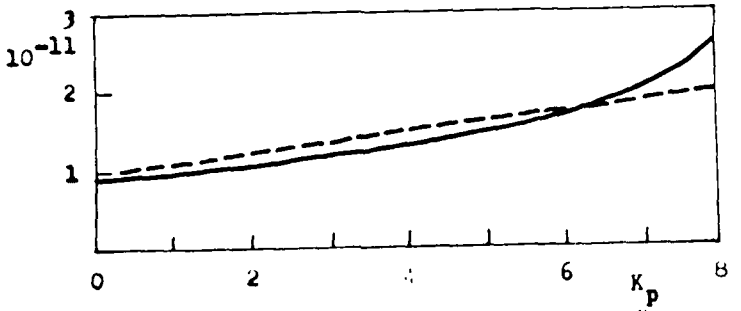

Fig. 2. Variations of thermospheric density (kg/m^3) with the geomagnetic index K_p, as given by CIRA 72 and MTD model.

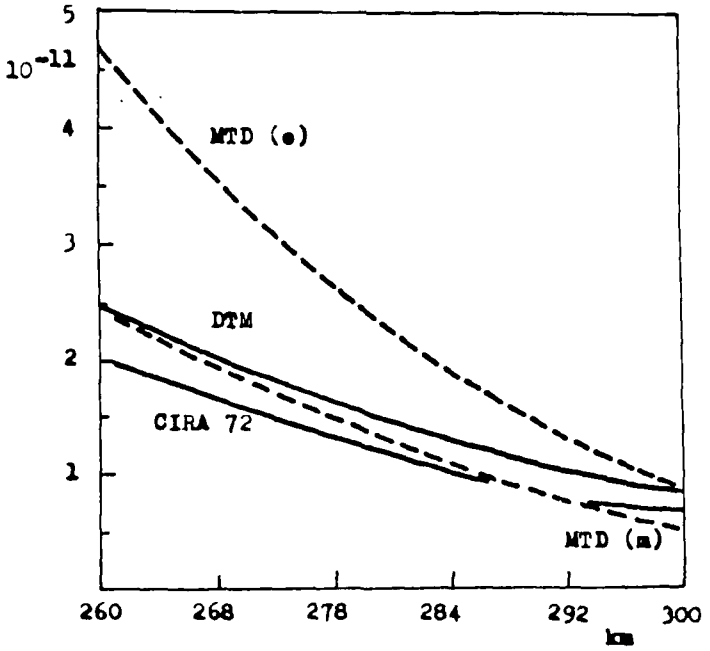

Fig. 3. Height changes of the thermospheric density (kg/m^3) compared to the MTD models, derived from the observations (o) or from the CIRA 72 values.

REFERENCES

1) F. A. Marcos and K. S. W. Champion, Paper presnnted at the XXII COSPAR Plenary Meeting, Bangalore, India, 1979.
2) W. L. Oliver, Lincln Laboratory, Lexington, Mass., USA, Tech. Note 1980-20, 1980.
3) F. Barlier, C. Berger, J. L. Falin, G. Kockards, G. Thuillier, Ann. Geophys., t. 34, fasc. 1, 1978, p. 9-24.

Adv. Space Res. Vol. 7, No. 10, pp. (10)207-(10)215, 1987
Printed in Great Britain. All rights reserved.

0273-1177/87 $0.00 + .50
Copyright © 1987 COSPAR

A COMPUTER MODEL OF GLOBAL THERMOSPHERIC WINDS AND TEMPERATURES

T. L. Killeen,* R. G. Roble** and N. W. Spencer***

*Space Physics Research Laboratory, The University of Michigan, Ann Arbor, MI 48109, U.S.A.
**High Altitude Observatory, National Center for Atmospheric Research,† Boulder, CO 80307, U.S.A.
***Goddard Space Flight Center, Greenbelt, MD 20771, U.S.A.
†The National Center for Atmospheric Research is sponsored by the National Science Foundation

ABSTRACT

A computer model of the global, time-dependent, thermospheric horizontal vector neutral wind and neutral temperature fields has been constructed based on output from the NCAR thermospheric general circulation model (NCAR-TGCM). The wind field is represented by a vector spherical harmonic (VSH) expansion in the horizontal, a fourier expansion in Universal Time, and a polynomial expansion in altitude. The global temperature field representation differs in that a scalar spherical harmonic expansion is used in the horizontal and a Bates model temperature profile is used in altitude. A set of suitably-truncated spectral coefficients contains the wind and temperature description for a diurnally-reproducible run of the NCAR-TGCM. The VSH model is coded in a FORTRAN subroutine that returns vector wind and temperature values for a given UT, geographic location, and altitude. The model has applicability for studies of thermospheric and/or ionospheric physics where reasonable time-dependent neutral wind and temperature values are of interest. The routine is novel since portable computer models of thermospheric wind fields have not previously been available to researchers. The current version of the model is valid for solar maximum, December solstice only, although the model can be extended to any season and specific set of geophysical conditions for which TGCM results are available. Results from the VSH computer model are presented to compare with global-scale wind measurements from the Dynamics Explorer (DE-2) satellite. The agreement between the computer model results and data from individual orbits of DE-2 is good, indicating that the model provides reasonable wind values, having the appropriate characteristic latitudinal, diurnal, and Universal-Time-dependent signatures observed from the satellite at upper thermospheric altitudes. The VSH thermospheric temperature values are in general agreement with MSIS-83 temperatures but illustrate smaller scale horizontal temperature structures than are resolved by MSIS-83, owing to the larger number of spectral harmonics retained.

1. INTRODUCTION

Significant progress has been made over the last several years in the modeling and empirical description of the global thermospheric neutral wind and temperature system. The Dynamics Explorer (DE-2) spacecraft, in particular, was instrumented to measure the thermospheric vector wind and temperature along the track of the polar-orbiting spacecraft [1-3]. Published results from this mission have served to characterize the global-scale thermospheric wind field for the solar maximum conditions pertaining to the 1981-1983 period [3-9]. In addition to the new information provided by the DE-2 spacecraft and other experimental techniques, the theoretical understanding of thermospheric motions has progressed rapidly. Various theoretical models exist that can simulate the dynamical response of the upper atmosphere for a variety of geophysical conditions. In particular, two numerical general circulation models, the NCAR-TGCM [10, 11] and the UCL-TGCM [12] have had a large measure of success in calculating wind and temperature fields similar to those observed from DE-2 [6, 9, 13-17]. The spectral model of *Mayr et al.* [18] has also provided significant additional insight into global-scale thermospheric dynamics.

In spite of these recent theoretical modeling efforts, no simple "user-friendly" computer model of the global thermospheric wind field has been previously constructed to enable neutral winds to be conveniently used in other theoretical studies or in straightforward comparisons with new data sets. The underlying reasons for this situation involve the sophistication and complexity of the TGCMs and the large physical size of the data arrays necessary to contain the numerically-simulated wind fields. Moreover, the fragmentary nature of the global-scale wind measurements collated to date from all experimental sources has postponed the construction of a purely empirical model. For thermospheric temperatures, the situation is better in that semi-empirical models, such as the MSIS-83 model of Hedin [19], have, for many years, provided researchers with reliable values for thermospheric temperatures, incorporating explicit dependences on geomagnetic activity, solar activity, and season.

The purpose of this report is to describe a new computer model of the global, horizontal, thermospheric vector wind and neutral temperature structure from 130 to 600km altitude. We call it the VSH model, since it contains a description of the wind field using vector spherical harmonics. The new model is based on a spectral expansion of the gridded output wind and temperature fields provided by specific runs of the NCAR-TGCM. As such, the physical description provided by the VSH model is determined by the physical, chemical and dynamical processes contained within the NCAR-TGCM structure. The VSH model formulation does not, as yet, include an explicit dependence on season, solar cycle or geomagnetic activity level. It does, however, allow for such effects to be catered for through generation of separate sets of VSH model coefficients, each of which describes specified geophysical conditions and shares a common retrieval subroutine.

The VSH model is coded in a FORTRAN subroutine that returns vector wind and temperature values for a given UT, geographic location, and altitude. It, therefore, has applicability for many studies of thermospheric and/or ionospheric physics where reasonable, UT-dependent neutral wind profiles or single-point values are of interest. We note that portable computer models of thermospheric wind fields have not previously been available to researchers. The VSH model temperature values are of interest for two reasons. Firstly, they enable the temperature predictions of the NCAR-TGCM to be made generally available for comparison with measurements and semi-empirical models. Secondly, since the number of spectral coefficients retained in the VSH representation is large compared with MSIS-83 and other semi-empirical models, the VSH temperature fields contain localized temperature structures, such as cusp temperature enhancements, that are commonly filtered out of the semi-empirical models. This last feature, of course, comes at the expense of computer time (see below).

The current version of the VSH model is valid for solar maximum, December solstice conditions only, although the model can be extended to any season and any set of geophysical conditions for which TGCM results are available. The formulation of the VSH model has been designed to allow for experimental data to be included in the fitting procedure, enabling the future development of a semi-empirical model of thermospheric winds through the suitable merging of experimental measurements with the TGCM gridded predictions.

In section 2, we describe the formulation of the new computer model. In section 3, we present results from the model for a solar maximum, December solstice case corresponding to moderately active geomagnetic conditions, and compare these with 1) global-scale wind measurements from the DE 2 spacecraft and 2) temperature profiles from the MSIS-83 semi-empirical model. In section 4 we summarize our results and discuss the utility of the VSH model and future planned developments.

2. VSH MODEL FORMULATION

The basis for the VSH model is a spectral expansion of output from the NCAR-TGCM. The expansion is performed as part of the TGCM diagnostic package described by Killeen and Roble /20/. We briefly discuss the TGCM and the specific output used in the present work before describing the formulation of the VSH model.

The NCAR-TGCM has been discussed in detail in a series of papers /10, 11, 13, 14/ and here we review only the basic features. The TGCM solves the hydrodynamic, thermodynamic and continuity equations appropriate to the Earth's thermosphere for a given set of geophysical, time-dependent input conditions and stores the calculated wind, temperature and composition (mass mixing ratio) output fields at selected Universal Times (UTs) during the model run. The model has a 5° latitude-by-longitude grid with 24 constant-pressure surfaces in the vertical, extending from approximately 97 to 500 km in altitude. The version of the TGCM used in this work incorporates the coupling of dynamics and composition /21/ and calculates the solar heating distribution and O_2 photodissociation rates using the procedure described by *Dickinson et al.* /10, 21/. The *Hinteregger* /22/ solar EUV flux values and the *Torr et al.* /23/ solar UV flux values are used to provide the direct solar input corresponding to the geophysical conditions appropriate to the particular model run. The ion convection model of *Heelis et al.* /24/ is used for the specification of high-latitude ion drifts. For the examples discussed here, the *Heelis et al.* model input parameters were chosen to yield a Volland-type symmetric ion-convection geometry. The *Chiu* /25/ model of ionospheric densities is supplemented by auroral particles according to the prescription of *Roble et al.* /26/ to provide the ion-drag tensor values necessary for the calculation of both the ion-drag momentum source and the Joule heat source to the thermosphere. The auroral oval used is similar to the statistical patterns described by *Spiro et al.* /27/ and *Whalen* /28/. The TGCM run used to construct the present VSH computer model has been employed previously in several theoretical studies and for comparisons with DE-2 data /6, 8, 28/. It is, therefore, well documented and we refer readers to these papers for more detailed information.

The TGCM diagnostic processor /20/ is exercised following the basic TGCM model run. It reads in the history file produced by the TGCM as well as other relevant input parameters and then proceeds to calculate diagnostic information at selected model grid points and UTs. The spectral analysis capability of the diagnostic package, to be described in more detail in a forthcoming paper, is used to provide the coefficients for the VSH model (see below). The history file contains records of the global wind, temperature and composition fields calculated by the TGCM at each hour of UT for the 24 hour simulation. Geophysical conditions corresponding to December solstice, solar maximum, and moderately active geomagnetic conditions (Kp ~ 3) were used for the specific TGCM run that has provided the coefficients for the first version of the VSH model, presented here. The TGCM was run until diurnal-reproducibility was attained, i.e., "steady-state," diurnally-modulated forcings were used.

For the purpose of the horizontal wind expansion, the gridded vector wind predictions at each of 24 UTs and at each of three constant-pressure levels ($z = -4$, corresponding to ~130km altitude; $z = -1$, corresponding to ~250km; $z = 1$, corresponding to ~400km) are expanded using vector spherical harmonic functions which are the appropriate eigen-functions for vector fields on the sphere. This expansion has the following form:

$$V = \Sigma(a_{m,n}P_{m,n} + b_{m,n}B_{m,n} + c_{m,n}C_{m,n}) \tag{1}$$

where V is the vector wind field and $a_{m,n}$, $b_{m,n}$, $c_{m,n}$ are the complex vector spherical harmonic coefficients; m is the zonal harmonic (order) and n is the degree. Here,

$$P_{m,n} = \begin{bmatrix} P_n^m \\ 0 \\ 0 \end{bmatrix} e^{im\phi};$$

$$B_{m,n} = \begin{bmatrix} 0 \\ A_n^m \\ iB_n^m \end{bmatrix} \frac{e^{im\phi}}{\sqrt{n(n+1)}};$$

$$C_{m,n} = \begin{bmatrix} 0 \\ iB_n^m \\ -A_n^m \end{bmatrix} \frac{e^{im\phi}}{\sqrt{n(n+1)}},$$

where ϕ is east longitude, and A_n^m and B_n^m are functions of θ (colatitude) only (2)

$$A_n^m = \frac{dP_n^m}{d\theta}$$

$$B_n^m = \frac{m}{\sin\theta} P_n^m \tag{3}$$

P_n^m are the associated Legendre functions given by

$$P_n^m(\theta) = \frac{1}{2^n n!} (\sin\theta)^m \frac{d^{(m+n)}}{dx^{(m+n)}} (x^2 - 1)^n; \quad x = \cos\theta \tag{4}$$

The complex coefficients are obtained using a least-squares fit of the TGCM output winds to the above formula. Conversely, once the coefficients are available, the global wind field can be readily reconstituted in whole or in part, using equation 1. Since the resolution of the TGCM grid is 5 degrees, only those coefficients for which $0 < n < 37$ and $0 < m < n$ are of significance. We note that equation 1 is an expression for the full vector wind, including the radial (vertical) component involving $P_{m,n}$. While the two horizontal wind components are coupled via the functions A_n^m and B_n^m, the vertical component is uncoupled and, therefore, can be simply expressed in terms of a (scalar) spherical harmonic expansion involving the associated Legendre functions. Since the vertical winds calculated by the TGCM are small in magnitude and, for some applications, not of particular interest, we (optionally) substitute for the vertical wind a scalar field such as temperature or mass mixing ratio and use the coefficients $a_{m,n}$ to describe the selected scalar field conveniently within our three-dimensional vector spherical harmonic representation. For the present VSH model, we choose to fit for neutral temperature to provide a direct comparison with the MSIS-83 model. The complete array of coefficients for the fit represents a large set of numbers, commensurate in size to the history file record of winds and temperatures itself. Thus, the desired reduction in the size of the set of numbers describing the output TGCM fields can only be attained by truncating the coefficients. Such truncation, of course, tends to destroy progressively the fidelity with which the wind fields can be reconstituted, and must be carried out carefully to ensure that important morphological features in the thermospheric wind pattern are not lost unwittingly.

Figure 1 presents contours of the log (base 10) amplitude for the VSH coefficients (real and imaginary) calculated for the spectral expansion of horizontal winds on the $z = 1$ and $z = -4$ constant pressure surfaces at 1200UT. As mentioned above, the specific TGCM run was chosen since it corresponds to the geophysical conditions for which much of the DE-2 data applies. In the figure, the bottom right triangular section is unfilled since only coefficients with $0 < m < n$ are non-zero. As can be seen, the amplitude and, therefore, the power in the expansion is a maximum at the lower wavenumbers. The amplitudes tend to diminish in magnitude with increasing wavenumber, as would be expected, though the amplitude drops much more rapidly with increasing m than with increasing n. The amplitudes for the $z = -4$ surface are smaller in magnitude than for the $z = 1$ surface since the wind speeds are generally much reduced at the lower altitudes (e.g., *Roble et al.*, 1987). The shape of the contours shown in figure 1 provides the key to the design of a suitable truncation scheme to reduce the mass of numbers required for the spectral representation of the thermospheric wind field

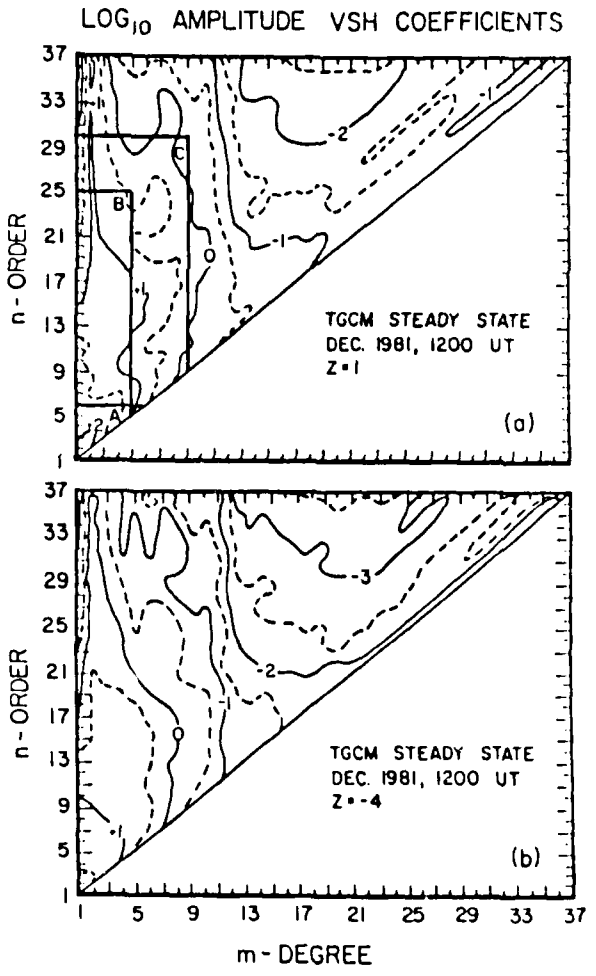

Fig. 1. Contours of the logarithmic amplitude (base 10) for the vector spherical harmonic coefficients calculated by fitting the global thermospheric wind field calculated by the NCAR-TGCM are plotted as a function of degree and order for the geophysical conditions discussed in the text and for 1200UT. Figure 1a is for the $z = 1$ constant-pressure surface and Figure 1b for the $z = -4$ constant pressure surface. Shown in Figure 1a are three regions illustrating various levels of truncation, level B is used for the VSH model

In setting the level of truncation for the VSH model we used the stringent criterion that the high-latitude reversals and vortices in the neutral wind pattern associated with ionospheric convection should be retained. It was found that a rectangular truncation scheme in n-m space gave excellent results in terms of the fidelity of the reconstituted high-latitude wind field for the minimum number of coefficients. Three levels of truncation are indicated in Figure 1a. Level A corresponds to the number of harmonics commonly retained for semi-empirical models (e.g., MSIS-83) employing scalar spherical harmonics. Level C (i.e., truncating the coefficients at n = 30, m = 9) was found to provide almost perfect fidelity for the neutral wind reconstitution. For the VSH model, we employ truncation at level B (n = 25, m = 5), which represents a good compromise between minimizing the size of the retained coefficient array (and therefore the computational time for wind syntheses) and keeping the required high-latitude wind structure. Note that the empirically-optimized truncation scheme favored higher values of n over m. This is due to the relatively large amplitudes of the fitted coefficients for large n, small m; these particular coefficients contain the information necessary to describe the relatively small-scale high-latitude neutral wind structure.

The VSH expansion, discussed above, is only for a single constant-pressure level and for a given UT. To extend the expansion to include the temporal evolution of the wind field over the 24 hour diurnal TGCM simulation, we repeat the vector spherical harmonic expansion for all 24 hourly history file records and then perform a conventional complex fourier time series to fit to the individual VSH coefficients. We have found that the fourier coefficients so obtained may be truncated such that only seven (including odd and even fourier coefficients) need to be stored to describe the diurnal variation of the "steady-state" neutral wind field reasonably well, incorporating the well-known "UT effects" associated with the diurnal revolution of the geomagnetic pole about the geographic pole. Clearly, for a situation where the thermosphere is disturbed, such as during a geomagnetic storm, additional fourier coefficients would be required to describe the more complex time dependences. The fourier series truncation used here, however, is adequate for the diurnally-reproducible case. The final part of the expansion deals with the altitudinal structure of the winds and temperatures. Since the variation in altitude of the neutral thermospheric horizontal wind predicted by the NCAR-TGCM is relatively smooth (see, for example, figure 12 of *Straus et al.*, 29), we complete the wind expansion by fitting the fourier time series coefficients to a simple, second order polynomial in altitude. The conversion from constant-pressure levels to altitudes is made using the calculated global averages for the heights of the specific constant-pressure levels carried forward to the VSH model. This conversion introduces small inconsistencies between the TGCM and VSH wind predictions that are not considered to be of importance for the stated purposes of the present work. In the case of the wind altitudinal variation, an additional constraint is placed on the VSH altitude profile to force the individual wind component values to reach constant (i.e., exospheric) values above ~400km. This constraint is justified, on theoretical grounds, by the high kinematic viscosity of the atmosphere at these heights (which tends to reduce vertical wind shears) and, on experimental grounds, by the DE 2 data which show little altitudinal structure above ~400km.

For temperatures, we replace the polynomial altitude expansion with a two-parameter fit to a Bates model profile /30, 31/ having the appropriate monotonic form, with the asymptotic (exospheric) temperature and scale-height parameter given by the fit.

The three expansions, namely, the VSH expansion in the horizontal (including the scalar spherical harmonic expansion for temperature), the fourier series in time, and the polynomial (or Bates profile) expansion in altitude, complete the full description of the TGCM wind and temperature simulations. The full set of numbers containing this description at the maximum accuracy would comprise an array of dimensions 37 × 18 × 6 × 25 × 24, corresponding to, respectively, the order (m), the degree (m), the components of the complex coefficients (a, b, and c), the fourier time series, and the altitude polynomial. With the truncation levels discussed above, we reduce the coefficient array size to the dimensions 25 × 5 × 6 × 7 × 3. Thus a total of 15750 coefficients are stored for the VSH model. We consider this to be close to the minimum number required to describe the full diurnal, spatial and altitudinal variation of the thermospheric vector neutral wind and temperature fields using spherical harmonics while retaining the important high-latitude wind structures (vortices and reversals) observed from DE 2. It might be possible in the future to further reduce the size of the required coefficient array by choosing a different set of orthonormal functions for the expansion, optimized to provide high spatial frequencies at high latitudes (*A. D. Richmond*, 1985, private communication).

The VSH model consists of the stored set of coefficients (occupying approximately 300 blocks of disk space on a VAX or PDP-type computer), plus a subroutine designed to reconstitute the vector wind and temperature values at any given geographic location, altitude and time. The subroutine performs the inverse set of transformations to those that provided the coefficients, recovering, successively, the temporal, spatial, and altitudinal information to return geophysical winds and temperatures. The computer time necessary for this "synthesis" of model predictions is significantly longer than for similar calculations using MSIS-83, due to the much larger number of calculations necessary. We have found that full global 5 degree × 5 degree wind and temperature fields can be calculated using the VSH model within a few minutes CPU time on a VAX 750 machine. Much shorter computer times, however, are required to calculate, for example, the diurnal variation of the neutral winds over a given ground-based observatory. For most applications, computer time can be reduced considerably by using the most efficient nesting of DO loop calls to the subroutine.

In the next section we present various results from the VSH model to illustrate its current capabilities. The VAX FORTRAN subroutine and documentation necessary for its use can be obtained from one of the authors (TLK).

3 EXAMPLES OF RESULTS FROM THE VSH MODEL

As mentioned earlier, the present version of the VSH model was designed to correspond with much of the DE 2 data base. In figures 2a (b), we show north (south) polar projections illustrating VSH model vector winds (in cyan) calculated for an altitude of 400km at the appropriate Universal Time corresponding to orbit 1819 (7438) of DE 2. The VSH winds are overlaid with the measured vector wind measurements from DE 2 (in yellow) made at altitudes of ~400km by the Fabry-Perot interferometer, FPI, /1/ and the Wind and Temperature Spectrometer, WATS, /2/. The DE 2 vector winds are generated from the measurements of these two instruments using the data-merging technique of *Killeen et al.* /3/. The DE 2 data shown were selected on the basis of the moderate-to-active levels of geomagnetic activity existing at the time of the orbital passes (see Kp values indicated). In both northern and southern cases, excellent qualitative agreement between the VSH model winds and the DE 2 measurements is evident, with the UT-dependent locations of the various high-latitude morphological wind features well described by the model. While exact agreement between individual DE 2 measurements and VSH model values is not obtained, nor expected, the VSH winds clearly provide reasonable results that are directly comparable with the observations, both in magnitude and direction. They are also useful in providing a hemispheric context for the interpretation of the DE 2 measurements.

The results shown in Figure 2 indicate that the various high-latitude features built into the NCAR-TGCM, such as the differing offsets between geographic and geomagnetic poles in the two hemispheres and the dominating influence on the neutral wind pattern of ion drag associated with the twin vortex ionospheric convection, are reflected in the VSH computer model. It is, of course, these high-latitude features that determine the VSH coefficient truncation criteria discussed above.

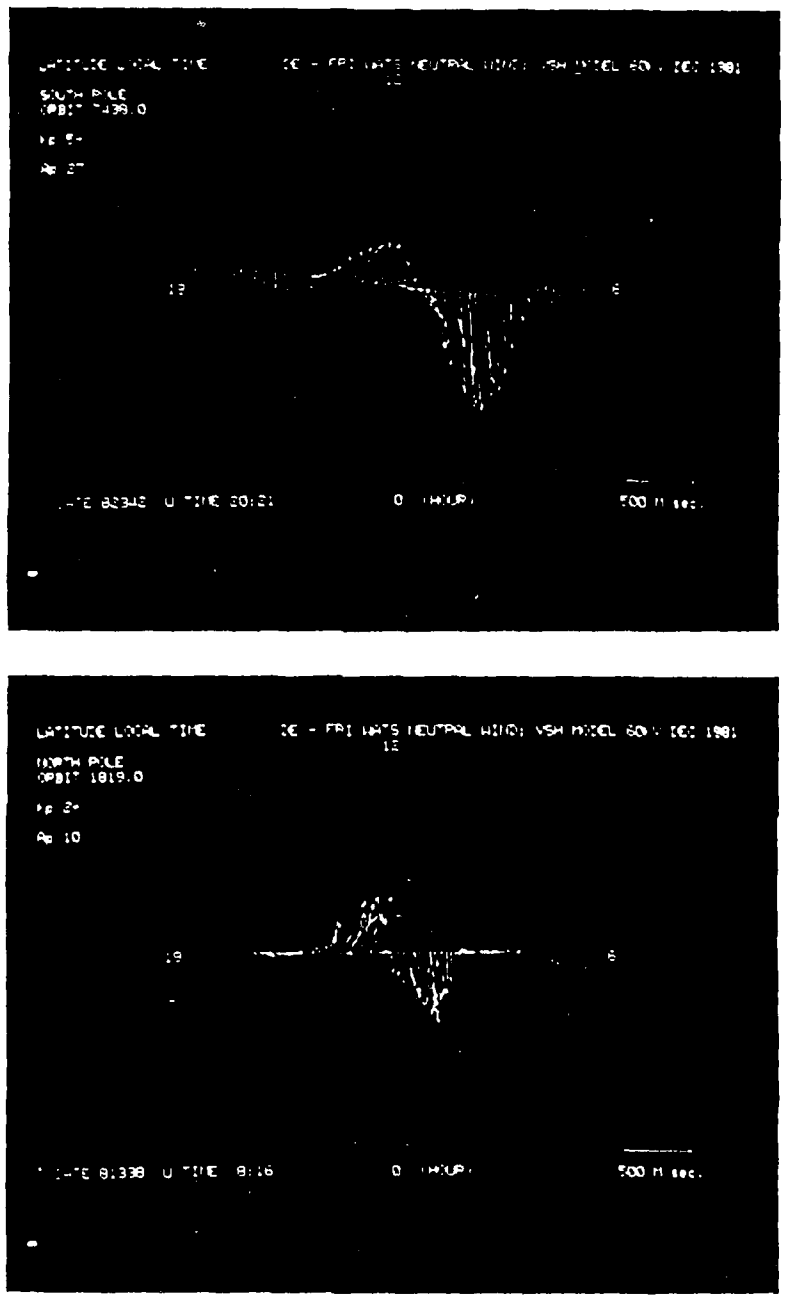

Fig. 2 Polar projections (solar local time and geographic latitude from pole to 40 degrees) illustrating the VSH model wind field (cyan arrows) for a) the Northern high-latitude region and b) the southern high-latitude region. The VSH wind vectors were calculated, in each case, at 400km and for the UT appropriate to the DE 2 observations shown in yellow. The solar terminator is given by the curved blue line. Dotted yellow arrows indicate sections of the DE 2 pass for which there were no FPI (meridional) wind measurements available. The wind scale is shown at lower right.

To provide a more fully global perspective of the VSH model winds, we show in figure 3 a cartesian plot of global vector winds calculated using the VSH subroutine at the 400km altitude level. Also shown for comparison are the DE 2 vector wind measurements made between altitudes of ~350-500km during orbit number 7431. The measured vector winds again illustrate reasonable qualitative agreement with the VSH model calculations in all regions, including the mid-latitude, high-latitude and equatorial regions. In general, for this orbit, the measured high-latitude winds were larger in magnitude than the VSH model values, although the reversal boundaries and the locations of the main morphological structures are in good agreement. Once again, our conclusion is that the VSH winds provide reasonable values (at least at upper thermospheric altitudes) that compare well with DE 2 global-scale measurements made during moderately-active geomagnetic conditions.

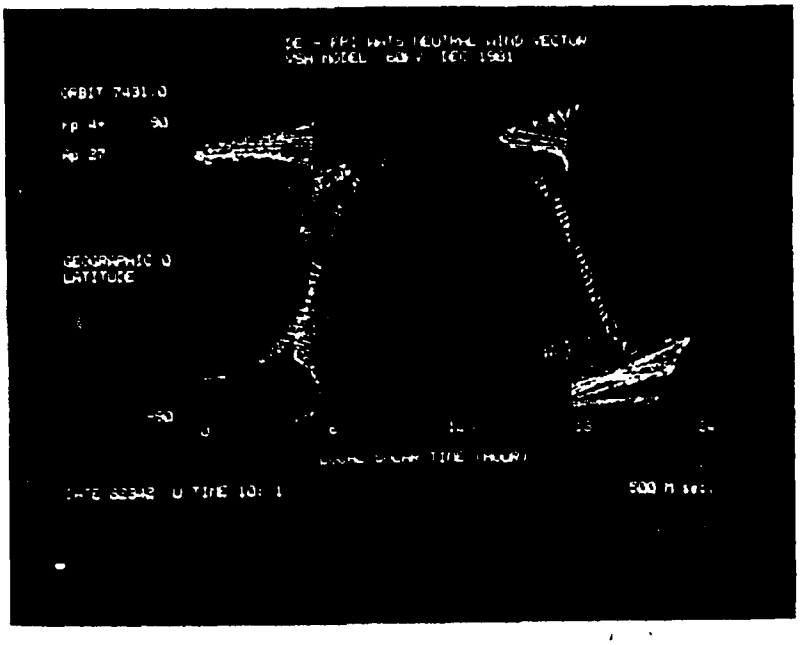

Fig. 3. Cartesian plot (geographic latitude and local solar time), illustrating the VSH global vector wind field at 400km (cyan arrows). Also shown for comparison are the observed vector winds (in yellow) from orbit 7431 of DE 2. The wind scale is to lower right and the curved red line represents the solar terminator.

A third example of VSH wind comparisons with DE 2 data is shown in figure 4. Here, we plot averaged zonal wind measurements made using the WATS instrument during 1981 and 1982 for measurements taken within 5° latitude of the geographic equator. These results are taken from the paper of *Wharton et al. /8/* and depict the average of many orbits of data. The VSH wind results are shown by the solid line together with a low-order fourier fit to the data made by *Herrero and Mayr /32/*. It can be seen that the VSH zonal winds provide a good first-order fit to the averaged WATS data at all local times, with a small phase lead.

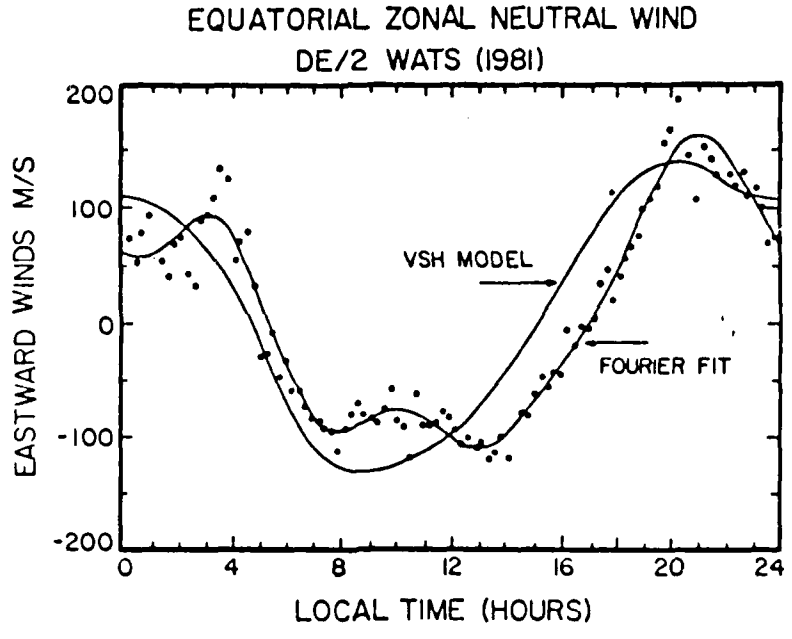

Fig. 4. Averaged equatorial zonal wind measurements from the WATS instrument on DE 2 taken from the paper by Wharton et al /33/. The results are plotted as a function of local solar time and correspond to data taken within ± 5° latitude of the equator.

As a further example of the utility of the VSH model, we show in Figures 5 and 6 the VSH model calculations for (a) zonal wind, (b) meridional wind and (c) temperature, calculated as a function of UT and altitude over locations at the geographic equator (Figure 5) and at Svalbard, Norway, (78.2°N, 15.6°W) (Figure 6). Also shown for comparison in these figures are (d) the MSIS-83 temperatures for the same solar maximum, December solstice conditions. These figures serve to illustrate the altitude structure given by the computer model for a low-latitude location and a high-latitude location. It can be seen that the altitude variations of the VSH wind and temperature results have the required asymptotic form. There are, unfortunately, no global-scale measurements of lower thermosphere winds available with which to compare the results at altitudes less than ~250km and the validity of the VSH model here is, therefore, linked solely to the confidence placed in the parent NCAR-TGCM calculations. Since the NCAR-TGCM solves the full set of "primitive equations" for thermospheric dynamics and since it has proved remarkably successful in the experimental tests at upper thermospheric altitudes, we believe that the VSH model provides valuable estimates for the entire altitude profile of thermospheric winds.

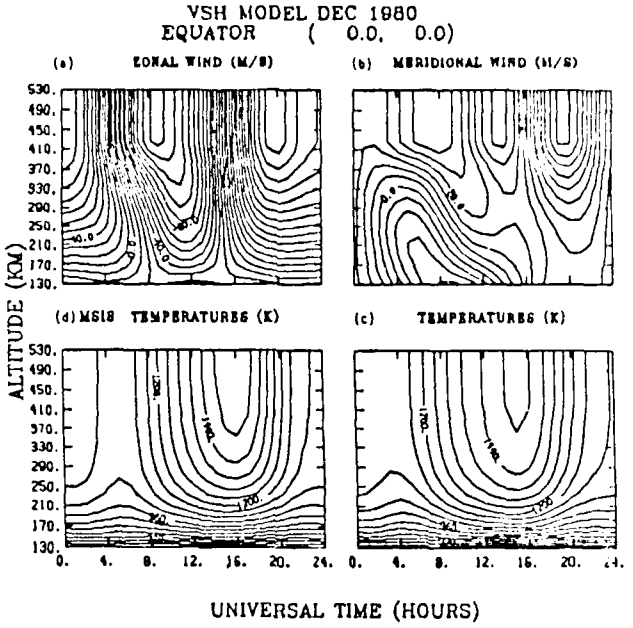

Fig. 5. Contour plots illustrating the altitudinal and UT-dependent variation of (a) the zonal wind, (b) the meridional wind, and (c) the temperature from the VSH model for calculations made at a location on the equator (latitude 0.0, longitude 0.0). Also shown (d) are results from the MSIS-83 model for solar maximum December solstice conditions.

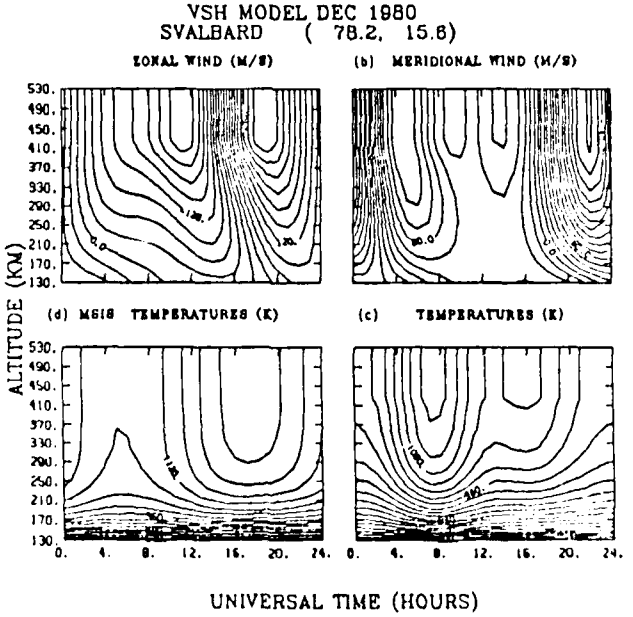

Fig. 6. Same as for Figure 5 except for the location at Svalbard, Norway (78.2 latitude, 15.6 longitude).

The comparisons between MSIS-83 and VSH model temperatures, shown in Figures 5c and d and 6c and d, are of interest since they point out the major difference between the two model profiles. For the equatorial location shown in Figure 5, the MSIS-83 and VSH temperature profiles are in excellent agreement, as would be expected since MSIS-83 provides the background model input atmosphere for the initial "spin-up" of the NCAR-TGCM. There are, however, appreciable differences evident between the VSH temperature contours and the corresponding MSIS-83 profiles at the high-latitude Svalbard location, shown in Figure 6c and d. The reason for the apparent discrepancy here is related to two factors, (1) the different number of spectral harmonics used in the MSIS-83 and VSH representations, and (2) the high-latitude heat source due to soft particle precipitation in the dayside cusp region employed in the NCAR-TGCM. MSIS-83 uses relatively few spherical harmonics and is, therefore, limited in the extent to which it can model local structures in the temperature field. The VSH model, on the other hand, uses ~3 times as many harmonics for the synthesis of its temperature field and is thereby able to model relatively smaller-scale features. The basic difference between the shapes of the MSIS-83 and VSH temperature contours in Figure 6 is due to the passage of the Svalbard location through the dayside cusp region near 0500-0900 hours UT. The NCAR-TGCM employs a high-altitude soft particle heat source in this region as discussed by *Roble et al. [2b]*, leading to a significant local, high-altitude temperature enhancement. The VSH model reflects this modeled dayside cusp high altitude heating, while the MSIS-83 model does not show the feature.

We conclude that the VSH model, by virtue of the relatively large number of harmonics retained in order to model the high-latitude wind structure, is capable of modeling local temperature features that are filtered out from models that use fewer harmonics. It remains an open experimental question whether features such as the cusp temperature enhancement illustrated in Figure 6 are indeed present in spacecraft data sets.

4. SUMMARY

A computer model of the thermospheric wind and temperature fields, based on output from the NCAR-TGCM, has been constructed using a vector spherical harmonic expansion technique. The model is coded in a portable FORTRAN subroutine that reads in a set of coefficients containing the diurnal, altitudinal and spatial information necessary to synthesize the global wind and temperature fields. The current version of the model is valid for solar maximum, December solstice conditions. It has applicability for users who require reasonable values of neutral winds and temperatures in theoretical or comparative experimental studies. Comparisons with DE 2 observations have been used to illustrate the validity of the wind results at upper thermospheric altitudes.

The model framework can be extended to incorporate seasonal, solar cyclical and geomagnetic activity dependencies simply by running the NCAR-TGCM for specified geophysical conditions and calculating a set of spectral coefficient arrays. We plan to create a family of coefficient arrays in this manner that will provide reasonable wind and temperature results for a systematic range of conditions (solstice, equinox, solar minimum, active, moderate, quiet, disturbed, etc.) The retrieval subroutine will be common to these coefficient arrays. We also plan to use the VSH model framework to develop a semi-empirical model of thermospheric winds by appropriately merging observational data from DE 2 with the TGCM gridded calculations prior to performing the vector spherical harmonic expansion described in this paper. This work is underway.

ACKNOWLEDGEMENTS

We acknowledge support from NSF grant numbers ATM-8412828 and ATM-8610085 and NASA grant number NAG5-465 to the University of Michigan. This work was partially performed when one of the authors (TLK) was a visiting scientist at the High Altitude Observatory of the National Center for Atmospheric Research. Support from the Observatory is gratefully acknowledged. The authors are particularly grateful to Dr. P. Swartztrauber of NCAR for invaluable assistance with the vector spherical harmonic expansion and to Drs. H. G. Mayr, A. E. Hedin, R. E. Dickinson and A. D. Richmond for generously-given advice and consultations.

REFERENCES

1. Hays, P. B., T. L. Killeen, and B. C. Kennedy, The Fabry-Perot interferometer on Dynamics Explorer, *Space Sci. Instrum.*, *5*, 395-416, 1981.

2. Spencer, N. W., L. E. Wharton, H.B. Niemann, A. E. Hedin, G. R. Carignan, and J. C. Maurer, The Dynamics Explorer wind and temperature spectrometer, *Space Sci. Instrum.*, *5*, 417-428, 1981.

3. Killeen, T. L., P. B. Hays, N. W. Spencer, and L. E. Wharton, Neutral winds in the polar thermosphere as measured from Dynamics Explorer, *Geophys. Res. Lett.*, *9*, 957-960, 1982.

4. Killeen, T. L., P. B. Hays, G. R. Carignan, R. A. Heelis, W. B. Hanson, N. W. Spencer, and L. H. Brace, Ion-neutral coupling in the high-latitude F-region: Evaluation of ion heating terms from Dynamics Explorer 2, *J. Geophys. Res.*, *89*, 7495-7508, 1984a.

5. Killeen, T. L., R. W. Smith, P. B. Hays, N. W. Spencer, L. E. Wharton, and F. G. McCormac, Neutral winds in the high-latitude winter F-region: Coordinated observations from ground and space, *Geophys. Res. Lett.*, *11*, 311-314, 1984b.

6. Killeen, T. L., R. G. Roble, R. W. Smith, N. W. Spencer, J. W. Meriwether, D. Rees, G. Hernandez, P. B. Hays, L. L. Cogger, D. P. Sipler, M. A. Biondi, and C. A. Tepley, Mean neutral circulation in the winter polar F-region, *J. Geophys. Res.*, *91*, 1633-1649, 1986.

7. Spencer, N.W., L. E. Wharton, G. R. Carignan, and J. C. Maurer, Thermosphere zonal winds, vertical motions and temperature as measured from Dynamics Explorer, *Geophys. Res. Lett.* *9*, 953-956, 1982.

8. Wharton, L. E., N. W. Spencer, and H. G. Mayr, The Earth's thermospheric superrotation from Dynamics Explorer 2, *Geophys. Res. Lett.* *11*, 531-533, 1984.

9. Hays, P. B., T. L. Killeen, N. W. Spencer, L. E. Wharton, R. G. Roble, B. E. Emery, T. J. Fuller-Rowell, D. Rees, L. A. Frank, and J. D. Craven, Observations of the dynamics of the polar thermosphere, *J. Geophys. Res*, *89*, 5597, 1984.

10. Dickinson, R. E., E. C. Ridley, and R. G. Roble, A three-dimensional general circulation model of the thermosphere, *J. Geophys. Res.*, *86*, 1499-1512, 1981.

11. Roble, R. G., R. E. Dickinson, and E. C. Ridley, Global circulation and temperature structure of the thermosphere with high-latitude plasma convection, *J. Geophys. Res.*, *87*, 1599-1614, 1982.

12. Fuller-Rowell, T. J., and D. Rees, A three dimensional time dependent global model of the thermosphere, *J. Atmos. Sci.*, *37*, 2545-2567, 1980.

13. Roble, R. G., R. E. Dickinson, E. C. Ridley, B. A. Emery, P. B. Hays, T. L. Killeen, and N. W. Spencer, The high latitude circulation and temperature structure of the thermosphere near solstice, *Planet. Space Sci.*, *31*, 1299-1314, 1983.

14. Roble, R. G., B. A. Emery, R. E. Dickinson, E. C. Ridley, T. L. Killeen, P. B. Hays, G. R. Carignan, and N. W. Spencer, Thermospheric circulation, temperature and compositional structure of the southern hemisphere polar cap during October-November, 198 , *J. Geophys. Res.*, *89*, 9057-9068, 1984.

15. Rees, D., T. J. Fuller-Rowell, R. Gordon, T. L. Killeen, P. B. Hays, L. E. Wharton, and N. W. Spencer, A comparison of wind observations of the upper thermosphere from the Dynamics Explorer satellite with the predictions of a global time-dependent model, *Plant. Space Sci.*, *31*, 1299-1314, 1983.

16. Rees, D., R. Gordon, T. J. Fuller-Rowell, M. Smith, G. R. Carignan, T. L. Killeen, P. B. Hays, and N. W. Spencer, The composition, structure, temperature and dynamics of the upper thermosphere in the polar regions during October to December, 1981, *Planet. Space Sci.*, *33*, 617-666, 1985.

17. Rees, D., T. J. Fuller-Rowell, R. Gordon, J. P. Heppner, N. C. Maynard, N. W. Spencer, L. E. Wharton, P. B. Hays, and T. L. Killeen, A theoretical and empirical study of the response of the high-latitude thermosphere to the sense of the "Y" component of the interplanetary magnetic field, *Planet. Space Sci.*, in press, 1986.

18. Mayr, H. G., I. Harris, F. Varosi, and F. A. Herrero, Global excitation of wave phenomena in a dissipative, multi-constituent medium, 1, Transfer Function of the Earth's Thermosphere, *J. Geophys. Res.*, *89*, 10929, 1984.

19. Hedin, A. E., A revised thermospheric model based on mass spectrometer and incoherent scatter data: MSIS-83, *J. Geophys. Res.*, *88*, 73-83, 10170-10188, 1983.

20. Killeen, T. L., and R. G. Roble, An analysis of the high latitude thermospheric wind pattern calculated by a thermospheric general circulation model, 1, Momentum forcing, *J. Geophys. Res.*, *89*, 7509-7522, 1984.

21. Dickinson, R. E., E. C. Ridley and R. G. Roble, Thermospheric general circulation with coupled dynamics and composition, *J. Atmos. Sci.*, *41* 205-219, 1984.

22. Hinteregger, H. E., Representations of solar EUV fluxes for aeronomical purposes, *Adv. Space Res.*, *86*, 801-813, 1981.

23. Torr, M. R., D. G. Torr, and H. E. Hinteregger, Solar flux variability in the Schumann-Runge continuum as a function of solar cycle 21, *J. Geophys. Res.*, *85*, 6063-6068, 1980.

24. Heelis, R. A., J. K. Lowell, and W. T. Kasprzak, A model of the high-latitude ionospheric convection pattern, *J. Geophys. Res.*, *87*, 6339-6345, 1982.

25. Chiu, Y. T., An improved phenomenological model of ionospheric density, *J. Atmos. Terr. Phys.*, *37*, 1563-1570, 1975.

26. Roble, R. G., E. C. Ridley, and R. E. Dickinson, An auroral model for the NCAR Thermospheric General Circulation Model, *J. Geophys. Res.*, submitted, 1986.

27. Spiro, R. W., P. H. Reiff, and L. J. Maher, Precipitating electron energy flux and auroral zone conductances — an empirical model, *J. Geophys. Res.*, *87*, 8215-8227, 1982.

28. Whalen, J. A., A quantitative description of the spatial distribution and dynamics of the energy flux in the continuous aurora, *J. Geophys., Res.*, *88*, 7155-7169, 1983.

29. Sica, R. J., M. H. Rees, G. J. Romick, G. Hernandez, and R. G. Roble, Auroral zone thermospheric dynamics: 1 Averages, *J. Geophys. Res.*, *91*, 3231-3244, 1986.

30. Bates, D. R., Some problems concerning the terrestrial atmosphere above about the 100 km level, *Proc. R. Soc. London, Ser. A*, *253*, 451-462, 1959.

31. Walker, J. C. G., Analytic representation of upper atmosphere densities based on Jacchia's static diffusion models, *J. Atmos. Sci.*, *22*, 462, 1965.

32. Herrero, F. A. and H. G. Mayr, Tidal decomposition of zonal neutral and ion flows in the Earth's upper equatorial thermosphere, *Geophys. Res. Lett.*, *13*, 359, 1986.

Adv. Space Res. Vol. 7, No. 10, pp. (10)217–(10)221, 1987
Printed in Great Britain. All rights reserved.

0273-1177/87 $0.00 + .50
Copyright © 1987 COSPAR

AN ANALYSIS OF THE EMPIRICAL MODELS AND THE MEASUREMENT RESULTS OF THE POLAR ATMOSPHERIC COMPOSITION AT 120–150 km HEIGHT

S. I. Avdiushin, A. A. Pokhunkov and G. F. Tulinov

Institute of Applied Geophysics, State Committee of the U.S.S.R. for Hydrometeorology and Natural Environment Control, 123376 Moscow, U.S.S.R.

$\delta = (O/N_2)_{exp}/(O/N_2)_{mod}$ ratios are analysed for the polar thermosphere depending on the season and the heliogeophysical activity where $(O/N_2)_{exp}$ values are measured at high latitudes with radiofrequency mass spectrometers at MP-12 rocket launchings and $(O/N_2)_{mod}$ values are calculated for the corresponding conditions of every experiment from 4 models (DTM, MSIS-77, MSIS-83 and Köhnlein model (KL)).

The analysis reveals certain regularities in variations for different models. In summer δ_{DTM} does not depend on the heliogeophysical activity and is within a factor of 2-3 for the polar cap and the daytime cusp at 150 km; during the polar night δ_{DTM} depends on the geomagnetic disturbance and varies with the solar activity cycle.

The $\delta_{MSIS-77}$ and δ_{KL} values have little dependence on the heliogeophysical conditions and have approximately the same seasonal variations. During the polar night $\delta_{MSIS-83}$ corresponds to 1 ± 0.25 at high and low solar activity. The increase in δ dispersion for every model considered is noted at low solar activity in the morning and evening sectors of the auroral oval.

The recent decade has witnessed the development of a great number of the thermospheric empirical models /1-8/ based on the use of the results of the satellite temperature and composition measurements by means of optical and mass-spectrometrical equipment. In some models /3-5/, along with the stated measurements, use was made of the results of satellite drag, as well as of some parameters of the atmospheric upper layers measured from mid- and low- latitude stations using the incoherent scatter technique. One of the recent models is MSIS-83 /8/. To build this model, along with a large amount of the above mentioned data, use was made of rocket sounding data at heights above 80 km. All the referenced models are empirical in which atmospheric parameter variations are given as expansions in spherical functions. Expansion coefficients depend upon the season, solar and geomagnetic activity, respectively, and in some cases upon the longitude and the universal time. All the mentioned models, with different degrees of validity, describe seasonal, latitudinal and diurnal effects in the composition variations in the thermosphere and their dependence upon the solar and geomagnetic activity.

A comparative analysis of the models was carried out in references /9,10/, where the best agreement is shown for moderate solar activity ($100 < F_{10.7} < 150$). Due to the use of a large amount of satellite data these models are known to give, as a rule, a satisfactory description of the atmosphere at 250-500 km height. For lower heights (100-200 km), due to a lack of sufficient experimental data, the models have been built mainly by extrapolation of the satellite measurements to the values of the lower boundary atmospheric parameters. Values of these parameters and the levels of the boundary itself are different for different models. Thus there is a certain degree of arbitrariness in model atmosphere descriptions of heights below satellite measurements.

The same is equally true of the lower thermosphere in the polar region. For this region the model description, due to the complexity and diversity

of physical processes caused by the specific character of magnetosphere - atmosphere relationships and the lack of necessary experimental data, is still in its infancy. In this respect it is of some interest to estimate the degree of applicability of the models already developed for the description of the lower thermosphere in the polar region.

To analyze and compare the calculated data with the experimental ones the following models have been chosen: DTM /4/, MSIS-77 /6/, Köhnlein (KL) /7/ and MSIS-83 /8/. The rocket measurements of the atomic oxygen / nitrogen ratio $/n(O)/n(N_2)/_{exp}$ obtained with a radiofrequency mass-spectrometer were used as the experimental data. This ratio is known to characterize the upper atmosphere state, in particular its thermal regime. This ratio is likely to decrease with temperature increase. The rocket experiments started as early as 1967 on Heyss Island (80°N 58°E) and from shipboard in the high latitude Atlantic region (66 - 74°N, 0 - 5°W). The measurements have been carried out at different phases of solar activity during the summer and winter seasons at geomagnetic disturbance levels characterized by Kp values, generally within 0 - 5.

While comparing the experimental and calculated values the analysis was made for a certain height making use of the δ - parameter, where $n(O)/n(N_2)_{mod}$ values were calculated for every model out of the 4 specified models using input parameters corresponding to each rocket experiment.

δ - values at a height of 150 km for the polar winter and summer are given for different models in Fig. 1 - 3. In these figures δ is given depending on the solar activity characterized by the index of the solar radio flux in the 10.7 cm wave length taken twenty four hours prior to the experiment.

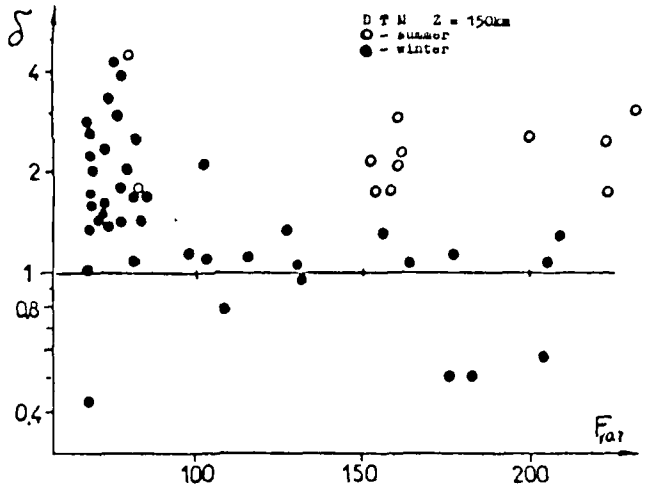

Fig. 1. Variations of the δ - parameter for the DTM model versus the index of the solar activity ($F_{10.7}$) for the polar night conditions (dark circles). For comparison the light circles designate δ - values corresponding to polar day conditions.

As is shown in Fig. 1 the DTM model, under winter conditions and at low solar activity ($60 < F_{10.7} < 100$) underestimates by up to a factor of 4 the values of $n(O)/n(N_2)$ at 150 km height. In addition a considerable scatter in δ is noted. At moderate solar activity ($100 < F_{10.7} < 150$) under the polar winter conditions the scatter decreases and the model values $n(O)/n(N_2)$ approach the experimental ones. With increase of the solar activity ($150 < F_{10.7} < 220$) the dispersion in δ again increases and a trend towards decreasing values is observed. For the polar summer (light circles in Fig.1) δ values are practically independent on the solar activity and the mean value is about 2.

As is shown in Fig. 2 the MSIS-77 model under winter conditions (dark triangles) and at low solar activity ($60 < F_{10.7} < 80$) both overestimates and underestimates by a factor of 2 the values of $n(O)/n(N_2)$, a considerable scatter in δ is also noted. At the moderate level of the solar

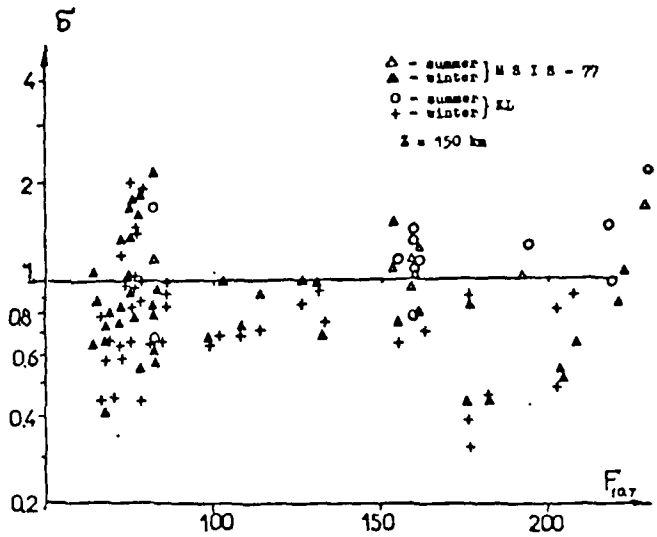

Fig. 2. Variations of δ parameters versus $F_{10.7}$ for MSIS-77, KL models and the experiments carried out on Heyss Island under polar night conditions ((▲) and (+) respectively). For comparison (△) and (○) designate δ values for the same models for the polar day conditions.

activity ($100 < F_{10.7} < 150$) a scatter in δ values decreases and on the average remains at 0.8 level. With increase of $F_{10.7}$ ($160 < F_{10.7} < 220$) a scatter in δ increases and its value is lowered to 0.4–0.3. It is characteristic that in winter at moderate and high activity the condition $\delta < 1$ holds true. For summer conditions δ values, as a rule, exceed 1 at all values of $F_{10.7}$.

The Köhnlein model (KL), as is seen in Fig. 2, describes the winter and summer atmosphere at 150 km height almost in the same way as model MSIS-77.

Model MSIS-83 δ values are presented in Fig. 3.

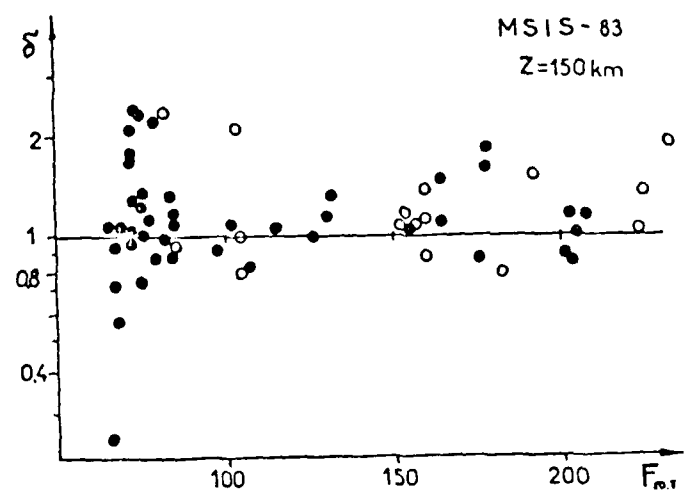

Fig. 3. Variations of the δ parameter for the MSIS-83 model and the experiments carried out under polar winter conditions on Heyss Island (●) and from research ships (○).

Dark circles designate winter conditions and light ones summer conditions. As in the previous models a considerable scatter in δ values is shown for low solar activity. However, a trend to group around one is noticeable.

It is of interest to compare the high latitude values with the same parameter taken at middle and low latitudes for the same season and at the same level of the solar activity.

To analyse the latitudinal profile of δ use was made of the results of the rocket experiments carried out in the Atlantic during the voyage of the "Professor Zubov" ship in May - June of 1980. During this period 8 MP-12 meteorological rockets equipped with mass-spectrometers were launched; 4 rockets were launched in the auroral region in the night sector of the auroral oval, 2 rockets at middle latitudes (45°N) under night and daytime conditions and 2 rockets were launched at the equator. The latitudinal profile of the experimental data deviations from the corresponding models (δ) for 125-150 km height is presented in Fig. 4. This figure shows

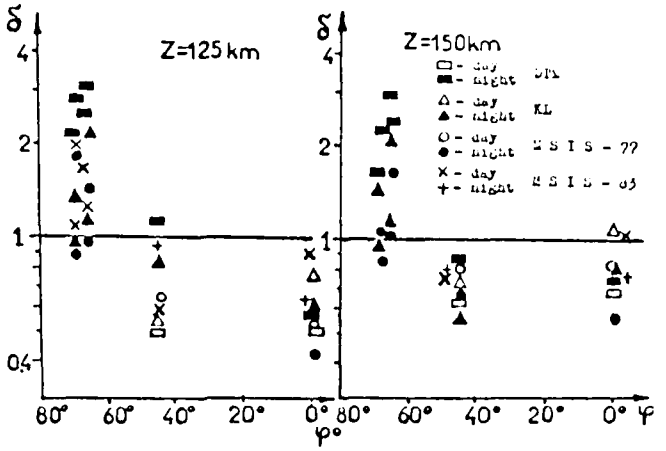

Fig. 4. Latitudinal and diurnal variations of the δ parameter obtained from the results of rocket experiments carried out during the voyage of "Professor Zubov" ship and the model calculations.

that under conditions close to the summer solstice at maximum solar activity (1980) the models considered give, on the whole, the enhanced temperature values for the polar region whereas for the middle and equatorial latitudes the reverse tendency is noted.

The experimental results presented in this paper appear to be insufficient to solve the problems of empirical modelling of the polar thermosphere. Nevertheless these results permit an estimate of the peculiarities and the degree of applicability of the models considered for the description of the low thermosphere state at polar latitudes.

Thus, for example, a relatively small scatter in δ at mean values of $F_{10.7}$ indicates that the models have been built on the basis of the satellite data summaries obtained mainly at moderate levels of solar activity. The DTM model seems to give enhanced temperature values (for $Kp \leq 5$) at low solar activity under polar night conditions. This excess probably occurs for the daytime polar thermosphere under all solar activity levels.

The MSIS-77 and KL models, on the contrary, give underestimated temperature values for the night polar thermosphere under all levels of solar activity and tend to give enhanced temperatures in summer period. The more complete and sophisticated MSIS-83 model, involving corrections for average mass transport, variations in the turbopause height and photochemistry is characterized by the absence of the δ - deviations from one observed in the previous models.

Further improvement of the models has to be directed towards the more detailed description of the polar thermosphere variations, with due regard for the specific character of the magnetosphere-atmosphere relationships involving the energetics of the current systems and the precipitating corpuscular fluxes characterized by a high degree of localization, depending on the level of heliogeophysical activity and the time of the day.

REFERENCES

1. A.E. Hedin, H.G. Mayr, C.A. Reber, N.W. Spencer, G.R.Carignan, J. Geophys. Res. 79, 215 (1974).

2. V.Von Zahn, W. Köhnlein, K.H. Fricke, U. Laux, H. Trinks, H, Volland, Geophys. Res. Letters 4, 33 (1977).

3. F. Barlier, C. Berger, J.L. Falin, G. Kockarts, G. Thuillier, Ann. Geophys. 34, 1 (1978).

4. G. Thuillier, J.L. Fallin, F. Barlier, J. Atmos. Terr. Phys., 39, 1195 (1977).

5. A.E. Hedin, C.A. Reber, G.P. Newton, N.W. Spencer, H.G. Brinton, H.G. Mayr, W.E. Potter, J. Geophys. Res. 82, 2148 (1977).

6. A.E. Hedin, C.A. Reber, N.W. Spencer, H.G. Brinton, D.G. Kayser, J. Geophys. Res. 84, 1 (1979).

7. W. Köhnlein, Planet. Space Sci. 28, 225 (1980).

8. A.E. Hedin, J. Geophys. Res. A12, 10170 (1983).

9. F. Barlier, C. Berger, J.L. Falin, G. Kockarts, G. Thuillier, J. Atmos. Terr. Phys. 41, 527 (1979).

10. F. Barlier, C. Berger, Planet. Space Sci. 31, 945 (1983).

Adv. Space Res. Vol. 7, No. 10, pp. (10)223–(10)235, 1987
Printed in Great Britain. All rights reserved.

0273-1177/87 $0.00 + .50
Copyright © 1987 COSPAR

THERMOSPHERIC STORMS

G. W. Prölss and M. Roemer

Institut für Astrophysik und Extraterrestrische Forschung, Universität Bonn, Auf dem Hügel 71, D-5300 Bonn 1, F.R.G.

ABSTRACT

Severe perturbations of the neutral upper atmosphere caused by the dissipation of solar wind energy have become known as thermospheric storms. This review summarizes the temperature and density changes observed during such events. The following topics are discussed: (1) the morphology and origin of composition changes at high and middle latitudes; (2) low-latitude effects; (3) time delays between magnetic and thermospheric perturbations; (4) systematic variations; and (5) accuracy of model predictions.

1. INTRODUCTION

In agreement with the more narrow meteorological definition, thermospheric storms are accompanied by winds of high velocity. However, they also include large changes in other state variables like the temperature and composition, which are the topic of the present review. In this respect, the term 'storm' is used in the more general sense of a severe disturbance, as is the case, for example, in the term 'ionospheric storm' or 'magnetic storm'.

Whereas a quantitative description of smaller perturbation effects is hampered by the lack of a reliable base line, this is not the case for storm associated changes. Here periods of low magnetic activity are entirely sufficient to serve as a reference. This is probably one reason why storm effects have been documented so frequently /e.g. 1-25 and the numerous references therein/. Another reason is the hope that larger events would emphasize the basic physical processes at work. And sometimes it may have been the sheer magnitude of the storm effects which fascinated the observer.

In spite of the large effort which went into the study of thermospheric storms, many of their properties remain incompletely documented and understood, testifying to the complexity of this phenomenon. This review attempts to summarize what is presently known from observations about this effect. The material is thereby organized in the following way. Section 2 describes the morphology and origin of composition changes at high and middle latitudes. A discussion of storm effects at low latitudes follows (Section 3). Section 4 is concerned with the time lag of atmospheric perturbations, and Section 5 documents some systematic variations of thermospheric storm effects. Finally, in Section 6 measurements are compared with model predictions to indicate the accuracy to be expected from present-day models.

2. COMPOSITION DISTURBANCE ZONE

At high and middle latitudes, thermospheric storms are characterized by

- an increase in the gas temperature
- an increase in the heavier gas constituents like argon, molecular oxygen, and molecular nitrogen
- a height-dependent behavior of the major constituent atomic oxygen with a moderate decrease at lower altitudes (< 300 km) and a moderate increase at higher altitudes.
- a decrease of the light constituents like helium
- and a complex behavior of reactive constituents like atomic nitrogen and nitric oxide, whose abundances are partly determined by chemical processes.

Figure 1 illustrates some of these changes for a large thermospheric storm. Variations of the exospheric temperature and of the argon, molecular nitrogen, atomic oxygen and helium densities are shown as a function of magnetic latitude. The exospheric temperature was derived from the N_2 density measurements using standard hydrostatic techniques /26-28/. Although of limited accuracy, this inferred temperature should reflect the basic large-

scale behavior of the temperature perturbations (e.g. /15,29/). Using this temperature, all densities have been reduced to a common altitude of 280 km. In addition, they have been normalized to prestorm conditions. Thus R(i) is defined as the storm-time value of the i^{th} constituent (or parameter) divided by the corresponding quiet-time value; and R(i)=1 serves as a reference, meaning no change with respect to quiet times. Note that in their normal mode of operation, gas analyzers (mass spectrometer instruments) cannot distinguish between atomic and molecular oxygen (an exception is the fly-through mode described in /30/). Instead, the total oxygen content $O+2\,O_2$ is measured. This presents no problem as long as one of the two components is a minor constituent, as is the case for the quiet-time upper thermosphere (say, above 200 km). Here the total oxygen content is close to the atomic oxygen density. During storm conditions, the situation may not be as simple, and the measured oxygen content should be considered an upper limit to the actual atomic oxygen density.

The prominent feature of Fig. 1 is the well-developed composition disturbance zone at high and middle latitudes. It is marked by a temperature increase of more than 500 K and - at 280 km altitude - by a 70-fold increase of the argon density, by an 8-fold increase of the nitrogen density, by moderate changes of the atomic oxygen density (±50 %) and by a large decrease of the helium density to one-tenth of its prestorm value.

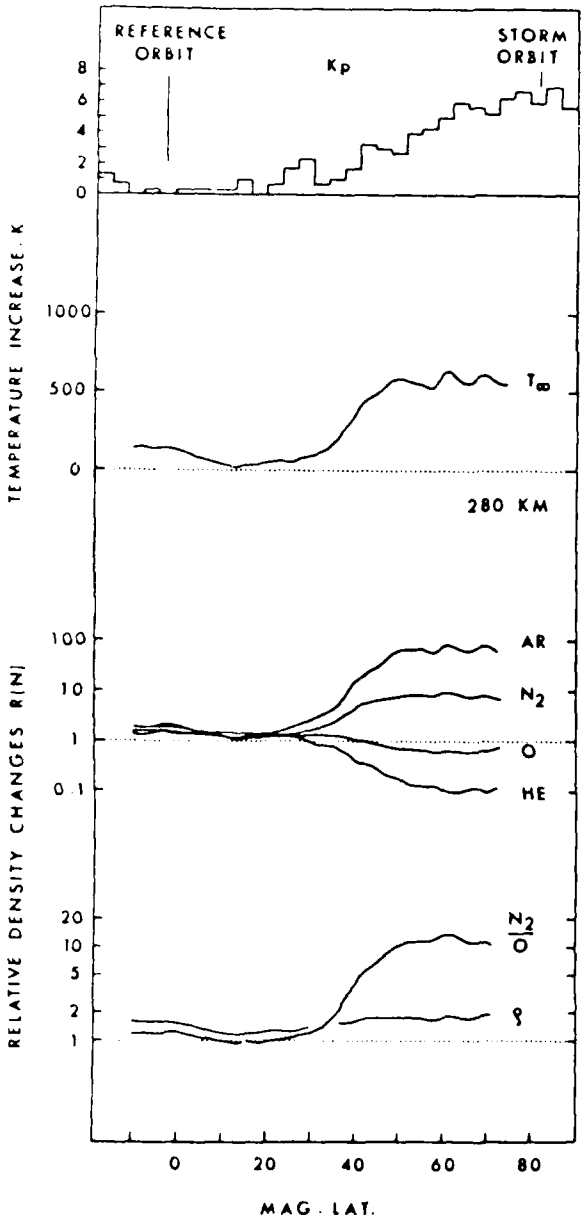

Fig. 1. Basic latitudinal structure of a thermospheric storm. The upper panel shows the development of the magnetic activity during the event. It also indicates the times at which the storm data and the quiet-time reference data were measured. The lower panel presents storm associated changes in the exospheric temperature (T_∞), in the argon (Ar), molecular nitrogen (N_2), atomic oxygen (O), and helium (He) densities, in the molecular nitrogen to atomic oxygen concentration ratio (N_2/O), and in the total mass density (ρ). The exospheric temperature has been inferred from the nitrogen data. All density data have been adjusted to a common altitude (280 km) and normalized to prestorm conditions. In this kind of presentation, R(n)=1 serves as a reference, meaning no change with respect to quiet times. The data refer to the morning local time sector (approximately 0900 SLT) and fall conditions. At the equator, the geographic longitude and universal time of observation were 246° E and 16:52, respectively.

The lower part of Fig. 1 demonstrates that the molecular nitrogen to atomic oxygen density ratio is well-suited to study the latitudinal structure of the composition disturbance. Whereas inside the perturbation zone this parameter shows a definite increase, indicating both the extent and magnitude of the composition disturbance, the lower latitude regime is characterized by a lack of change in this ratio. Additional advantages of this parameter are its large-scale height, which makes it less sensitive to height adjustment procedures, and its close association with ionospheric perturbation effects (e.g. /20/). In contrast, the total mass density ρ, also shown in Fig. 1, is certainly ill-suited to study the disturbance morphology. In the height range considered, variations in this parameter are closely linked to changes in the atomic oxygen density. Therefore the effects are relatively small, and, in addition, height dependent. An exception is the low latitude regime, where changes in ρ reflect those of the individual constituents.

Whereas the basic latitudinal variation of the composition disturbance is similar to that shown in Fig. 1, more complex structures are sometimes observed. This is documented in Fig. 2, which presents thermospheric storm data obtained during three consecutive satellite orbits. All densities have been normalized to low-latitude reference values. The feature of interest here is a mid-latitude disturbance zone which is well-separated from the polar disturbance zone. Ionospheric data not only confirm the existence of this localized perturbation structure, they also show its relatively stable nature /11,31/. Another point of interest is the large variability observed from one orbit to the next. Ionospheric data indicate that these variations are primarily due to longitudinal gradients and not to temporal changes.

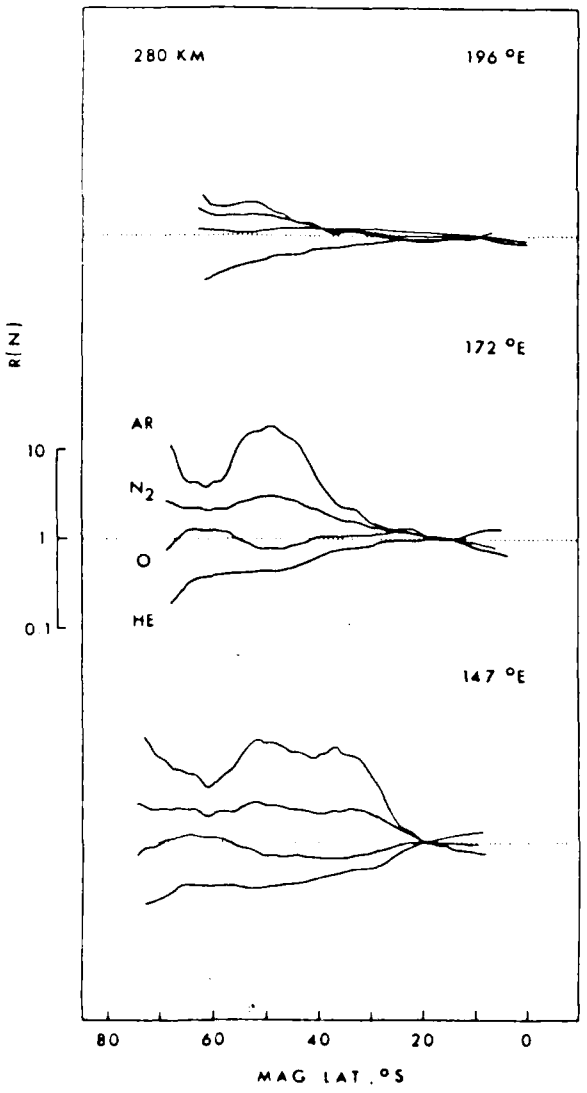

Fig. 2. Complex changes in the latitudinal structure of a thermospheric storm. For three consecutive orbits, storm-induced changes in the argon (Ar), nitrogen (N_2), oxygen (O) and helium (He) densities are shown as a function of magnetic latitude. All data have been adjusted to a common altitude of 280 km and normalized to densities observed outside the disturbance zone, (R(n)=1 serves as a reference with respect to these values). The measurements refer to the late morning sector (approximately 1100 hours local time) and to late summer conditions (21/22 February, southern hemisphere). For each orbit, the geographic longitude (east) of the equator crossing is given on the right.

Besides these large-scale structures, considerable smaller scale fluctuations are a permanent feature of the composition disturbance zone. This is illustrated in Fig. 3, which shows the initial phase of a moderately disturbed period. Whereas some of these fluctuations appear to be localized disturbance peaks, others are more wave-like in character.

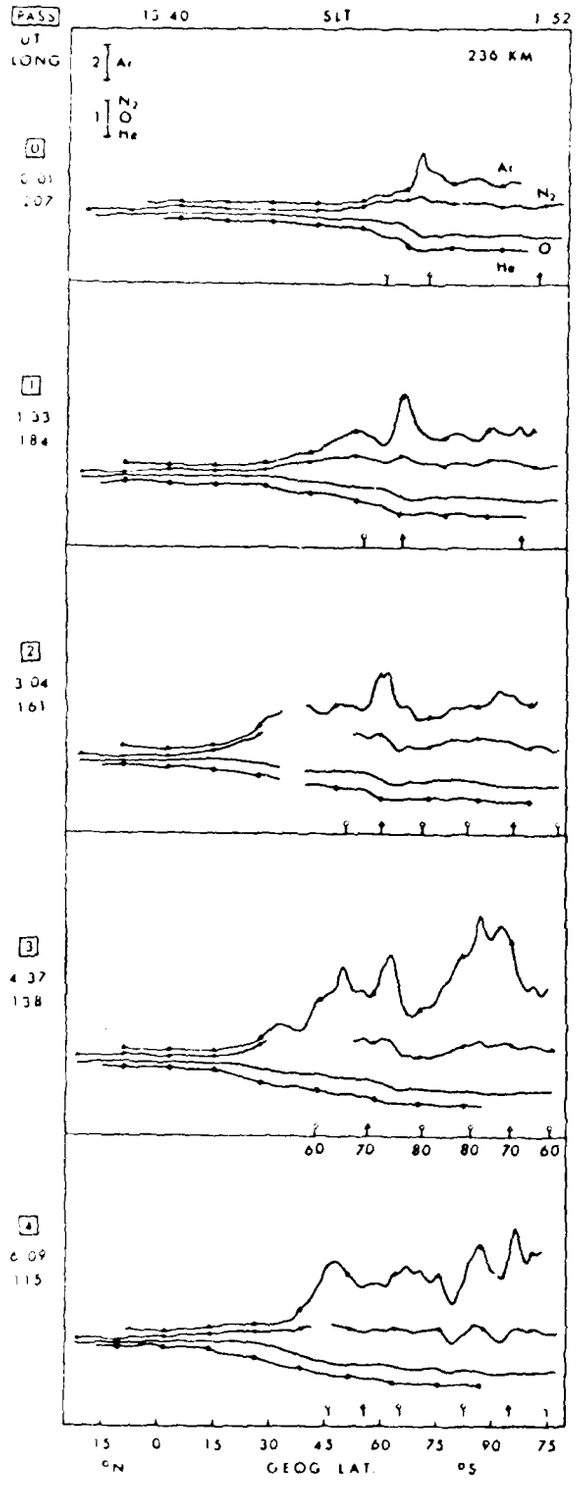

Fig. 3. Smaller-scale structures in storm-induced composition changes. Composition changes for five consecutive satellite passes are presented as a function of geographic latitude. The data refer to a common altitude of 236 km and have been normalized to density values measured outside the disturbance region. The linear scales (different for argon and the other three constituents) are indicated in the upper left-hand corner. The local time sectors covered by the measurements are specified at the top. On the left, pass number, universal time, and geographic longitude at 45° S are given. Symbols indicate 60, 70, and 80 degree invariant latitude and are identified in pass 3 /32/.

The increase of the heavier gases and the simultaneous decrease of the lighter gases is not a trivial matter, and several mechanisms have been invoked to explain this phenomenon. Three of these mechanisms - which are by no means mutually exclusive - are illustrated in Figs. 4 to 6.

The first was originally based on a simultaneous increase of the homopause altitude and the gas temperature (e.g. /33,34/). Raising the homopause altitude will decrease the lighter gases like helium and increase the heavier gases like argon. Molecular diffusion, as the major constituent, will remain essentially unchanged. Raising in addition the gas temperature will increase all gas densities in the upper thermosphere, but not to the extent that the original decrease of the lighter gases is neutralized. Only atomic oxygen may show a change-over from a moderate depletion at lower altitudes to a moderate increase at higher altitudes, in agreement with the observations.

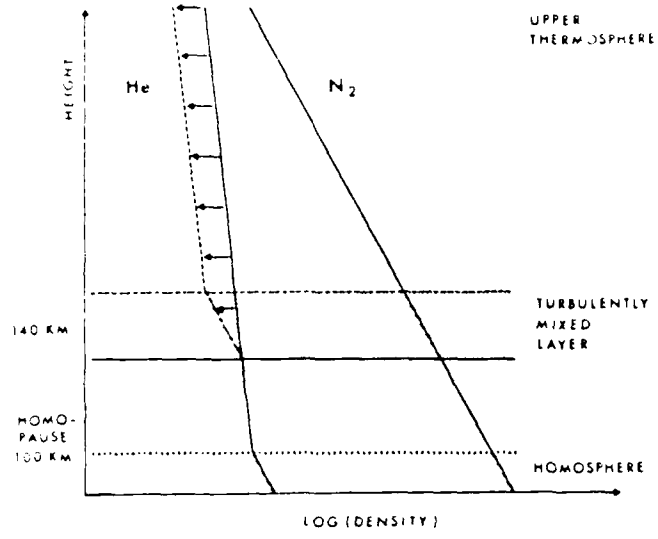

Fig. 4. Density perturbation of a minor gas (He) caused by a turbulently mixed layer above the homopause region.

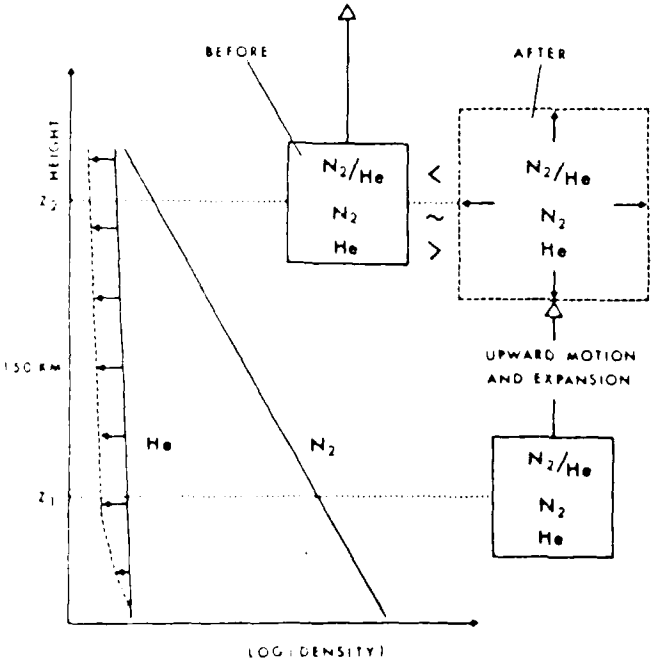

Fig. 5. Density perturbation of a minor gas (He) caused by an upward lifting and expansion of air parcels.

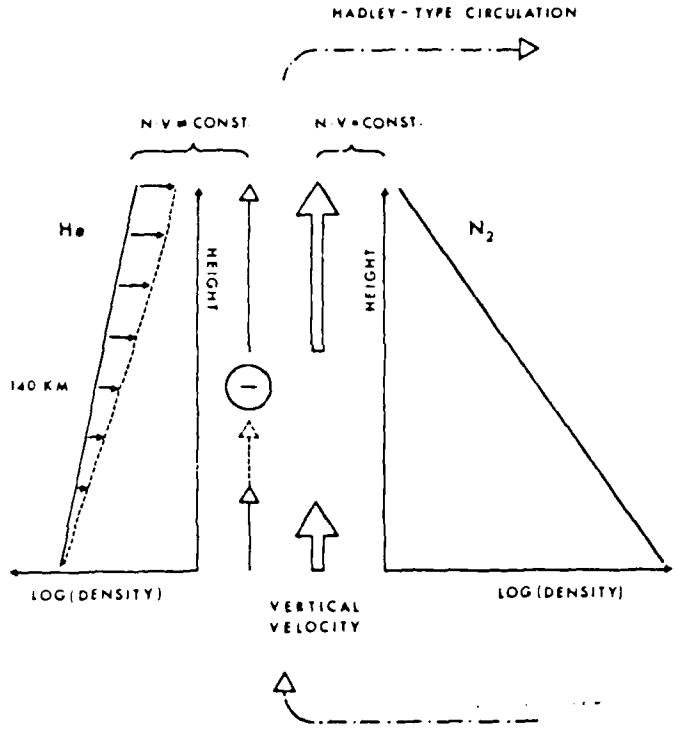

Fig. 6. Density perturbation of a minor gas (He) caused by wind-induced deviations from the diffusive equilibrium distribution.

It has been argued that disturbance effects produced by homopause changes will take too long (days) to propagate to higher altitudes. This problem does not arise if a transient mixing layer is produced above the homopause region (Fig. 4). Strongly irregular heating or the mixing action of breaking waves could be responsible for such a feature.

The second mechanism is based on the dynamics of the disturbance (Fig. 5). Heat input in the lower thermosphere produces an upward motion of gases. This upwelling lifts air rich in heavier gases (like N_2) and poor in lighter gases (like He) to higher altitudes. A simultaneous expansion causes an effective depletion of the lighter gases (He), whereas the major constituent (N_2) remains essentially unchanged (or remains moderately enhanced). At the same time, the heavier gas components will remain strongly enhanced. Hays et al. /35/ suggest that this mechanism should be most effective during the initial phase and in the central region of a disturbance.

The third mechanism is also based on the upward motion of hot air. This time, however, a complete circulation cell of the Hadley-type is considered. Continuity within this system requires that in the region of upwelling, where the horizontal divergence is small, the particle flux of the major gas (assumed to be N_2 in Fig. 6) is approximately constant with height. Therefore the upward velocity has to increase in proportion to the decrease of the major gas density. This increase in vertical velocity is much larger than would be required for a lighter gas (like helium) with a much larger scale height. Also, it is much smaller than would be required for the flux preservation of a heavier gase like argon. Thus if a circulation cell is established in the major gase and if this motion is impressed on the minor gas, this will lead to a depletion or enhancement of the minor gas. For example, more helium is transported away by the large velocities at higher altitudes than is supplied by the smaller velocities in the lower altitude region. Indeed, if both gases were tightly coupled through collisional interactions, the depletion of the lighter gases (and the simultaneous increase of the heavier gases) would continue until both gases had the same scale heights. This is, of course, counteracted by diffusion, which tries to reestablish the original state of equilibrium. In the lower thermosphere, however, diffusive separation is too slow to fully compensate for the wind effects. Accordingly, lighter gases are depleted and heavier gases are enriched. This mechanism also predicts a reverse effect at places where downward-directed winds close the circulation cell (see Section 3). The wind effects are accompanied by temperature effects which increase all gas densities and which dominate the atomic oxygen behavior at higher altitudes. The above mechanism has been thoroughly explored by Mayr and Volland (e.g. /36,37/). Similar results (although restricted to the one-dimensional case) have been obtained by Shimazaki /38/.

Another point of interest is the expansion of the disturbance effects: whereas the dissipation of solar wind energy is essentially restricted to the high latitude region, neutral composition changes are also observed at middle latitudes. This requires an effective disturbance transport, and various mechanisms have been proposed to explain this phenomenon (see, e.g., Fig. 4 in /39/). Since molecular transfer is too slow, only dynamical processes have been considered. The first mechanism is based on the excitation of planetary scale standing waves with vertical wind fields extending to middle latitudes and locally producing neutral composition changes /36,37,40/. The second mechanism assumes that neutral composition changes are produced exclusively within the high latitude heating zone and are subsequently transported convectively toward lower latitudes (e.g. /41,42/). The third mechanism postulates the excitation of large traveling atmospheric disturbances (TADs) which are capable of mixing the neutral composition down to altitudes where the recovery time constant is of the order of many hours /42/. Finally, a fourth mechanism assumes the generation of cyclonic-type disturbances in the upper atmosphere which carry a strong upward-directed wind field towards lower latitudes, locally producing the observed composition changes /44/. Again, these mechanisms are by no means mutually exclusive.

3. LOW-LATITUDE EFFECTS

Outside the composition disturbance zone, storm effects consist of a moderate increase of all constituents. This is documented in Fig. 7, which shows magnetic storm associated changes in the argon, molecular nitrogen, atomic oxygen, and helium densities observed at low latitudes. All data refer to a common altitude of 290 km, and measurements taken prior to the disturbance serve as a quiet-time reference. As is evident, all constituents show a moderate increase, but of different magnitude. In general, the density increase of argon is largest, followed by those of nitrogen, oxygen and helium. This suggests that a significant part of the geomagnetic activity effect at low latitudes may be attributed to changes in the neutral gas temperature. However, there are cases when non-thermal effects cannot be

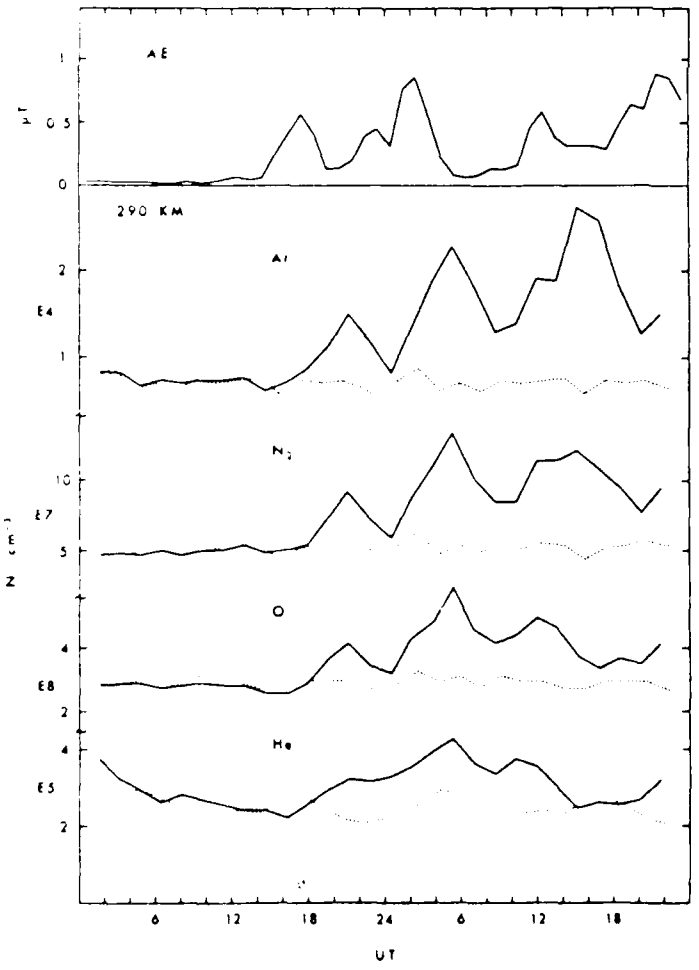

Fig. 7. Thermospheric storm effects at low latitudes. The lower panel shows changes in the argon (Ar), molecular nitrogen (N_2), atomic oxygen (O) and helium (He) densities as a function of universal time. Measurements taken one day earlier (dotted lines) serve as a quiet-time reference. The density values are averages which refer to the 5-10° S geographic latitude range. They have been adjusted to a common altitude of 290 km. Solar local time of observation is approximately 0:45. Different linear scales have been used for the four constituents ($E4=10^4$ etc.). For comparison, the upper panel shows the time variation of the AE index during this disturbance event /45/.

neglected (especially for O and He) and even dominate the low-latitude behavior /45/. Although less conspicuous, these effects may have important implications for theoretical considerations. They have been attributed to the downward-directed wind component of planetary-scale circulation /36,37,40,46,47/, to the heating action of large-scale traveling atmospheric disturbances (e.g. /48-54/ and references therein), and to the dissipation of ring current energy /55,56/.

4. TEMPORAL VARIATIONS

The temporal development of thermospheric storms is essentially determined by the changing intensity of the solar wind energy source. The sluggish response of the thermosphere somewhat smoothes this primary time variation and also leads to a prolonged recovery phase ('memory effect'). Additional temporal variations are introduced locally by changes in the spatial distribution of the energy injection and globally by the large-scale dynamics of the thermosphere.

The temporal association of magnetic and thermospheric perturbations has long been considered a key problem of the geomagnetic activity effect /57/. The reliable determination of this time sequence is not an easy task because a single satellite cannot distinguish between temporal and spatial changes, and both are usually contained in the data. Accordingly, only upper bounds can be established. Add to this the difficulty of identifying related features in the magnetic and the thermospheric storm effects. Thus only a limited number of cases are available to study this important connection.

Figure 8 compares the temporal variation of the magnetic AE index and of the associated changes in the N_2 density at high latitudes. The time resolution is 1 hour for the AE index and 1 1/2 hours for the density data. As before, the N_2 data have been adjusted to a common altitude. This comparison shows that at high latitudes the time delay between the magnetic and thermospheric disturbance may be rather short and of the order of one hour (or less). Somewhat larger time lags are expected and observed at low latitudes (e.g. /21,45/). Here time delays between (sub-) storm onset and thermospheric response are of the order of 4 hours (or less). This is illustrated in Fig. 9. Note that since the low-latitude response cannot be expected to be uniform, different time lags may be observed at different locations!

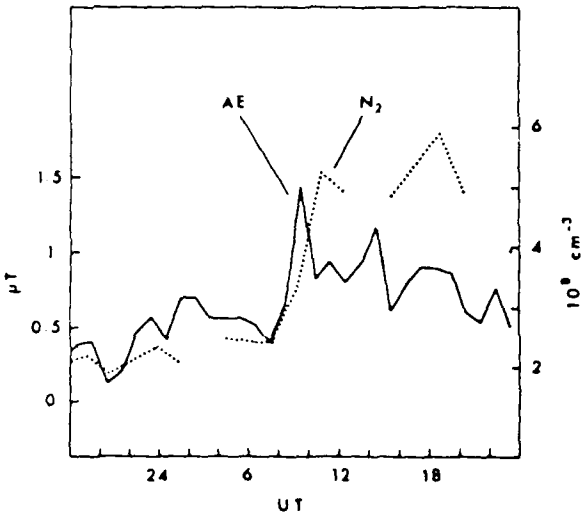

Fig. 8. Time delay between magnetic activity and thermospheric perturbations at high latitudes. The level of magnetic activity is indicated by the auroral electrojet index (AE, left-hand scale). The associated atmospheric disturbance at 60° N magnetic latitude is indicated by changes in the molecular nitrogen density (N_2, right-hand scale). The densities have been adjusted to a common altitude of 280 km. Solar local time of observation was approximately 0900 hours.

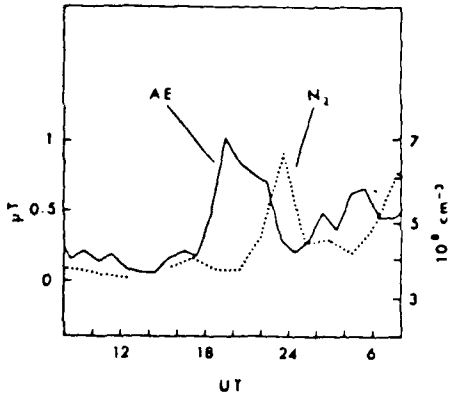

Fig. 9. Time delay between high-latitude magnetic activity and low-latitude atmospheric perturbations. The level of magnetic activity at high latitudes is indicated by the auroral electrojet index (AE, left-hand scale). The associated atmospheric disturbance at low latitudes is documented by changes in the molecular nitrogen density (N_2, right-hand scale). The density values are averages which refer to the 5-10° S geographic latitude region. They have been adjusted to a common altitude of 290 km. Solar local time of observation is approximately 0:45 /45/.

5. SYSTEMATIC VARIATIONS

Besides a strong irregular component, certain systematic trends are observed in thermospheric storm effects. Their documentation, however, is often difficult and far from complete. In the following, four of the better known variations will be considered.

Changes with magnetic activity. Changes in the level of magnetic activity affect thermospheric perturbations in two ways: first, the amplitude of the temperature and density perturbation is related to the intensity of the magnetic disturbance. And secondly, the extent of the composition disturbance zone increases with increasing magnetic activity. Magnetic activity, of course, is only a measure of the intensity of the solar wind energy dissipation. Since any of the numerous magnetic activity indices monitors this dissipation rate, all of them are correlated with thermospheric perturbation effects. Fig. 10 illustrates the dependence of the exospheric temperature increase in the polar region on three of these indices for one particular data set. This figure also documents the direct correlation of the temperature increase with solar wind conditions /58/.

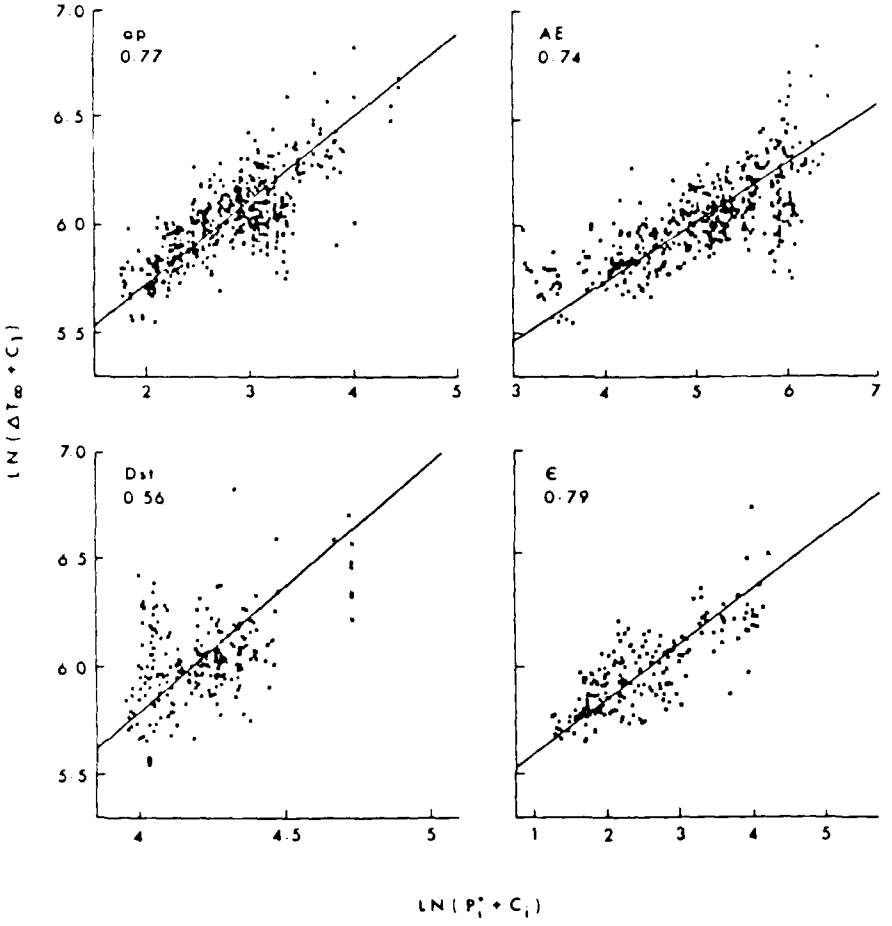

Fig. 10. Increase in the exospheric temperature as a function of magnetic activity and solar wind conditions. The temperature has been inferred from molecular nitrogen measurements obtained in the polar heating oval during winter nighttime conditions. The solar wind conditions are described by the ε parameter /62/. The previous history of the magnetic and solar wind activity has been taken into account up to 23 hours before the actual temperature measurement using a simple algorithm ($P_1^* = f(P_1(t-t_o))$ with P_1=ap, AE, Dst, and ε, respectively, at time t prior to the temperature measurement at time t_o /58,61/). The temperature increase is measured in Kelvin, the ε parameter in 10^{10} W. C_1, C_2, C_3, C_4 and C_5 are constants equal to 300 K, 5, 5nT, 50nT, and 30 GW, respectively. The correlation coefficient is given in the upper left-hand corner.

which of the many magnetic indices is actually best correlated with thermospheric storm effects has not yet been established. Also, the form in which these indices are to be used in modeling these effects is still a matter of intuition. Agreement exists on the fact that the thermosphere integrates the irregular energy injections, and also 'remembers' previous perturbations. Therefore, the history and development of the magnetic activity has to be taken into account (e.g. /59-61/).

Changes with location. The spatial structure of thermospheric storm effects is primarily determined by their latitudinal variation. Here systematic differences between the high and low latitude region are evident and have been discussed in sections 2 and 3. In addition, longitudinal variations are observed (e.g. /17,31,62,63/) and are documented in Fig. 11. These changes are primarily due to the magnetic control of the solar wind energy dissipation, and this control is also impressed on the thermospheric response. Accordingly, thermospheric storm effects are better ordered in a magnetic rather than in a geographic coordinate system /64,65/.

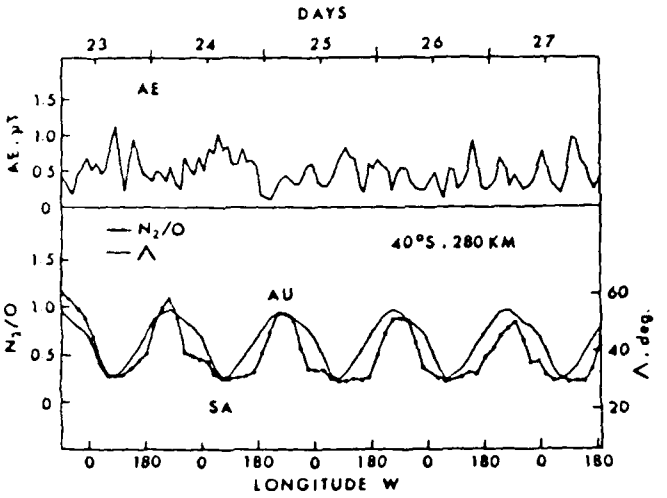

Fig. 11. Longitudinal variations of thermospheric storm effects. The lower part shows a comparison between the longitudinal variation of the N_2/O concentration ratio and the longitudinal variation of the invariant latitude along a constant geographic latitude of 40° S. Time (UT) and longitude (west) of the measurements are indicated at the top and bottom of the figure. The composition data have been adjusted to a common altitude of 280 km, and solar local time of observation is approximately 10:30 hours. Using the AE index as an indicator, the upper panel shows the level of magnetic activity during the time interval of interest /20/.

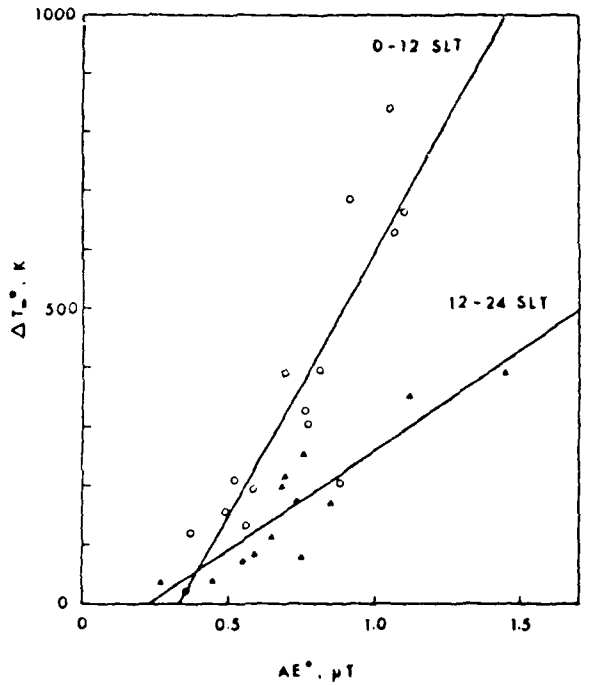

Fig. 12. Temperature increase at middle latitudes as a function of magnetic activity for two different local time sectors. ΔT^* denotes the maximum temperature increase - as indicated by the upper envelope of the disturbance profiles - averaged between 40° and 50° magnetic latitude. AE^* denotes the maximum 3-hourly averaged AE index. Open circles and filled triangles distinguish between morning (0-12 SLT) and afternoon/evening (12-24 SLT) data, respectively. Also shown are the corresponding regression lines /68/.

weaker longitudinal/universal time variations are also observed in a magnetic coordinate system and are attributed to the influence solar radiation has on the disturbance morphology.

Changes with local time. Both the magnitude and extent of the composition disturbance depend on local time, and perturbations are found to be largest in the early morning sector (e.g. /4,15,20,66,67/). As an example, Fig. 12 illustrates that the maximum temperature increase at middle latitudes is significantly larger in the morning sector than in the afternoon/evening sector. These findings are consistent with the idea that the major transfer of disturbance energy from the polar to the mid-latitude thermosphere takes place during the early morning hours (e.g. /68-71/).

Changes with season. Seasonal variations of thermospheric storm effects provide additional evidence for the complex interplay of solar wind and solar radiation effects. This interplay leads to an increased spreading of the disturbance effects toward lower latitudes during the summer season, especially in the early morning sector /72/. One consequence of

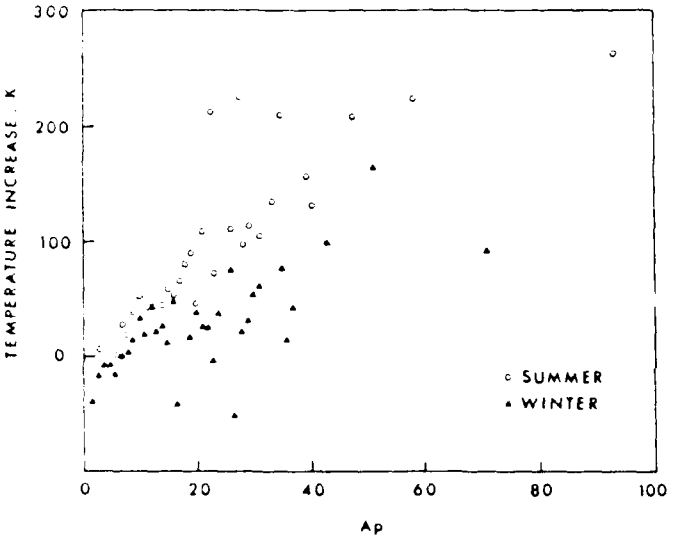

Fig. 13. Temperature increase at middle latitudes as a function of magnetic activity for two different seasons. The incoherent scatter temperature measurements have been grouped into half-year seasons centered on midsummer (open circles) and midwinter (filled triangles) day and averaged into Ap bins of unity width after suppression of other geophysical variations (adapted from /73/).

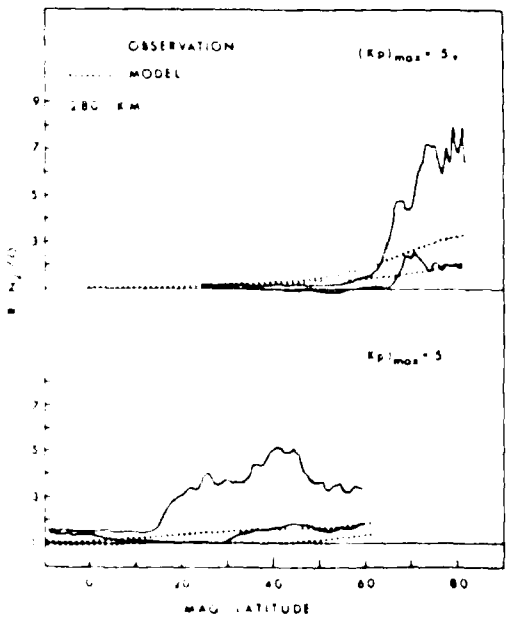

Fig. 14. Observed and predicted latitudinal structure of thermospheric storms. The intensity of the composition disturbance is indicated by changes in the N_2/O concentration ratio. All data refer to the same altitude of 280 km, and $R(N_2/O)=1$ serves as the quiet-time reference. In each case, the ten most disturbed latitudinal profiles have been superimposed. The range of the observed values is indicated by the shaded area. These observations are compared to the MSIS-83 /79/ model predictions for the same geophysical conditions. The predicted range of values is bounded by the dotted lines.

this increased spreading are larger summer disturbance effects at middle latitudes /73/. Figure 13 shows that these differences may be quite significant. Statistical studies also indicate that in the heating oval and for the same level of magnetic or solar wind activity, the temperature increase is larger in the summer than in the winter hemisphere (e.g. /58/). These findings are not at variance with observations that the relative N_2 density increase is larger in the winter hemisphere /61/.

6. MODELING THERMOSPHERIC STORM EFFECTS

Present-day models (e.g. /64,74-79/ and references therein) can only attempt to reproduce the large-scale and average properties of a thermospheric storm. A more detailed description is impeded (1) by our incomplete understanding of this phenomenon; (2) by its complex morphology and (3) by its partly irregular behavior. Hence larger discrepancies between model predictions and actual measurements must be taken into account and have been observed repeatedly. Fig. 14 serves to illustrate the magnitude and nature of these differences.

Based on changes in the N_2/O density ratio, the latitudinal structure of the composition disturbance zone is shown for two different storm events. In each case, the most disturbed latitudinal profiles have been superimposed. This range of storm-time values is compared with corresponding model predictions. The observed differences are sometimes quite large. They may be explained by the irregularity of storm effects and also by the limitations of present-day model algorithms.

We conclude that during storm conditions, model predictions become less reliable. Whereas the basic features may be well-reproduced, a more detailed prediction is not yet possible. This also applies to the presently available theoretical models of thermospheric storms (e.g. /80,81/).

Acknowledgments: We are very grateful to U. von Zahn, who provided the ESRO 4 data used in this study, and to P. Blum and H. Volland for their helpful comments and continued support. This research was financed by the Deutsche Forschungsgemeinschaft under grant No 446/7-2.

REFERENCES

1. L. G. Jacchia, Nature 183, 1662 (1959).
2. P.B. Hays, A.F. Nagy, and R.G. Roble, J. Geophys. Res. 74, 4162 (1969).
3. D.R. Taeusch, G.R. Carignan, and C.A. Reber, J. Geophys. Res. 76, 8318 (1971).
4. J.E. Blamont and J.M. Luton, J. Geophys. Res. 77, 3554 (1972).
5. L.L. DeVries, Space Research XII, 777 (1972).
6. A.D. Anderson, Planet. Space Sci. 21, 2049 (1973).
7. R.R. Allan, Nature 247, 23 (1974).
8. Y.A. Romanovsky and V.V. Katyushina, Space Research XIV, 163 (1974).
9. U. von Zahn, Early aeronomy results from the satellite Esro 4, in: Atmospheres of Earth and the Planets, B.M. McCormac (ed.), Reidel Publ. Co., Dordrecht, Holland, pp. 133-157 (1975).
10. G.W. Prölss and K.H. Fricke, Planet. Space Sci. 24, 61 (1976).
11. H. Trinks, K.H. Fricke, U. Laux, G.W. Prölss, and U. von Zahn, J. Geophys. Res. 80, 4571 (1975).
12. S. Chandra and N.W. Spencer, J. Geophys. Res. 81, 5018 (1976).
13. K. Marubashi, C.A. Reber, and H.A. Taylor, Jr., Planet. Space Sci. 24, 1031 (1976).
14. C.R. Philbrick, J.P. McIsaac and G.A. Faucher, Space Research XVII, 349 (1977).
15. J.S. Nisbet, B.J. Wydra, C.A. Reber, and J.M. Luton, Planet. Space Sci. 25, 59 (1977).
16. A.E. Hedin, P. Bauer, H.G. Mayr, G.R. Carignan, L.H. Brace, H.C. Brinton, A.D. Parks, and D.T. Pelz, J. Geophys. Res. 82, 3183 (1977).
17. T.E. Cravens and A.I. Stewart, J. Geophys. Res. 83, 2446 (1978).
18. W.E. Potter, D.C. Kayser, and A.O. Nier, Space Research XIX, 259 (1979a).
19. D.P. Sipler and M.A. Biondi, J. Geophys. Res. 84, 37 (1979).
20. G.W. Prölss, Rev. Geophys. Space Phys. 18, 183 (1980).
21. C. Berger and F. Barlier, J. Atmos. Terr. Phys. 43, 121 (1981).
22. G.R. Carignan, T. Dachev, A.E. Hedin, C.A. Reber, and N.W. Spencer, Geophys. Res. Lett. 9, 949 (1982).
23. M.J. Engebretson, M.J. and K. Mauersberger, J. Geophys. Res. 88, 6331 (1983).
24. G. Hernandez and R.G. Roble, J. Geophys. Res. 89, 9049 (1984).
25. T. Yagi and P.L. Dyson, J. Atmos. Terr. Phys. 47, 1075 (1985).
26. D.R. Bates, Proc. Roy. Soc. London, A253, 451 (1959).
27. L.G. Jacchia, Smithson. Astrophys. Obs. Spec. Rept. 170, Cambridge, Mass. (1964)
28. J.C.G. Walker, J. Atmos. Sci. 22, 462 (1965).

S. Chandra, N.W. Spencer, D. Krankowsky, and P. Lämmerzahl, Geophys. Res. Lett. 3, 718 (1976).
W.E. Potter, D.C. Kayser, and A.O. Nier, J. Geophys. Res. 84, 10 (1979).
G.W. Prolss and U. von Zahn, J. Geophys. Res. 79, 2535 (1974).
G.W. Prolss, Veroffentl. Astron. Inst. Bonn No. 94, Inst. f. Astrophysik, Bonn (1981)
A.K. Sinha and S. Chandra, J. Atmos. Terr. Phys. 36, 2055 (1974).
P.W. Blum, C. Wulf-Mathies and H. Trinks, Space Research XV, 209 (1975).
P.B. Hays, R.A. Jones, and M.H. Rees, Planet. Space Sci. 21, 559 (1973).
H.G. Mayr and H. Volland, Planet. Space Sci. 20, 379 (1972).
H.G. Mayr and H. Volland, J. Geophys. Res. 78, 2251 (1973).
T. Shimazaki, Space Research 12, 1039 (1972).
G.W. Prolss and M. Roemer, Adv. Space Res. 5, No. 7, 193 (1985).
H. Volland and H.G. Mayr, J. Geophys. Res. 76, 3764 (1971).
H. Rishbeth, Radio Sci. 9, 183 (1974).
J.-C. Gérard and R.G. Roble, Planet. Space Sci. 30, 1091 (1982).
G.A.M. King, J. Atmos. Terr. Phys. 957 (1966).
P.M. Banks and A.F. Nagy, Geophys. Res. Lett. 1, 305 (1974).
G.W. Prolss, J. Geophys. Res. 87, 5260 (1982).
H.G. Mayr and A.E. Hedin, J. Geophys. Res. 82, 1227 (1977).
H. Volland, J. Atmos. Terr. Phys. 41, 853 (1979).
W. Blumen and R.G. Hendl, J. Atmos. Sci. 26, 210 (1969).
J. Kostermeyer, J. Atmos. Terr. Phys. 34, 764 (1973).
J. Testud, P. Amayenc, and M. Blanc, J. Atmos. Terr. Phys. 37, 989 (1975).
A.D. Richmond, J. Geophys. Res. 84, 1880 (1979).
A.D. Richmond, J. Geophys. Res. 84, 5259 (1979).
K.D. Cole and M.P. Hickey, Adv. Space Res. 1, No. 12, 65 (1981).
H.G. Mayr, I. Harris, F. Varosi, and F.A. Herrero, J. Geophys. Res. 89, 10961 (1984).
G.W. Prolss, K. Najita, and P.C. Yuen, J. Atmos. Terr. Phys. 35, 1889 (1973).
B.A. Tinsley, J. Atmos. Terr. Phys. 43, 617 (1981).
M. Roemer, Recent observational results on the thermosphere and exosphere, CIRA 1972 (exec. ed. A.C. Stickland), Akademie-Verlag, Berlin, pp. 341-396 (1972).
G.W. Prolss, J. Geophys. Res. 90, 11096 (1985)
A.E. Hedin, N.W. Spencer, H.G. Mayr, and H.S. Porter, J. Geophys. Res. 86, 3515 (1981).
J.S. Nisbet, C. Stehle, and E. Bleuler, J. Geophys. Res. 88, 2175 (1983).
G.W. Prolss and M. Roemer, Adv. Space Res. 3, No. 1, 99 (1983).
L.G. Jacchia, J.W. Slowey, and U. von Zahn, J. Geophys. Res. 81, 36 (1976).
G. Thuillier, J.L. Falin, and F. Barlier, J. Atmos. Terr. Phys. 42, 653 (1980).
L.G. Jacchia, J.W. Slowey, and U. von Zahn, J. Geophys. Res. 82, 684 (1977).
G.W. Prolss, Adv. Space Res. 3, No. 1, 55 (1983).
D.R. Taeusch, J. Geophys. Res. 82, 455 (1977).
J.W. Slowey, Adv. Space Res. 1, 213 (1981).
G.W. Prolss, Ann. Geophys. 2, 481 (1984).
J.S. Nisbet and D.A. Glenar, J. Geophys. Res. 82, 4685 (1977).
G.W. Prolss and U. von Zahn, Space Research XVIII, 159 (1978).
R.R. Babcock and J.V. Evans, J. Geophys. Res. 84, 5349 (1979).
G.W. Prolss and U. von Zahn, J. Geophys. Res. 82, 5629 (1977).
W.L. Oliver, J. Geophys. Res. 85, 4237 (1980).
U. von Zahn, W. Kohnlein, K.H. Fricke, U. Laux, H. Trinks, and H. Volland, Geophys. Res. Lett. 4, 33 (1977).
M.J. Engebretson, K. Mauersberger, D.C. Kayser, W.E. Potter, and N.A. Nier, J. Geophys Res. 82, 461 (1977).
F. Barlier, C. Berger, J.L. Falin, G. Kockarts, and G. Thuillier, Ann. Geophys. 34, 9 (1978).
W. Kohnlein, Planet. Space Sci. 28, 225 (1980).
C.G. Stehle, J.S. Nisbet, and E. Bleuler, J. Geophys. Res. 87, 1615 (1982).
A.E. Hedin, J. Geophys. Res. 88, 10170 (1983).
H. Rishbeth, R. Gordon, D. Rees, and T.J. Fuller-Rowell, Planet. Space Sci. 33, 1283 (1985).
H.G. Mayr and H. Trinks, Planet. Space Sci. 25, 607 (1977).
P. Perreault and S.-I. Akasofu, Geophys. J. R. astr. Soc. 54, 547 (1978).

Adv Space Res Vol 7, No 10, pp (10)237–(10)245, 1987
Printed in Great Britain. All rights reserved.

0273-1177/87 $0.00 + .50
Copyright © 1987 COSPAR

THERMOSPHERIC STORM EFFECTS

J. W. Slowey

Harvard-Smithsonian Center for Astrophysics, Cambridge MA 02138, U.S.A.

ABSTRACT

A brief review is given of our current understanding of the atmospheric perturbations in the thermosphere and exosphere that are related to geomagnetic disturbances and of current efforts to represent these in empirical models of the upper atmosphere. A particular model, based on ESRO4 mass spectrometer observations of neutral composition and density, is presented in detail. This model gives the effects on the principal constituents of the upper atmosphere as a function of the geomagnetic coordinates and the K_p geomagnetic index. It is a modification of an earlier model, the most important difference being the inclusion of the variation with magnetic *local time*.

INTRODUCTION

Significant heating of the neutral upper atmosphere during large geomagnetic storms had long been suspected from auroral and ionospheric research. The first direct evidence of such heating did not come until the early years of the space age, however, when Jacchia /1,2/ was able to show a very clear correlation between magnetic storms and sudden, short-lived, increases in the atmospheric drag on artificial satellites. These early results showed global increases in atmospheric density at all heights in the earth's upper atmosphere accessible to satellites.

Subsequent to Jacchia's initial discovery, satellite drag was used extensively to study the geomagnetic variation in the thermosphere and exosphere. At first, it was thought that the exospheric temperature increase that could be associated with the atmospheric disturbance varied more or less linearly with the *3-hourly* a_p geomagnetic index and that, as a consequence, only relatively large magnetic disturbances could be detected in the drag on satellites. Analysis of the drag on the Explorer 17 satellite, however, revealed small density variations /3/ that Jacchia and Slowey /4/ then found to also be present in the densities derived from other satellites and to be correlated with small variations in geomagnetic activity during what would otherwise be described as "quiet" conditions. Except for very large storms, the associated increase in exospheric temperature was, in fact, shown to vary nearly linearly with the K_p geomagnetic index, the quasi-logarithmic equivalent of a_p, so that detectable thermospheric effects could be expected as a result of even the smallest magnetic perturbations. Slightly earlier, Jacchia and Slowey /5/ had analyzed the drag on the high-inclination satellite Injun III and found the geomagnetic variation to be substantially enhanced in the auroral zones and that the time lag between the geomagnetic and atmospheric disturbances increased in going from high to low latitudes. These effects were seen as evidence of the transport of energy from high to low latitudes, as was later corroborated by observations of winds /6,7/ and waves /8,9/ in the thermosphere. Later, Roemer /10/ analyzed the drag on a number of satellites at heights between 250 and 800 km and was able to detect a sinusoidal dependence of the geomagnetic variation on local time, with a maximum in the derived exospheric temperature increase at 3 am that was systematically larger by a factor of 1.3 with respect to a 3 pm minimum. Just such a dependence is confirmed by more recent measurements made by satellite-borne gas analyzers and other instruments and can be seen to result both from the locations of the high-latitude heat sources and the dynamic processes driven by them.

Concurrently with these studies, models of the geomagnetic variation were being developed. These consisted primarily of an expression for the increase in exospheric temperature associated with a disturbance as a function of either the a_p or the K_p geomagnetic index. This temperature increase was to be added to the "quiet" exospheric temperature appropriate to the other prevailing conditions and the sum used to determine the density at any height from the corresponding static diffusion model of the thermosphere. Implicit in this approach was the assumption that the temperature profile used to

generate the static model was not perturbed by the geomagnetic disturbance. This is clearly not the case, of course, and additional "engineering" was later found to be necessary in order to adequately represent the geomagnetic variation at lower heights. These extremely simple models were adequate at greater heights, however, and the data then available were reasonably well represented by them. Such a model /4/ was recommended in the CIRA65 model and directly incorporated in Jacchia's highly successful 1965 empirical models of the thermosphere /11/.

The development of models of the geomagnetic variation from satellite drag essentially culminated with the model derived by Jacchia *et al.* /12/ in 1967. This model was incorporated without modification in Jacchia's 1970 thermospheric models /13/. At about that time, however, significant new data from the drag on low-altitude satellites became available /14,15,16/ that showed density variations related to geomagnetic activity which could not be adequately represented by a variation in exospheric temperature alone. Thus, when Jacchia published a revised version of his model a year later /17/, a hybrid formula including both temperature and density components was introduced to represent the geomagnetic variation at low heights. It was Jacchia's 1971 model, complete with this dual representation of the geomagnetic variation, that was incorporated as the thermospheric part of the CIRA72 model.

The models derived entirely from atmospheric drag are still widely used, especially in connection with problems relating to orbital dynamics. To show the simplicity of the model of the geomagnetic variation of CIRA72 and to provide a basis for later comparison, we will reproduce that model here. According to CIRA72, the geomagnetic variation at heights above 350 km is given entirely by the following expression for the increase in exospheric temperature (equation (18) of CIRA72):

$$\Delta_G T_\infty = 28K_p' + 0.03\exp(K_p')$$

where K_p' is the 3-hourly K_p geomagnetic index at a time $t - \tau$ and the time lag τ is given as 6.7 hours. At heights below 350 km, the density variations are represented by the expressions (equation (20) of CIRA72):

$$\Delta_G \log \rho = 0.012K_p' + 1.2\times10^{-5}\exp(K_p') \qquad \text{(a)}$$

$$\Delta_G T_\infty = 14K_p' + 0.02\exp(K_p') \qquad \text{(b)}$$

where K_p' is the same as in the first equation and the increase in total density is to be obtained by adding the variation given by (a) to that corresponding to the exospheric temperature increase given by (b). The computer code for the thermospheric models that was included in CIRA72 uses an interpolation scheme to make a smooth but rather abrupt transition between the high-height and low-height versions of the geomagnetic model in the vicinity of 350 km.

THE NATURE OF THE VARIATION

The resolution provided by the satellite-drag method could only give a smoothed picture of a phenomenon that is characterized by rapid changes and extreme spatial complexity. Time resolution as short as 0.1 day has been achieved using the most precise optical observations /18/, but a resolution of 0.20 - 0.25 day during even the largest magnetic storms is more typical of the data from orbital analysis. Since the drag effect cannot be resolved within a single revolution, the derived density necessarily also represents an average over a fairly long arc in the vicinity of the satellite's perigee. Thus, while the geomagnetic variation was expected to be complex in nature, the available data could only hint at some of the major details of that complexity.

The first high-resolution measurements of density and composition from satellite-borne accelerometers /19/ and gas analyzers /20/ became available at about the time that CIRA72 was published. Since that time, large quantities of data have been added by numerous other missions bearing similar instrumentation. Prominent among these have, of course, been the Atmosphere Explorer and Atmosphere Dynamics series of instrumented satellites of NASA. These data have been used extensively both to study individual disturbances and to derive more detailed empirical models of the geomagnetic variation. The accelerometer data have, of course, been important because of their greatly improved resolution as opposed to drag analysis. The gas-analyzer results have, however, been especially important because they also provide data on composition. Large variations in composition have been found to be a very significant feature of the geomagnetic variation in the thermosphere.

In Figure 1 we show a plot of molecular nitrogen density measured during a portion of one orbit of the Atmosphere Explorer-C satellite by the OSS mass-spectrometer. The data were collected during a

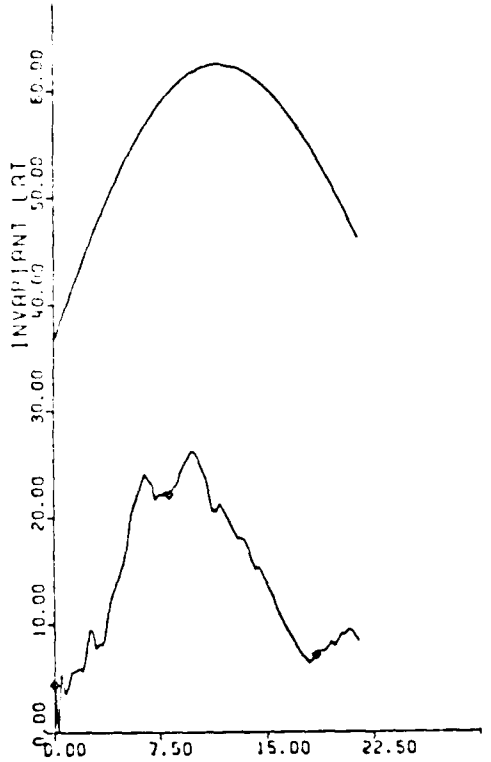

Fig. 1. Logarithm of N_2 density at a height of 250 km as measured by the OSS mass spectrometer on AE-C during a portion of orbit 4919. The abscissa is the time in minutes from an arbitrary zero point and the ordinate is not given (see text). The smooth curve is the invariant geomagnetic latitude with ordinate scale on the left (from /25/)

period of relatively high geomagnetic activity (1.5 hours earlier, K_p was 6+) and when the satellite was in a nearly circular orbit. Since the height varied so little, it was safe to reduce them to a single height for purposes of analysis and that is the way they are shown here. The abscissa is the time in minutes, starting from an arbitrary zero point. The scale of the ordinate of the N_2 number density is not shown, but it represents the change in the logarithm of the number density. The maximum density here corresponds to a change of 0.5 in $\log_{10} n(N_2)$, an increase by a factor of more than 3 in number density, relative to the density at the origin of the plot. The smooth curve at the top of the figure is the (adiabatic invariant) geomagnetic latitude plotted on the scale at the left of the figure.

The strong dependence of the geomagnetic variation on geomagnetic latitude is well established and we can see it in orbit after orbit of the AE-C and other satellite-borne mass spectrometer data, not only in N_2 but in all constituents. Not all constituents behave the way N_2 does, however, and this is another important aspect of the geomagnetic variation. The behavior of the lighter constituents, such as He, is just the opposite of that of N_2: their number densities decrease where those of N_2 increase. And the density of atomic oxygen, which is of primary importance as far as total density is concerned throughout much of the thermosphere, may either increase, decrease or remain unchanged. In addition to a purely thermal effect, there is obviously another factor involved in which the molecular mass plays an important role. The observed "signature" is, of course, not unique to any one particular process. It can be seen in thermospheric gravity waves and would be expected as a result of vertical winds in the vicinity of the homopause. Blum *et al.* /21/ have also suggested a variation in the height of the homopause as a mechanism that would produce such a result. The later process, whether or not it is physically realistic, provides a very convenient device with which to model this aspect of the geomagnetic variation.

In Figure 2, we show plots of Ar, N_2, O, and He number densities as well as total density as measured by the ESRO4 mass spectrometer during an interval of sustained geomagnetic disturbance. The data are those for the points when the satellite crossed the 280 km level. There are two such crossings in each orbital revolution, one on the ascending branch and the other on the descending branch of the orbit, and the data are accordingly divided into two separate groups. The geomagnetic latitude, ϕ_{gm}, of the subsatellite point is also plotted for each group as is the K_p index. The general dependence on geomagnetic latitude is quite obvious in the figure. The geographic latitude of the subsatellite point changes very little during the interval shown, but the geomagnetic latitude oscillates on a daily basis due to the offset of the geomagnetic pole and the rotation of the earth under the satellite orbit. Those oscillations are clearly reflected in the data of the upper plot of the figure, where the 280-km crossings were in middle latitudes, but are much less prominent in the lower plot, where the crossings were in very

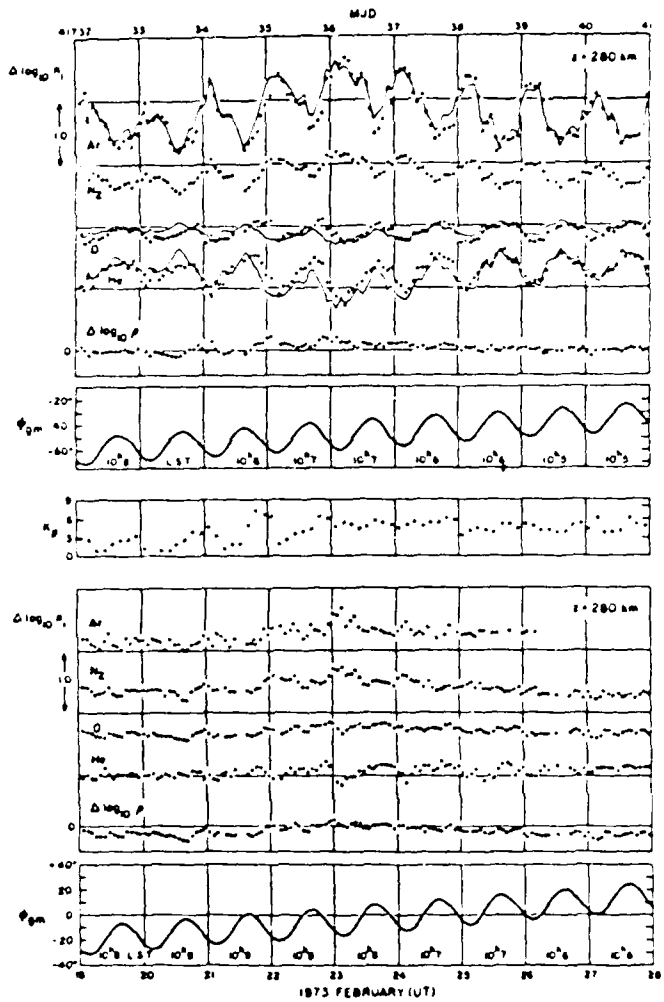

Fig. 2. Variations of four constituents at 280 km at middle and low latitudes as measured by the ESRO4 mass spectrometer during an interval of sustained geomagnetic activity. The dots are data points and the solid lines are values computed from the N_2 variations. ϕ_{gm} is the geomagnetic latitude and K_p is the geomagnetic index. Note the regular 24-hour variations at middle latitudes and their absence at low latitudes (from /22/).

low latitudes. The upper plot of the figure also illustrates the behavior of the different constituents we've described above and demonstrates how a variation in the height of the homopause can be used to represent that behavior. If we assume the height of the homopause, z_H, to change in proportion to the change in exospheric temperature and compute the temperature variation from the N_2 density, which would be little affected by a change in homopause height, the effect on the other constituents can be easily calculated. This was done for the data in the upper plot, taking dz_H/dT = 53 m/°K, with the results shown by the solid lines. In Figure 3, we again show data from the ESRO4 mass spectrometer as in Figure 2, but during an interval when there was an intense magnetic storm followed by a period of sustained geomagnetic activity. Here the major point of interest is in the lower plot, where the data are for low latitudes and the variations of all four species are in-phase and have comparable amplitudes. This is typical of the data at low latitudes and is indicative of a different regime from that found in middle and high latitudes. Only occasionally is the behavior seen at higher latitudes observed near the equator, as it is around 22 and 23 February, 1973 in the lower plot of Figure 2.

The atmospheric variations are not just dependent on the geomagnetic latitude, however. There are two distinct maxima in the data of Figure 1 that represent separate regions of enhancement in the vicinity of the auroral oval. As that figure demonstrates, there is also an appreciable over-all asymmetry with respect to geomagnetic latitude.

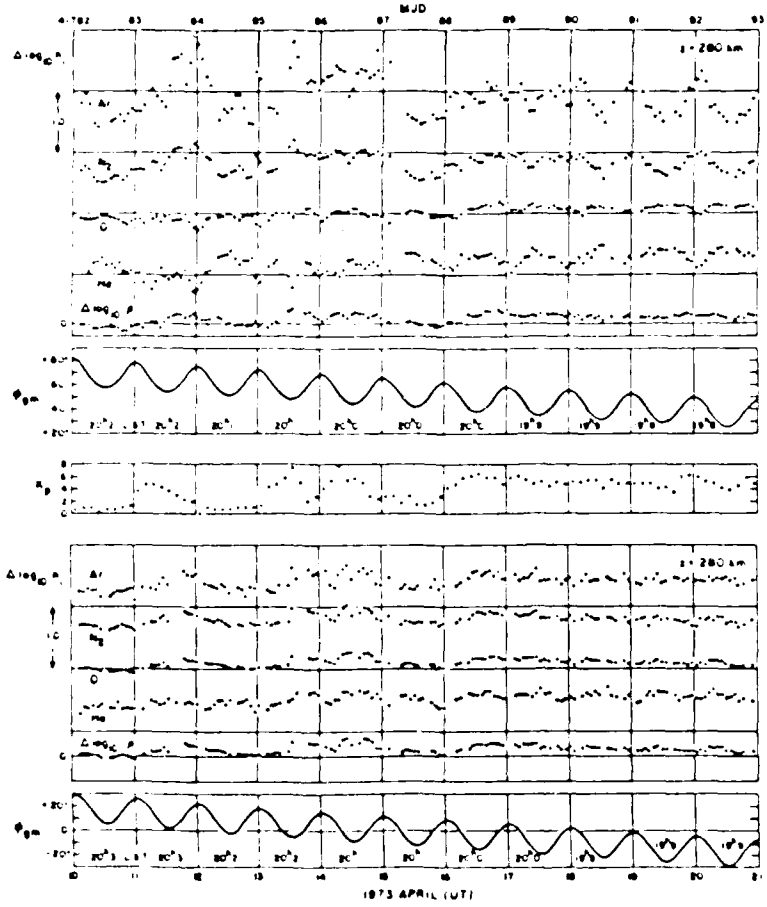

Fig. 3. Same as Figure 2, but at middle and low latitudes during an intense storm followed by a period of sustained geomagnetic activity. Note the in-phase oscillations of all four species in the low latitude region (from /22/).

ESRO4 MODEL

There are, at present, theoretical models that are capable of representing the disturbed thermosphere in great detail and with considerable precision, given the parameters appropriate to the particular situation. As a practical matter, however, the need for empirical models continues to exist and, since the theoretical models are discussed elsewhere in this issue, we will devote the remainder of the discussion here to empirical models. Also, since there are really only two such models based on high-resolution data in prominent use and one of these is a part of the MSIS empirical thermospheric models that are likewise discussed elsewhere, we have only one model left to discuss. That model is the one derived by Jacchia *et al.* /22,23/ from the ESRO4 mass spectrometer data and that is incorporated in Jacchia's 1977 model of the thermosphere /24/. Here, however, we will present a modified version of that model similar to the one given recently by Slowey /25/. The modifications that will be introduced are as follows.

1) Include the most significant features of the variation with local magnetic time. The original model includes only the mean variation with latitude.

2) Allow the latitudinal form of the model to vary with the level of disturbance. The latitudinal variation has been shown to broaden in high latitudes with increasing levels of disturbance /26/, apparently due to the changing position of the polar cusp region /27/.

3) Allow for the prior heat input in establishing an index for the level of disturbance. Theoretical calculations /28/ and semiempirical modeling /29/ both indicate that the disturbance history over the preceding 5 days is probably significant.

4) Allow for an increase in exospheric temperature at the equator. In the original model, the effect at the equator is represented entirely in terms of an "equatorial wave" of density. While it is clear that such a wave is a significant component of the low latitude response, it is equally clear that a thermal component can also exists in low latitudes.

The model of Jacchia *et al.* /23/ represents the density and composition changes that occur in association with a geomagnetic disturbance by a local increase in exospheric temperature and a proportional increase in the height of the homopause. Superimposed on these two effects is the "equatorial wave" referred to above, in which the number densities of all constituents increase in the same proportion and that is centered on the equator. We will adopt the same representation here and model the change in the logarithm of the number density of the species i as the sum of three components:

$$\Delta_G \log n_i = \Delta_T \log n_i + \Delta_H \log n_i + \Delta_e \log n_i \tag{1}$$

where $\Delta_T \log n_i$ is the thermal component, $\Delta_H \log n_i$ is the component due to the change in the height of the homopause and $\Delta_e \log n_i$ is the component due to the equatorial wave.

The thermal component $\Delta_T \log n_i$ is to be evaluated from an atmospheric model assuming an increase in exospheric temperature $\Delta_G T_\infty$ given by

$$\Delta_G T_\infty = A\, F(\phi, \lambda) \tag{2}$$

where A is the amplitude given by

$$A = 57.5 K_p' \left[1 + 0.027 \exp(0.4 K_p')\right] , \tag{3}$$

as in the original model, and $F(\phi, \lambda)$ is given by

$$\begin{aligned} F(\phi,\lambda) = {} & a_{01} + a_{02}\sin^2\phi + \cos^2\phi(a_{11}\sin\lambda + a_{12}\cos\lambda) + \\ & \sin 2\phi(a_{21}\sin\lambda + a_{22}\cos\lambda) + \sin^4\phi \sin 2\phi(a_{31}\sin\lambda + a_{32}\cos\lambda), \end{aligned} \tag{4}$$

where ϕ and λ are the geomagnetic latitude and local magnetic time, respectively.

To take the effects of the prior heat input into account, we assume K_p' in equation (3) to be the weighted mean of the lagged 3-hourly K_p geomagnetic index taken over the 41 values in the preceding 5-day interval as follows:

$$K_p'(t) = \frac{\sum_{i=1}^{41} K_p(t_i) e^{c(t_i - t)}}{\sum_{i=1}^{41} e^{c(t_i - t)}} \tag{5}$$

where t is the time in days, $c = 1.0\ \mathrm{d}^{-1}$ and τ is the time lag given by

$$\tau = 0.05 + 0.1\cos^2\phi \ \text{(day)} \tag{6}$$

In equation (4), the first two terms represent the mean latitudinal variation of the increase in exospheric temperature. The remaining three terms represent the variation of the temperature increase with local magnetic time (LMT) in low, middle and high latitudes, respectively. To introduce a variation in the mean shape of the latitudinal variation with the level of disturbance that is consistent with observation, we take n in equation (4) as

$$n = 5.0 - K_p'/3.0 \tag{7}$$

A determination of the remaining parameters in equation (4) was made by a least squares fit to values of the exospheric temperature increase inferred from N_2 measurements made by the ESRO4 mass spectrometer. Exospheric temperatures were obtained from N_2 densities by inverse interpolation in an atmospheric model. The temperature increase was taken to be the difference between the exospheric temperature corresponding to the observed N_2 density and that corresponding to the density computed for quiet conditions from the ESRO4 "quiet time" model of von Zahn *et al.* /30/. The resulting coefficients are

$$
\begin{aligned}
a_{01} &= .1425 & a_{02} &= .8137 \\
a_{11} &= .1184 & a_{12} &= -.0360 \\
a_{21} &= -.0735 & a_{22} &= .1038 \\
a_{31} &= .3706 & a_{32} &= -.1441
\end{aligned} \tag{8}
$$

In Figure 4, the isotherms of the relative temperature increase as given by equation (4) are plotted over the globe in geomagnetic coordinates for the case where $K_p' = 3$ ($n = 4$). As can be seen, there is a considerable asymmetry with respect to the pole. The maximum is between 6^h and 9^h at a latitude of about 80 degrees. This probably reflects both Joule heating by the westward auroral electrojet and particle precipitation in the cusp region. The extent of the asymmetry can perhaps be better seen in Figure 5, where the profiles for 6^h and 18^h LMT—near the extremes—are plotted together with the mean latitudinal profile. Of course, the difference in high latitudes as seen by an orbiting object would tend to be smoothed out over intervals on the order of a day because of the earth's rotation. This would not be the case in low latitudes, however, which explains how Roemer /10/ was able to detect the asymmetry in densities determined from drag analysis.

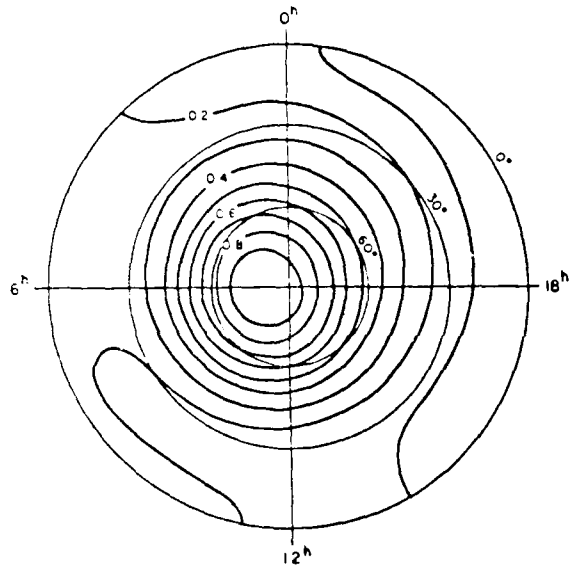

Fig. 4. Global isotherms of the relative temperature increase as given by equation (4) for $K_p' = 3$. The coordinates are geomagnetic latitude and magnetic local time (from /25/).

Jacchia /24/ has found that the response of the lower thermosphere to geomagnetic disturbance can be represented by perturbing the temperature profiles of his static models by an amount given by

$$\Delta_G T(z) = \Delta_G T_\infty \tanh[c(z - z_0)], \tag{9}$$

where $c = 0.006$ and $z_0 = 90$ km. The disturbed temperature profiles defined by equation (9) yield species densities that are in good agreement with observations at heights as low as 150 km. To apply equation (9) directly, however, requires that the diffusion equation be integrated from the lower boundary of the thermospheric models to the height in question. Fortunately, analytical expressions can be derived from the results of numerical integration of the disturbed profiles from which $\Delta_T \log n_i$, including the effect of equation (9), can be computed. Jacchia /31/ has, in fact, derived the following analytic expression for use with the model:

$$\Delta_T \log n_i = \beta_i \left(\frac{800}{T_\infty}\right)^m f(z) \sinh^{-1}(0.003\,\Delta_G T_\infty), \tag{10}$$

where

$$f(z) = 0.560 + 0.6\frac{z}{100} - 0.00636\left(\frac{z}{100}\right)^2 + \frac{0.29}{1 + 1.7\left(\frac{z}{100} - 1.27\right)^2 + \left(0.3322\frac{z}{100}\right)^{13}} \tag{11}$$

$$m = 1.7 \tanh[0.005(z - 100)]. \tag{12}$$

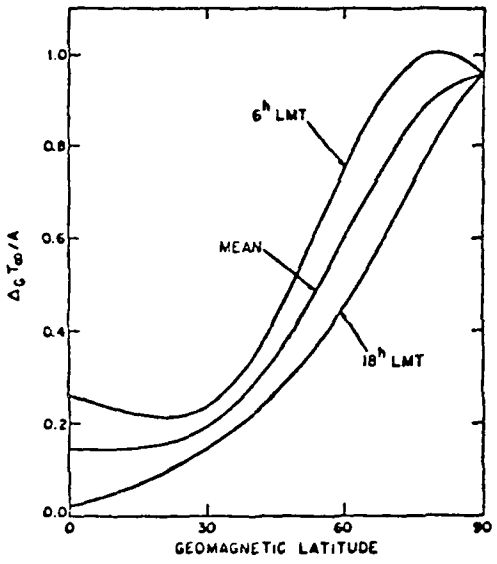

Fig. 5. Latitude profiles of the relative temperature increase for $K_p' = 3$ as given by equation (4) for 6^h and 18^h LMT. The profile of the mean latitudinal variation is also shown (from /25/).

The values of the β_i for the individual constituents are as follows:

$$\begin{array}{ll} \beta(Ar) = 1.50 & \beta(O) = 0.52 \\ \beta(O_2) = 1.16 & \beta(N) = 0.46 \\ \beta(N_2) = 1.00 & \beta(He) = 0.10\,. \end{array} \tag{13}$$

T_∞' in equation (10) denotes the "quiet" value of T_∞.

The component due to the change in the height of the homopause can be computed as in the original model:

$$\Delta_B \log n_i = \alpha_i \Delta z_B, \tag{14}$$

where Δz_B (meters) is obtained from

$$\Delta z_B = 5.02 \times 10^3 \sinh^{-1}(0.01\, \Delta_G T_\infty)\,, \tag{15}$$

with $\Delta_G T_\infty$ given by equation (2), and the α_i's are:

$$\begin{array}{ll} \alpha(Ar) = +3.07 \times 10^{-4} & (mks) \\ \alpha(O_2) = +1.03 \times 10^{-5} & (mks) \\ \alpha(N_2) = 0.0 & \\ \alpha(O) = -4.85 \times 10^{-5} & (mks) \\ \alpha(He) = -6.30 \times 10^{-4} & (mks). \end{array} \tag{16}$$

Finally, the component due to the equatorial wave is computed as in the original model, but with the smaller exponent in the latitudinal response determine by Slowey /32/, by the expression

$$\Delta_e \log n_i = \Delta_e \log \rho = 5.2 \times 10^{-4} A \cos^2 \phi\,, \tag{17}$$

where ρ is the total density and A is given by equation (3).

REFERENCES

1. L.G. Jacchia, *Nature* **183**, 1662 (1959)
2. L.G. Jacchia, *Space Research* II, 747 (1961)
3. J.W. Slowey, *Smithsonian Astrophys. Obs. Spec. Rpt. No. 157* (1964)
4. L.G. Jacchia and J. Slowey, *J. Geophys. Res.* **69**, 4145 (1964)
5. L.G. Jacchia and J. Slowey, *J. Geophys. Res.* **69**, 905 (1964)
6. L.B. Smith, *J. Geophys. Res.* **73**, 4959 (1968)
7. P.B. Hays and R.G. Roble, *J. Geophys. Res.* **76**, 5316 (1976)
8. G.P. Newton, D.T. Pelz and H. Volland, *J. Geophys. Res.* **74**, 183 (1969)
9. K.S.W. Champion, F.A. Marcos and J.P. McIsaac, *Space Research* V, 450 (1970)
10. M. Roemer, *Space Research* XI, 965 (1971)
11. L.G. Jacchia, *Smithsonian Contr. Astrophys.* **8**, 215 (1965)
12. L.G. Jacchia, J. Slowey, and F. Verniani, *J. Geophys. Res.* **72**, 1423 (1967)
13. L.G. Jacchia, *Smithsonian Astrophys. Obs. Spec. Rep. No. 313* (1970)
14. D.G. King-Hele and D.M.C. Walker, *Planet. Space Sci.* **17**, 985 (1969)
15. D.G. King-Hele and D.M.C. Walker, *Planet. Space Sci.* **17**, 1539 (1969)
16. L. Schusterman, Evaluation of low-altitude satellite density data, *TDR-0059(6755)-1*, Aerospace Corp. (1970)
17. L.G. Jacchia, *Smithsonian Astrophys. Obs. Spec. Rep. No. 332* (1971)
18. L.G. Jacchia and J. Slowey, *Space Research* IV, 257 (1963)
19. L.L. DeVries, *Space Research* XII, 777 (1972)
20. D.R. Taeusch, G.R. Carignan and C.A. Reber, *J. Geophys. Res.* **76**, 8313 (1971)
21. P.W. Blum, C. Wulf-Mathies, and H. Trinks, *Space Research* XV, 209 (1975)
22. L.G. Jacchia, J.W. Slowey and U. von Zahn, *J. Geophys. Res.* **81**, 36 (1976)
23. L.G. Jacchia, J.W. Slowey and U. von Zahn, *J. Geophys. Res.* **82**, 684 (1977)
24. L.G. Jacchia, *Smithsonian Astrophys. Obs. Spec. Rep. No. 375* (1977)
25. J.W. Slowey, A new model of the geomagnetic variation in the upper atmosphere, *AFGL-TR-83-0253*, (1983)
26. J.W. Slowey, *Adv. Space Res.* **1**, 213 (1981)
27. C.-I. Meng, *Geophys. Res. Lett.* **9**, 60 (1982)
28. T.J. Fuller-Rowell and D. Rees, *J. Atmos. Ter. Phys.* **43**, 701 (1981)
29. A.E. Hedin, H.W. Spencer, H.G. Mayr, and H.S. Porter, *J. Geophys. Res.* **86**, 3515 (1981)
30. U. von Zahn, W. Köhnlein, K.H. Fricke, U. Laux, H. Trinks and H. Volland, *Geophys. Res. Lett.* **4**, 33 (1977)
31. L.G. Jacchia, private communication (1977)
32. J.W. Slowey, *Adv. Space Res.* **3**, 67 (1983)

Adv. Space Res. Vol. 7, No. 10, pp. (10)247–(10)254, 1987
Printed in Great Britain. All rights reserved.

0273-1177/87 $0.00 + .50
Copyright © 1987 COSPAR

CHANGES IN THERMOSPHERIC DENSITY CAUSED BY TURBULENCE VARIATIONS

P. Blum and G. W. Prölss

Institut für Astrophysik und Extraterrestrische Forschung, Universität Bonn, Auf dem Hügel 71, D-5300 Bonn 1, F.R.G.

ABSTRACT

Seasonal and geomagnetic density variations in the thermosphere can be explained either by a system of thermally driven winds or, equally well, by changes in the turbulence structure. Observations show that both processes take place, but their relative importance has not yet been established. In this paper, a model incorporating both mechanisms is presented. Whereas seasonal changes may be generated by changes in the turbopause height, geomagnetic perturbations may be associated with a turbulent layer above the homopause region.

INTRODUCTION

Observations of thermospheric densities have shown that in the winter hemisphere the relative density of lighter gases, like helium, is increased, while heavier gases, like argon, are depleted as compared to the yearly average densities. In the summer hemisphere, the opposite situation is found. These observations have been incorporated into all empirical models of the thermosphere.

A situation like in the summer hemisphere also exists during increased geomagnetic activity: the relative density of light gases decreases, while the density of heavier constituents increases. These changes are observed not only in the polar regions, where the energy is injected into the thermosphere, but also at subauroral latitudes.

A theoretical explanation of these observations is derived from the diffusion equation. For a binary gas mixture consisting of a major and a minor component, the difference between the vertical transport velocities is given approximately by /e.g. 1/

$$\Delta w = -D\left[\frac{1}{n}\frac{dn}{dz} + \frac{1}{H} + (1+\alpha_T)\frac{1}{T}\frac{dT}{dz}\right] - K\left[\frac{1}{n}\frac{dn}{dz} + \frac{1}{H_H} + \frac{1}{T}\frac{dT}{dz}\right] \quad (1)$$

with

n = density of minor constituent

T = temperature

H = scale height of minor constituent

H_H = homospheric scale height of gas mixture

D = diffusion coefficient

K = eddy diffusion coefficient

α_T = thermal diffusion coefficient

This equation can be solved for the vertical distribution of the minor constituent $n(z)$. A qualitative discussion of the result is facilitated by introducing a sharp boundary – the turbopause – between the region where turbulent mixing is perfect (homosphere, D=0) and the

region where molecular diffusion is perfect (heterosphere, K=0). Neglecting thermal diffusion effects and integrating stepwise from a lower boundary z_o to the turbopause height z_T and from there to some higher altitude z, we obtain

$$n(z) = n(z_o) \cdot \frac{T(z_o)}{T(z)} \exp - \left(\int_{z_o}^{z_T} \frac{dz}{H_H} + \int_{z_T}^{z} \frac{dz}{H} + \int_{z_o}^{z} \frac{\Delta W}{K+D}\, dz \right) \qquad (2)$$

As can be seen, the vertical density profile of a minor species is determined by the density at a certain base level z_o, by the temperature profile, by the molecular and eddy diffusion coefficients D and K, by the turbopause height z_T, and by the relative velocity difference between the minor constituent and the main gas.

Both the density at z_o and the temperature profile need not be considered here as they are assumed to be known. Their contribution to the observed seasonal changes is clear and requires no further explanation.

Seasonal changes of the density above those caused by temperature variations therefore can be explained only by changes in the turbopause height z_T (Fig. 1) and the associated changes in the diffusion coefficients or by changes in the diffusion velocity height profile. In particular, it should be pointed out that the horizontal wind motion does not directly influence the vertical distribution of a species. The effect a horizontal wind system has on the vertical density profile is only indirect. It is governed by the equation of continuity, which connects the divergences of the horizontal and vertical motions. This indirect effect may be considerable.

In the following, models of the seasonal or magnetic-activity-associated thermospheric density changes based on turbopause height variations or turbulent layers will be called "turbulence models", models based on global wind systems "wind models".

SEASONAL VARIATIONS

It has been suggested /e.g. 2/ that the seasonal variation of the thermospheric density is caused by a seasonal change in the turbopause height. While models based on this assumption provide an explanation for the characteristic changes observed, they also suffer from some shortcomings. These deficiencies may be summarized as follows:

(1) The required changes in the turbopause height appear to be rather large (up to 2.5 scale heights).
(2) The observations presently available /e.g. 3,4,5,6/ do not provide a firm basis for the postulated turbopause height variations.
(3) Competing mechanisms (like wind-induced diffusion) are neglected.

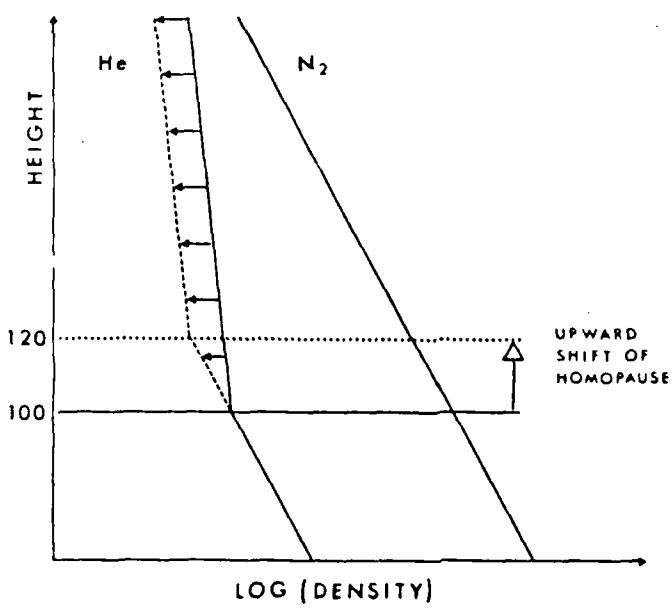

Fig. 1 Density changes of a minor constituent (helium) caused by changes in the turbopause height.

An alternate explanation for the observed seasonal variations is offered by global circulation models (e.g. 7,8,9/. This explanation is based on the divergence of horizontal wind systems and the associated vertical diffusion effects. These models also suffer from some difficulties:

- Three-dimensional calculations of thermospheric wind cells pose serious computational difficulties which may affect the validity of the results obtained. Also, many of the required input parameters are not well known at the present.
- Firm observational support for the predicted and required wind system is not yet available, especially in the all important height region below, say, 200 km /e.g. 10/.
- As was the case for the turbulence models, competing mechanisms (like turbopause height changes) are neglected.

To overcome some of these difficulties, a new model has been constructed which considers both seasonal changes introduced by turbopause height variations and seasonal changes caused by global wind circulation /11,12/. In this "wind-turbulence" model, the respective

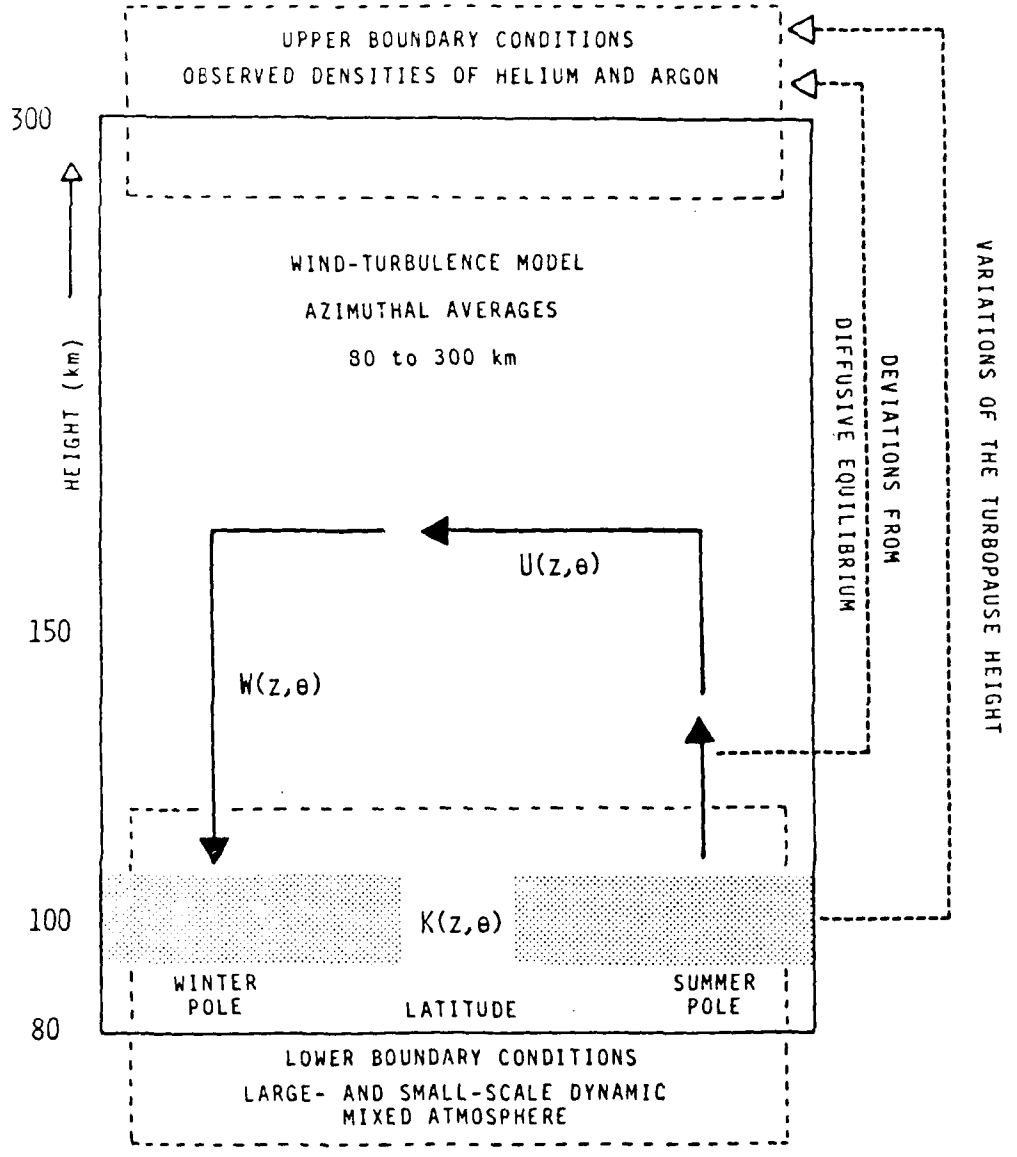

Fig. 2 Basic processes included in the wind-turbulence model. Model parameters and boundary conditions are indicated in a meridional cross section of the atmosphere.

seasonal variations of the turbopause height are assumed, and the wind system, which in addition is required to explain the observations, is calculated. The advantages of this model as compared to the previous ones are the following:

(1) Both seasonal changes in turbulence and in the global wind system, which are certain to exist, are included in the model.
(2) The required height variation of the turbopause is much smaller than in the pure turbulence models.
(3) Even a turbulence lower in summer than in winter could be accommodated by the model. It would require a stronger wind system than is presently predicted by the wind models.

Of course, this model cannot establish the relative importance of the two processes considered. This would require conclusive observational evidence on either the magnitude of the wind system or the magnitude of the turbulence variation. However, it does indicate which combination of the two is compatible with the data.

A detailed discussion of the wind-turbulence model of the thermosphere has been presented by Schuchardt /13/. The principal processes underlying the wind-turbulence model are shown in Fig. 2. It is assumed that the horizontal wind system in the height region between 100 and 150 km transports a mixture of gases present at these heights. This horizontal flow takes place from the summer to the winter pole. A vertical transport of gases at high latitudes and a return flow at altitudes lower than the turbopause closes the circuit. While it is assumed that the horizontal velocities of all constituents are equal, this cannot be the case for the vertical velocities, because above the turbopause the density ratios of the constituents are height-dependent. A downward excess velocity at the winter pole is calculated for helium. According to equation (2), this means a higher helium

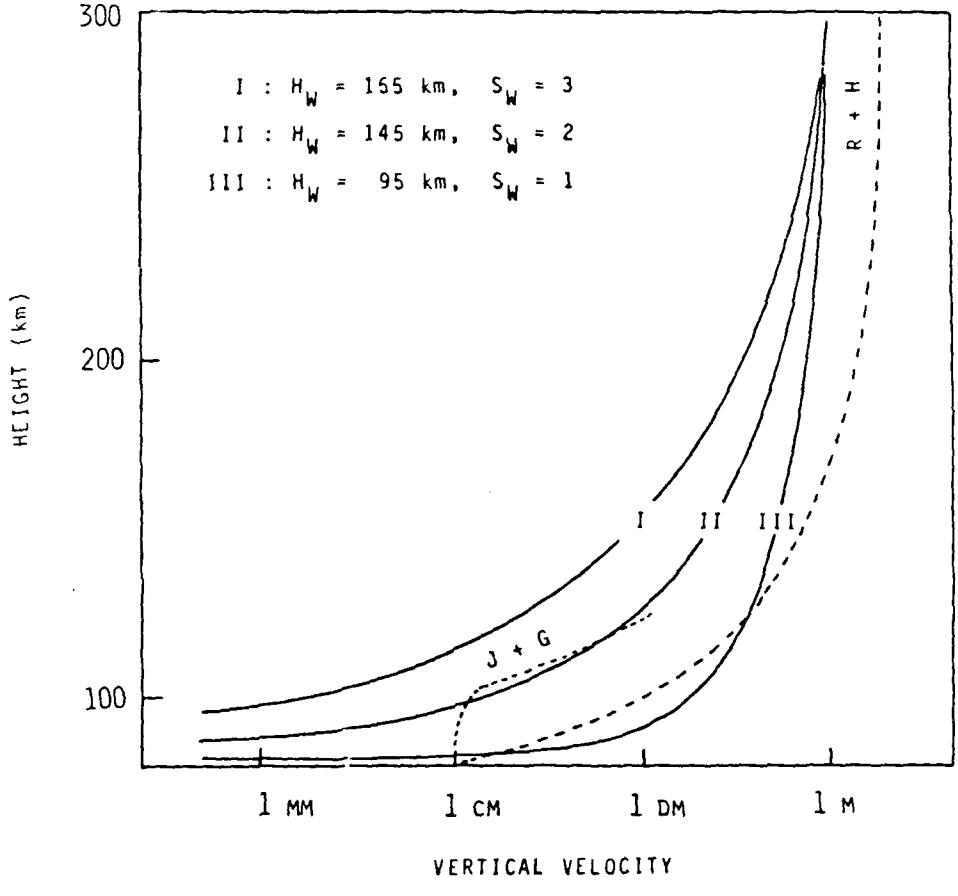

Fig. 3 Height profiles of the vertical velocity used in the wind-turbulence model. H_W (wind scale height) and S_W (form factor) are parameters which determine the profile shape. Velocity profiles inferred from theoretical considerations by Johnson and Gottlieb ((J+G, /14/) and Reber and Hays (R+H, /15/) are indicated by dashed lines.

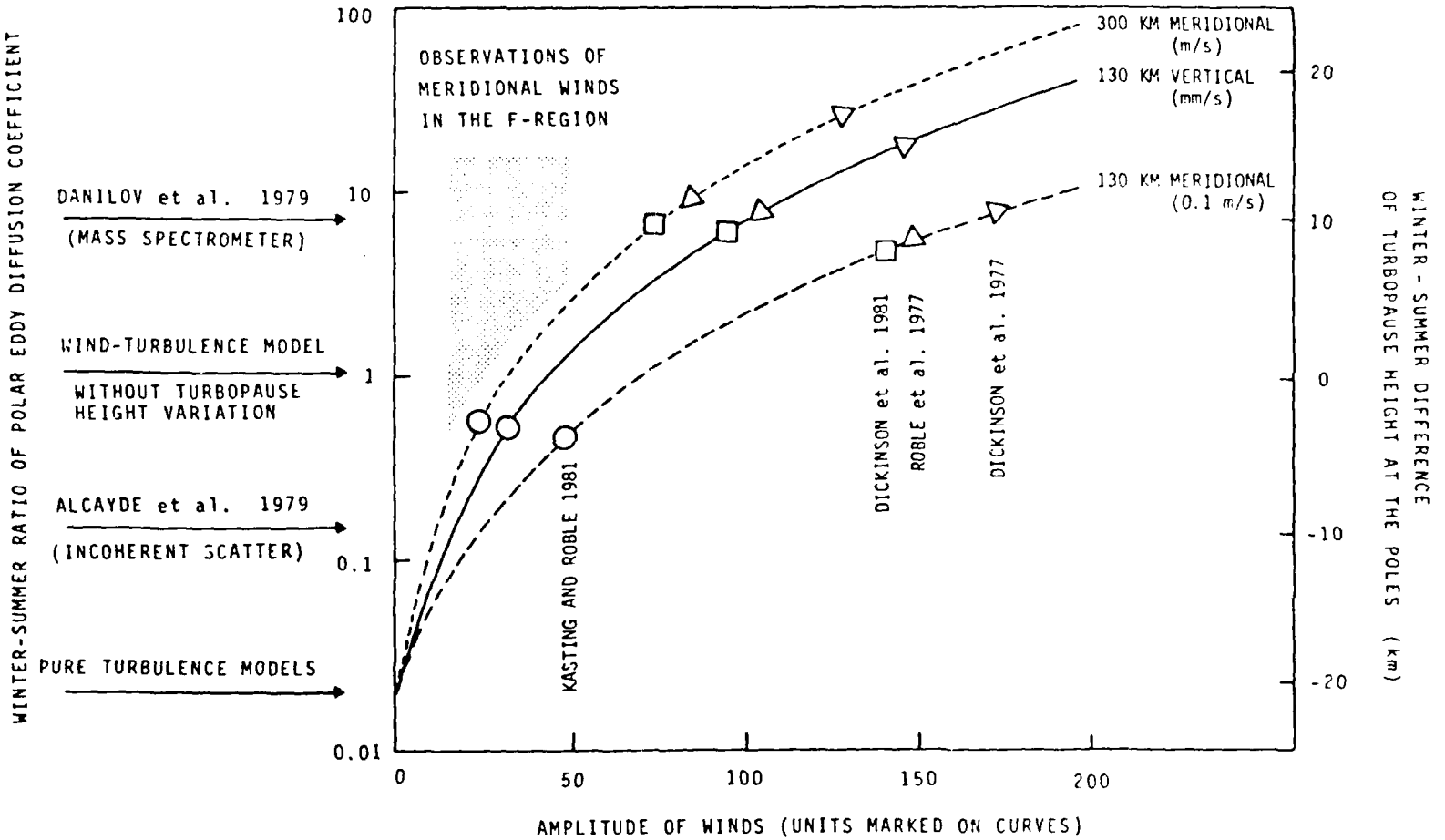

Fig. 4 Results derived from the wind-turbulence model: combinations of turbopause height changes and wind speeds which are consistent with the observed density variations for solstice conditions. Wind velocities observed at F-region heights and those calculated by Kasting and Roble /20/, Dickinson et al. 1981 /8/, Roble et al. /22/, and Dickinson et al. 1977 /21/ are included as a reference. Changes in the polar eddy diffusion coefficient inferred from measurements by Danilov et al. /3/ and Alcayde et al. /4/ are also indicated.

density than for the diffusive equilibrium situation obtained from equation (2) by assuming $\Delta W = 0$. The turbopause acts like a barrier to this dynamic process and causes the differing velocities of the various constituents to become equal below the turbopause.

Together with this dynamic process, there exists a periodic seasonal up and down movement of the turbopause. Both processes are responsible for the strong increase of the helium densities in winter and the correlated decrease of the argon densities. Of course, the model critically depends on the height profile of the vertical diffusion velocities of the minor constituents. In the wind-turbulence model, no attempt has been made to calculate these height profiles, as they depend on various parameters whose accuracy is not well known. To overcome this difficulty, a parametric approach has been chosen, and several models for the height profile of the diffusion velocities have been assumed. This procedure is really not less reliable than calculating these velocities, except that in the parametric approach the assumptions made are more evident than in theoretical models, where the diffusion velocities are calculated, but the unknown factors are not really eliminated. In Fig. 3, three models for the vertical diffusion velocities are shown and compared to theoretical estimates by Johnson and Gottlieb /14/ and Reber and Hays /15/.

Results of the wind-turbulence model are presented in Fig. 4 and are compared to seasonal winds as proposed in various theoretical models. The figure shows the combination of turbopause height variation and wind system necessary to explain the observed seasonal density changes of helium and argon. The required amplitudes of the meridional winds at 300 and 130 km and of the vertical wind at 130 km are given by the curves. The conditions are representative for the winter solstice. The turbopause models would correspond to points on the curves with a zero wind amplitude, while the wind models are represented by the horizontal line corresponding to a vanishing winter-summer turbopause height difference. Results for winds obtained by four theoretical models have been marked on the curves. Observations of meridional daily winds at 300 km are also shown in the figure to indicate which combinations of winds and turbulence would have some observational support.

GEOMAGNETIC ACTIVITY EFFECT

Increased turbulence may also play an important role during thermospheric storms. For example, at middle latitudes significant composition changes are maintained for extended periods of time and presumably long after the actual disturbance process has ceased to operate /16/. A possible explanation for this long recovery phase are deviations from diffusive equilibrium in the lower thermosphere generated by increased turbulence. This increased turbulence is not necessarily associated with changes in the turbopause height, but may occur in a transient layer above the homopause region. The effect such a layer will have on the upper thermospheric composition is illustrated in Fig. 5 for the minor constituent helium. If temperature effects are included, these effects would be consistent with the observations /17/.

Thereby, it is not important whether the mixing initially took place in a restricted altitude region or in the whole upper thermosphere. What is essential is that the mixing extended to the lower thermosphere where the recovery-time constants are large. Whereas the

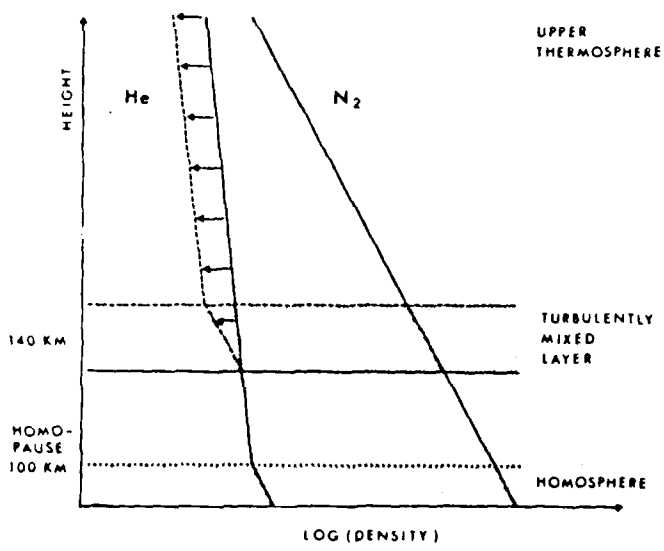

Fig. 5 Density perturbations of a minor gas (helium) caused by a turbulently mixed layer above the homopause region.

upper thermosphere will always quickly return to a diffusive equilibrium situation (τ_D<1h at 250 km altitude), the lower thermosphere will remain disturbed (τ_D>6h at 140 km altitude).

There are several possibilities how this initial mixing could have been affected. For example, dissipation of large-scale traveling atmospheric disturbances (TADs) may thoroughly mix the upper atmosphere /18/. Also, convective transport from high to middle latitudes may contribute to the observed mid-latitude perturbation. This latter mechanism, however, is not supported by numerical simulations /19/.

CONCLUSION

In most of the recently published theoretical models of the seasonal and storm-time variations of the thermosphere, the observations have been explained by global wind cells and a resulting wind-induced diffusion. Variations of turbulence as an additional cause have been excluded. The authors suggest that presently available observations of turbulence and winds are not sufficient to justify such an approach to thermospheric modeling. Both turbulence variations and dynamic processes exist side by side. Most probably, both play a role in thermospheric behavior and should be included in the models.

REFERENCES

1. P.M. Banks and G. Kockarts, Aeronomy, Academic Press, New York and London, 1973

2. P.W. Blum and K.G.H. Schuchardt, The role of eddy turbulence for long periodic variations of upper atmospheric density, Space Research XVIII, 191 (1978)

3. S.P. Zimmerman, Meteor trails and atmospheric turbulence, J. Geophys. Res. 78, 3927 (1973)

4. D. Alcayde, J. Fontanari, G. Kockarts, P. Bauer and R. Bernard, Temperature, molecular nitrogen concentration and turbulence in the lower thermosphere inferred from incoherent scatter data, Ann. Geophys. 35, 41 (1979)

5. A.D. Danilov, U.A. Kalgin and A.A. Pokhunkov, Variation of the turbopause level at polar region, Space Research XIX, 173 (1979)

6. W.K. Hocking, Turbulence in the altitude region 80-120 km, MAP-Handbook 16, 290 (1986)

7. H. Volland and H.G. Mayr, Theoretical aspects of tidal and planetary wave propagation at thermospheric heights, Rev. Geophys. Space Phys. 15, 203 (1977)

8. R.E. Dickinson, E.C. Ridley and R.G. Roble, A three-dimensional general circulation model of the thermosphere, J. Geophys. Res. 86, 1499 (1981)

9. D. Rees, Theoretical thermospheric models, Adv. Space Res. 5, No. 7, 215 (1985)

10. D. Dartt, G. Nastrom and A. Belmont, Seasonal and solar cycle wind variations, 80-100 km, J. Atmos. Terr. Phys. 45, 707 (1983)

11. P.W. Blum and K.G.H. Schuchardt, Principles of a global wind-turbulence model of the latitudinal-seasonal variation of the thermosphere as deduced from satellite data, Space Research XX, 97 (1980)

12. K.G.H. Schuchardt and P.W. Blum, A global wind-turbulence model deduced from satellite data - discussion of results, Space Research XX, 101 (1980)

13. K.G.H. Schuchardt, Modelle zur zonal gemittelten Dynamik der Thermosphäre, dissertation, Universität Bonn (1982)

14. F.S. Johnson and B. Gottlieb, Eddy mixing and circulation at ionospheric levels, Planet. Space Sci. 18, 1707 (1970)

15. C.A. Reber and P.B. Hays, Thermospheric wind effects on the distribution of helium and argon in the earth's upper atmosphere. J. Geophys. Res. 78, 2977 (1973)

16. G.W. Proiss, Local time dependence of magnetic storm effects on the atmosphere at middle latitudes, Ann. Geophys. 2, 481 (1984)

17. P.w. Blum, C. Wulf-Mathies und H. Trinks, Interpretation of local thermospheric disturbances of composition observed by ESRO 4 in the polar region, Space Research XV, 209 (1975)

18. G.A.M. King, The ionospheric disturbance and atmospheric waves, J. Atmos. Terr. Phys. 28, 957 (1966)

19. H. Rishbeth, R. Gordon, D. Rees and T.J. Fuller-Rowell, Modelling of thermospheric composition changes caused by a severe magnetic storm, Planet. Space Sci. 33, 1238 (1985)

20. J.F. Kasting and R.G. Roble, A zonally averaged chemical-dynamical model of the lower thermosphere, J. Geophys. Res. 86, 9641 (1981)

21. R.E. Dickinson, E.C. Ridley and R.G. Roble, Meridional circulation in the thermosphere. II. Solstice conditions, J. Atmos. Sci. 34, 178 (1977)

22. R.G. Roble, R.E. Dickinson and E.C. Ridley, Seasonal and solar cycle variations of the zonal mean circulation in the thermosphere, J. Geophys. Res. 82, 5493 (1977)

END

DATE

FILMED

4-88

DTIC